Department of Chemistry

Electrochemical Sensing of Toxic Gases in Room Temperature Ionic Liquids

Krishnan S/O Murugappan

This thesis is presented for the Degree of
Doctor of Philosophy
of
Curtin University

June 2015

Declaration

To the best of my knowledge and belief this thesis contains no material previously published by any other person except where due acknowledgment has been made.

This thesis contains no material which has been accepted for the award of any other degree or diploma in any university.

Krishnan S/O Murugappan

“Simplicity is the ultimate sophistication”

- Leonardo da Vinci

Abstract

The sensing of highly toxic gases such as methylamine, chlorine and hydrogen chloride is of wide importance due to their use in various applications. Existing electrochemical amperometric gas sensors (AGSs) typically employ aqueous electrolyte/solvents that are not stable in extreme conditions such as high temperatures and pressures. By replacing these solvents with room temperature ionic liquids (RTILs) and utilising their properties such as negligible vapour pressure and high thermal stability, more robust sensors can be created. However before RTILs can replace conventional solvents in AGSs for the detection of these toxic gases, the electrochemical behaviour and analytical utility of the target gases has to be fully understood. Cyclic voltammetry (CV) and chronoamperometry were chosen as the two main electrochemical techniques to study the behaviour of these gases in RTILs.

In this thesis the electrochemical behaviour of methylamine gas was studied in several RTILs on a Pt microelectrode and the analytical utility was studied in two chosen RTILs. A highly complex mechanism has been proposed for the oxidation of methylamine gas and it was found to be the same in all RTILs, involving the formation of ammonia as a by-product which is itself instantly oxidised. A limit of detection (LOD) of approximately 30 ppm was obtained in the two RTILs, which suggests that RTILs can be used to detect methylamine gas. Chronoamperometric analysis revealed a high solubility of methylamine in RTILs of approximately 230-400 mM which is advantageous for using RTILs in AGSs.

The electrochemical behaviour of chlorine gas was then investigated in one chosen RTIL on a Pt microelectrode and it was found that the analytical response is diffusion controlled at low concentrations unlike what was seen previously at high concentrations (complex adsorption process). Analytical studies showed good linearity in the concentration range studied and the current, with comparable LODs for the two techniques, CV (106 ppm) and chronoamperometry (112 ppm). Chronoamperometric analysis allowed the determination of the Henry's law constant which suggested that the solubility of chlorine gas is approximately 35 times more in the gas phase compared to the RTIL phase. This method provides a facile way to determine the solubility of highly toxic gases in different RTIL solvents.

The electrochemical behaviour of hydrogen chloride gas was studied in six RTILs on a Pt microelectrode. In two RTILs degradation of the RTIL occurred in the presence of HCl gas showing that not all RTILs are suitable for the detection of HCl gas, which is valuable information for the choice of solvent used in AGSs. HCl gas is believed to exist in its dissociated form of H^+ and $[HCl_2]^-$ in RTILs. The mechanism for the oxidation is highly complex, involving the formation of several electrogenerated products. However by using the peaks in the CV for the oxidation of $[HCl_2]^-$ and the reduction of protons the analytical utility was studied in $[C_2mim][NTf_2]$ and linear calibration graphs with LODs of 102 and 69 ppm were obtained for the two methods, respectively. The lower LOD obtained for the reduction of protons provides an alternative indirect method of determining the concentration of HCl gas.

Generally, it was concluded that RTILs can be used as favourable solvents for the detection of all three toxic gases which would allow for more robust AGSs to be created. To extend the study to alternative electrode surfaces the electrochemical behaviour of these gases was then investigated on various screen printed electrodes (SPEs). Pt SPEs was found to be the best surface to obtain clear analytical responses for all three gases. The responses on the Pt SPEs were then compared to Pt microelectrodes and comparable LODs were obtained suggesting that these low cost SPEs can be utilised in AGSs. This allows us to exploit properties which are unique to SPEs, such as smaller volume of electrolyte (thin layer), which would allow faster response times and cheaper manufacturing costs due to the smaller amount of expensive electrode material/metal.

Finally nanomaterials such as magnetic magnetite nanoparticles and Pt macroporous frameworks were synthesised and characterised using various physical and electrochemical techniques. Preliminary studies using these nanomaterials for methylamine gas sensing have been reported, where the magnetite nanoparticles do not appear to take part in the reaction and the Pt macroporous frameworks are active for the oxidation of methylamine gas.

Overall the use of RTILs to replace conventional solvents appears to be very promising for the three target gases.

Acknowledgments

First and foremost I would like to express my deep gratitude to both my supervisors, Dr Debbie Silvester and Prof. Damien Arrigan for their patient guidance and enthusiastic encouragement during my Ph.D. Their supervision and useful critiques throughout the last three years has been instrumental in the completion of this thesis. I would also like to offer my special thanks to Dr. Debbie Silvester for giving me the opportunity to work with her on her Discovery research project. I would also like to thank Dr Debbie Silvester and Curtin University for a postgraduate research scholarship. I am also particularly grateful for the assistance given by Prof. Damien Arrigan while Dr Debbie Silvester was away on maternity leave. His quirky science jokes are all you needed, to brighten up your day!

The completion of this thesis would not have been possible without the technical expertise of Mr. Peter Chapman. His advice on the gas mixing setup, used throughout this thesis, was vital to prevent any gas leaks and ensure safety and I am particularly grateful for his assistance. I would like to thank Dr. Kane O' Donell for his help with all the XPS measurements and great insights on analysing XPS data. My grateful thanks are extended to Dr Tom Becker for his help in obtaining data using confocal Raman spectroscopy. I wish to also acknowledge Dr Deeptangshu Chaudhary and Dr Petra Szilagyi for the collaboration on the magnetite nanoparticle and Pt macroporous framework studies respectively. I would like to acknowledge Dr Ching Goh for helping me run the NMR samples. I would also like to extend my thanks to the technicians of the Curtin University electron microscopy laboratory for training me in the use of a SEM. I would like to take this opportunity to thank Dr Leigh Aldous for all the useful discussions on certain aspects of my thesis. I would also like to take this opportunity to thank the electrochemistry and sensors group for all the coffee breaks, lunches, insightful discussions and the great atmosphere in the lab! Special mentions to Eva, Junie, Yang, Shane and Colin.

I would like to thank my parents, Murugappan Krishnan and Alagammai Rama Sundaram, and my brother, Lakshman Murugappan, for all the support and love they have provided me over the years. Although they are 3,912 km away in Singapore I know they are always thinking about me! I would also like to take this opportunity to thank my Aunt, Rajaletchimi Rajagopal, who took special care of me when I was

young and has been waiting eagerly for me to complete my thesis so that she can see me again!

I can never forget my Perth family who made my stay in Perth truly unforgettable. Special mention to Brodene Straw, Emilie Pascal, Yen Hieu and Elspeth Meikle who supported me throughout the 3 years of my Ph.D. Thanks to all the current and previous residents of flat 37 in Kurrajong Village (KV), especially Elspeth Meikle, Jason Lee, Rebecca White, Rachael Wood, Cameron Tysoe, Lily Winer, Reilly Evetts, Brae Price and Emily Wilks who had to make do with me as their flatmate and kept me sane during the past 3 years. Special mention to Elspeth Meikle for all the TV shows that we watched; Rebecca White for all the jokes and innuendos; Jason Lee, Rachael Wood and Reilly Evetts for all the board games and late night drinks; Jean Clarel and Vincent Goilet for all the soccer talk and Arsenal games; Jessica Armitage, Yen Hieu and Brodene Straw for all the food escapades.

I need to thank the Kurrajong Village housing team especially the housing staff, Norman Johnson, Amanda Tan and Yen Hieu for all the support they gave me while I was working there as a Housing Assistant during both my undergraduate and my postgraduate studies. Thanks also to all the current and past Housing Assistants who I worked with. Special mentions to Rachael Wood and Sushil Ramchandani. Thanks also to the Cardosos, Micael, Sonia and Adriano for taking good care of me in Portugal. Once a KVian always a KVian!

I would like to thank all my Singapore friends for all the chats in the OM Bros chat group on WhatsApp. I always feel that I am not that far away from Singapore with you guys.

I also would like to thank everyone else who names I might have missed out and helped me out in one way or another in the last 3 years!

Contents

Abstract ***iii***

Acknowledgements ***v***

Table of Contents ***vii***

Glossary ***xiv***

1. INTRODUCTION **1**

1.1 Gas Sensing **3**

1.1.1 Amperometric Gas Sensors 4

1.1.1.1 Electrolytes in AGSs *6*

1.1.1.2 Electrodes in AGSs *8*

1.2 Introduction to Room Temperature Ionic Liquids (RTILs) **8**

1.2.1 Properties of RTILs 10

1.2.1.1 Wide Electrochemical Window *10*

1.2.1.2 Negligible Vapour Pressure/Low Volatility *11*

1.2.1.3 Conductivity *12*

1.2.1.4 High Thermal Stability *12*

1.2.1.5 High Viscosity *13*

1.2.2 Gas Solubility in RTILs 13

1.2.3 Previous and Future Gas Studies in RTILs 14

1.3 Introduction to Screen Printed Electrodes (SPEs) **19**

1.4 Modification of Surfaces **24**

1.5 Aims **24**

1.6 References **26**

2. BACKGROUND TO ELECTROCHEMISTRY AND CHARACTERISATION TECHNIQUES **35**

2.1 Dynamic Electrochemistry **37**

2.2 Electrical Double Layer **38**

2.3 Faradaic and Non-Faradaic Process **39**

2.4 Mass Transport **40**

2.5 Electron Transfer **42**

2.6 Testa and Reinmuth Notation **43**

2.7 Practical Aspects of Electrochemistry **44**

2.7.1 Electrochemical Cells 44

2.7.2 Electrodes Used in this Thesis 46

2.8 Electrochemical Techniques **48**

2.8.1 Cyclic Voltammetry 48

2.8.2 Chronoamperometry 52

2.9 Voltammetry in RTILs **53**

2.10 Background to Scanning Electron Microscopy, Confocal Raman Spectroscopy and X-Ray Photoelectron Spectroscopy **54**

2.10.1 Scanning Electron Microscopy (SEM) 54

2.10.1.1 Components of a SEM *55*

2.10.1.2 Electron-Sample Interactions *57*

2.10.2 X-Ray Photoelectron Spectroscopy (XPS) 60

2.10.3 Confocal Raman Spectroscopy 61

2.11 References **62**

3. EXPERIMENTAL CHAPTER **65**

3.1 Chemical Reagents and Gases **67**

3.2 Electrodes and Cells **67**

3.3 Electrochemical Experiments **75**

3.4 Gas Mixing Setup **76**

3.5 XPS, SEM, NMR and Raman Spectroscopy Experiments **80**

3.6 References **81**

4. ELECTROCHEMICAL OXIDATION AND SENSING OF METHYLAMINE GAS IN ROOM TEMPERATURE IONIC LIQUIDS **83**

4.1 Introduction **85**

4.2. Experimental Section **87**

4.2.1 Chemical Reagents 87

4.2.2 Electrochemical Experiments 88

4.2.3 Gas Mixing Setup 88

4.3 Results and Discussion 89

4.3.1 Electrochemical Response of Methylamine Gas in $[C_4mpyrr][NTf_2]$ on a Pt Microelectrode. 89

4.3.2 Electrochemical Response of Methylamine Gas in $[C_4mpyrr][NTf_2]$ on a Au Microelectrode 93

4.3.3 Electrochemical Study of Methylamine Gas on a Pt microelectrode in Different RTILs 94

4.3.4 Analytical Utility of Methylamine Gas in $[C_2mim][NTf_2]$ and $[C_4mpyrr][NTf_2]$ 99

4.4 Conclusions 101

4.5 References 102

5. ELECTROCHEMICAL REDUCTION AND SENSING OF CHLORINE GAS IN A ROOM TEMPERATURE IONIC LIQUID 105

5.1 Introduction 107

5.2 Experimental Section 110

5.2.1 Chemical Reagents 110

5.2.2 Electrochemical Experiments 111

5.2.3 Gas Mixing Setup 111

5.2.4 Safety Considerations 112

5.3 Results and Discussion 112

5.3.1 Electrochemical Reduction of Chlorine Gas on a Pt Microelectrode 113

5.3.2 Analytical Utility of Chlorine Gas 116

5.3.3 Chronoamperometry Analysis for the Electrochemical Reduction of Chlorine Gas 119

5.3.4 Henry's Law Constant of Chlorine Gas in $[C_2mim][NTf_2]$ 121

5.4 Conclusions 122

5.5 References 123

6. ELECTROCHEMICAL OXIDATION AND SENSING OF HYDROGEN CHLORIDE GAS IN ROOM TEMPERATURE IONIC LIQUIDS 127

6.1 Introduction 129

6.2 Experimental Section **131**

6.2.1 Chemical Reagents 131

6.2.2 Electrochemical Experiments 132

6.2.3 Gas Mixing Setup 132

6.2.4 Nuclear Magnetic Resonance Experiments 133

6.3 Results and Discussion **133**

6.3.1 Electrochemical Behaviour of Hydrogen Chloride Gas in Various RTILs on a Pt Microelectrode 133

6.3.2 Electrochemical Oxidation of Hydrogen Chloride Gas in RTILs at Various Scan Rates on a Pt Microelectrode 140

6.3.3 Analytical Utility of HCl Gas in $[C_2mim][NTf_2]$ 151

6.4 Conclusions **155**

6.5 References **156**

7. SCREEN PRINTED ELECTRODES FOR THE DETECTION OF METHYLAMINE, CHLORINE AND HYDROGEN CHLORIDE GAS **159**

7.1 Introduction **162**

7.2 Experimental **164**

7.2.1 Chemical Reagents 164

7.2.2 Electrochemical Experiments 164

7.2.3 Scanning Electron Microscopy Experiments 165

7.2.4 X-Ray Photoelectron Spectroscopy Experiments 165

7.2.5 Gas Mixing Setup 166

7.3 Physical Characterisation of SPEs **166**

7.3.1 SEM 166

7.3.2 XPS 168

7.3.2.1 Pt SPE *168*

7.3.2.2 Au SPE *172*

7.3.2.3 C SPE *177*

7.4 Methylamine Gas **181**

7.4.1 Electrochemical Oxidation of Methylamine Gas on Pt SPEs 181

7.4.2 Analytical Utility of Methylamine Gas on Pt SPEs 183

7.4.3 Electrochemical Behaviour and Analytical Utility of Methylamine Gas on Au and C SPEs 185

7.5 Chlorine Gas 187

7.5.1 Electrochemical Reduction of Chlorine Gas on Pt SPEs 187

7.5.2 Analytical Utility of Chlorine Gas on Pt SPEs 189

7.5.3 Electrochemical Behaviour and Analytical Utility of Chlorine gas on Au, C, Graphene Modified C and Carbon Nanotubes Modified C SPEs 191

7.6 Hydrogen Chloride Gas 193

7.6.1 Electrochemical Oxidation of Hydrogen Chloride Gas on Pt SPEs 193

7.6.2 Analytical Utility of Hydrogen Chloride Gas on Pt SPEs 201

7.6.3 Electrochemical Behaviour of Hydrogen Chloride Gas on Au and C SPEs 204

7.7 Comments about the Reproducibility, Reusability and Advantages of SPEs 206

7.8 Conclusions 207

7.9 References 208

8. ELECTROCHEMICAL CHARACTERIZATION OF AN OLEYL - COATED MAGNETITE NANOPARTICLE-MODIFIED ELECTRODE 211

8.1 Introduction 213

8.2 Experimental 217

8.2.1 Chemical Reagents 217

8.2.2 Synthesis of Particles 217

8.2.3 SEM 218

8.2.4 Confocal Raman Spectroscopy/Microscopy 219

8.2.5 XPS 219

8.2.6 Electrochemical Experiments 219

8.3 Results and Discussion 220

8.3.1 Characterisation of Fe_3O_4 Nanoparticles 220

8.3.1.1 Physical Characterisation *220*

8.3.1.2 Confocal Raman Spectroscopy *221*

8.3.1.3 XPS *223*

8.3.2 Electrochemical Characterisation 224

8.3.2.1 Electrochemical Behaviour in 0.1 M H_2SO_4 *225*

8.3.2.2 Electrochemical Characterisation in Varying Concentrations of H_2SO_4 *231*

8.4 Conclusions **233**

8.5 References **234**

9. SYNTHESIS AND CHARACTERIZATION OF PLATINUM MACROPOROUS FRAMEWORK **239**

9.1 Introduction **241**

9.2 Experimental **242**

9.2.1 Chemical Reagents 242

9.2.2 Electrochemical Experiments 243

9.2.3 SEM 243

9.3 Results and Discussion **243**

9.3.1 Synthesis of Metal Frameworks 243

9.3.2 SEM Characterisation 246

9.3.3 Electrochemical Characterisation 248

9.4 Conclusions **252**

9.5 References **253**

10. PRELIMINARY STUDIES OF NANOMATERIALS FOR METHYLAMINE GAS SENSING IN A ROOM TEMPERATURE IONIC LIQUID **255**

10.1 Introduction **257**

10.2 Experimental **257**

10.2.1 Chemical Reagents 257

10.2.2 Electrochemical Experiments 257

10.3 Results and Discussion **258**

10.3.1 Magnetite Nanoparticles 258

10.3.2 Platinum Macroporous Framework 260

10.4 Conclusions 262

10.5 References 263

11. CONCLUSIONS AND FUTURE WORK 265

11.1 Conclusions 267

11.2 Future Work 269

11.3 References 272

Appendix A 274

Appendix B 278

Appendix C 280

Glossary

Symbol	Definition
α	charge transfer coefficient
ρ	density
τ	dimensionless time parameter
η	viscosity
v	scan rate
$\frac{dc}{dx}$	direction of concentration gradient
a	hydrodynamic radius
A	area of electrode
c	concentration
C	homogeneous chemical step
c_{bulk}	bulk concentration
D	diffusion coefficient
E	potential
E	homogeneous electron transfer step
E_1	start potential
$E_{1/2}$	half wave potential
E_2	end potential
E_{app}	applied potential
E_f^0	formal electrode potential
E_{RE}	potential difference across the reference electrode/solution interface
E_{WE}	potential difference across the working electrode/solution interface
ΔE_p	Peak to peak separation
F	Faraday Constant (96485 C/mol)
H^{cc}	Henry's law dimensionless "volatility constant"

Table 1: List of symbols commonly used throughout this thesis

Symbol	Definition
i	current
i_d	diffusion limiting current
j	flux
J_d	diffusion flux
k_0	standard electrochemical rate constant
k_B	Boltzmann constant (1.38×10^{-23}J/K)
k_b	backward rate constant
K_e	partitioning coefficient
k_f	Forward rate constant
m	electrochemically-active material
n	number of electrons
O	solution species prone to undergoing a one-electron reduction
$[O]_0$	concentration of species O at electrode
Q	charge
R	solution species prone to undergoing a one-electron oxidation
$[R]_0$	concentration of species R at electrode surface
R	universal gas constant
r_e/r_d	radius of the electrode
R_s	resistance of the solvent
T	temperature
t	time
x	direction

Table 2: List of symbols commonly used throughout this thesis contd…

Unit	Definition
%	percentage
°C	degree Celsius
A	amp
C	coulomb
eV	electron volt
K	Kelvin
m	metre
M	molar
Pa	Pascal
ppm	parts per million
s	seconds
V	voltage

Table 3: List of units commonly used throughout this thesis

Prefix	Definition
M	Mega
k	Kilo
m	Milli
c	Centi
µ	Micro
n	nano

Table 4: List of prefixes of units used throughout this thesis

Abbreviation	Definition
A^-	anion
AGS	amperometric gas sensor
BSE	Back scattered electrons
CA	chronoamperometry
CE	counter electrode
CNT	carbon nanotubes
CPE	carbon paste electrode
CRS	confocal Raman spectroscopy
CSTR	continuously stirred tank reactor
CV	cyclic voltammetry
DMSO	dimethyl sulfoxide
DPS	deep purge system
EDS	energy dispersive X-ray spectroscopy
FC	field-cooling
FESEM	field emission Scanning electron microscopy
FIBSEM	focussed ion beam Scanning electron microcopy
GC	glassy carbon
IR	infra-red
LOD	limit of detection
MA	methylamine

Table 5: List of abbreviations used throughout this thesis

Abbreviation	Definition
MDEA	monodimethylethanolamine
MMEA	monomethylethanolamine
NMR	nuclear magnetic resonance spectroscopy
OHP	outer Helmholtz plane
OSHA PEL	occupational safety and health administration permissible exposure limit
PC	personal computer
PEEK	polyether ether ketone
PID	photoionization detector
PTFE	polytetrafluroethylene
RE	reference electrode
RH	relative humidity
RTIL	room temperature ionic liquid
SEM	scanning electron microscopy
SPE	screen printed electrode
SQUID	superconducting quantum interference device
TBAP	tetra-*N*-butylammonium perchlorate
THF	tetrahydrofuran
vdW	van der Waals
WE	working electrode
XPS	x-ray photoelectron spectroscopy
ZFC	zero-field-cooling

Table 6: List of abbreviations used throughout this thesis contd…

1. Introduction

Gas detection is an important aspect of numerous industries and many lives are saved on a daily basis due to precautionary measurements taken by using gas sensing devices. The importance of monitoring toxic gas leaks cannot be emphasized enough. There are various types of gas sensors that are used for the detection of gases and the most common type of gas sensor that is used is an amperometric gas sensor (AGS). Different types of gas sensors are introduced in this chapter and the many advantageous for using AGSs are discussed. The principles behind the working of AGSs are presented and discussed paying particular attention to the electrolyte and the electrodes. The electrolytes used in an AGS are usually aqueous solvents that do not allow the AGS to operate under drastic conditions such as high temperatures and pressures due to evaporation/breakdown of the solvent. By replacing the solvents with room temperature ionic liquids (RTILs) and exploiting their properties such as negligible vapor pressure and high thermal stability, more robust sensors can be made. The electrodes used in an AGS are usually made from an expensive metal. By using screen-printed electrodes (SPEs), cheap manufacturing costs due to the small amount of expensive electrode material/metal required and fast response times due to small volumes of electrolyte used (e.g. thin layer), can be achieved which are both attractive improvements for an AGS. Therefore in this chapter first the properties and advantageous of using RTILs and SPEs will be presented from a gas sensing perspective. An extensive literature review on the most relevant research carried out using RTILs and SPEs will also be presented at the end of each section.

1. INTRODUCTION **1**

1.1 Gas Sensing **3**

1.1.1 Amperometric Gas Sensors 4

1.1.1.1 Electrolytes in AGSs *6*

1.1.1.2 Electrodes in AGSs *8*

1.2 Introduction to Room Temperature Ionic Liquids (RTILs) **8**

1.2.1 Properties of RTILs 10

1.2.1.1 Wide Electrochemical Window *10*

1.2.1.2 Negligible Vapour Pressure/Low Volatility *11*

1.2.1.3 Conductivity *12*

1.2.1.4 High Thermal Stability *12*

1.2.1.5 High Viscosity *13*

1.2.2 Gas Solubility in RTILs 13

1.2.3 Previous and Future Gas Studies in RTILs 14

1.3 Introduction to Screen Printed Electrodes (SPEs) **19**

1.4 Modification of Surfaces **24**

1.5 Aims **24**

1.6 References **26**

1. Introduction

1.1 Gas Sensing

People all over the world are affected by toxic gases in everyday life in ways such as natural gas leaks or in worst case scenarios as chemical warfare weapons.[1-10] Therefore it is essential to be able to detect and monitor harmful gases. There are various methods to detect toxic gases such as catalytic bead sensors, infra-red (IR) sensors, photoionization detectors (PID), metal oxide semiconductor sensors and amperometric sensors.[11]

In a catalytic bead sensor a wire coil encased with a ceramic or glass material is coated with a catalyst which is specific to the type of gas to be detected. The system is then electrically heated which allows the gas to burn on the surface which generates a temperature rise which in turn causes an increase in resistance.[12] An external circuit detects this resistance and immediately reduces the electric power to the wire until the original resistance is restored. The concentration of gas is directly proportional to the amount of electric power removed. One major limitation of catalytic bead sensors is that the catalyst can be poisoned due to contamination.[12] These sensors also have limitations in high humidity environments and oxygen has to be present for the sensor to work (combustion reaction).[12]

The IR sensor works by a beam of IR wavelength being irradiated at a sample and then depending on the gas being detected some of the energy is absorbed (based on the gas molecules' natural frequency) and some of the energy is transmitted.[12,13] The decrease in the energy that is transmitted is then detected.[12] However an IR sensor cannot operate at high temperatures and high humidity due to its mode of operation.

Another type of gas sensor is the PID where the sample is irradiated with high energy photons, typically in the UV region and this breaks up the gas molecules into charged ions. These charged ions are then collected at an electrode producing a current which is proportional to the concentration of gas.[12] The major issue with these sensors is that they require frequent cleaning of the PID lamps that produce the high energy photons.[12]

The next type is the semiconductor sensor, also known as a solid state sensor. These sensors work by measuring resistance change, which is proportional to the concentration of gas that is absorbed onto the surface of a semiconductor material such as a metal oxide.[14] Solid state sensors have many advantages such as long life, sensitivity and resistant to poisoning however they are very sensitive to temperature and humidity changes. Another major limitation is cross interferences due to non-specificity.[12,15] There is also a long recovery time between expose of gases which might not be advantageous for continuous monitoring.[13]

Amperometric sensors are the next type of gas sensors and they are often the most popular for the measurement of toxic gases.[11] They are cheap, portable and do not require a lot of power to run.[11] The focus of the work carried out in this thesis is on amperometric gas sensors (AGSs), so an in-depth analysis of AGSs and how they work will be discussed in the next section.

1.1.1 Amperometric Gas Sensors

AGSs have many advantages over other sensing methods, including inexpensive fabrication steps, high sensitivity, wide linear range, low power consumption and the ability to be miniaturized. A particular advantage is that “on-the-spot” analysis can be performed and the sample does not have to be taken back to the laboratory to be

analysed by slow and costly methods. The Clark cell invented by Professor Leland Clark was the first amperometric sensor developed and was used for oxygen sensing in blood in the 1950s and still used now with modifications.[16-18] The setup consisted of a Pt cathode, a potassium chloride calomel/ Ag wire anode, a cellophane membrane and a power supply. Oxygen diffused through the membrane, entered the solution and got reduced at the working electrode (Pt cathode) when a potential of 0.6 V was applied between the two electrodes from the power supply.[11,18] This reduction reaction caused a movement of electrons which produced a current which is proportional to the concentration of the gas. This work by Clark paved the way for the future of AGSs.

Current AGSs usually employ a 3-electrode approach where the counter, reference and working (sensing) electrode are all connected through an electrolyte medium.[17,19] Currently commercial gas sensors are produced by companies such as Honeywell, Draeger, Membrapor and Alphasense. Figure 1.1 shows a commercial amperometric oxygen gas canister from Membrapor. The three pins on the bottom are inserted into a detector case which gives the user digital values of gas concentrations. Figure 1.2 shows a cartoon of what the interior of such a commercial gas canister looks like in a simplified manner. There is a porous membrane on top of the canister that allows the gas to pass through, and then the gas diffuses through the electrolyte to reach the working electrode which is the sensing electrode. Depending on the gas, either an oxidation or reduction reaction occurs which produces movement of electrons which in turns produces a current which is proportional to the concentration of gas. The three pins at the bottom provide electric contact to the three electrodes and the electrolyte provides electrical contact between the three electrodes. In this thesis the

improvement of such an AGS canister is considered on two fronts. One is the electrolyte and the other is the electrodes.

Figure 1.1: Commercial amperometric gas sensor canister from Membrapor (reproduced with permission)

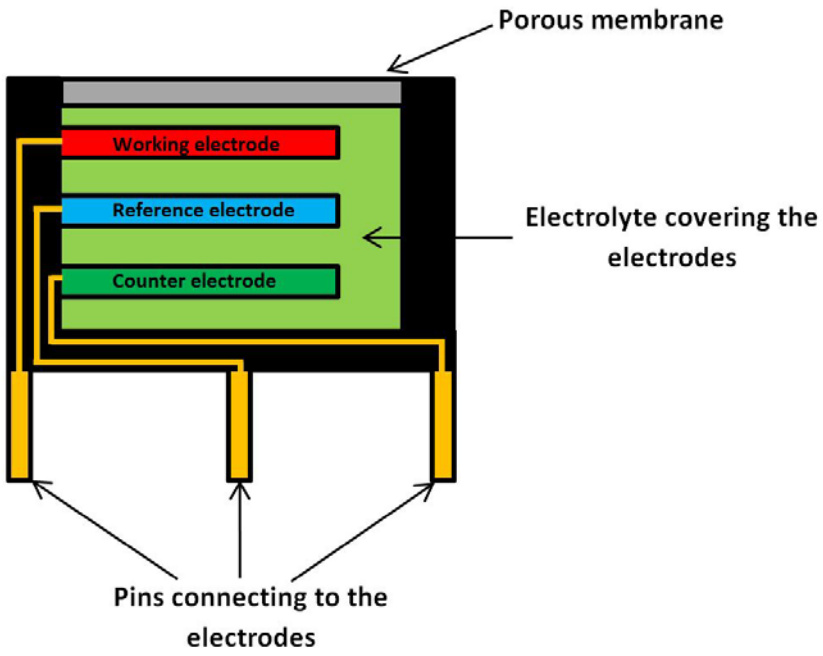

Figure 1.2: Cartoon of a simplified commercial amperometric gas sensor canister (interior)

1.1.1.1 Electrolytes in AGSs

The electrolyte plays a very important role in amperometric gas sensing. It is the phase where the gas and the electrode (solid phase) meet. The electrolyte provides ionic electrical contact between the three electrodes and allows the electroactive species to come in contact with the working electrode surface so that either an oxidation or reduction reaction can occur. The lifetime of an AGS is dependent on

the stability of the electrolyte used. Common aqueous electrolyte/solvents (H_2SO_4/H_2O) are not able to last in extreme conditions such as high temperatures and pressures.[20,21] By replacing the solvent/electrolyte with solvents such as room temperature ionic liquids (RTILs) more robust sensors may be created. By using RTILs (utilising their low vapour pressure property), pathways for membrane free gas sensors which would simplify device calibration, can also be created.[22] In a commercial gas sensor the membrane plays a big role in the diffusion of the gas, in fact the response time is limited by the diffusion time through the membrane as diffusion of gases through air and the solvent will be faster. Therefore, the type and thickness of the membrane both play a huge role in the response time.[11] These membranes also serve another purpose which is to retain the solvent and make sure that the solvents do not evaporate out. By replacing solvents in these sensors with RTILs there is no need to worry about solvent loss. The required sensing range in the real world is between -60 °C to 60 °C which is much larger than conventional solvents can handle (-45 °C to 50 °C).[11] Recently experiments performed by Alphasense demonstrated the issue with conventional solvents (H_2SO_4) where there was 50 % loss by mass of the solvent at temperatures of 20 $^{\circ}$C and at relative humidity between 0-25 % RH . At a humidity value of 95 %, flooding in the sensing chamber occurred as a result of 100 % increase by mass of solvent. Due to the drastic changes in the solvent composition due to temperature and humidity changes constant calibration of the sensors is needed. This makes RTILs more attractive as solvents of choice in AGSs as calibration of the sensors can be limited. However RTILs are much more viscous than conventional solvents therefore the diffusion of the gases may take longer, which would also need to be considered in the design of a sensor. In this thesis the electrochemical behaviour of three toxic gases will be

investigated in RTILs, opening up possibilities of creating membrane free AGSs with more robustness for these three target gases.

1.1.1.2 Electrodes in AGSs

Miniaturization has been the driving force for many industries and the gas sensing industry is no different. Being able to have low cost portable sensors (e.g. sensors on clothing of personnel exposed to toxic gases[23]) has been the motivation and screen printing technology is a platform for the fabrication of chemical sensors with those properties.[24,25] In a commercial AGS canister (figure 1.1) the electrode material is usually made with relatively large amounts of expensive metal such as platinum or gold. In this work screen printed electrodes (SPEs), where all three electrodes are screen printed in a small area on a ceramic substrate, will be investigated for their suitability in gas sensing. By using SPEs, AGSs can be made more cost effective as less metal is required (cheaper manufacturing costs) and also much less electrolyte/solvent would be needed which would give faster response times.

This thesis also aims to explore the possibility of electrochemical gas sensing, using RTILs on low cost SPEs. Combined with the low volatility of ionic liquids these SPEs could not only propose to be a cheap alternative to commercial sensors but also be robust for their sensing applications. In the upcoming sections RTILs and SPEs will be introduced.

1.2 Introduction to Room Temperature Ionic Liquids (RTILs)

RTILs are increasingly being investigated as replacement solvents in various industries such as batteries, lubricants, solar cells, fuel cells, solvents for synthesis, extraction[26-40] and the gas sensing industry is slowly catching up. RTILs typically consist of a bulky asymmetric organic cation and small inorganic anion and are

liquids at room temperature.[41] The low melting points of RTILs are due to the high asymmetry between the cation and the anion which makes it unlikely to form a crystal lattice like NaCl. They possess various intrinsic properties such as low volatility, high viscosity, wide electrochemical windows, tuneability and the ability to dissolve a wide range of species.[42] In a conventional ionic solution (e.g. NaCl), the ions are dissociated and surrounded by a solvation shell created by the solvent molecule (H_2O) as shown in figure 1.3. It is important to note here that RTILs act as both the electrolyte and the solvent, unlike commercial gas sensors where you have the H_2O/H_2SO_4 solvent/electrolyte combination. Therefore the behaviour inside RTILs may be different to conventional solvents. This is the subject of many investigations and the behaviour in RTILs has mostly followed that in conventional solvents but there are some exceptions.[15] Figure 1.4 shows the common anions and cations used in this work. Some properties of RTILs will be discussed in greater detail now.

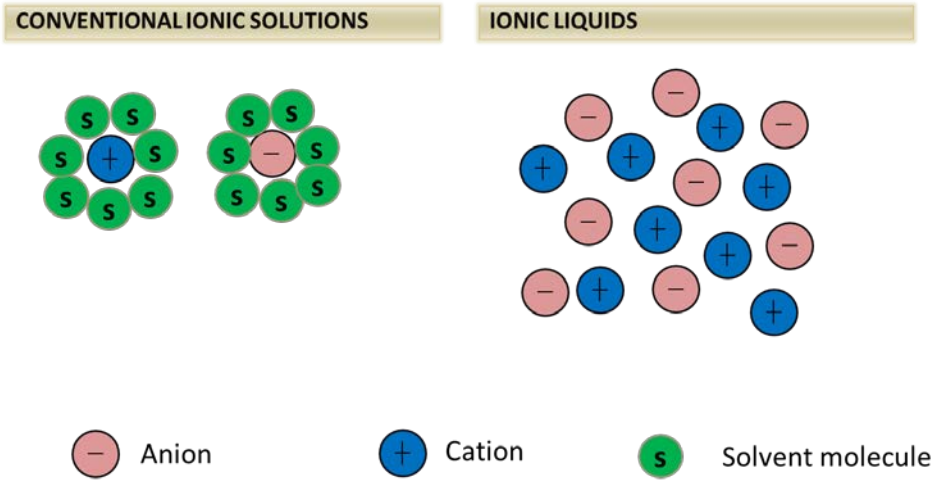

Figure 1.3: Simplified diagram showing the difference between conventional ionic solutions and RTILs

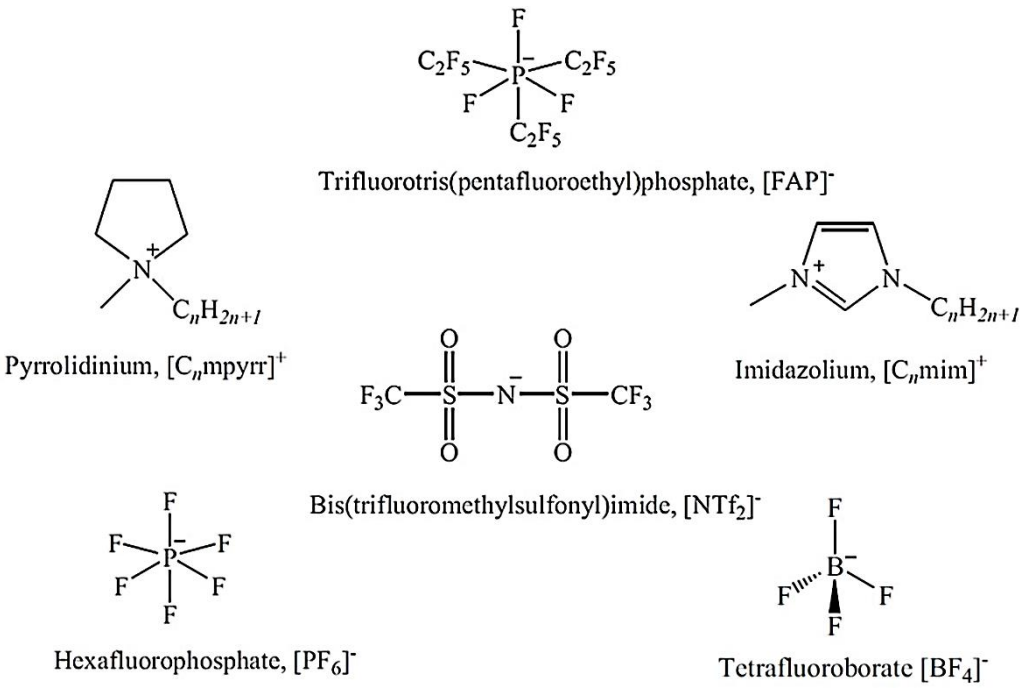

Figure 1.4: Molecular structures of cations and anions that made up the ionic liquids and the nomenclature used throughout this thesis

1.2.1 Properties of RTILs

The properties of RTILs will now be discussed with comparison being drawn to conventional solvents, and their use in AGSs, as their inherent properties provide a valuable medium for the development of stable and robust AGSs.

1.2.1.1 Wide Electrochemical Window

The potential difference between the anodic and cathodic decomposition potential of a solvent is termed the 'electrochemical window'. A wide electrochemical window is a very important property for gas sensing purposes. Some gases oxidise at strongly positive or negative potentials; conventional solvents may degrade at these conditions but ionic liquids are more stable which make them ideal solvents.[15,20,43] In a conventional AGS the common electrolyte/solvent mix used is sulphuric acid/water which has a narrow electrochemical window of approximately 2 V [44] due to oxidation of water and reduction of protons, whereas RTILs have electrochemical

windows of between 4 and 7 V [42] due to the robustness of the cation and anions. It also opens up opportunities for new gases that could not be oxidised or reduced previously in an aqueous medium due to the narrow electrochemical window.

However, impurities when present in ionic liquids are known to decrease the electrochemical window and the decrease occurs on both the cathodic and anodic limits.[42] Water is the biggest impurity in ionic liquids and even hydrophobic RTILs are known to absorb water.[42] An increase in water content has known to decrease the electrochemical window by a process known as water electrolysis.[45] Impurities that are left over from the synthesis of these ionic liquids can also affect the electrochemical window.

1.2.1.2 Negligible Vapour Pressure/Low Volatility

Low volatility is probably the most attractive property of RTILs that makes them interesting solvents for their use in AGSs as they prevent sensor failure due to evaporation which is very common with conventional solvents. The vapour pressure of RTILs is negligible (a few mPa as compared to water which is 3167.73 Pa at 298 K[46]) which would mean that it will be able to withstand high temperatures and low pressures without any evaporation.[47] This ability is clearly demonstrated as they are used in X-ray photoelectron spectroscopy where ultra-high vacuum is required.[48-51] This ability to withstand extreme conditions would mean that sensor calibration will not be frequent as in the case of conventional solvents where solvent changes are expected. The low volatility also allows for a new generation of AGSs termed membrane-less AGSs which would not have been possible with conventional solvents.

1.2.1.3 Conductivity

It has been mentioned earlier that RTILs are composed entirely of ions which gives them their inherent conductivity. The conductivity of a RTIL depends on the mobility of the ions. Therefore each RTIL with a different anion and cation combination will have a different conductivity ranging from 0.12-9 $m\Omega^{-1}cm^{-1}$ at a temperature of 298 K.[11] Due to the mobility dependence of the conductivity, as temperature increases the conductivity increases as the ions are allowed to move faster and this dependence follows the Vogel-Tammann-Fulcher relationship which states that the temperature is directly proportional to the logarithmic viscosity.[52] For example the conductivity of a typical ionic liquid such as $[C_2mim][NTf_2]$ increases from 1.5 to 9.2 $m\Omega^{-1}cm^{-1}$ from 258 K to 298 K.[53]

1.2.1.4 High Thermal Stability

If RTILs replace conventional solvents as the solvent of choice in AGSs, then AGSs become much more robust as they can be used in much harsher conditions such as high temperature and pressures without worrying about solvent degradation. This can be clearly seen in the RTIL $[C_4mim][NTf_2]$ which is a liquid between 184 K and 723 K as compared to water which is a liquid between 273 K to 373 K.[11] Stability of RTILs are due to the strong nature (inability to breakdown easily) of the bulky organic cation and the inorganic anion. Thermal stability is known to increase with the size of the anions from $[BF_4]^-$ to $[NTf_2]^-$ to $[PF_6]^-$ and increasing alkyl chain length of the cation from $[C_2mim]^+$ to $[C_8mim]^+$.[54,55] This wide liquid range is very advantageous and is being exploited in various industries where applications involve much higher temperatures.

1.2.1.5 High Viscosity

RTILs have a very high viscosity compared to other solvents which is a major drawback as it significantly slows down the rate of diffusion of the analyte species. RTILs have viscosities that are comparable to oils and in the range of 30-450 cP. The high viscosity arises due to van der Waals (vdW) forces and hydrogen bonding. Increase in these intramolecular forces means more energy is required for the molecules to move. The longer the alkyl chain the higher the vdW forces, and the more fluoride ligands the stronger the hydrogen bonding, both of which causes an increase in the viscosity.[56-58] The slow rate of diffusion because of the high viscosity can be prevented by adding organic solvents but this comes with loss of properties such as low volatility and thermal stability which is not ideal for an amperometric gas sensor to operate under extreme conditions. So RTILs are being investigated in this thesis as a pure electrochemical solvent.

1.2.2 Gas Solubility in RTILs

Understanding the solubility of gases in RTILs is extremely vital for the functioning of AGSs. Before the analyte gas can be oxidised/reduced on the surface of the working electrode, the gas first needs to partition into the solvent and this depends greatly on the solubility of the gas in the chosen RTIL. There has been a lot of work done on the solubility of gases in RTILs.[59-64] Most of the work has been on understanding the solubilities of carbon dioxide in RTILs due to its great environmental impact.[65-68] It has been found that carbon dioxide has a very high solubility in ionic liquids, significantly higher than other solvents. Because of this property, RTILs are now being investigated as a scrubbing agent to remove CO_2 from the atmosphere. RTILs are also being used to store and transport reactive gases such as PH_3, AsH_3 and BF_3.[69]

It is also been shown that the solubility of certain gases is higher in RTILs as compared to other solvents which could improve limits of detection.[15] The solubility of gases into RTILs depends on many factors such as how the gas interacts with the RTIL in addition to the structure of the RTIL, temperature and pressure. The structure (cation and anion) of the RTIL plays a huge role in the solubility as it dictates how much free volume there is in the RTIL for the gases to occupy.[59] The free volume is calculated by the differences between the molar volume and the molar van der Waals volume and the higher the free volume the higher the solubility.[59] The free volume can be thought of as pockets of spaces/cavities that are created because of the rearrangements of the ions in the RTILs. Due to the great tunability of RTILs, thousands of combinations of RTILs can be created and each RTIL will have a different solubility for gases. The more flexible the RTIL is, which is induced by the weak interactions between the cation and the anion, the more the free volume.[60] After a cavity/free volume is created by the RTIL for the gases to occupy, intermolecular forces between the gas and the RTIL keep the gases in the cavity. There are various interactions that can take place between the gas and the RTILs and they could range between Lewis acid-base[70] and hydrogen bonds.[60] Temperature dependence of gas solubility is also vital for AGSs as it will give information on how a sensor has to be calibrated for different applications. Up until now there are no known reports that investigate the solubility of chlorine, methylamine and hydrogen chloride, which are the three target gases in this study. However their solubilities in RTILs will be determined electrochemically.

1.2.3 Previous and Future Gas Studies in RTILs

Before RTIL based gas sensors can be commercialised the behaviour of the target gases in RTILs first has to be understood. In this section previous work on gas

sensing in RTILs will be described, to give a good understanding on how other gases behave in RTILs and then also on the three gases that will be studied in this thesis. The fundamental electrochemistry of gases including O_2, CO_2, H_2, NH_3, H_2S, SO_2, NO_2 have been studied in RTILs and is described in a review paper by Rogers et al.[15]

Oxygen is by far the most common gas that is being investigated[20,71-78] due to its use in numerous industries and also because it's non-hazardous and economical to work with as compared to the toxic and expensive gases that will be investigated in this thesis. Oxygen gets reduced by one electron forming the radical anion $O_2^{\cdot-}$ in most RTILs.[79]

$$O_2 + e^- \leftrightharpoons O_2^{\cdot-} \qquad (1.1)$$

The diffusion coefficient of oxygen in a typical RTIL $[C_2mim][NTf_2]$ is 9.3×10^{-10} m^2s^{-1} with a solubility of 3.9 mM, as determined by chronoamperometry.[15] Oxygen has also been used as the target gas for many new amperometric gas studies as it is a safe and cheap gas to work with. Huang's group have reported a membrane-free amperometric gas sensor using a RTIL-nanoparticle approach with oxygen as the target gas.[80] Zhou's group has reported a printed ionic liquid microarray achieved by microcontact printing for oxygen detection.[78] Huang et al.[22] reported a membrane free oxygen sensor using microelectrode arrays as the sensing surface. Oxygen reduction has also been reported on a screen printed electrode by Lee et al.[75] These studies are big advances in amperometric gas sensing as they exploit the versatile properties of RTILs.

Hydrogen sensing has become essential due to its various applications but the importance of hydrogen in fuel cells has pushed for better sensing devices. It is believed that hydrogen gas gets oxidised by one electron in the presence of the RTIL

anion forming a protonated cation and this is only seen on platinum surfaces as hydrogen gas is not active on gold surfaces in RTILs.[81,82]

$$H_2 + 2A^- \leftrightharpoons 2HA + e^- \quad (1.2)$$

This is another issue with amperometric gas sensing where the target gas of interest has to be active on the electrode surface, if not no current can be recorded. In this work various electrode surfaces will be tested to see their suitability for each gas of choice. Diffusion coefficient of hydrogen in a typical RTIL $[C_2mim][NTf_2]$ is 5.3×10^{-10} m^2s^{-1} with a solubility of 4.2 mM, as determined, again, by chronoamperometry.[81]

Ammonia gas is toxic and harmful to humans above concentrations of 50ppm.[83] Due to its high toxicity it is essential to be able to determine ammonia in areas such as environmental protection, clinical diagnosis and industrial processes.[84] It is believed that ammonia gets oxidised in the presence of the RTIL anion forming nitrogen.[83,85]

$$4NH_3 \leftrightharpoons 3NH_4^+ + \frac{1}{2}N_2 + 3e^- \quad (1.3)$$

This mechanism for the oxidation of ammonia gas will be reviewed again in this work in chapter 4 when methylamine gas detection is carried out. Ammonia oxidation has also been reported on screen printed electrodes in RTILs by Murugappan et al.[86] with reasonable limits of detection obtained, comparable to microelectrodes. Although a definitive value for the solubility of ammonia gas in RTILs cannot be given, the high currents measured for the oxidation is indicative of a high solubility.

Sulfur dioxide is another toxic gas of interest as it is one of the main gases involved in atmospheric pollution such as acid rain.[87,88] In RTILs SO_2 gets reduced by one

electron to the radical anion $SO_2^{\cdot-}$ and in $[C_2mim][NTf_2]$ a diffusion coefficient of 8.7×10^{-9} m^2s^{-1} with a solubility of 230 mM was reported.[89]

$$SO_2 + e^- \leftrightharpoons SO_2^{\cdot-} \quad (1.4)$$

Amperometric gas sensors for sulfur dioxide using ionic liquids as the solvent has also been patented.[90]

Hydrogen sulphide is a highly toxic gas with a rotten egg smell.[91,92] H_2S gets reduced by one electron to form HS^- and adsorbed $H^{\cdot}$ in RTILs.[89]

$$H_2S + e^- \leftrightharpoons HS^- + H^{\cdot}_{(ads)} \quad (1.5)$$

The reported diffusion coefficient and solubility in the RTIL $[C_2mim][NTf_2]$ is 3.2×10^{-10} m^2s^{-1} and 529 mM, respectively.[93] This high level of solubility, greater than in conventional solvents, is very advantageous for sensing purposes as lower limits of detection can be obtained.[15]

Nitrogen dioxide is a toxic gas that is mainly produced in combustion facilities and is a great risk to the human respiratory organs.[94,95] In solution nitrogen dioxide is believed to be in its dimer form, N_2O_4. N_2O_4 first disproportionates to NO_2 which gets oxidised to the nitronium cation NO_2^+ losing an electron.[96]

$$N_2O_4 \leftrightharpoons 2NO_2 \quad (1.6)$$

$$NO_2 \leftrightharpoons NO_2^+ + e^- \quad (1.7)$$

A diffusion coefficient of 1.59×10^{-10} m^2s^{-1} and a solubility 51 mM, have been reported in $[C_2mim][NTf_2]$.[96]

Carbon dioxide is a gas that has significant use in the food processing industry[97] and also the medical industry.[98,99] As mentioned earlier it is extremely soluble in RTILs especially imidazolium based ionic liquids[100] and therefore is being investigated for sequestration purposes. Carbon dioxide is believed to be reduced by 2 electrons to $C_2O_4^{2-}$ or by 2 electrons to carbon monoxide and CO_3^{2-}.

$$2CO_2 + 2e^- \leftrightharpoons C_2O_4^{2-} \quad (1.8)$$

$$2CO_2 + 2e^- \leftrightharpoons CO + CO_3^{2-} \quad (1.9)$$

In the ionic liquid $[N_{6,2,2,2}][NTf_2]$ a diffusion coefficient of 2.3×10^{-10} m^2s^{-1} and solubility of 55 mM was reported (solubility values up to 1520 mM was reported in the RTIL, $[C_2mim][acetate]$).[101]

In this thesis the three main gases being investigated are chlorine, hydrogen chloride, and methylamine. The electrochemical behaviour of 100 % chlorine gas on platinum electrodes has been studied by the Compton Group.[102] They have reported one broad reduction peak which was attributed to the two electron reduction of chlorine and one sharp oxidation peak which was due to the reverse reaction (oxidation of chloride to form chlorine). They have also found highly unusual voltammetry where an increase in the voltage scan rates caused a decrease in the currents obtained for the reduction. Through theoretical modelling it was shown that the adsorption of chlorine onto the electrode surface was the reason for the unusual behaviour. It was assumed in the modelling that the reduction of chlorine can only occur on unoccupied electrode sites. When chlorine is consumed by the electrode during the reduction process it causes a shift in the equilibrium for adsorption which allows for the net desorption of chlorine. This makes more of the electrode surface available for the electron transfer reaction and therefore the current increases as time progresses. At high scan rates due

to the lower time scale you have less desorption therefore there are fewer sites for electron transfer hence a lower current. This adsorption effects could be detrimental for gas sensing purposes. In our work the focus was to understand the electrochemical behaviour of lower concentrations of chlorine gas in the RTIL $[C_2mim][NTf_2]$ and determine the analytical utility.

There has been no previous work on the electrochemical behaviour of methylamine gas in RTILs. Therefore the first step would be to understand the mechanism of methylamine in a range of RTILs and then determine the analytical utility for a specific RTIL.

The electrochemical behaviour of hydrogen chloride gas has been briefly studied in the RTIL $[C_4mim][NTf_2]$ on platinum and gold electrodes. One oxidation peak was seen, which was attributed to the two electron oxidation of $[HCl_2]^-$ forming chlorine.[103] In RTILs it is believed that HCl exists in the form $[HCl_2]^-$ and H^+. On gold surfaces however there were a lot of other peaks that were seen which interfered with the redox peaks from the voltammetry. In this thesis the electrochemical behaviour of HCl gas will be studied in several RTILs and the analytical utility in one RTIL.

In this work the first step was to understand the fundamental electrochemical behaviour of these three target gases namely Cl_2, CH_3NH_2 and HCl in RTILs on a microelectrode and then to move on to investigating their behaviour on SPEs.

1.3 Introduction to Screen Printed Electrodes (SPEs)

As with many industries, recent developments in amperometric gas sensors is towards miniaturization of electrodes and sensing devices. Electrochemical “lab-on-a-chip”-type systems are highly desirable in applications where portability is

essential. Screen-printed electrodes (SPEs) consist of three electrodes that are deposited using screen-printing techniques onto an inert ceramic substrate.[24] The use of these SPEs may lead to many advantages for an AGS, such as smaller volume of electrolyte (thin layer) needed, which would allow faster response times and greater sensitivity as compared to macro or micro electrodes and cheaper manufacturing costs due to the smaller amount of expensive electrode material/metal (e.g. Pt or Au) required by miniaturization of the solid electrodes. This would allow SPEs to be used as portable sensing devices, whilst also being relatively low-cost and easy to manufacture.

In screen printing technology a fluid containing many different substances such as graphite, carbon black and polymeric binders is squeezed through a mesh screen which defines the shape and size of the electrode.[104] In this work commercial SPEs purchased from Dropsens (Spain) were tested for their suitability for gas sensing. A commercial SPE is shown in figure 1.5 where it has all three electrodes screen printed on a ceramic substrate and the connection points running underneath the substrate to the end of the electrode. The dimensions of the SPE shown in figure 1.5 are 3.4 × 1.0 × 0.05 cm which is a significant advancement towards miniaturization compared to traditional electrochemical cells.

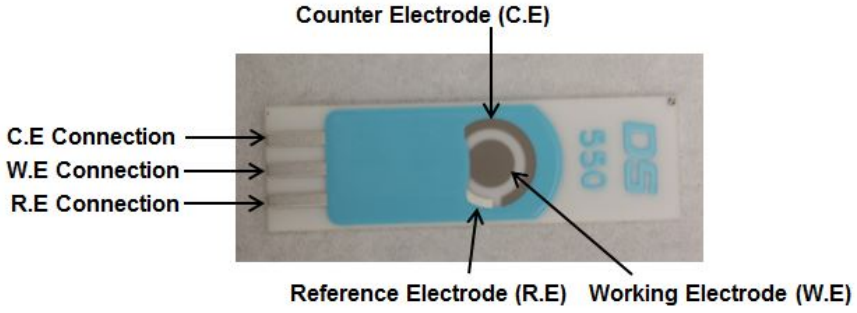

Figure 1.5: Photograph of SPE purchased from DropSens

Another major advantage of SPEs is the ability to easily modify these surfaces. By changing the paste and ink to include particles such as gold nanoparticles, enzymes, graphene or carbon nanotubes, SPEs that are task specific can be generated in a mass production for a relatively cheap cost. This adaptability is significant and researchers are trying to exploit this.[24,105-108] By increasing the surface area with the addition of nanoparticles or carbon nanotubes, larger currents can be produced resulting in a subsequent increase in the sensitivity.

SPEs basically contain three main components, the substrate and two types of ink for printing. The most common types of ink are carbon and silver ink which contains graphite, carbon black/ Ag, polymeric binders and additives for better dispersion and printing. The carbon ink is mixed together with the metal of choice and then used to print the electrodes. The silver ink is usually used as electrical contacts running from the electrode to the connection points. For the substrate, ceramic, plastic or now even paper is chosen depending on the application. One issue with SPEs is to do with the non-insulating polymeric binders that are used in the printing, which sometimes causes sluggish electron kinetics.[24,105,106] This can be solved by precleaning/activating the electrode, however in this thesis these electrodes will be used ‘as-is’ with no activation or electrochemical cleaning which represents more clearly the conditions required for a real sensor where activation or cleaning steps may not be feasible.

SPEs have been used to a great extent in the medical industry for protein and glucose sensing. A quick overview of the uses of SPEs will be presented now followed by its use in gas sensing.

The glucose biosensor is one of the most noticeable examples of commercialisation of SPEs and is being used for diabetes which is a billion dollar per year global market.[109-112] SPEs are also used heavily in environmental monitoring especially water quality, heavy metals detection, and naturally occurring biomolecules detection.

Water quality monitoring is significant to the human race for obvious reasons. There are two main uses of SPEs in water quality management. The first is pH monitoring and the second is the measurement of dissolved oxygen. A plastic, fully disposable SPE was created by Koncki et al.[113] by using a pH-sensitive metal oxide, ruthenium oxide, that can be used either in an acidic or pH neutral medium. Another SPE that was created to determine pH changes was reported by Kampuris et al.[114] where phenanthraquinone was used as the pH sensitive agent which undergoes a Nernstian shift in its redox potential with the pH. A copper plated SPE was developed by Zen et al.[115] for the measurement of dissolved oxygen based on cathodic electrochemiluminescence at neutral pH. Nitrates and phosphates are also compounds that are found in water that need sensing due to their presence, causing growth of algae resulting in depletion of oxygen and death of fish. Various types of SPEs are being used to detect both these two chemicals.[116-118] Toxic organic compounds such as phenols,[119] pesticides,[120-122] and herbicides[123,124] have also been detected using SPEs. Due to the negative impact that heavy metals have towards human health, it is extremely important to be able to detect them and again SPEs are vastly used for their detection. Lead,[125-127] cadmium,[126,128] copper,[129] zinc,[128] and mercury,[127] are few of the heavy metal ions that are being detected using SPEs by exploiting their cheap and disposable nature.

The detection of toxic gases with the aid of SPEs have gained a lot of interest recently as it offers the possibility to lower cost and produce portable devices. The potentiometric detection of carbon monoxide on SPEs has been performed by using gold as the working electrode and zirconia as the solid electrolyte.[130] Nitrogen dioxide has also been sensed potentiometrically on SPEs with the aid of tin doped and indium oxide thin films.[131] Disposable amperometric sulfur dioxide sensors based on SPEs in a phosphate buffer has been created by Hart et al.[132] The possibility of a spill-less and membrane-less oxygen sensor with the aid of a SPE was investigated by Panchompoo et al.[133] by using a ferrofluidic electrolyte, therefore controlling the movement of solvent with the aid of a magnet being held on the other side of the SPE.

However the use of RTILs for amperometric gas detection on screen printed electrodes is only gaining interest recently including two reports from our research group. Murugappan et al.[86] reported the oxidation of ammonia in the RTIL, $[C_2mim][NTf_2]$ and obtained reasonable limits of detection (LOD) of 50 ppm on a commercial Pt SPE. Lee et al.[75] reported the reduction of oxygen on a commercial Pt SPE, and obtained LOD of 3.3 % in the RTIL $[C_2mim][NTf_2]$. However they did find that the product of the electrochemical reduction of oxygen, superoxide, was reacting with the paste in the SPE which could be detrimental from a sensing perspective. Despite this the analytical response was good. Dossi et al[134] reported the use of a homemade SPE, made of paper, to detect butanethiol. The same homemade paper SPE was used by Toniolo[135] for the detection of volatile amines to determine fish spoilage. More recently Stetter et al.[136] patented a screen printed electrode based gas sensor that uses RTIL as the electrolyte. They were able to compare the performance with different RTILs for ammonia gas sensing and found that

hydrophilic RTILs produced more effective gas sensors as compared to their hydrophobic counterparts due to the greater wettability of the electrode surface.[107] LODs between 0.1 to 5 ppm were reported for the range of RTILs studied which were far better as compared to a conventional electrolyte (5 M H_2SO_4). They also compared the performance with a commercial canister based gas sensor and found that the RTIL/SPE sensor had a better sensitivity after normalising the currents with the electrode area.[107] This is very promising work and it proves that RTIL/SPE gas sensors can become competitive in the real world. To make it even more cost effective, Metters et al. have presented the concept of screen printed 'back-to-back' sensors where there are 2 sensors on one SPE.[137] Therefore the redundant side of a normal SPE is no longer redundant as both sides have electrodes printed making this a dual sensor. This only shows the great versatility of SPEs and widens the prospects of use of these SPEs. Combining the excellent properties of RTILs and SPEs, a new generation of AGSs can be created.

1.4 Modification of Surfaces

Recently a lot of work has gone into modification of sensing surfaces to improve sensitivity and therefore LODs for gas detection. Graphene,[138] carbon nanotubes,[139] magnetite nanoparticles[140-142] and macroporous frameworks[143,144] are some of the exciting materials that have been investigated for their use in sensing. They will be discussed in greater detail in their respective results and discussion chapters.

1.5 Aims

The primary aim of this thesis is to determine if the three toxic gases of interest can be detected electrochemically in RTILs. The three target gases of interest are chlorine, methylamine and hydrogen chloride which are all highly toxic with

Occupational Safety & Health Administration Permissible Exposure Limits (OSHA PELs) of 1, 10 and 5 ppm respectively. The first step would be to study the reaction mechanisms of the gases in RTILs and compare them to conventional aprotic solvents. The behaviour of the gases will be investigated in different RTILs on conventional microelectrodes. The best RTIL/electrode surface combination will be used to determine the analytical utility (linear range, sensitivity and limit of detection) of the toxic gases. These studies should provide an assessment as to whether RTILs can be used as replacement solvents in AGSs for sensing these highly toxic gases.

The next aim in this thesis is to investigate the behaviour of these toxic gases in RTILs on SPEs. This will allow us to understand if it would be possible to detect these gases on low cost SPEs and if the mechanism is similar to conventional microelectrodes. SPEs with different working electrode surfaces (Pt, Au, C and C modified with graphene and carbon nanotubes) will be investigated to determine which surface is the most promising for the detection of these gases. Then the analytical utility will be studied on SPEs and compared with conventional microelectrodes to suggest if these low cost devices can be used as alternative surfaces for membrane-free gas sensing. These studies hopefully opens up the possibilities of using SPEs in conjunction with RTILs in an AGS which will allow a new generation of AGSs to be created that exploits the advantageous properties of both RTILs and SPEs.

The secondary aim in this thesis is to modify electrode surfaces with materials such as magnetite nanoparticles and Pt macroporous frameworks to see if there is any enhancement in current/sensitivity for methylamine gas sensing. However before

these nanomaterials are employed as new electrode materials, their electrochemical behaviour must be first fully understood. Therefore magnetite nanoparticles and Pt macroporous frameworks will be synthesised and characterised using various physical and electrochemical techniques in conventional solvent media.

1.6 References

(1) Consonni, D.; Pesatori, A. C.; Zocchetti, C.; Sindaco, R.; D'Oro, L. C.; Rubagotti, M.; Bertazzi, P. A. Mortality in a population exposed to dioxin after the Seveso, Italy, accident in 1976: 25 years of follow-up. *Am. J. Epidemiol.* **2008**, *167*, 847-858.
(2) Dahiwal, A.; Dahitule, K.; Natu, N. 24 hospitalised after chlorine gas leakage in Pune. *DNAIndia.* 18/01/2011.
(3) Lupiani, J. Chlorine gas leak reported at Timet Henderson plant. *ABC13.* 09/03/2012.
(4) March, S. Bhopal gas leak disaster's toxic legacy lives on 30 years later. *ABC.* 02/12/2014.
(5) Holland, S. Emergency services contain ammonia gas leak in Welshpool. *WAtoday.com.au.* 28/11/2014.
(6) Lac, F. d. 'Furries' sent scrambling by chlorine gas leak at convention hotel. *The Washington Post.* 08/12/2014.
(7) Long, K. Perth worker blasted in face by ammonia is rushed to hospital, six others also injured. *ABC.* 11/12/2014.
(8) Corder, M. Weapons Watchdog: Chlorine Gas Was Likely Used In Syria Earlier This Year. *HuffingtonPost.* 09/10/2014.
(9) Fitzgerald, G. J. Chemical Warfare and Medical Response During World War I. *Am. J. of Public Health* **2008**, *98*, 611-625.
(10) Brewer, J. Toxic gas leak at Texas Dupont plant kills four. *World Socialist Web Site.* 17/11/2014.
(11) Xiong, L.; Compton, R. G. Amperometric gas detection: A review. *Int. J. Electrochem. Sc.* **2014**, *9*, 7152-7181.
(12) Chou, J.: *Hazardous gas monitors: A practical guide to selection, operation and applications*; McGraw-Hill, 2000.
(13) Liu, X.; Cheng, S.; Liu, H.; Hu, S.; Zhang, D.; Ning, H. A survey on gas sensing technology. *Sensors* **2012**, *12*, 9635-9665.
(14) Wang, C.; Yin, L.; Zhang, L.; Xiang, D.; Gao, R. Metal oxide gas sensors: Sensitivity and influencing factors. *Sensors* **2010**, *10*, 2088-2106.
(15) Rogers, E. I.; O'Mahony, A. M.; Aldous, L.; Compton, R. G. (Invited) Amperometric gas detection using room temperature ionic liquid solvents. *ECS Trans.* **2010**, *33*, 473-502.
(16) Clark Jr, L. C.; Wolf, R.; Granger, D.; Taylor, Z. Continuous recording of blood oxygen tensions by polarography. *J. Appl. Physiol.* **1953**, *6*, 189-193.
(17) Knake, R.; Jacquinot, P.; Hodgson, A. W. E.; Hauser, P. C. Amperometric sensing in the gas-phase. *Anal. Chim. Acta* **2005**, *549*, 1-9.
(18) Stetter, J. R.; Li, J. Amperometric gas sensors a review. *Chem. Rev.* **2008**, *108*, 352-366.

(19) Cao, Z.; Buttner, W. J.; Stetter, J. R. The properties and applications of amperometric gas sensors. *Electroanal.* **1992**, *4*, 253-266.
(20) Buzzeo, M. C.; Hardacre, C.; Compton, R. G. Use of room temperature ionic liquids in gas sensor design. *Anal. Chem.* **2004**, *76*, 4583-4588.
(21) Plechkova, N. V.; Seddon, K. R. Applications of ionic liquids in the chemical industry. *Chem. Soc. Rev.* **2008**, *37*, 123-150.
(22) Huang, X.-J.; Aldous, L.; O'Mahony, A. M.; del Campo, F. J.; Compton, R. G. Toward membrane-free amperometric gas sensors: A microelectrode array approach. *Anal. Chem.* **2010**, *82*, 5238-5245.
(23) Malzahn, K.; Windmiller, J. R.; Valdes-Ramirez, G.; Schoning, M. J.; Wang, J. Wearable electrochemical sensors for in situ analysis in marine environments. *Analyst* **2011**, *136*, 2912-2917.
(24) Metters, J. P.; Kadara, R. O.; Banks, C. E. New directions in screen printed electroanalytical sensors: An overview of recent developments. *Analyst* **2011**, *136*, 1067-1076.
(25) Crowley, K.; O'Malley, E.; Morrin, A.; Smyth, M. R.; Killard, A. J. An aqueous ammonia sensor based on an inkjet-printed polyaniline nanoparticle-modified electrode. *Analyst* **2008**, *133*, 391-399.
(26) Wei, D.; Ivaska, A. Applications of ionic liquids in electrochemical sensors. *Anal. Chim. Acta* **2008**, *607*, 126-135.
(27) Pandey, S. Analytical applications of room-temperature ionic liquids: A review of recent efforts. *Anal. Chim. Acta* **2006**, *556*, 38-45.
(28) Ye, C.; Liu, W.; Chen, Y.; Yu, L. Room-temperature ionic liquids: A novel versatile lubricant. *Chem. Commun.* **2001**, 2244-2245.

(29) de Souza, R. F.; Padilha, J. C.; Gonçalves, R. S.; Dupont, J. Room temperature dialkylimidazolium ionic liquid-based fuel cells. *Electrochem. Commun.* **2003**, *5*, 728-731.
(30) Hallett, J. P.; Welton, T. Room-temperature ionic liquids:Solvents for synthesis and catalysis. 2. *Chem. Rev* **2011**, *111*, 3508-3576.
(31) Welton, T. Room-temperature ionic liquids. Solvents for synthesis and catalysis. *Chem. Review* **1999**, *99*, 2071-2084.
(32) Wang, Y.; Zaghib, K.; Guerfi, A.; Bazito, F. F.; Torresi, R. M.; Dahn, J. Accelerating rate calorimetry studies of the reactions between ionic liquids and charged lithium ion battery electrode materials. *Electrochim. Acta* **2007**, *52*, 6346-6352.
(33) Ue, M.; Takeda, M.; Toriumi, A.; Kominato, A.; Hagiwara, R.; Ito, Y. Application of low-viscosity ionic liquid to the electrolyte of double-layer capacitors. *J. Electrochem. Soc.* **2003**, *150*, A499-A502.
(34) McEwen, A. B.; Ngo, H. L.; LeCompte, K.; Goldman, J. L. Electrochemical properties of imidazolium salt electrolytes for electrochemical capacitor applications. *J. Electrochem. Soc.* **1999**, *146*, 1687-1695.
(35) Frackowiak, E.; Lota, G.; Pernak, J. Room-temperature phosphonium ionic liquids for supercapacitor application. *Appl. Phys. Lett.* **2005**, *86*, 164104.
(36) McEwen, A. B.; McDevitt, S. F.; Koch, V. R. Nonaqueous electrolytes for electrochemical capacitors: Imidazolium cations and inorganic fluorides with organic carbonates. *J. Electrochem. Soc.* **1997**, *144*, L84-L86.
(37) Galiński, M.; Lewandowski, A.; Stępniak, I. Ionic liquids as electrolytes. *Electrochim. Acta* **2006**, *51*, 5567-5580.

(38) MacFarlane, D. R.; Forsyth, M.; Howlett, P. C.; Pringle, J. M.; Sun, J.; Annat, G.; Neil, W.; Izgorodina, E. I. Ionic Liquids in electrochemical devices and processes: Managing interfacial electrochemistry. *Accounts Chem. Res.* **2007**, *40*, 1165-1173.
(39) Silvester, D. S. Recent advances in the use of ionic liquids for electrochemical sensing. *Analyst* **2011**, *136*, 4871-4882.
(40) Lu, W.; Norris, I. D.; Mattes, B. R. Electrochemical actuator devices based on polyaniline yarns and ionic liquid electrolytes. *Aust. J. Chem.* **2005**, *58*, 263-269.
(41) Buzzeo, M. C.; Evans, R. G.; Compton, R. G. Non-haloaluminate room-temperature ionic liquids in electrochemistry—a review. *ChemPhysChem* **2004**, *5*, 1106-1120.
(42) Silvester, D. S.; Compton, R. G. Electrochemistry in room temperature ionic liquids: A review and some possible applications. *Z. Phys. Chem.* **2006**, *220*, 1247-1274.
(43) MacFarlane, D. R.; Seddon, K. R. Ionic liquids—progress on the fundamental issues. *Aust. J. Chem.* **2007**, *60*, 3-5.
(44) Ramasubramanian, N. Anodic behavior of platinum electrodes in sulfide solutions and the formation of platinum sulfide. *J. Electroanal Chem. Interfacial Electrochem.* **1975**, *64*, 21-37.
(45) Schroder, U.; Wadhawan, J. D.; Compton, R. G.; Marken, F.; Suarez, P. A. Z.; Consorti, C. S.; de Souza, R. F.; Dupont, J. Water-induced accelerated ion diffusion: voltammetric studies in 1-methyl-3-[2,6-(S)-dimethylocten-2-yl]imidazolium tetrafluoroborate, 1-butyl-3-methylimidazolium tetrafluoroborate and hexafluorophosphate ionic liquids. *New J. Chem.* **2000**, *24*, 1009-1015.
(46) Tunnell, G. A.: *World distribution of atmospheric water vapour pressure*; H.M. Stationery Office, 1958.
(47) Chowdhury, A.; Thynell, S. T. Confined rapid thermolysis/FTIR/ToF studies of imidazolium-based ionic liquids. *Thermochim. Acta* **2006**, *443*, 159-172.
(48) Licence, P. In situ XPS monitoring of bulk ionic liquid reactions: shedding light on organic reaction mechanisms. *Angew. Chem. Int. Edit.* **2012**, *51*, 4789-4791.
(49) Foelske-Schmitz, A.; Weingarth, D.; Kötz, R. XPS analysis of activated carbon supported ionic liquids: Enhanced purity and reduced charging. *Surf Sci.* **2011**, *605*, 1979-1985.
(50) Hurisso, B. B.; Lovelock, K. R. J.; Licence, P. Amino acid-based ionic liquids: using XPS to probe the electronic environment via binding energies. *Phys. Chem. Chem. Phys.* **2011**, *13*, 17737-17748.
(51) Niedermaier, I.; Kolbeck, C.; Taccardi, N.; Schulz, P. S.; Li, J.; Drewello, T.; Wasserscheid, P.; Steinrück, H.-P.; Maier, F. Organic reactions in ionic liquids studied by in situ XPS. *ChemPhysChem* **2012**, *13*, 1725-1735.
(52) McFarlane, D. R.; Sun, J.; Golding, J.; Meakin, P.; Forsyth, M. High conductivity molten salts based on the imide ion. *Electrochim. Acta* **2000**, *45*, 1271-1278.
(53) Schreiner, C.; Zugmann, S.; Hartl, R.; Gores, H. J. Fractional Walden rule for ionic liquids: Examples from recent measurements and a critique of the so-called ideal KCl line for the Walden plot. *J Chem. Eng. Data* **2009**, *55*, 1784-1788.
(54) Fredlake, C. P.; Crosthwaite, J. M.; Hert, D. G.; Aki, S. N. V. K.; Brennecke, J. F. Thermophysical properties of imidazolium-based ionic liquids. *J Chem. Eng. Data* **2004**, *49*, 954-964.
(55) Ngo, H. L.; LeCompte, K.; Hargens, L.; McEwen, A. B. Thermal properties of imidazolium ionic liquids. *Thermochim. Acta* **2000**, *357–358*, 97-102.

(56) Wasserscheid, P.; Keim, W. Ionic liquids-new" solutions" for transition metal catalysis. *Angew. Chem.* **2000**, *39*, 3772-3789.
(57) Xu, W.; Wang, L.-M.; Nieman, R. A.; Angell, C. A. Ionic liquids of chelated orthoborates as model ionic glassformers. *J. Phys. Chem. B* **2003**, *107*, 11749-11756.
(58) Endres, F.; El Abedin, S. Z. Air and water stable ionic liquids in physical chemistry. *Phys. Chem. Chem. Phys.* **2006**, *8*, 2101-2116.
(59) Hu, Y.-F.; Liu, Z.-C.; Xu, C.-M.; Zhang, X.-M. The molecular characteristics dominating the solubility of gases in ionic liquids. *Chem. Soc. Rev.* **2011**, *40*, 3802-3823.
(60) Lei, Z.; Dai, C.; Chen, B. Gas Solubility in Ionic Liquids. *Chem. Rev.* **2013**, *114*, 1289-1326.
(61) Vega, L. F.; Vilaseca, O.; Llovell, F.; Andreu, J. S. Modeling ionic liquids and the solubility of gases in them: Recent advances and perspectives. *Fluid Phase Equilibr.* **2010**, *294*, 15-30.
(62) Oliferenko, A. A.; Oliferenko, P. V.; Seddon, K. R.; Torrecilla, J. S. Prediction of gas solubilities in ionic liquids. *Phys. Chem. Chem. Phys.* **2011**, *13*, 17262-17272.
(63) Camper, D.; Scovazzo, P.; Koval, C.; Noble, R. Gas solubilities in room-temperature ionic liquids. *Ind. Eng. Chem. Res.* **2004**, *43*, 3049-3054.
(64) Dirk, T.; Gerd, M.: Gas solubility in ionic liquids: mixed gases in pure ionic liquids and single gases in binary liquid mixtures. In *ionic liquids: science and applications*; ACS Symposium Series 1117; *Am. Chem. Soc.*, **2012**, *1117*, 217-238.
(65) Torralba-Calleja, E.; Skinner, J.; Gutierrez-Tauste, D. CO_2 capture in ionic liquids: A review of solubilities and experimental methods. *J. Chem.* **2013**, *2013*, 16.
(66) Yunus, N. M.; Mutalib, M. I. A.; Man, Z.; Bustam, M. A.; Murugesan, T. Solubility of CO_2 in pyridinium based ionic liquids. *Chem Eng. J.* **2012**, *189–190*, 94-100.
(67) Muldoon, M. J.; Aki, S. N. V. K.; Anderson, J. L.; Dixon, J. K.; Brennecke, J. F. Improving Carbon Dioxide Solubility in Ionic Liquids. *J. Phys Chem. B* **2007**, *111*, 9001-9009.
(68) Supasitmongkol, S.; Styring, P. High CO_2 solubility in ionic liquids and a tetraalkylammonium-based poly(ionic liquid). *Energ. Environ. Science* **2010**, *3*, 1961-1972.
(69) Keskin, S.; Kayrak-Talay, D.; Akman, U.; Hortaçsu, Ö. A review of ionic liquids towards supercritical fluid applications. *J Supercrit. Fluid.* **2007**, *43*, 150-180.
(70) Kazarian, S. G.; Briscoe, B. J.; Welton, T. Combining ionic liquids and supercritical fluids: ATR-IR study of CO dissolved in two ionic liquids at high pressures. *Chem. Commun.* **2000**, 2047-2048.
(71) Buzzeo, M. C.; Klymenko, O. V.; Wadhawan, J. D.; Hardacre, C.; Seddon, K. R.; Compton, R. G. Voltammetry of oxygen in the room-temperature ionic liquids 1-ethyl-3-methylimidazolium bis ((trifluoromethyl) sulfonyl) imide and hexyltriethylammonium bis ((trifluoromethyl) sulfonyl) imide: One-electron reduction to form superoxide. Steady-state and transient behavior in the same cyclic voltammogram resulting from widely different diffusion coefficients of oxygen and superoxide. *J. Phys. Chem. A* **2003**, *107*, 8872-8878.
(72) Evans, R. G.; Klymenko, O. V.; Saddoughi, S. A.; Hardacre, C.; Compton, R. G. Electroreduction of oxygen in a series of room temperature ionic liquids composed of group 15-centered cations and anions. *J. Phys. Chem. B* **2004**, *108*, 7878-7886.

(73) Wang, R.; Okajima, T.; Kitamura, F.; Ohsaka, T. A novel amperometric O_2 gas sensor based on supported room-temperature ionic liquid porous polyethylene membrane-coated electrodes. *Electroanal.* **2004**, *16*, 66-72.
(74) AlNashef, I. M.; Leonard, M. L.; Kittle, M. C.; Matthews, M. A.; Weidner, J. W. Electrochemical generation of superoxide in room-temperature ionic liquids. *Electrochem. Solid St. Lett.* **2001**, *4*, D16-D18.
(75) Lee, J.; Murugappan, K.; Arrigan, D. W. M.; Silvester, D. S. Oxygen reduction voltammetry on platinum macrodisk and screen-printed electrodes in ionic liquids: Reaction of the electrogenerated superoxide species with compounds used in the paste of Pt screen-printed electrodes? *Electrochim. Acta* **2013**, *101*, 158-168.
(76) Wang, R.; Hoyano, S.; Ohsaka, T. O2 gas sensor using supported hydrophobic room-temperature ionic liquid membrane-coated electrode. *Chem. Lett.* **2004**, *33*, 6-7.
(77) Morgan, D.; Ferguson, L.; Scovazzo, P. Diffusivities of Gases in Room-Temperature Ionic Liquids: Data and Correlations Obtained Using a Lag-Time Technique. *Ind. Eng. Chem. Res.* **2005**, *44*, 4815-4823.
(78) Gunawan, C. A.; Ge, M.; Zhao, C. Robust and versatile ionic liquid microarrays achieved by microcontact printing. *Nat. Commun.* **2014**, *5*.3744
(79) Huang, X.-J.; Rogers, E. I.; Hardacre, C.; Compton, R. G. The reduction of oxygen in various room temperature ionic liquids in the temperature range 293−318 K: Exploring the applicability of the Stokes−Einstein relationship in room temperature ionic liquids. *J. Phys. Chem. B* **2009**, *113*, 8953-8959.
(80) Xiong, S.-Q.; Wei, Y.; Guo, Z.; Chen, X.; Wang, J.; Liu, J.-H.; Huang, X.-J. Toward membrane-free amperometric gas sensors: An ionic liquid–nanoparticle composite approach. *J. Phys. Chem. C* **2011**, *115*, 17471-17478.
(81) Silvester, D. S.; Aldous, L.; Hardacre, C.; Compton, R. G. An electrochemical study of the oxidation of hydrogen at platinum electrodes in several room temperature ionic liquids. *J. Phys. Chem. B* **2007**, *111*, 5000-5007.
(82) Silvester, D. S.; Ward, K. R.; Aldous, L.; Hardacre, C.; Compton, R. G. The electrochemical oxidation of hydrogen at activated platinum electrodes in room temperature ionic liquids as solvents. *J. Electroanal. Chem.* **2008**, *618*, 53-60.
(83) Ji, X.; Silvester, D. S.; Aldous, L.; Hardacre, C.; Compton, R. G. Mechanistic studies of the electro-oxidation pathway of ammonia in several room-temperature ionic liquids. *J. Phys. Chem. C* **2007**, *111*, 9562-9572.
(84) Timmer, B.; Olthuis, W.; Berg, A. v. d. Ammonia sensors and their applications—a review. *Sensor. Actuat. B-Chem.* **2005**, *107*, 666-677.
(85) Ji, X.; Banks, C. E.; Silvester, D. S.; Aldous, L.; Hardacre, C.; Compton, R. G. Electrochemical ammonia gas sensing in nonaqueous systems: A comparison of propylene carbonate with room temperature ionic liquids. *Electroanal.* **2007**, *19*, 2194-2201.
(86) Murugappan, K.; Lee, J.; Silvester, D. S. Comparative study of screen printed electrodes for ammonia gas sensing in ionic liquids. *Electrochem. Commun.* **2011**, *13*, 1435-1438.
(87) Carmichael, G. R.; Streets, D. G.; Calori, G.; Amann, M.; Jacobson, M. Z.; Hansen, J.; Ueda, H. Changing trends in sulfur emissions in Asia: implications for acid deposition, air pollution, and climate. *Environ. Sci. Technol.* **2002**, *36*, 4707-4713.
(88) Hawksworth, D.; Rose, F. Qualitative scale for estimating sulphur dioxide air pollution in England and Wales using epiphytic lichens. *Nature.* **1970**, *227*, 145-148.

(89) Barrosse-Antle, L. E.; Silvester, D. S.; Aldous, L.; Hardacre, C.; Compton, R. G. Electroreduction of sulfur dioxide in some room-temperature ionic liquids. *J. Phys. Chem. C* **2008**, *112*, 3398-3404.
(90) Eckhardt, R.; Warratz, R.: Electrochemical gas sensor with an ionic liquid electrolyte system including at least one monoalkylammonium, dialkylammonium, or trialkylammonium cation. 2011. U.S Patent No. 8623189
(91) Beauchamp, R.; Bus, J. S.; Popp, J. A.; Boreiko, C. J.; Andjelkovich, D. A.; Leber, P. A critical review of the literature on hydrogen sulfide toxicity. *CRC Cr. Rev. Toxicol.* **1984**, *13*, 25-97.
(92) McCabe, L. C.; Clayton, G. Air pollution by hydrogen sulfide in Poza Rica, Mexico; an evaluation of the incident of Nov. 24, 1950. *AMA Arch. Ind. Hyg. Occ. Med.* **1952**, *6*, 199.
(93) O'Mahony, A. M.; Silvester, D. S.; Aldous, L.; Hardacre, C.; Compton, R. G. The electrochemical reduction of hydrogen sulfide on platinum in several room temperature ionic liquids. *J. Phys. Chem. C* **2008**, *112*, 7725-7730.
(94) Mustafa, M. G.; Tierney, D. F. Biochemical and metabolic changes in the lung with oxygen, ozone, and nitrogen dioxide toxicity. *Am. Rev. Respir. Dis.* **1978**, *118*, 1061-1090.
(95) Bauer, M.; Utell, M.; Morrow, P.; Speers, D.; Gibb, F. Inhalation of 0.30 ppm nitrogen dioxide potentiates exercise-induced bronchospasm in asthmatics. *Am. Rev. Respir. Dis.* **1986**, *134*, 1203-1208.
(96) Broder, T. L.; Silvester, D. S.; Aldous, L.; Hardacre, C.; Compton, R. G. Electrochemical oxidation of nitrite and the oxidation and reduction of NO2 in the room temperature ionic liquid [C_2mim][NTf_2]. *J. Phys. Chem. B* **2007**, *111*, 7778-7785.
(97) Neethirajan, S.; Jayas, D. S.; Sadistap, S. Carbon Dioxide (CO_2) sensors for the agri-food industry—a review. *Food. Bioprocess. Tech.* **2009**, *2*, 115-121.
(98) Van Slyke, D. D.; Neill, J. M. The determination of gases in blood and other solutions by vacuum extraction and manometric measurement.I. *J. Bio. Chem.* **1924**, *61*, 523-573.
(99) Falk, J. L.; Rackow, E. C.; Weil, M. H. End-tidal carbon dioxide concentration during cardiopulmonary resuscitation. *New Engl. J. Med.* **1988**, *318*, 607-611.
(100) Cadena, C.; Anthony, J. L.; Shah, J. K.; Morrow, T. I.; Brennecke, J. F.; Maginn, E. J. Why is CO_2 so soluble in imidazolium-based ionic liquids? *J. Am. Chem. Soc.* **2004**, *126*, 5300-5308.
(101) Buzzeo, M. C.; Klymenko, O. V.; Wadhawan, J. D.; Hardacre, C.; Seddon, K. R.; Compton, R. G. Kinetic analysis of the reaction between electrogenerated superoxide and carbon dioxide in the room temperature ionic liquids 1-ethyl-3-methylimidazolium bis (trifluoromethylsulfonyl) imide and hexyltriethylammonium bis (trifluoromethylsulfonyl) imide. *J. Phys. Chem. B* **2004**, *108*, 3947-3954.
(102) Huang, X.-J.; Silvester, D. S.; Streeter, I.; Aldous, L.; Hardacre, C.; Compton, R. G. Electroreduction of chlorine gas at platinum electrodes in several room temperature ionic liquids: evidence of strong adsorption on the electrode surface revealed by unusual voltammetry in which currents decrease with increasing voltage scan rates. *J. Phys. Chem. C* **2008**, *112*, 19477-19483.
(103) Aldous, L.; Silvester, D. S.; Pitner, W. R.; Compton, R. G.; Lagunas, M. C.; Hardacre, C. Voltammetric studies of gold, protons, and $[HCl_2]^-$ in ionic liquids. *J. Phys. Chem. C* **2007**, *111*, 8496-8503.

(104) Choudhry, N. A.; Kampouris, D. K.; Kadara, R. O.; Jenkinson, N.; Banks, C. E. Next generation screen printed electrochemical platforms: Non-enzymatic sensing of carbohydrates using copper(II) oxide screen printed electrodes. *Anal. Meth.* **2009**, *1*, 183-187.
(105) Li, M.; Li, Y.-T.; Li, D.-W.; Long, Y.-T. Recent developments and applications of screen-printed electrodes in environmental assays—a review. *Anal. Chim. Acta* **2012**, *734*, 31-44.
(106) Hayat, A.; Marty, J. L. Disposable screen printed electrochemical sensors: Tools for environmental monitoring. *Sensors* **2014**, *14*, 10432-10453.
(107) Carter, M. T.; Stetter, J. R.; Findlay, M. W.; Patel, V. Rational design of amperometric gas sensors with ionic liquid electrolytes. *ECS Trans.* **2014**, *64*, 95-103.
(108) Hart, J. P.; Wring, S. A. Recent developments in the design and application of screen-printed electrochemical sensors for biomedical, environmental and industrial analyses. *Trac-Trend. Anal. Chem.* **1997**, *16*, 89-103.
(109) Heller, A.; Feldman, B. Electrochemical glucose sensors and their applications in diabetes management. *Chem. Rev.* **2008**, *108*, 2482-2505.
(110) Kumar, A. S.; Zen, J.-M. Electrochemical investigation of glucose sensor fabricated at copper-plated screen-printed carbon electrodes. *Electroanal.* **2002**, *14*, 671.
(111) Huang, T.-K.; Lin, K.-W.; Tung, S.-P.; Cheng, T.-M.; Chang, I.; Hsieh, Y.-Z.; Lee, C.-Y.; Chiu, H.-T. Glucose sensing by electrochemically grown copper nanobelt electrode. *J. Electroanal. Chem.* **2009**, *636*, 123-127.
(112) Rahman, M. M.; Ahammad, A.; Jin, J.-H.; Ahn, S. J.; Lee, J.-J. A comprehensive review of glucose biosensors based on nanostructured metal-oxides. *Sensors* **2010**, *10*, 4855-4886.
(113) Koncki, R.; Mascini, M. Screen-printed ruthenium dioxide electrodes for pH measurements. *Anal. Chim. Acta* **1997**, *351*, 143-149.
(114) Kampouris, D. K.; Kadara, R. O.; Jenkinson, N.; Banks, C. E. Screen printed electrochemical platforms for pH sensing. *Anal. Meth.* **2009**, *1*, 25-28.
(115) Zen, J.-M.; Song, Y.-S.; Chung, H.-H.; Hsu, C.-T.; Senthil Kumar, A. photoelectrochemical oxygen sensor using copper-plated screen-printed carbon electrodes. *Anal. Chem.* **2002**, *74*, 6126-6130.
(116) Renedo, O. D.; Alonso-Lomillo, M. A.; Martínez, M. J. A. Recent developments in the field of screen-printed electrodes and their related applications. *Talanta* **2007**, *73*, 202-219.
(117) Metters, J. P.; Kadara, R. O.; Banks, C. E. Electroanalytical properties of screen printed graphite microband electrodes. *Sensor. Actuat. B-Chem.* **2012**, *169*, 136-143.
(118) Gilbert, L.; Jenkins, A. T. A.; Browning, S.; Hart, J. P. Development of an amperometric, screen-printed, single-enzyme phosphate ion biosensor and its application to the analysis of biomedical and environmental samples. *Sensor. Actuat. B-Chem* **2011**, *160*, 1322-1327.
(119) Kotte, H.; Gruendig, B.; Vorlop, K.-D.; Strehlitz, B.; Stottmeister, U. Methylphenazonium-modified enzyme sensor based on polymer thick films for subnanomolar detection of phenols. *Anal. Chem.* **1995**, *67*, 65-70.
(120) Arduini, F.; Ricci, F.; Tuta, C. S.; Moscone, D.; Amine, A.; Palleschi, G. Detection of carbamic and organophosphorous pesticides in water samples using a cholinesterase biosensor based on prussian blue-modified screen-printed electrode. *Anal. Chim. Acta* **2006**, *580*, 155-162.

(121) Andreescu, S.; Barthelmebs, L.; Marty, J.-L. Immobilization of acetylcholinesterase on screen-printed electrodes: comparative study between three immobilization methods and applications to the detection of organophosphorus insecticides. *Anal. Chim. Acta* **2002**, *464*, 171-180.
(122) Cagnini, A.; Palchetti, I.; Lionti, I.; Mascini, M.; Turner, A. P. Disposable ruthenized screen-printed biosensors for pesticides monitoring. *Sensor. Actuat. B-Chem.* **1995**, *24*, 85-89.
(123) Kröger, S.; Turner, A. P.; Mosbach, K.; Haupt, K. Imprinted polymer-based sensor system for herbicides using differential-pulse voltammetry on screen-printed electrodes. *Anal. Chem.* **1999**, *71*, 3698-3702.
(124) Touloupakis, E.; Giannoudi, L.; Piletsky, S.; Guzzella, L.; Pozzoni, F.; Giardi, M. A multi-biosensor based on immobilized Photosystem II on screen-printed electrodes for the detection of herbicides in river water. *Biosens. Bioelectron.* **2005**, *20*, 1984-1992.
(125) Laschi, S.; Palchetti, I.; Mascini, M. Gold-based screen-printed sensor for detection of trace lead. *Sensor. Actuat. B-Chem.* **2006**, *114*, 460-465.
(126) Kadara, R. O.; Tothill, I. E. Stripping chronopotentiometric measurements of lead (II) and cadmium (II) in soils extracts and wastewaters using a bismuth film screen-printed electrode assembly. *Anal. Bioanal. Chem* **2004**, *378*, 770-775.
(127) Mandil, A.; Idrissi, L.; Amine, A. Stripping voltammetric determination of mercury (II) and lead (II) using screen-printed electrodes modified with gold films, and metal ion preconcentration with thiol-modified magnetic particles. *Microchim. Acta* **2010**, *170*, 299-305.
(128) Rico, M.; Olivares-Marín, M.; Gil, E. P. Modification of carbon screen-printed electrodes by adsorption of chemically synthesized Bi nanoparticles for the voltammetric stripping detection of Zn (II), Cd (II) and Pb (II). *Talanta* **2009**, *80*, 631-635.
(129) Kadara, R. O.; Newman, J. D.; Tothill, I. E. Stripping chronopotentiometric detection of copper using screen-printed three-electrode system—application to acetic-acid bioavailable fraction from soil samples. *Anal. Chim. Acta* **2003**, *493*, 95-104.
(130) Morata, A.; Viricelle, J. P.; Tarancón, A.; Dezanneau, G.; Pijolat, C.; Peiro, F.; Morante, J. R. Development and characterisation of a screen-printed mixed potential gas sensor. *Sensor. Actuat B-Chem.* **2008**, *130*, 561-566.
(131) Fergus, J. W. Materials for high temperature electrochemical NO_x gas sensors. *Sensor. Actuat. B-Chem.* **2007**, *121*, 652-663.
(132) Hart, J. P.; Abass, A. K.; Cowell, D. Development of disposable amperometric sulfur dioxide biosensors based on screen printed electrodes. *Biosens. Bioelectron.* **2002**, *17*, 389-394.
(133) Panchompoo, J.; Ge, M.; Zhao, C.; Lim, M.; Aldous, L. The oxygen reduction reaction in ferrofluids: Towards membrane-less and spill-less gas sensors. *ChemPlusChem* **2014**, *79*, 1498-1506.
(134) Dossi, N.; Toniolo, R.; Pizzariello, A.; Carrilho, E.; Piccin, E.; Battiston, S.; Bontempelli, G. An electrochemical gas sensor based on paper supported room temperature ionic liquids. *Lab Chip* **2012**, *12*, 153-158.
(135) Toniolo, R.; Dossi, N.; Svigely, R.; Susmel, S.; Casella, I. G.; Bontempelli, G. Amperometric sniffer for volatile amines based on paper-supported room temperature ionic liquids enabling rapid assessment of fish spoilage. *Electroanal.* **2014**, *26*, 1966-1974.

(136) Stetter, J. R.; Patel, V.; Findlay, M. W.; Carter, M. T.: Printed gas sensor. 2014. U.S. Patent No. 20140311905
(137) Metters, J. P.; Randviir, E. P.; Banks, C. E. Screen-printed back-to-back electroanalytical sensors. *Analyst* **2014**, *139*, 5339-5349.
(138) Gan, T.; Hu, S. Electrochemical sensors based on graphene materials. *Microchim. Acta* **2011**, *175*, 1-19.
(139) Varghese, O.; Kichambre, P.; Gong, D.; Ong, K.; Dickey, E.; Grimes, C. Gas sensing characteristics of multi-wall carbon nanotubes. *Sensor. Actuat. B-Chem.* **2001**, *81*, 32-41.
(140) Belle, C. J.; Bonamin, A.; Simon, U.; Santoyo-Salazar, J.; Pauly, M.; Bégin-Colin, S.; Pourroy, G. Size dependent gas sensing properties of spinel iron oxide nanoparticles. *Sensor. Actuat. B-Chem.* **2011**, *160*, 942-950.
(141) Ai, Z.; Deng, K.; Wan, Q.; Zhang, L.; Lee, S. Facile microwave-assisted synthesis and magnetic and gas sensing properties of Fe3O4 nanoroses. *J. Phys. Chem. C* **2010**, *114*, 6237-6242.
(142) Ahuja, T.; Kumar, D. Recent progress in the development of nano-structured conducting polymers/nanocomposites for sensor applications. *Sensor. Actuat. B-Chem.* **2009**, *136*, 275-286.
(143) Tiemann, M. Porous Metal Oxides as Gas Sensors. *Chem. Eur. J.* **2007**, *13*, 8376-8388.
(144) Sadr, S.; Azim-Araghi, M.; Rahimi, M.; Dariani, R. Effect of gold electrode annealing on gas sensing properties of nano-and microstructures of macroporous silicon. *Indian J. Pure Ap. Phys.* **2013**, *51*, 860-863.

2. Background to Electrochemistry and Characterisation Techniques

In this chapter the background to the electrode processes that give rise to the electrochemical results will be explained. The theory behind the two main electrochemical techniques, cyclic voltammetry and chronoamperometry, used in this thesis are also described. This is followed by introducing the theory behind the three main characterisation techniques in this thesis, scanning electron microscopy, confocal Raman spectroscopy and X-ray photoelectron spectroscopy.

2. BACKGROUND TO ELECTROCHEMISTRY AND CHARACTERISATION TECHNIQUES **35**

2.1 Dynamic Electrochemistry **37**

2.2 Electrical Double Layer **38**

2.3 Faradaic and Non-Faradaic Process **39**

2.4 Mass Transport **40**

2.5 Electron Transfer **42**

2.6 Testa and Reinmuth Notation **43**

2.7 Practical Aspects of Electrochemistry **44**

2.7.1 Electrochemical Cells 44

2.7.2 Electrodes Used in this Thesis 46

2.8 Electrochemical Techniques **48**

2.8.1 Cyclic Voltammetry 48

2.8.2 Chronoamperometry 52

2.9 Voltammetry in RTILs **53**

2.10 Background to Scanning Electron Microscopy, Confocal Raman Spectroscopy and X-Ray Photoelectron Spectroscopy **54**

2.10.1 Scanning Electron Microscopy (SEM) 54

2.10.1.1 Components of a SEM *55*

2.10.1.2 Electron-Sample Interactions *57*

2.10.2 X-Ray Photoelectron Spectroscopy (XPS) 60

2.10.3 Confocal Raman Spectroscopy 61

2.11 References **62**

2. Background to Electrochemistry and Characterisation Techniques

Now that the background to the project has been described, the results obtained in this thesis can be reported. However before the results are presented, it is important to introduce the background to the electrode processes that gives rise to the results obtained and also the characterisation techniques that were used in this thesis. This chapter introduces the background to electrochemistry and the characterisation techniques mainly scanning electron microscopy, confocal Raman spectroscopy and X-ray photoelectron spectroscopy.

2.1 Dynamic Electrochemistry

Electrochemistry is the study of chemical reactions occurring at the interface between an electrode and an ionic conductor (electrolyte). There are two main types of electrochemistry; equilibrium and dynamic[1] but the work performed in this thesis is focused on the latter and the fundamental principles and methods are briefly described below. A more detailed description can be found in various electrochemistry textbooks.[2-4]

Dynamic electrochemistry (non-equilibrium electrochemistry) is the study of electron transfer reactions between an electrode and an analyte species in electrolyte/solution. A potential difference is applied between the electrolyte and electrode and the current is monitored as a function of the applied potential. The resulting plot is known as a voltammogram and provides both kinetic information and thermodynamic information on the electron transfer process. Being able to interpret a cyclic voltammogram is crucial in understanding the mechanism of the electrochemical behaviour of the gases studied in this work. The next few sections

will describe the three types of transport of reactant molecules in solution and how these species undergo electron transfer. However, first the structure of the interfacial region between the electrode and electrolyte (electrical double layer) has to be introduced.

2.2 Electrical Double Layer

In an electrochemical experiment, the electrode acts as a source or sink of electrons. When an electrode is immersed into a solution, there is a distribution of charge at the interface, and an electric field gradient is established extending out towards the bulk solution creating what is termed a 'double layer'. There have been several different models proposed to describe the structure of the double layer, however, the Stern model[1,2] is the most commonly used and widely accepted. In this model there is a layer of counter ions of opposite charge present on the charged electrode surface (figure 2.1) called the outer Helmholtz plane (OHP). At a short distance from the electrode, there is a region called the 'diffuse double layer' consisting of ions that are treated as spheres of realistic dimensions (rather than point charges).[3] The potential drops linearly from the electrode surface to the OHP through the inner Helmholtz plane and then it drops exponentially through the diffuse layer to the bulk solution.

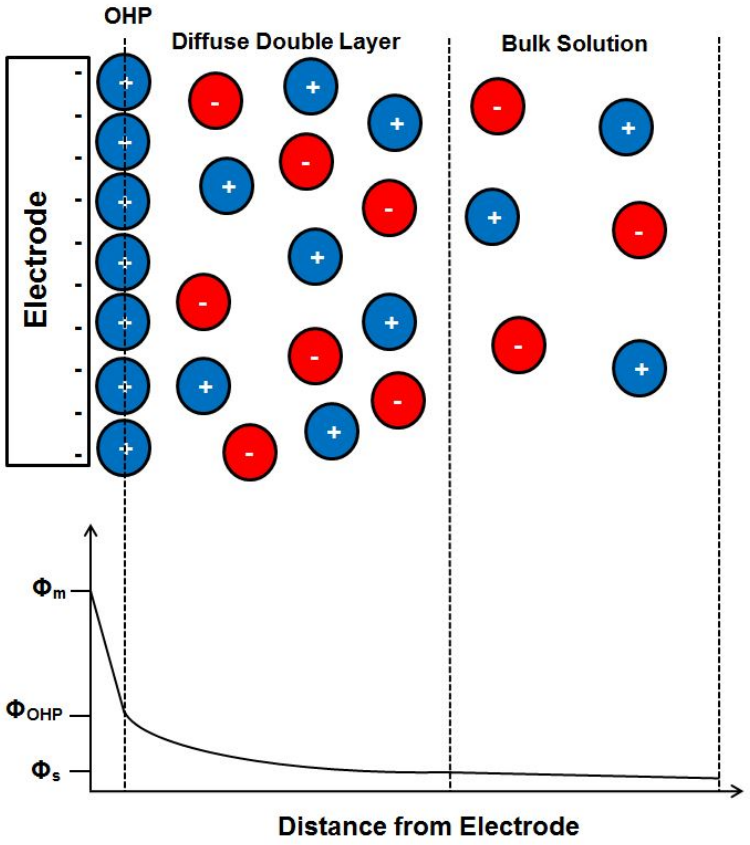

Figure 2.1: Diagram depicting the Stern[2] model for the diffuse double layer

Due to the nature of room temperature ionic liquids (RTILs) it might not be possible for them to follow the Stern model[5,6] therefore a multilayer model has been proposed where the cations and anions adjacent to the electrode align themselves to produce alternating layers of positive and negative charges with the excess charge buried several layers deep.[7-9]

2.3 Faradaic and Non-Faradaic Process

There are two types of processes that cause a current in a voltammogram, one being Faradaic and the other non-Faradaic, named after Sir Michael Faraday.[10] The Faradaic process is caused by the electron transfer between the electroactive species and the metal electrode and this can be either oxidation or reduction depending on the direction of the flow of electrons. The charge passed for one mole of electrons is

96485 C which is also termed the Faraday constant. Adsorption/desorption processes occurring at the electrode surface and changes in the interfacial region as the potential is varied are the main reasons for the non-Faradaic current which causes charging and discharging currents. This charging and discharging of current is also termed the capacitive current and experimental conditions are usually designed to limit this as the Faradaic process is where useful analytical information can be obtained. The non-Faradaic process is an additional process that occurs at the electrode and is usually the unwanted process as it can sometimes swamp the Faradaic process that occurs at the electrode surface (This will be looked at in greater detail in our experiments).

2.4 Mass Transport

For a reaction to occur an electroactive species must be transported from the bulk solution to the electrode surface. This can occur by one (or more) of three modes of mass transport: diffusion, convection or migration which is described below.

1) Diffusion is the movement of species from an area of high concentration to an area of low concentration due to the presence of a concentration gradient. The concentration gradient occurs as a result of electroactive species being depleted at the electrode surface during an electrochemical reaction. The rate of diffusion is described mathematically by Fick's Law[11]

$$j_d = -D\frac{\delta c}{\delta x} \qquad (2.1)$$

where j_d is the flux due to the diffusion of a species with concentration c in direction x. $\frac{\delta c}{\delta x}$ is the concentration gradient in the direction from x to a planar surface, and D is the measure of the ease at which the species can diffuse, known as the 'diffusion

coefficient'. *D* is dependent on factors such as the molecular size, solvent viscosity, temperature etc. This diffusion coefficient is an important entity that describes the rate at which the electroactive material reaches the electrode surface. The diffusion coefficient usually follows the Stokes-Einstein relationship;

$$D = \frac{k_B T}{6\eta\pi a} \tag{2.2}$$

Where k_B is the Boltzmann constant, T is the temperature, η is the viscosity and a is the hydrodynamic radius of the species that is diffusing.

2) Convection is the movement of species due to natural or forced mechanical forces acting on a solution. Natural convection arises from thermal gradients and density differences within a given solution and forced convection occurs through external forces, such as gas bubbling through a solution, pumping, stirring or motion of the electrode. The experimental set-up is usually designed so that contributions from convection are minimised, e.g. by measuring on short timescales (where natural convection is negligible) or by working in still/quiescent solutions (where there is no bubbling or motion of the solution).

3) Migration is the movement of charged species along an electric potential gradient. In voltammetry, the application of a potential results in an electric potential difference between the electrode and the bulk solution. In practice the effect of migration is often hard to calculate accurately, due to complex diffusion layer and ion solvation effects. Therefore it is usual to minimise migration by adding a large excess (e.g. 50× compared to the quantity of reactants) of an inert supporting electrolyte, which reduces the size of the electrical double layer (see section 2.2) and maintains a relatively constant electrical field throughout the solution.

2.5 Electron Transfer

We have explained how the electroactive material can be transported to the electrode surface, hence now we consider the useful Faradaic currents produced as a result of the electron transfer reaction. A typical one-electron transfer is described as:[2]

$$O + e^- \rightleftharpoons R \tag{2.3}$$

where R is the reduced form of the analyte species O. The forward and backward reactions are governed by rate constants k_f and k_b respectively. The current observed at the electrode is given by

$$i = FAj \tag{2.4}$$

where F is the Faraday constant, A is the area of the electrode and j is the flux of the electroactive species at the electrode. The flux is dependent on the rate at which the species react at the electrode; hence equation 2.4 can be expressed as:

$$i = FA(k_b[R]_0 - k_f[O]_0) \tag{2.5}$$

where $[R]_0$ and $[O]_0$ are the concentrations of the species. Transition state theory can be applied and the rate constants are expressed as:

$$k_b = k_0 \exp\left(\frac{(1-\alpha)\left(E-E_f^0\right)F}{RT}\right) \tag{2.6}$$

$$k_f = k_0 \exp\left(\frac{(-\alpha)\left(E-E_f^0\right)F}{RT}\right) \tag{2.7}$$

where k_0 is the standard electrochemical rate constant, $(E-E_f^0)$ is the overpotential (the difference between the applied potential and the standard potential). α is the transfer coefficient which represents the position of the transition state along the reaction coordinate between the reactants and products and has a value between 0

and 1, usually close to 0.5, which indicates that the transition state exhibits intermediate behaviour. Equation 2.6 and 2.7 can be substituted into 2.5 to yield the Butler-Volmer [12,13] equation:

$$i = FA(k_0 \exp(\frac{(1-\alpha)\left(E-E_f^0\right)F}{RT})[\mathrm{R}]_0 - k_0 \exp(\frac{(-\alpha)\left(E-E_f^0\right)F}{RT})[\mathrm{O}]_0) \qquad (2.8)$$

The Butler-Volmer equation provides a good theoretical model for the relationship between the potential and current with the aid of the mass transport equations.

Sometimes the heterogeneous electron transfer at the electrode is coupled with a homogeneous chemical step, which influences the observed voltammetry. In the case of the electrochemical oxidation of methylamine there is a homogenous chemical step after the electrochemical step and in hydrogen chloride gas there is a chemical step before the electrochemical step whereas in chlorine there are no chemical steps involved in the reaction. Each reaction has different steps and amounts of steps, therefore to be able to describe the observed voltammetry homogeneous kinetic terms must also be included together with the mass transport and Butler-Volmer equations. The Testa and Reinmuth[14] notation was used to describe the electrochemical reaction sequences in this thesis.

2.6 Testa and Reinmuth Notation

The letter ‘E’ is used to describe an electrochemical step and the letter ‘C’ for a chemical process. These terms are combined in the sequence in which they occur in the reaction mechanism. In a ‘CE’ process, electron transfer (E) is preceded by a homogeneous reaction (C). The current is determined by the kinetics of the chemical process (C). In an ‘EC’ process the product of the electrochemical step (E) is unstable and hence undergoes a chemical reaction (C). In an ‘ECE’ process the

product formed after the 'EC' step undergoes an electrochemical process as it is electrochemically active in the potential window of study. The electrochemical oxidation of methylamine gas in ionic liquids is believed to follow an ECE mechanism while that of Cl_2 follows a E mechanism and that of HCl follows a CEE and will be explained in the results and discussion section of each gas.

2.7 Practical Aspects of Electrochemistry

We have thus far described the theory of electron transfer and processes that occur at the electrode surface and now will move onto the practical aspects of the electrochemical experiments.

2.7.1 Electrochemical Cells

In an electrochemical experiment, a three electrode set-up is typically employed, consisting of a working electrode (WE), reference electrode (RE) and counter electrode (CE) (figure 2.2). In dynamic electrochemistry the process being measured occurs at the WE, but an opposite reaction also occurs at the CE (usually involving the solvent). The potential of the RE remains fixed through an experiment. The voltage of the WE is then measured relative to the RE, given by[1]

$$E_{app} = E_{WE} - E_{RE} - iR_s \qquad (2.9)$$

where E_{WE} and E_{RE} are the potential differences across the WE/solution and RE/solution interface, respectively, E_{app} is the applied potential, i is the current and R_s is the uncompensated resistance of the electrolyte solution termed 'Ohmic drop'. The magnitude of Ohmic drop depends on the area of the electrode, conductivity of the solution and separation of the WE/RE. In some experiments in this thesis, a two-electrode set-up is employed, consisting of a WE and a combined RE and CE. This can be used when passing small currents (e.g. at microelectrodes) where the iR_s term

is negligible. Counter electrodes are typically good electronic conductors with a large surface area. It can be seen from figure 2.2 that a Pt coil is used as a counter electrode. A coil exposes more of the surface area of the counter electrode so that electron transfer at the working electrode is not limited. For all aqueous experiments a Ag/AgCl wire is used as the reference electrode and widely accepted. For experiments involving RTILs a Ag wire is used as a quasi-reference electrode as there isn't a standard reference electrode available for use in RTILs. However in recent times there has been a lot of development in the area of reference electrodes in RTILs. Roling[15] et al. reported a miniaturized Ag/Ag^+ reference electrode with a frit where the Ag ions were provided from a solution of $Ag[NTf_2]$. However these electrodes will not be suitable in this instance due to the geometric constraints/miniaturized electrode. When using quasi-reference electrode it is common practice to use a redox couple such as ferrocene/ferrocenium to report peak potentials. However by dissolving ferrocene in RTILs and using it as a reference to measure peak potentials it could affect the diffusion of the target gases to the electrode surface and this is not ideal from an analytical point of view.[16]

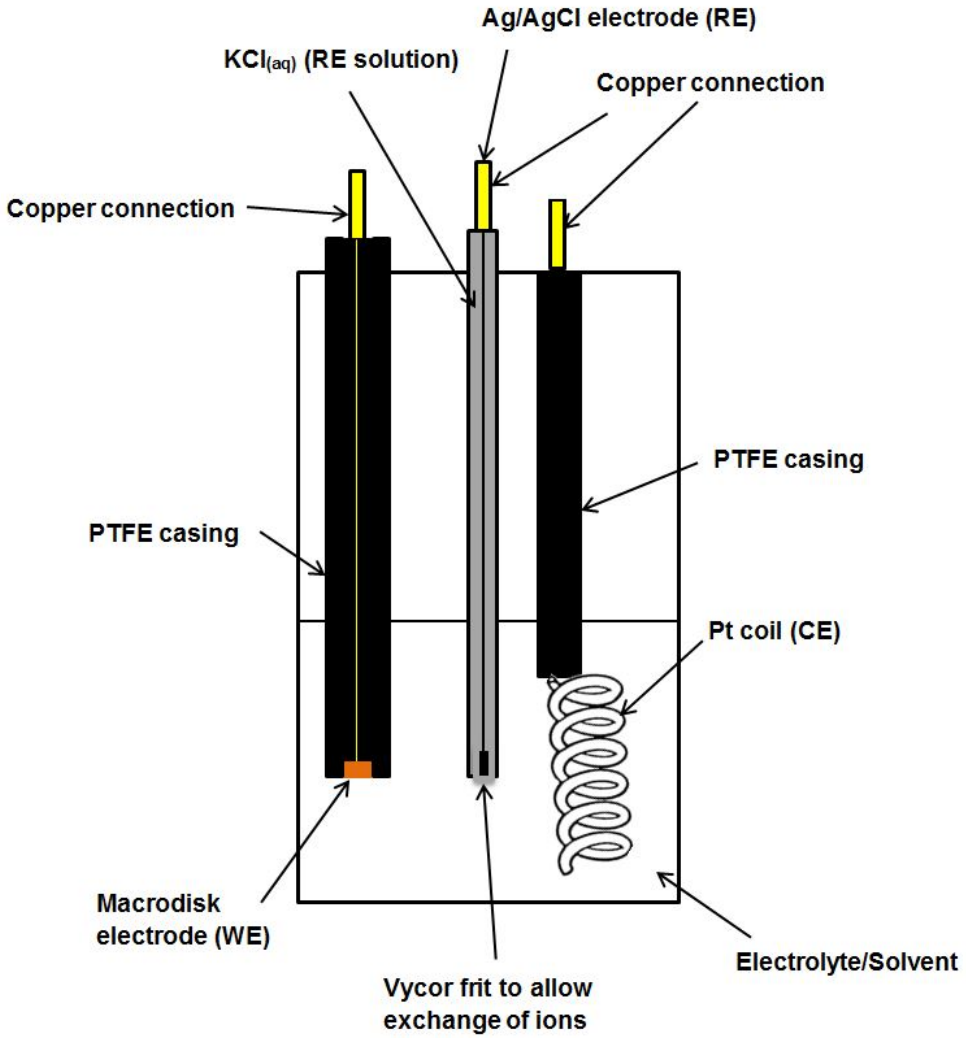

Figure 2.2: Diagram of a conventional three electrode system composed of a macrodisk (WE), Ag/AgCl (RE) and Pt coil (CE) in a solvent with electrolyte.

2.7.2 Electrodes Used in this Thesis

Macro- and micro- disk electrodes are the most commonly used working electrodes. They are utilized to study the mechanisms of the reactions in this thesis, alongside screen-printed electrodes where the dimensions of the working electrode makes it a macro sized electrode.

There are two main types of diffusion that can occur at these electrodes: 1) Convergent diffusion where diffusion takes place at the edges of the disk surface, and 2) planar diffusion, where diffusion takes place at all points normal to the disk

surface.[3] For micro electrodes convergent diffusion dominates due to their smaller size and for macro electrodes planar diffusion dominates (figure 2.3).

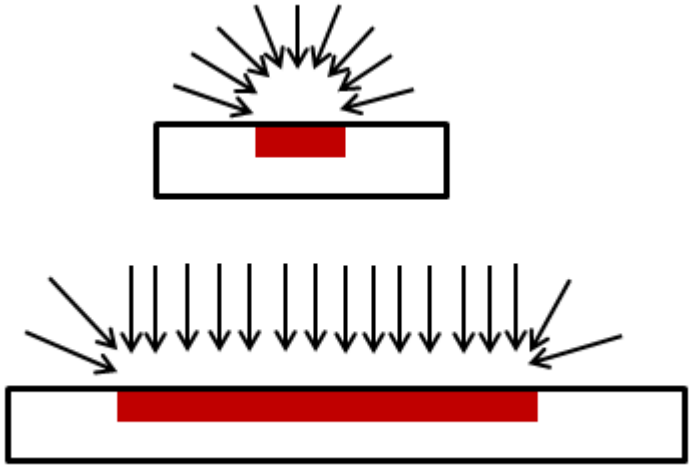

Figure 2.3: Comparison of diffusion patterns micro electrodes (top) and macro electrodes (bottom)

Macro electrodes are widely available, easy to use and higher currents can be measured. Micro electrodes have a much faster rate of mass transport and are useful for the measurement of fast electrochemical process. Micro electrodes measure much smaller currents than macro electrodes and thus have a lower ohmic drop. Micro electrodes also have a larger current density then macro electrodes and this is one of the reasons why micro electrodes are preferred in sensing applications. In this thesis micro electrodes were first used to study the mechanism of the gases in RTILs before moving onto screen-printed electrodes so that a good comparison is achieved. Macro electrodes in an aqueous medium were used to study the electrochemical behaviour of macroporous metal frameworks and magnetite nanoparticles as it is possible to modify the surfaces of a macro electrode much more easily as compared to a micro electrode.

2.8 Electrochemical Techniques

Two main electrochemical techniques, cyclic voltammetry and chronoamperometry, were employed throughout this thesis. The understanding of these two methodologies 1) cyclic voltammetry, where the potential is swept linearly through a chosen range and the current is measured as a function of potential,[1] and 2) chronoamperometry where the potential is stepped to a fixed value and the current is measured as a function of time,[1] allows the interpretation of the graphs presented later in this work.

2.8.1 Cyclic Voltammetry

Cyclic voltammetry (CV) involves the measurement of current as the potential is varied as a function of time. This can be seen in figure 2.4 where the potential is swept from E_1 to E_2 and then back to E_1 at a constant scan rate which is typical of a CV and is termed the 'triangular potential ramp'. A plot of current vs potential is the experimental output of a cyclic voltammetric experiment and is termed a voltammogram. The shape of the voltammogram depends on factors such as mass transport and the size of the working electrode.[3]

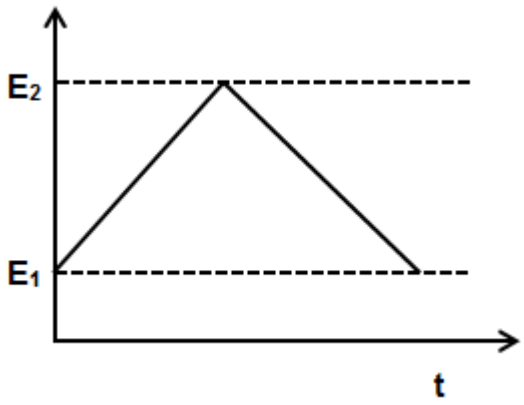

Figure 2.4: Graph showing triangular waveform applied during a CV

On macro electrodes there are three main types of voltammetry that can be observed (figure 2.5). The first is reversible where the electron transfer process is fast, the

second is quasi-reversible where electron transfer is slow and a larger overpotential is required to drive the electron transfer. The third is termed 'irreversible' where the kinetics of the electron transfer is not fast enough to maintain equilibrium.[3] This can also indicate a chemical step following the electron transfer (e.g. EC mechanism).

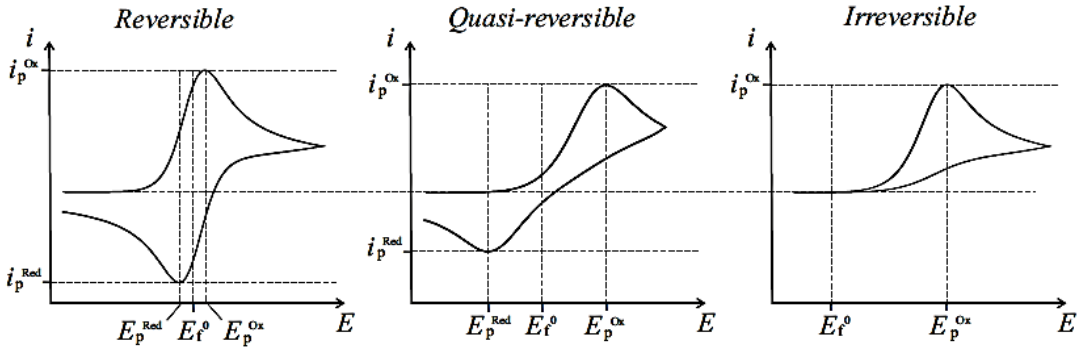

Figure 2.5: A comparison of cyclic voltammetric wave-shapes at macroelectrodes

For a reversible process, initially there is no current as the potential is not high enough for electron transfer to occur. As the potential increases, electron transfer becomes possible, and the current increases exponentially. The maximum current observed at $E_p{}^{Ox}$ is due to the balance between electron transfer and diffusion. The current then falls off at higher potentials due to the diffusion layer becoming thicker; hence the electroactive species has to diffuse a larger distance to reach the surface of the working electrode. On the reverse sweep, the electro generated product is reduced back to the initial species. The peak current follows the Randles-Sevcik equation,[17]

$$i_p = (2.69 \times 10^5) n^{\frac{3}{2}} A D^{\frac{1}{2}} v^{\frac{1}{2}} c_{bulk} \qquad (2.10)$$

Where n is the number of electrons, A is the area of the electrode, D is the diffusion coefficient, v is the scan rate and c_{bulk} is the concentration of the electroactive species in the bulk solution. When the system is fully reversible, the separation

between the forward and reverse peaks is 57/*n* mV at 298 K [2] (where *n* is the number of electrons involved in the reaction) and the peak potentials are independent of the scan rates. In this thesis experiments are done at different scan rates to obtain information with regards to the process occurring at the electrode surface. At high scan rates, the timescale of the experiment is much shorter as compared to a lower scan rate, therefore there is much lesser depletion of material at the surface of the electrode. This produces a smaller diffusion layer and therefore a greater flux of material gets transported to the electrode surface due to the steeper concentration gradient. This produces the higher peak currents that are seen for higher scan rate experiments. For a diffusional process the peak current varies linearly with the square root of the scan rate.

For a quasi-reversible (figure 2.5) system the shape of the voltammogram is very similar to the reversible case except for two main differences, one where the peak currents are much smaller and the other is where the peaks are more separated showing the slower kinetics involved in this type of reaction.

For an irreversible system the peak current follows;[4]

$$i_p = (2.99 \times 10^5) n (\alpha n_{rd})^{\frac{1}{2}} A D^{\frac{1}{2}} v^{\frac{1}{2}} c_{bulk} \qquad (2.11)$$

where α is the charge transfer coefficient. For an irreversible system a large overpotential is needed to push the reaction through therefore the oxidation peak will occur at higher peak potentials as compared to a reversible case. The absence of a reduction peak could mean two things; 1) that the reduction if it does occur, occurs at higher negative potentials outside the potential window shown or 2) a chemical step is involved after the electrochemical step (EC mechanism).

On micro electrodes due to the differences in the diffusion patterns the type of voltammetry seen is different and is termed sigmoidal (figure 2.6). Once the maximum current is achieved it plateaus and this phenomenon is termed steady state behaviour. This occurs because the rate of mass transport is sufficiently fast that the concentration of the electroactive species at the electrode surface is continually being replenished.[3] $E_{1/2}$ is the formal potential for a redox couple with fast electrode kinetics. The steady state limiting current (i_{ss}) is often used to calibrate the radius of the microelectrode (r_d) with the equation;[3]

$$i_{ss} = -4nFDcr_d \qquad (2.12)$$

Where *F* is the Faraday's constant, *c* is the concentration and *D* is the diffusion coefficient of the electroactive material (both known quantities).

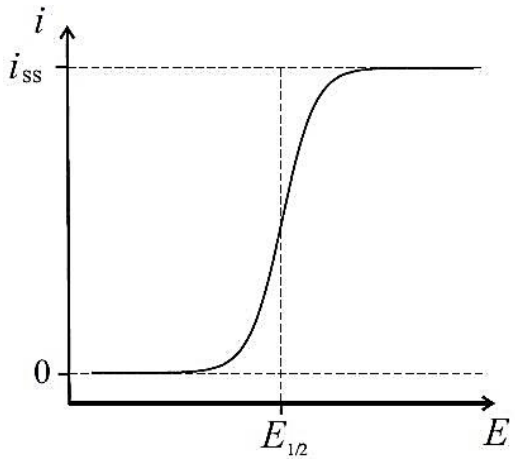

Figure 2.6: Voltammetry at a microelectrode (steady state)

It is important to note here that the shape in a CV can also be influenced by the viscosity of the medium and will be described further in section 2.9.

2.8.2 Chronoamperometry

In chronoamperometry the potential is stepped from an initial value, E_1 (no current) to a final value E_2 where the electron transfer occurs (figure 2.7a). The large current initially recorded falls due to the depletion of the species at the surface.

The behaviour is different on macro and micro electrodes due to their difference in diffusion processes. On micro electrodes where radial diffusion dominates the limiting current is given by the Shoup and Szabo expression where the current can be described as a function of a dimensionless parameter τ;[3,18]

$$I = 4nFcDr_e f(\tau) \tag{2.13}$$

Where,

$$f(\tau) = 0.7854 + 0.8863\tau^{-\frac{1}{2}} + 0.2146\exp(-0.7823\tau^{-\frac{1}{2}}) \tag{2.14}$$

n is the number of electrons, F is the faraday's constant, c is the concentration, and D is the diffusion coefficient of the electroactive material and r_e is the radius of the electrode. By fitting the chronoamperometric transients obtained with the Shoup and Szabo expression, values for the diffusion coefficients, concentration of analyte species and the number of electrons transferred in the reaction can be obtained. In this thesis all three gases will be investigated using the Shoup and Szabo expression. However it is important to note here that no information regarding the kinetics of the reaction can be obtained because the potential is usually stepped up to after where the reaction occurs which is more negative than the formal potential of the reaction.

On macro electrodes where planar diffusion dominates, the diffusion limiting current i_d is given by the Cottrell equation;[2]

$$i_d = \frac{nFAD^{\frac{1}{2}}c}{\pi^{\frac{1}{2}}t^{\frac{1}{2}}} \quad (2.15)$$

Where *n* is the number of electrons transferred, *F* is the Faraday constant, *A* is the electrode surface area, *c* is the concentration of the electroactive species and *t* is the time. The SPEs used in this thesis have a WE diameter of 4 mm hence they can be modelled as a macro electrode.

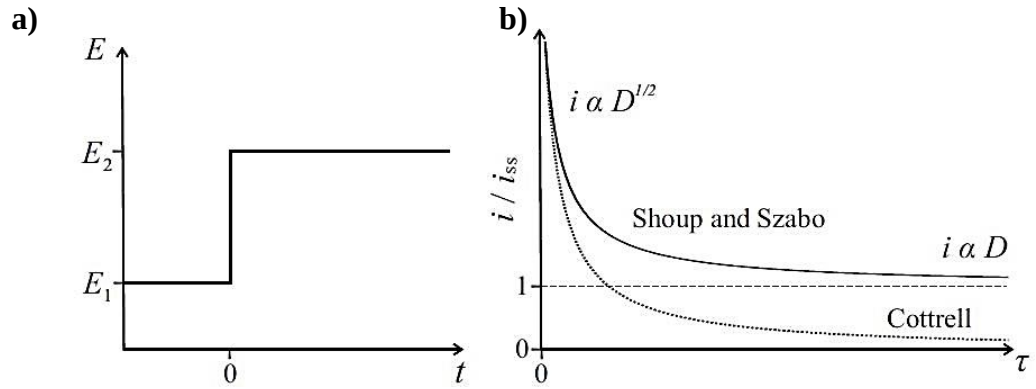

Figure 2.7: a) Graph of applied potential vs time and b) experimental output depicting the change in current over time for macro (Cottrell) and micro (Shoup and Szabo) electrodes

2.9 Voltammetry in RTILs

As mentioned earlier most of the experiments in this thesis involve the use of RTIL as the solvent for electrochemical experiments. It is important to note that the high viscosity of RTILs influences electrochemical experiments to a large extent.

The high viscosity of RTILs means that when they are used in conjunction with a microelectrode, steady state current seen on a cyclic voltammogram cannot be taken as the true steady state limiting current. True steady state behaviour is only seen at either very slow scan rates of 10 mVs^{-1} or less ,or electrodes with a radius of 5 µm and follows the inequality;[9]

$$v \ll \frac{RTD}{nFr_{d^2}} \quad (2.16)$$

Where v is the scan rate, R is the universal gas constant, T is the absolute temperature, F is the Faraday constant, D is the diffusion coefficient and r_d is the radius of the electrode. This was very well described in the work done by Evans et al.[19] They showed that the reduction of oxygen in the RTIL $[N_{6,2,2,2}][NTf_2]$ produces a steady state current (radial diffusion) which is due to oxygen reducing to the superoxide and then on the reverse scan they observed a peak shaped current (linear diffusion) which is due to the superoxide oxidising back to oxygen. This is due to the drastic differences in the diffusion coefficients between the two species. The existence of both types of behaviour, steady state and transient in a RTIL on a microelectrode clearly shows that you don't always only see steady state behaviour. This behaviour was also observed in our experiments and will be discussed in greater detail in the results and discussion chapters.

2.10 Background to Scanning Electron Microscopy, Confocal Raman Spectroscopy and X-Ray Photoelectron Spectroscopy

Now that the background to the electrochemistry is given the next step is to have a look at the three main characterisation techniques used in this thesis.

2.10.1 Scanning Electron Microscopy (SEM)

Scanning electron microscopy (SEM) is an imaging technique that is widely used by many researchers to obtain information such as topography, morphology and composition[20] and is able to provide magnification up to 1,000,000 ×. In this work SEM is used to characterise all the various surfaces of the SPEs, the distribution of the magnetite nanoparticles on an electrode surface and the porosity of the macroporous metallic frameworks.

The limitations of a light microscope (10,000 × magnifications) are the main reason for the development of an electron microscope. The first scanning electron microscope was developed in 1937 by Von Ardenne[21] and then commercial instruments followed in 1965. SEMs give us information on topography, morphology, composition and crystallographic structure. Topography is how the "surface looks", its roughness and texture which can all be related to its electrochemical properties. Morphology refers to the shape and size of the particles making up the sample. By using the energy dispersive X-ray spectroscopy (EDS) component of a SEM the composition of the material and the relative amounts can be obtained. Crystallographic information can be obtained by looking at how the atoms/crystals are arranged in the sample which will give us information with regards to the properties of the material. The large depth of field obtained when using a SEM makes it an attractive tool for analysis of 3D samples.

2.10.1.1 Components of a SEM

Figure 2.8 shows the basic layout of the interior of a SEM. The electron gun at the top produces the electrons that are first condensed by the first condenser lens. A typical electron beam source is a Tungsten filament cathode which is heated to emit electrons. The condenser lens also limits the amount of current that is passed through. This new formed beam goes through the condenser aperture where high angle electrons are eliminated. The job of the second condenser lens is to form the electron beam into a tight, thin and coherent one. The formed beam then passes through the objective aperture where off energy and off axis electrons are eliminated. Then the beam passes through the scanning coils where the beam is deflected in the X and Y axes so that scanning over the sample can occur in a raster fashion. The role of the final lens which is the objective lens is to focus the scanning beam onto the

sample where the user desires. Of course this whole system is in vacuum so that there is no drift of electrons. It is important to note here that the lenses used in a SEM are electromagnets and not glass lens that are used in a light microscope. The electrons are controlled by varying the strength of the electromagnetic field of these magnets. Once the beam hits the sample electrons are released which are captured by various detectors depending on their energy. When an electron beam strikes the sample, various signals are generated such as backscattered electrons, secondary electrons, cathodoluminescence and X-rays.[22] The two main types of signals that we are interested are secondary electrons and backscattered electrons. Before venturing in trying to detect these electrons it is important to introduce the concept of interaction volume.

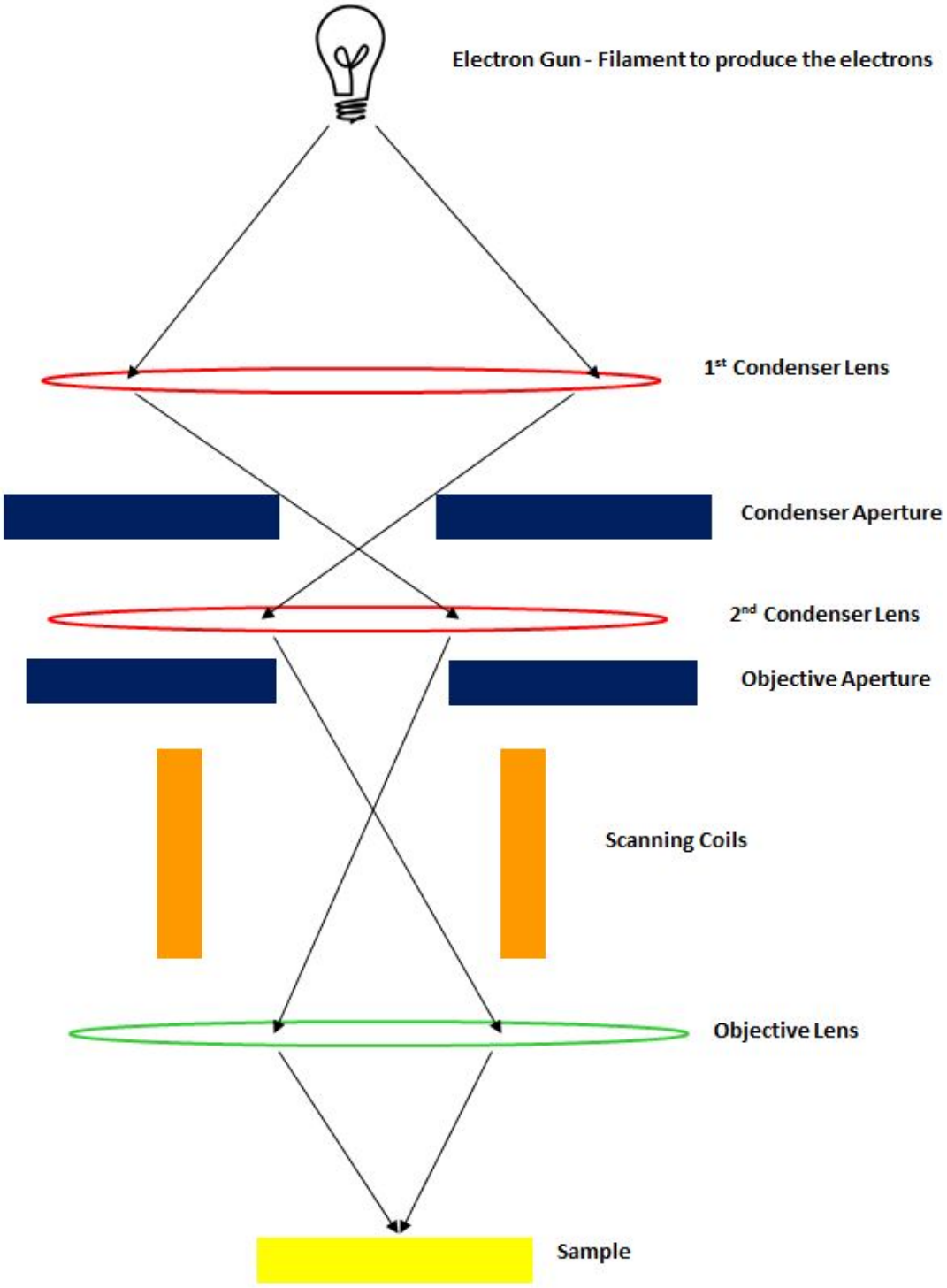

Figure 2.8: Cartoon depicting the interior components of a SEM

2.10.1.2 Electron-Sample Interactions

When an electron beam hits a sample various signals are generated depending on the interaction volume. The size of the interaction volume depends on the strength of the

electron beam hitting the sample. The higher the eV of the electron beam the higher the interaction volume. Figure 2.9 shows the various signals that are generated at various depth of the sample. Auger electrons with energies of 10 to 30 Å are released from the top most part of the surface.

Then there are secondary electrons which are released within a few nanometres and they have energies of around 100 Å. Secondary electrons are produced by inelastic collisions between beam and specimen electrons. Secondary electrons have a low escape depth of around a few nm, therefore they produce an image with excellent topography details and hence high resolution. There are various secondary electron detectors and the most common one that is used is the Everhart-Thornley[23] detector. It consists of a scintillator inside a Faraday cage. A positive voltage is applied to the Faraday cage which attracts the low energy secondary electrons. The electrons are then converted to light photons with the aid of the scintillator.

Then next we have backscattered electrons (BSEs) which are produced by elastic collisions between the incoming electrons and the nucleus of the target atom. Elastic scattering results in little (< 1 eV) or no change in energy of the scattered electrons hence they have a relatively large energy. They are also dependent on the atomic number Z. Higher atomic number elements produce more scattering hence appear brighter on screen. Due to their escape depth being greater because of their high energy, they provide sub surface information. A surface barrier detector which sits directly on top of the sample is used to detect BSEs.

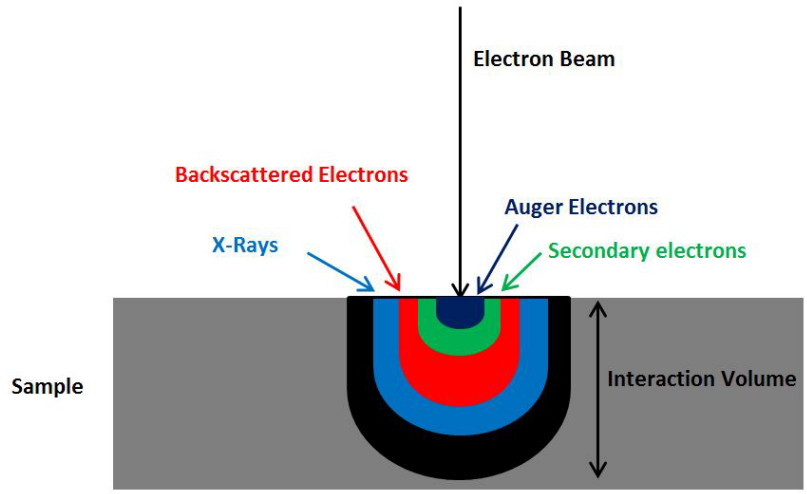

Figure 2.9: Interaction volume of a sample showing the various signals when an electron beam hits a sample.

It is important to note here that by tuning the electron beam, different information about the sample can be obtained. A high accelerating voltage maximizes the gun brightness and also increases the interaction volume, hence it reduces the tendency of obtaining information from secondary electrons and it increases the information obtained from backscattered electrons therefore more information from 'inside' the sample can be obtained.

Because of the nature of the SEM the sample has to be conductive. Therefore nonconductive samples have to be coated with a thin layer of platinum, gold or carbon before experiments. The coating thickness has to be thin if maximum resolution is to be obtained as a thin sample will allow more secondary electrons to escape. Thicker coats will not allow many of the electrons to leave the sample hence it will decrease the secondary electron yield and therefore the resolution. In this thesis all of the samples were conductive and therefore no sample coating was need (except for imaging polystyrene beads, which were used for the Pt macroporous framework, where a thin Pt layer of 1-2 nm was used).

For the purpose of this thesis, SEM was utilised as an imaging tool for screen printed electrodes to obtain topographic information, morphology of the metal frameworks and to characterise the size and distribution of magnetite nanoparticles on an electrode surface.

2.10.2 X-Ray Photoelectron Spectroscopy (XPS)

X-ray photoelectron spectroscopy (XPS) is another characterisation technique that was used in this work and a brief summary will be given below, for a more detailed description several textbooks can be looked up.[24-26]

XPS is a semi quantitative and surface sensitive technique, based on the photoelectric effect, used to investigate the chemical structure of surfaces (top 10 nm of a sample). A sample is hit with X-Ray photons either a Al Kα or Mg Kα in a vacuum. This X-ray transfers its energy to the electrons in the core shell causing it to be emitted from its initial state with a kinetic energy dependent on the incident X-ray and the binding energy associated with its atomic orbital. The emitted photoelectrons are characteristic of each element and are analysed to identify and determine the concentration of elements present according to their energy and intensity. It is important to note here that XPS is a very surface sensitive technique as the photoelectrons emitted have a very low escape depth of about 10 nm. Ultra high vacuum conditions are required for XPS so no wet samples can be analysed as it will cause the electrons to drift. In this thesis XPS will be used as a complimentary technique to SEM to study the surface of SPEs. XPS will also be used to characterise the magnetite nanoparticles.

2.10.3 Confocal Raman Spectroscopy

Raman spectroscopy was invented by Sir C. V. Raman in 1928[27] and it gives us useful information about a molecule's vibrational and rotational states. When a monochromatic laser/light with a certain frequency hits a sample, some of the light interacts with the molecules and causes the energy to either shift up or down, which is termed inelastic scattering or Raman scattering.[28] This energy shift can be used to obtain information with regards to the vibration modes in a molecule. By plotting the energy shifts with the frequency of the laser a Raman spectrum is obtained which is characteristic of the sample. It is a very powerful technique that can be used for both quantitative and qualitative applications. Since each bond vibrates to a certain frequency, for an unknown sample using fingerprinting from a database, the identity can be determined. In this thesis confocal Raman spectroscopy (CRS) is used to characterise the magnetite nanoparticles. CRS is a Raman spectrometer coupled with a standard optical microscope. The advantage of a using a CRS is the ability to obtain an optical image and then scan a particular area within that image which gives the homogeneity of the sample.

2.11 References

(1) Fisher, A. C.: *Electrode dynamics*; Oxford University Press, 1996.
(2) Bard, A. J.; Faulkner, L. R.: *Electrochemical methods: fundamentals and applications*; Wiley India Pvt. Ltd., 2006.
(3) Compton, R. G.; Banks, C. E.: *Understanding voltammetry*; Imperial College Press, 2011.
(4) Brett, C. M. A.; Brett, A. M. O.: *Electrochemistry: Principles, methods, and applications*; Oxford University Press, 1993.
(5) Kornyshev, A. A. Double-Layer in Ionic Liquids: Paradigm Change? *J. Phys. Chem. B* **2007**, *111*, 5545-5557.
(6) Bazant, M. Z.; Storey, B. D.; Kornyshev, A. A. Double layer in ionic liquids: Overscreening versus crowding. *Phys. Rev. Lett.* **2011**, *106*, 046102.
(7) Graves, A. D.; Inman, D. The electrical double layer in molten salts: Part 2. The double-layer capacitance. *J. Electroanal. Chem. Interfacial Electrochem.* **1970**, *25*, 357-372.
(8) Nanjundiah, C.; McDevitt, S. F.; Koch, V. R. Differential Capacitance Measurements in Solvent-Free Ionic Liquids at Hg and C Interfaces. *J. Electrochem. Soc.* **1997**, *144*, 3392-3397.
(9) Buzzeo, M. C.; Evans, R. G.; Compton, R. G. Non-Haloaluminate Room-Temperature Ionic Liquids in Electrochemistry—A Review. *ChemPhysChem* **2004**, *5*, 1106-1120.
(10) Faraday, M. Experimental researches in electricity. *Philos. Trans. R. Soc. Lond.* **1832**, *122*, 125-162.
(11) Atkins, P.; Paula, J. D.: *Physical chemistry*; W. H. Freeman and Co., 2009.
(12) Butler, J. A. V. *Trans. Faraday Soc.* **1924**, *19*, 729.
(13) Erdey-Gruz, T.; Volmer, M. *Z. Phys. Chem.* **1930**, *150*, 203.
(14) Testa, A. C.; Reinmuth, W. H. Chronopotentiometry with Step-Functional Change in Current. *Anal. Chem.* **1961**, *33*, 1324-1328.
(15) Huber, B.; Roling, B. Development of a Ag/Ag+ micro-reference electrode for electrochemical measurements in ionic liquids. *Electrochim. Acta* **2011**, *56*, 6569-6572.
(16) Torriero, A. A. J.; Sunarso, J.; Howlett, P. C. Critical evaluation of reference systems for voltammetric measurements in ionic liquids. *Electrochim. Acta* **2012**, *82*, 60-68.
(17) Randles, J. E. B. A cathode ray polarograph. Part II.-The current-voltage curves. *Trans. Faraday Soc.* **1948**, *44*, 327-338.
(18) Shoup, D.; Szabo, A. Chronoamperometric current at finite disk electrodes. *J. Electroanal. Chem. Interfacial Electrochem.* **1982**, *140*, 237-245.
(19) Evans, R. G.; Klymenko, O. V.; Saddoughi, S. A.; Hardacre, C.; Compton, R. G. Electroreduction of oxygen in a series of room temperature ionic liquids composed of group 15-centered cations and anions. *J. Phys. Chem. B* **2004**, *108*, 7878-7886.
(20) Reimer, L.: *Scanning electron microscopy: Physics of image formation and microanalysis*; Springer, 1998.
(21) von Ardenne, M. On the history of scanning electron microscopy, of the electron microprobe, and of early contributions to transmission electron microscopy. *The beginnings of electron microscopy (PW Hawkes ed) Adv. Electron. Electron Phys. Suppl.* **1985**, *16*, 1-21

(22) Goldstein, J.: *Scanning electron microscopy and x-ray microanalysis*; Kluwer Academic/Plenum Publishers, 2003.
(23) Everhart, T. E.; Thornley, R. F. M. Wide-band detector for micro-microampere low-energy electron currents. *J. Sci. Instrum.* **1960**, *37*, 246.
(24) Watts, J. F.; Wolstenholme, J.: *An introduction to surface analysis by XPS and AES*; Wiley, 2003.
(25) Briggs, D.; Seah, P.: *Practical surface analysis, auger and x-ray photoelectron spectroscopy*; Wiley, 1990.
(26) van der Heide, P.: *X-ray photoelectron spectroscopy: An introduction to principles and practices*; Wiley, 2011.
(27) Raman, C. V. A new radiation. *Indian J. Phys.* **1928**, *2*, 387-398.
(28) Colthup, N. B.; Daly, L. H.; Wiberley, S. E.: *Introduction to infrared and Raman spectroscopy*; Elsevier Science, 1990.

3. Experimental Chapter

This chapter contains the general experimental procedures used in this thesis. The different types of electrodes and cells used will be described. The gas mixing setup used for the study of hydrogen chloride, methylamine and chlorine will be presented.

3. EXPERIMENTAL CHAPTER **65**

3.1 Chemical Reagents and Gases **67**

3.2 Electrodes and Cells **67**

3.3 Electrochemical Experiments **75**

3.4 Gas Mixing Setup **76**

3.5 XPS, SEM, NMR and Raman Spectroscopy Experiments **80**

3.6 References **81**

3. Experimental Chapter

3.1 Chemical Reagents and Gases

All chemical reagents and gases used will be listed in the experimental section for each chapter.

3.2 Electrodes and Cells

Various types of electrodes were used in the experiments throughout this thesis and therefore a different cell was used to accommodate each of these electrodes. In this section the four different cells that were used in this thesis will be discussed in detail. The first type of electrode that was used for gas sensing experiments was a homemade Pt or Au microelectrode (figure 3.1) enclosed in glass that were kindly donated to us by Dr Neil Rees (then at Oxford University). A similar type of electrode has been previously used for studying the electrochemical behaviour of hydrogen, hydrogen sulphide, ammonia, oxygen and sulfur dioxide.[1-5] The electrode was modified with a section of disposable pipette tip at the top to hold small quantities of solvent (20-30 µL), secured by parafilm (figure 3.1).

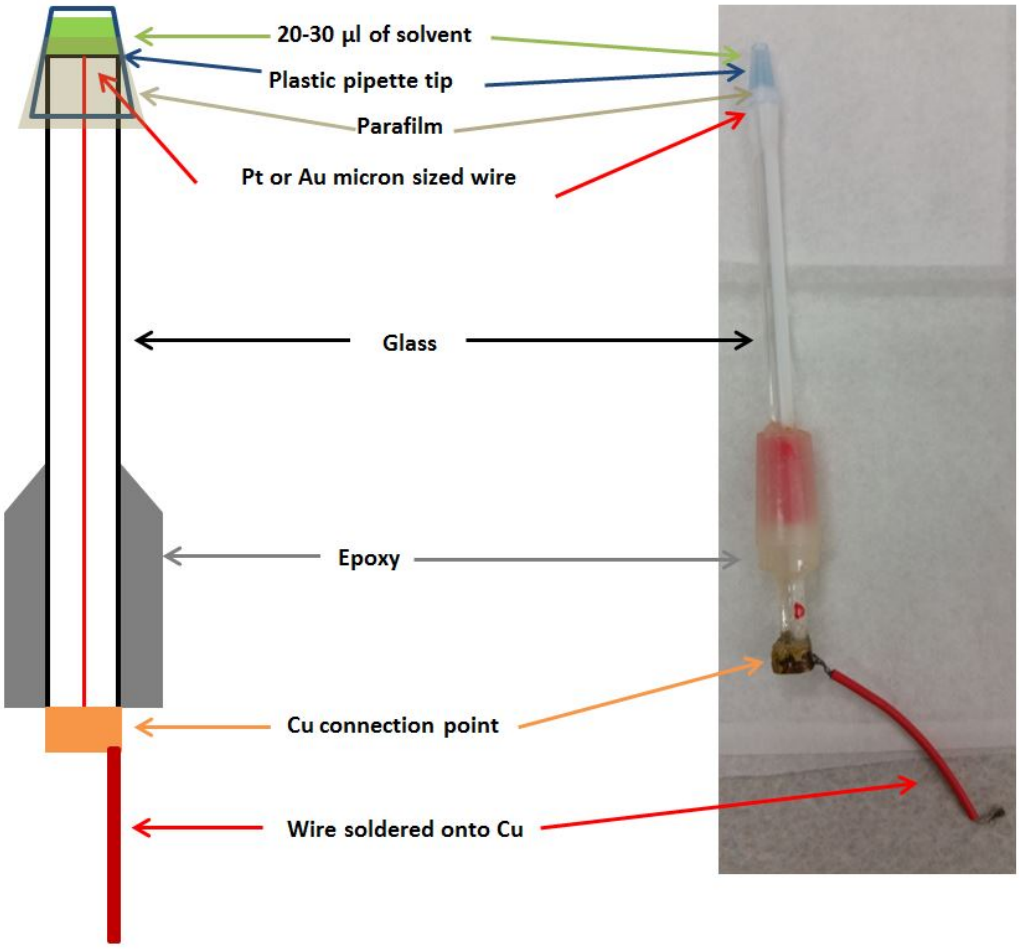

Figure 3.1: Photograph and cartoon of homemade microelectrode used for experiments

This electrode was placed in a glass 'T-cell' (figure 3.2) that allowed for gas experiments with a gas inlet and gas outlet. A silver wire was used as a combined reference and counter electrode, which was inserted from the top of the T-cell and into the solvent. The working electrode connection was made via copper connection points at the end of the electrode. The counter and reference electrode connections were made with the Ag wire.

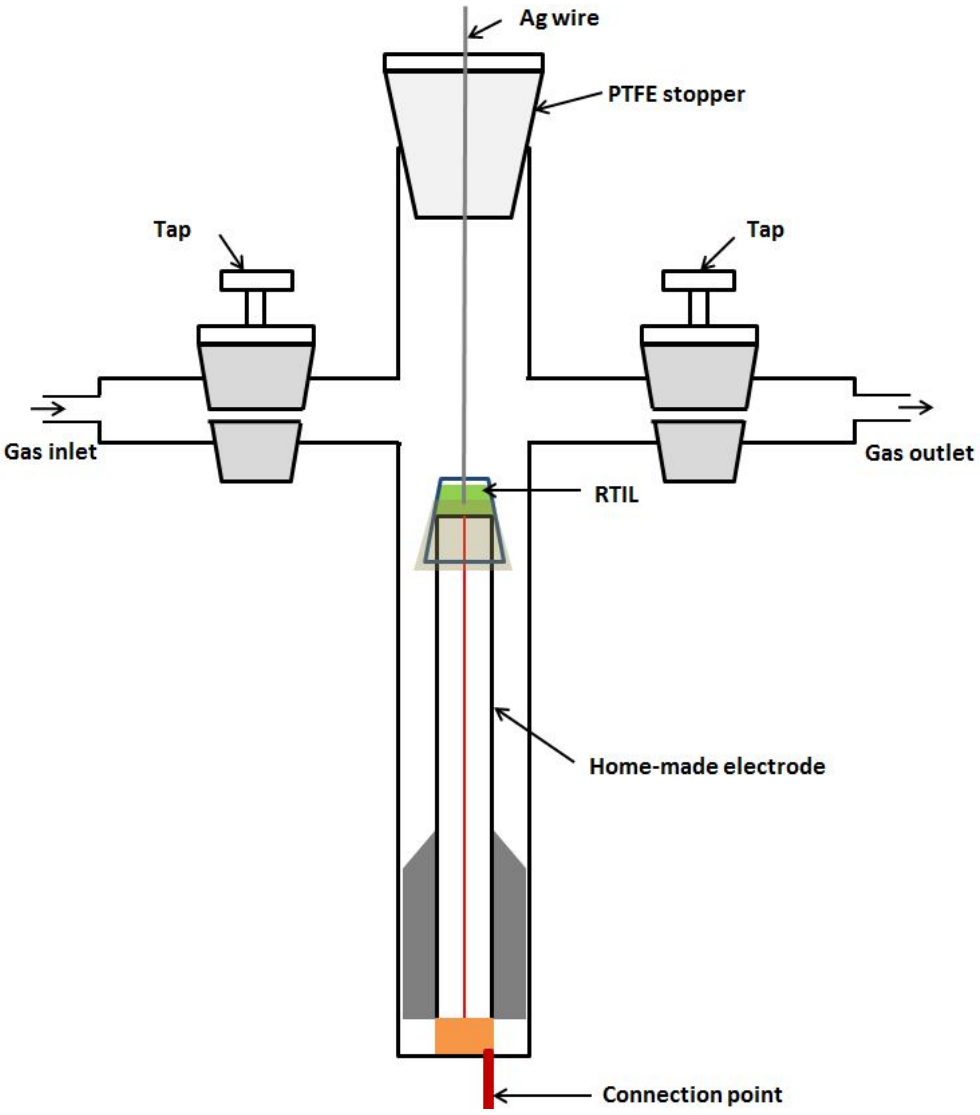

Figure 3.2: Image of glass T-cell showing the placement of the homemade microelectrode

The second type of electrode that was used was called screen printed electrodes (SPEs). There were five different types of SPEs and all of them were purchased from DropSens (Oviedo, Spain) with the following codes: DRP-110, DRP-550, DRP-220AT, DRP-110CNT, DRP-110GPH. Figure 3.3 shows a photograph of the SPEs. A drop of solvent, 10 µL, is sufficient to cover the three electrodes.

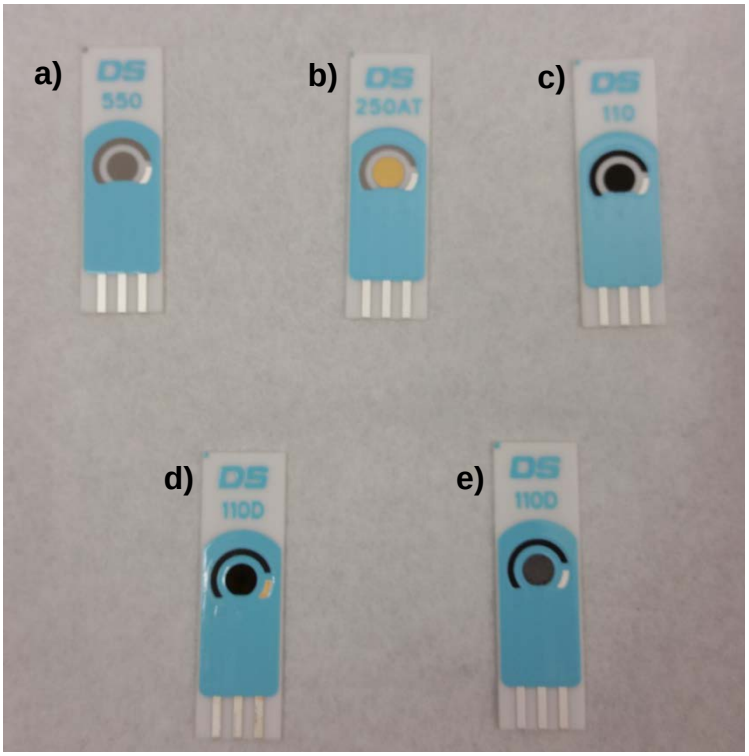

Figure 3.3: Photograph of SPEs used for electrochemical experiments purchased from DropSens a) platinum, b) gold, c) carbon, d) CNT modified carbon and e) graphene modified carbon WE surfaces)

The SPEs consists of a three electrode set-up with working, counter and reference electrodes. The working electrode (WE) surfaces employed in this study were platinum, gold, carbon and carbon modified with carbon nanotubes (CNT) and graphene. A silver quasi-reference electrode was used in all five SPEs. The counter electrode (CE) was typically made from the same material as the WE surface (e.g Pt for Pt SPEs, Au for Au SPEs and C for C and C-modified SPEs). The SPEs were first inserted into a rubber bung (silicone bung for HCl and Cl_2 due to the corrosive nature of these two gases on rubber) and then soldered with wires at the connection points and then placed in a modified version of the glass T-cell designed in-house and constructed by Sarah Davis (independent glass-blower in Perth, WA) as shown in figures 3.4 and 3.5.

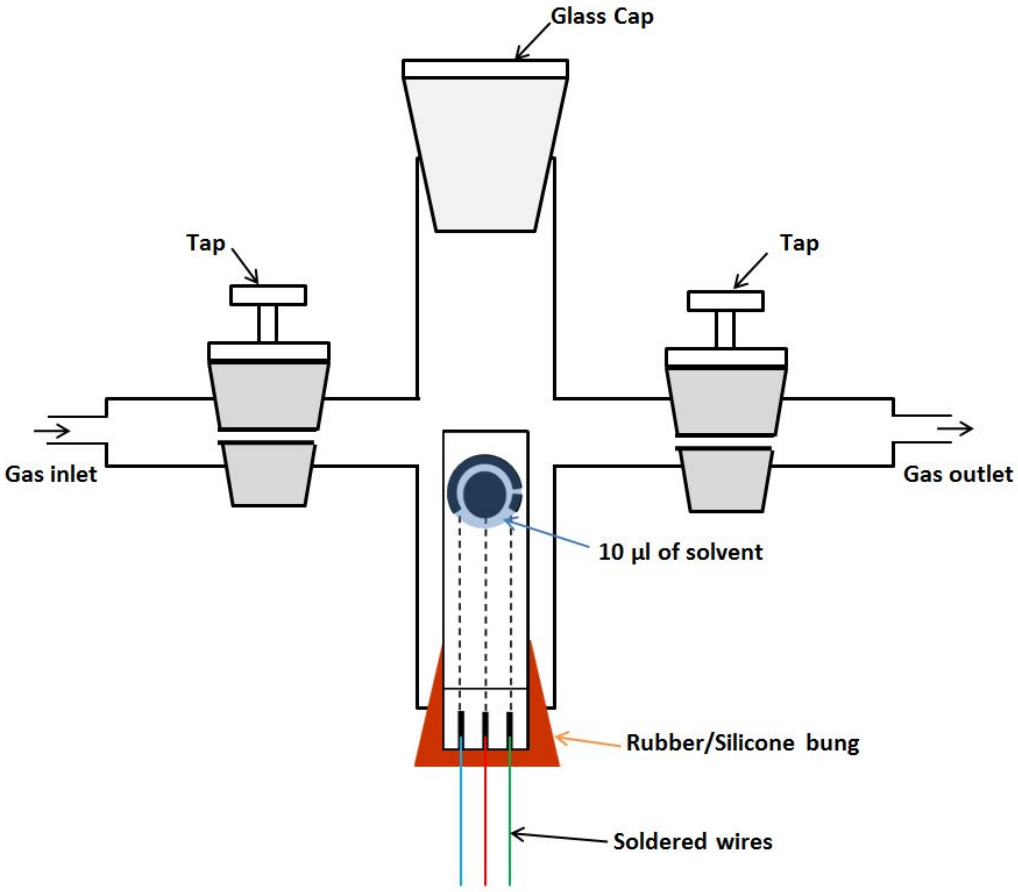

Figure 3.4: Cartoon image of T-cell showing the placement of a SPE.

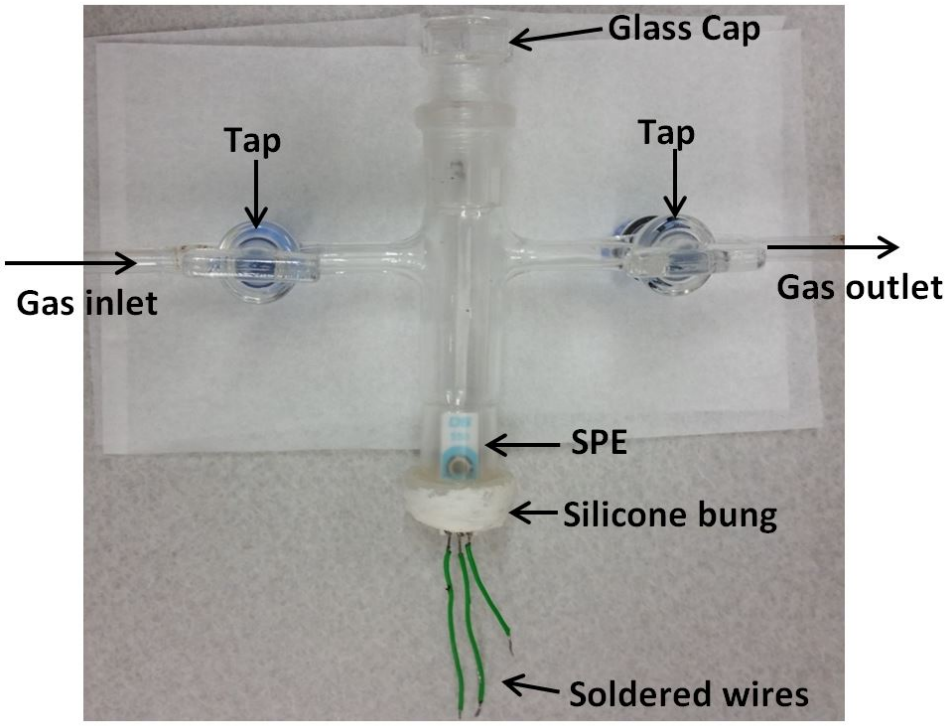

Figure 3.5 Photograph of T-cell showing the placement of a SPE

The third type of electrode that was used was a glassy carbon (GC) disk electrode (figure 3.6, 5 mm diameter). The electrode/cell design was made with specific requirements so that gas experiments can be performed. Pine Research Instruments (www.pineinst.com/echem/, North Carolina, USA) were consulted and using their existing rotating disk electrode setup (RDE E5 model), modifications was suggested. From now on this electrode setup will be referred to as the PINE setup.

Figure 3.6: Photograph of GC stub (5 mm diameter) used for electrochemical experiments.

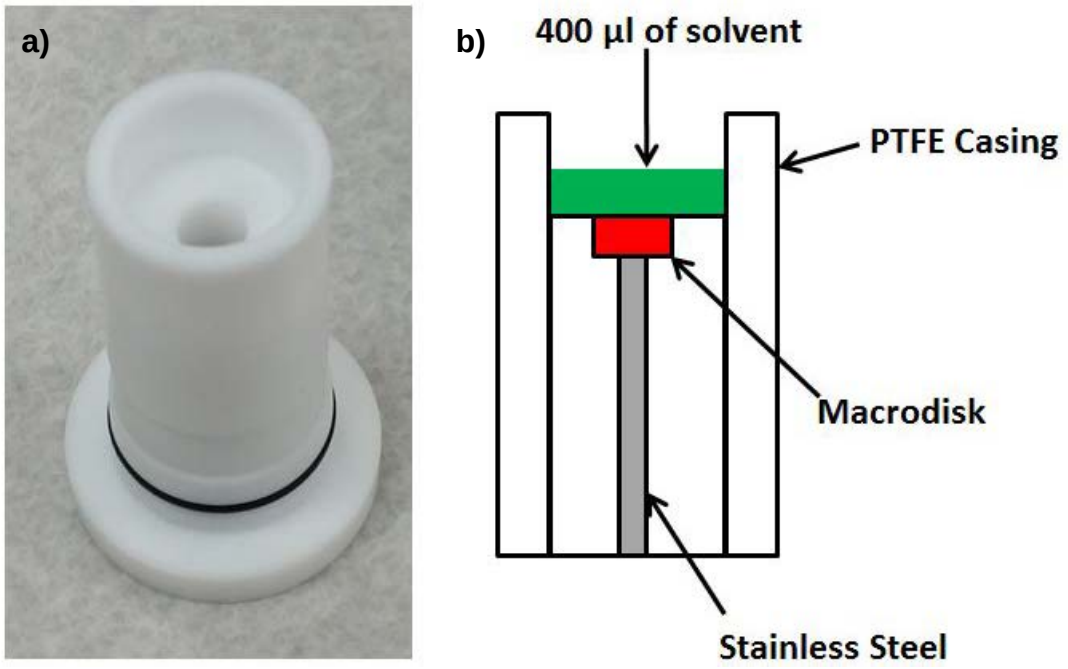

Figure 3.7: a) Photograph of custom made electrode casing from Pine Research Instruments (without metal disk inserted) and b) cartoon of the cross section of PINE electrode setup used for experiments.

Figure 3.7 shows the setup of the electrode in the PTFE casing. Due to the design, a larger volume of solvent (400 µL) is needed to cover the electrode and also allow for insertion of a Pt coil counter electrode and a Ag wire quasi-reference electrode. The

major advantage of this setup is the ability to modify the electrode surface and be able to remove the electrode for imaging using scanning electron microscopy (SEM). A drawback is that 400 µl of solvent is needed which is unfavourable for gas sensing experiments as saturation times will be very long (approximately 4 hours for the RTIL [C_2mim][NTf_2]). Figures 3.8 and 3.9 show how the electrode is setup in the glass T-cell. Two holes are drilled at the top to allow insertion of the Pt wire (counter electrode) and the Ag wire (reference electrode). The Pt wire is coiled to have a higher surface area as it acts as the counter electrode. A stainless steel rod was screwed in at the bottom as an extension so that it could be connected as the working electrode to the potentiostat.

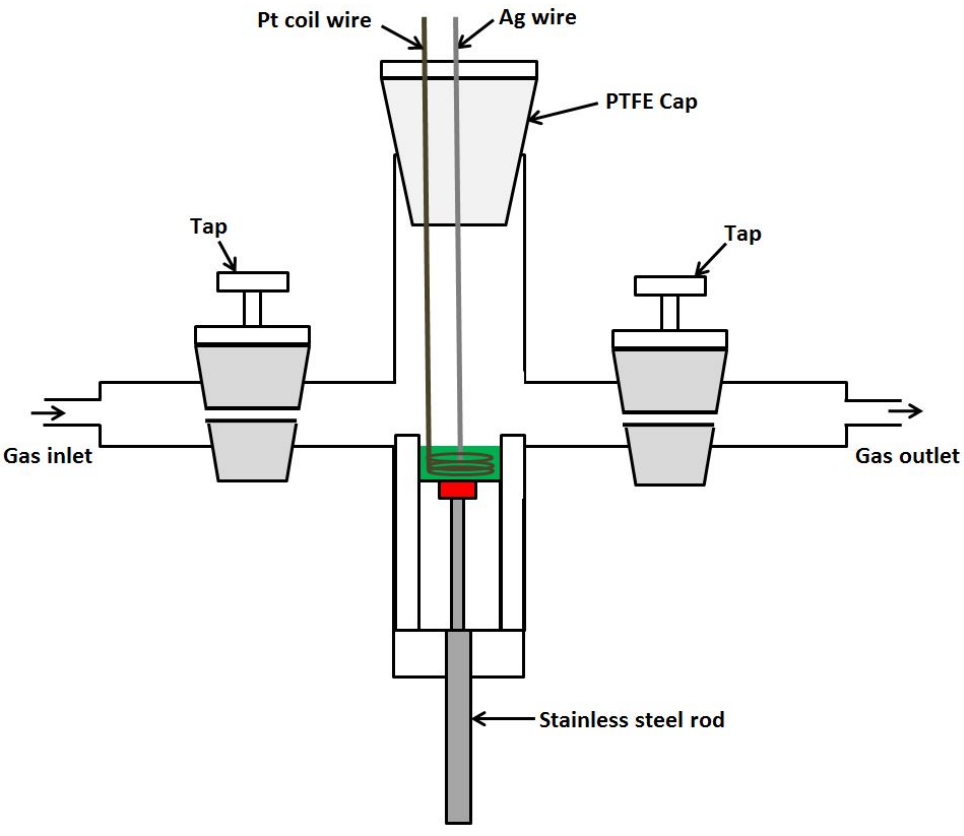

Figure 3.8: Cross section of PINE electrode setup used for experiments

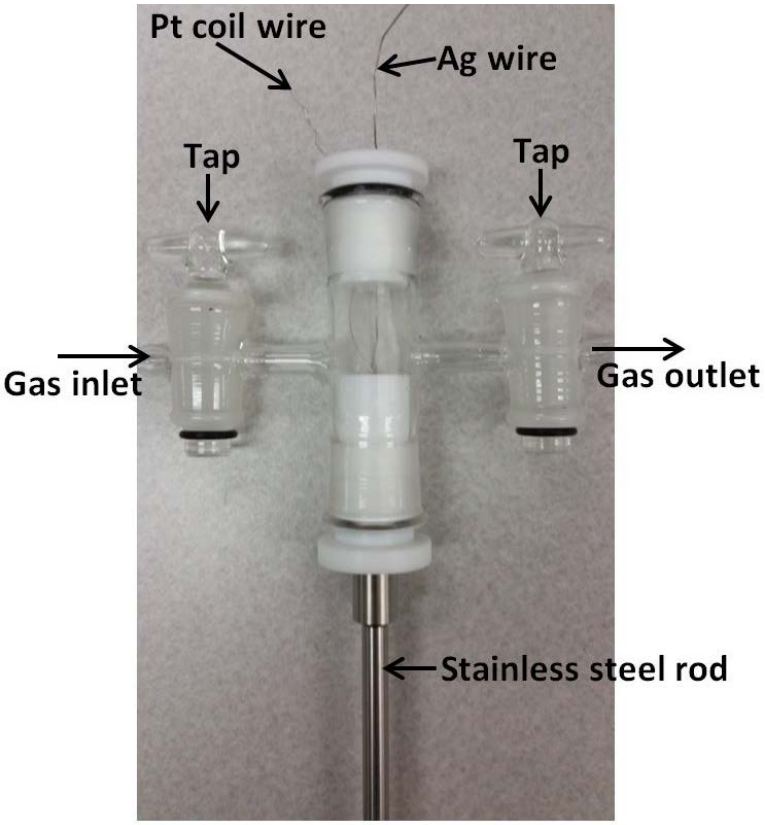

Figure 3.9: Photograph of PINE electrode setup

The fourth type of electrode was a conventional macroelectrode consisting of a macrodisk (3 mm diameter glassy carbon) insulated with polyether ether ketone (PEEK) from BASi (Indiana, USA). At the other end of the macrodisk is a copper connection point (Figure 3.10) to attach the working electrode to the potentiostat. A glass beaker or a simple glass cell was used for experiments as they were not used for gas experiments. A typical setup is shown in chapter 2, figure 2.2.

Figure 3.10: Photograph of macroelectrodes used for electrochemical experiments purchased from BASi

3.3 Electrochemical Experiments

All electrochemical experiments were performed using a computer controlled PGSTAT101 Autolab potentiostat (Eco-Chemie, Netherlands) interfaced to a PC with NOVA version 1.8/1.9 software. For experiments on the microelectrode, a two-electrode system was employed with a silver wire as the combined reference and counter electrode. For experiments with the macroelectrode in the PINE set-up a three electrode system was employed with a Pt coil as the counter electrode and a Ag wire as the quasi-reference electrode. The microelectrode and the macroelectrode were polished on soft lapping pads (Buehler, Illinois) with alumina powder of decreasing size (3, 1 and 0.5 μm, Kemet, NSW, Australia) before electrochemical experiments. For experiments with the SPEs, all the three electrodes (silver quasi reference electrode and the counter electrode was typically made from the same material as the WE surface) were used as is without any prior cleaning or activation which reflects more accurately a real world sample. Experiments with the conventional macro electrodes from BASi were used with a Pt coil as the counter and a Ag/Ag^+ as the reference electrode (in aqueous solutions).

For all experiments that involved the use of RTILs, an Edwards high vacuum pump (Model ES 50) was used to remove atmospheric impurities (oxygen/water) naturally present in the RTIL, except in the case of SPEs where the cell was purged with N_2 gas to remove impurities. For all other solvents used in this thesis, oxygen was removed by bubbling with nitrogen gas before electrochemical experiments. Cyclic voltammetry and chronoamperometry were the two main electrochemical techniques that were used in this thesis and the theory behind them has been discussed in great detail in chapter 2. All experiments were performed inside an aluminium Faraday cage contained within a fume cupboard, at a temperature of 298 (±2 K).

3.4 Gas Mixing Setup

In this thesis the electrochemical behaviour of three gases (methylamine, chlorine and hydrogen chloride) will be investigated. To avoid any cross- contamination, each gas had an individual gas mixing setup. This gas mixing setup was achieved with the aid of polytetrafluroethylene tubings (PTFE 1/8 inch internal diameter and 1/4 inch outer diameter), Swagelok fittings (metal and PTFE), gas PTFE tape, regulators, flowmeters (analogue and digital), deep purge system (DPS) and gas cylinders. The methylamine, chlorine and hydrogen chloride gas cylinders were purchased from CAC Gas & Instrumentation (NSW, Australia) and the nitrogen gas cylinders were bought from BOC Gas and Gear (Perth, WA, Australia). The PTFE tubing, Swagelok fittings and PTFE tape were bought from Swagelok (Perth, WA, Australia). Figures 3.11 and 3.12 show photographs of various parts of the gas mixing setup connected with PTFE tubing. The analyte gas cylinder is connected directly to a DPS (Chem-Master, Gas Arc Group Ltd, UK) which is then connected to a regulator (Chem-Master, Gas Arc Group Ltd, UK) to control the flow to the analogue flowmeter (0-60 cm^3/min, Dwyer, NSW, Australia). This is then connected to one side of the Swagelok T-joint and on the other side it is connected to a digital flowmeter (0-1.2 L/min, John Morris Scientific, NSW, Australia) that controls the flow of nitrogen gas (nitrogen gas cylinder and regulator purchased from BOC gases, Perth, WA, Australia). This allows mixing of the two gases before it enters the inlet of the various gas cells. All the threads of metal Swagelok fitting are wrapped around with gas PTFE tape to ensure good seals. The purpose of the DPS is to flush the whole system with nitrogen gas before and after experiments so that no residual gases or moisture are present. Chlorine and hydrogen chloride are extremely corrosive gases and react with moisture to form HCl and HClO which corrodes steel to form rust.

Therefore all Swagelok fittings that were connected to the chlorine and hydrogen chloride gas flowmeter were made of PTFE. Experiments performed in the absence of the DPS caused corrosion of all metal fitting and regulators. In the case of less corrosive methylamine gas the DPS was not used and the gas cylinder was connected directly to the regulator. The gas mixing setup was designed and constructed "in-house". The electrochemical cell was first purged with N_2 gas/vacuum to remove impurities naturally present in the ionic liquid (e.g. oxygen and water). Once the baseline was stable after the N_2/vacuum purging, the analyte gas was introduced into one arm of the cell via PTFE tubing. The gas was then allowed to partition into the ionic liquid until equilibrium was obtained. An outlet gas line (PTFE) tubing was connected to the other arm of the cell that lead into the top of the fume cupboard. The ppm concentration of gas that was introduced into the T-cell was calculated by the relative flow rates of the two flow meters. Tables 3.1, 3.2 and 3.3 show the flow rates used for the gas experiments. The limit of detections (LODs) for each gas was then calculated based on three times the standard deviation (3σ) of the calibration graph (plot of current vs concentration). Figure 3.13 shows a cartoon of the whole gas mixing setup that includes a glass cell and a SPE.

It is also important to note here that the three gases of interest are extremely toxic and safety is of utmost importance. The gas cylinders need to be handled with great care and after experiments, the gas mixing setup have to be examined to make sure no leakage of gas can occur. If a leak is suspected proper protocols need to be taken to contain the leak. Together with safety goggles, lab coat and enclosed shoes, a respiratory mask (3M^{TM} Professional series 7500 with a 6002 cartridge) was used for experiments involving chlorine and hydrogen chloride. The current Occupational Safety and Health Administration Permissible Exposure Limit (OSHA PEL) for

methylamine, chlorine and hydrogen chloride are 10 ppm, 1 ppm and 5 ppm respectively. At these concentrations many health effects can occur and they are discussed in the relevant results and discussion chapters.

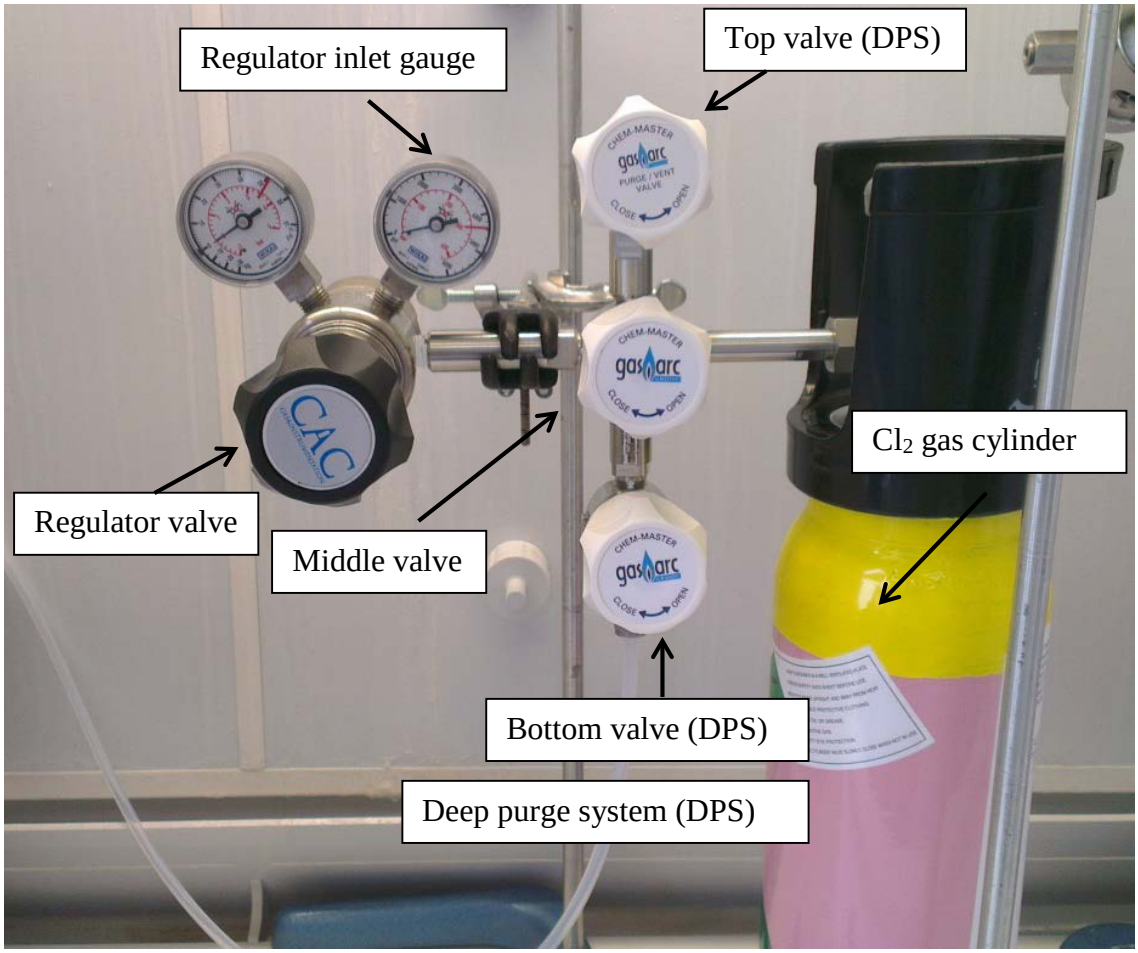

Figure 3.11: Photograph of gas mixing setup (1)

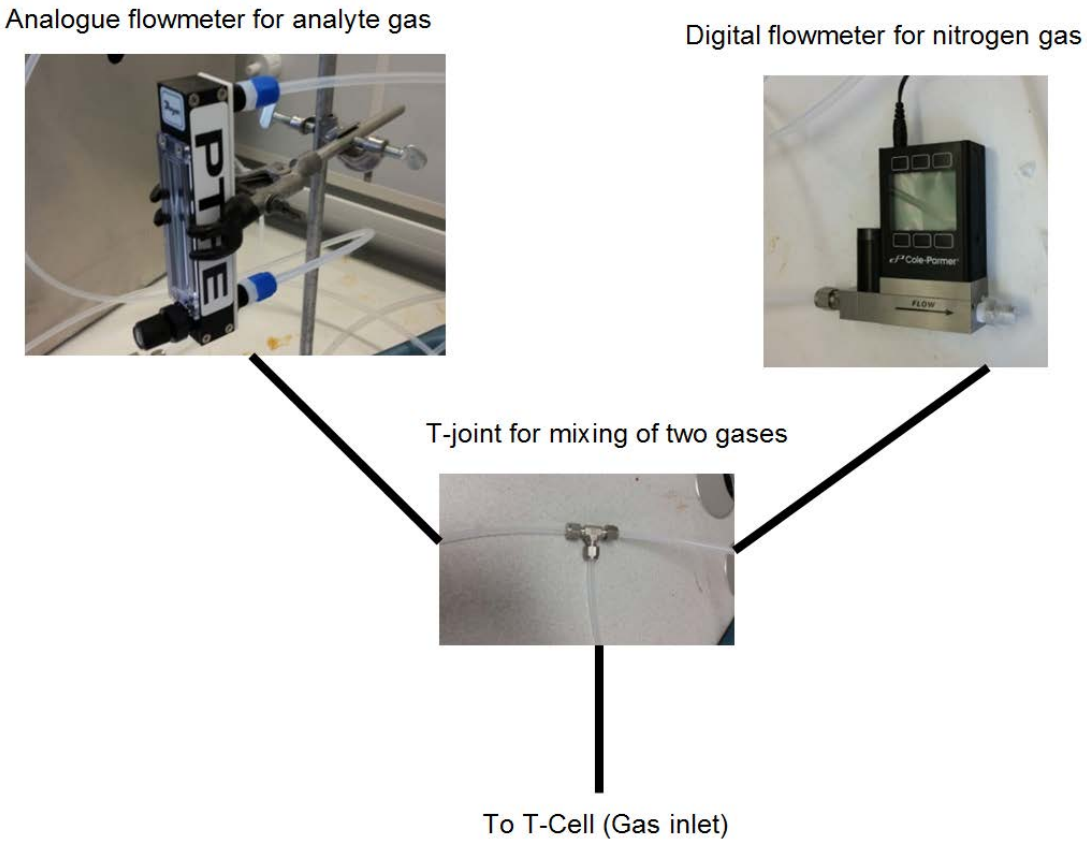

Figure 3.12: Photograph of gas mixing setup (2)

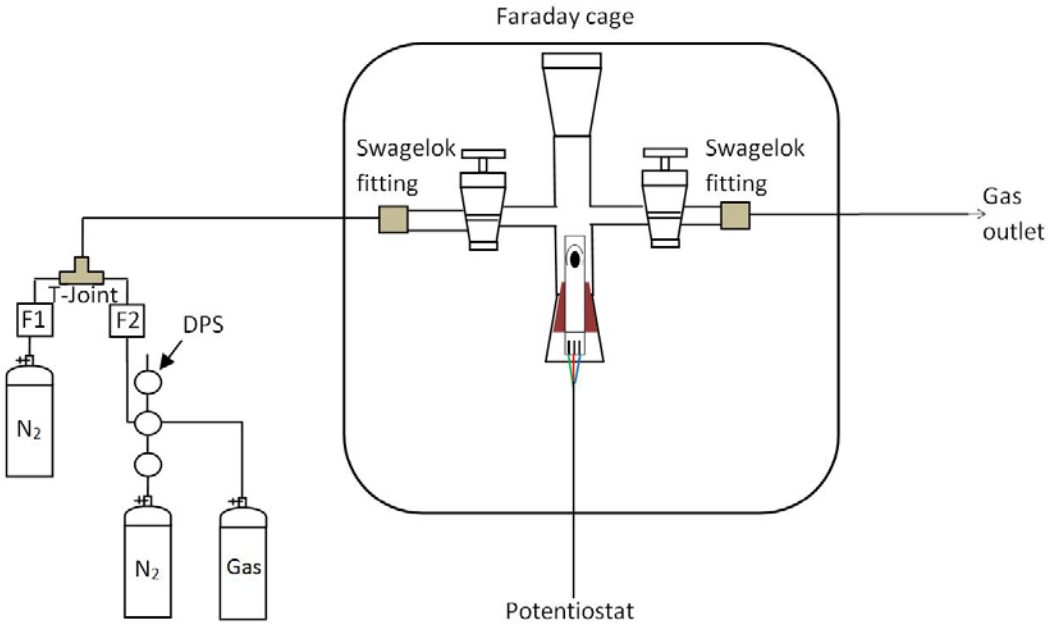

Figure 3.13: Cartoon showing gas mixing setup with T-cell/electrode. In this figure, a SPE is shown as the electrode.

MA/HCl flow rate (cm^3/min)	N_2 flow rate (cm^3/min)	Total flow rate (cm^3/min)	Fraction of MA/HCl in 0.2 % Cylinder	% concentration of MA/HCl	ppm concentration of MA/HCl
55	50	105	0.523809524	0.104761905	1048
55	100	155	0.354838710	0.070967742	710
55	200	255	0.215686275	0.043137255	431
55	400	455	0.120879121	0.024175824	242
55	600	655	0.083969466	0.016793893	168
55	1000	1055	0.052132701	0.010426540	104

Table 3.1: Actual flow rates used for 0.2 % hydrogen chloride/methylamine and 100 % nitrogen gas cylinders. Final column shows the concentration calculated from the relative flowrates.

Cl_2 flow rate (cm^3/min)	N_2 flow rate (cm^3/min)	Total flowrate (cm^3/min)	Fraction of Cl_2 in 0.2 % Cylinder	% concentration of Cl_2	ppm concentration of Cl_2
57	15	72	0.791667	0.158333	1583
57	50	107	0.532710	0.106542	1065
57	100	157	0.363057	0.072611	726
57	200	257	0.221790	0.044358	444
57	600	657	0.086758	0.017352	174

Table 3.2: Actual flow rates used for 0.2 % chlorine and 100 % nitrogen gas cylinders. Final column shows the concentration calculated from the relative flowrates.

Cl_2 flow rate (cm^3/min)	N_2 flow rate (cm^3/min)	Total flowrate (cm^3/min)	Fraction of Cl_2 in 4.5 % Cylinder	% concentration of Cl_2	ppm concentration of Cl_2
40	900	940	0.042553	0.191489	1915
40	800	840	0.047619	0.214286	2143
40	700	740	0.054054	0.243243	2432
40	600	640	0.062500	0.281250	2813
40	500	540	0.074074	0.333333	3333

Table 3.3: Actual flow rates used for 4.5 % chlorine and 100 % nitrogen gas cylinders. Final column shows the concentration calculated from the relative flowrates.

3.5 XPS, SEM, NMR and Raman Spectroscopy Experiments

X-ray photoelectron spectroscopy (XPS) analysis was performed either on a Kratos AXIS Ultra DLD using a Al K α radiation or on a Quantum 2000 Scanning ESCA Microprobe having a Mg Kα radiation as the X-Ray source. Scanning electron microscopy (SEM) characterisation was performed using either a Zeiss Neon 40 EsB

FIBSEM or a Tescan Mira3 FESEM. Nuclear magnetic resonance (NMR) spectra were recorded using a Bruker Advance 400 spectrometer. Confocal Raman experiments were conducted using a WITec alpha300SAR equipped with a frequency doubled Nd:YAG laser (excitation wavelength: 531.87nm). A detailed experimental for the characterisation techniques is discussed in the relevant experimental component in the upcoming chapters.

3.6 References

(1) Barrosse-Antle, L. E.; Silvester, D. S.; Aldous, L.; Hardacre, C.; Compton, R. G. Electroreduction of Sulfur Dioxide in Some Room-Temperature Ionic Liquids. *J. Phys. Chem. C* **2008**, *112*, 3398-3404.
(2) Huang, X.-J.; Rogers, E. I.; Hardacre, C.; Compton, R. G. The Reduction of Oxygen in Various Room Temperature Ionic Liquids in the Temperature Range 293−318 K: Exploring the Applicability of the Stokes−Einstein Relationship in Room Temperature Ionic Liquids. *J. Phys. Chem. B* **2009**, *113*, 8953-8959.
(3) Ji, X.; Silvester, D. S.; Aldous, L.; Hardacre, C.; Compton, R. G. Mechanistic Studies of the Electro-oxidation Pathway of Ammonia in Several Room-Temperature Ionic Liquids. *J. Phys. Chem. C* **2007**, *111*, 9562-9572.
(4) Silvester, D. S.; Aldous, L.; Hardacre, C.; Compton, R. G. An Electrochemical Study of the Oxidation of Hydrogen at Platinum Electrodes in Several Room Temperature Ionic Liquids. *J. Phys. Chem. B* **2007**, *111*, 5000-5007.
(5) O'Mahony, A. M.; Silvester, D. S.; Aldous, L.; Hardacre, C.; Compton, R. G. The Electrochemical Reduction of Hydrogen Sulfide on Platinum in Several Room Temperature Ionic Liquids. *J. Phys. Chem. C* **2008**, *112*, 7725-7730.

4. Electrochemical Oxidation and Sensing of Methylamine Gas in Room Temperature Ionic Liquids

The electrochemical behavior of methylamine gas in several room temperature ionic liquids (RTILs), [C_2mim][NTf_2], [C_4mim][NTf_2], [C_6mim][FAP], [C_4mpyrr][NTf_2], [C_4mim][BF_4], and [C_4mim][PF_6] has been investigated on a Pt microelectrode using cyclic voltammetry. A broad oxidation wave at approximately 3 V, two reduction peaks and another oxidation peak was observed. A complicated mechanism is predicted based on the voltammetry obtained, with ammonia gas as a likely by-product. The currents obtained suggest that methylamine has a high solubility in RTILs, which is important for gas sensing applications. The analytical utility of methylamine was then studied in [C_4mpyrr][NTf_2] and [C_2mim][NTf_2]. A linear calibration graph with an R^2 value of 0.99 and limits of detection of 33 and 34 ppm were obtained respectively, suggesting that RTILs are favorable non-volatile solvents for the electrochemical detection of highly toxic methylamine gas.

4. ELECTROCHEMICAL OXIDATION AND SENSING OF METHYLAMINE GAS IN ROOM TEMPERATURE IONIC LIQUIDS 83

4.1 Introduction 85

4.2. Experimental Section 87

4.2.1 Chemical Reagents 87

4.2.2 Electrochemical Experiments 88

4.2.3 Gas Mixing Setup 88

4.3 Results and Discussion 89

4.3.1 Electrochemical Response of Methylamine Gas in $[C_4mpyrr][NTf_2]$ on a Pt Microelectrode. 89

4.3.2 Electrochemical Response of Methylamine Gas in $[C_4mpyrr][NTf_2]$ on a Au Microelectrode 93

4.3.3 Electrochemical Study of Methylamine Gas on a Pt Microelectrode in Different RTILs 94

4.3.4 Analytical Utility of Methylamine Gas in $[C_2mim][NTf_2]$ and $[C_4mpyrr][NTf_2]$ 99

4.4 Conclusions 101

4.5 References 102

Work presented in this section has been published in the journal, Journal of Physical Chemistry C titled, “Electrochemical Oxidation and Sensing of Methylamine Gas in Room Temperature Ionic Liquids”.

4. Electrochemical Oxidation and Sensing of Methylamine Gas in Room Temperature Ionic Liquids

4.1 Introduction

Methylamine is a colourless, toxic and flammable gas at room temperature with a distinct fish or ammonia like odour at concentrations of 100 ppm and above.[1] Methylamine is prepared commercially by reacting methanol with amine in the presence of a silicoaluminate catalyst.[2] Together with monomethylamine, di and tri methylamine are also produced but by controlling the reaction kinetics and reaction ratios together with the catalyst this can be controlled to yield the methylamine of choice.[2] Methylamine is used to make a wide range of agricultural chemicals such as insecticides and herbicides and used extensively in the production of catalysts, fuel additives, personal care materials and pharmaceuticals. It is also the prime ingredient in mono methylammonium nitrate which is used as a water gel explosive[3] in the mining industry. Methylamine is also required for the formation of alkanolamines such as methyldiethanolamine (MDEA) and monomethylethanolamine (MMEA) which are essential for gas and oil treatment as they are used for the purification of natural gas.[4,5] It is also used in the reductive amination of phenyl-2-propanone to produce methamphetamine which is an illegal substance found in clandestine laboratories and is sold illegally as a mind altering drug.[6] Preparation methods for illegal drugs using methylamine gas as a precursor can be easily found on the internet or books[6] and this information can be used by non-professionals for

prohibited practices. Furthermore the need for detection arises as methylamine is a possible indicator for liver or renal diseases.[7] The current occupational safety and health administration permissible exposure limit (OSHA PEL) is 10 ppm in the gas phase. Given its high toxicity and its numerous uses, it is therefore essential to be able to monitor and detect low concentrations of methylamine.

There has been some work on the fundamental behaviour of methylamine in water-based solvents. For example, Aldaz et al.[8] reported the electrochemical oxidation of liquid methylamine in an acidic medium on Pt single crystal electrodes and suggested that adsorbed cyanide layers are formed, followed by either carbon monoxide or nitrogen oxide depending on the polarizing potential. Luczak[9] reported the oxidation of methylamine in an alkaline medium on a gold electrode and found that methylamine is only oxidised in the potential range of gold oxide layer formation. A reaction pathway was proposed, where the amine in solution is adsorbed and then undergoes an oxidation reaction to form an aldehyde and ammonia gas.

Methylamine (in the liquid form) has also been studied in aprotic solvents. Barnes and Mann et al.[10] reported the electrochemical oxidation of methylamine in acetonitrile on a platinum electrode and proposed two competing mechanisms, one at low potentials and one at high potentials. At low potentials they suggested a one electron oxidation to form a cation radical which decomposes to form a carbonium ion and an amidogen radical. At higher potentials methylamine is believed to be oxidised by two electrons to form an iminium salt which hydrolyzes to form aldehyde and ammonia. However all of these experiments were performed using liquid methylamine and there are no obvious reports of the behaviour and sensing of methylamine in the gaseous form.

In this work, for the first time we have studied the electrochemical oxidation of methylamine gas in room temperature ionic liquids (RTILs) as electrochemical solvents.

4.2. Experimental Section

4.2.1 Chemical Reagents

The RTILs 1-ethyl-3-methylimidazolium bis(trifluoromethylsulfonyl)imide ($[C_2mim][NTf_2]$), 1-butyl-3-methylimidazolium bis(trifluoromethylsulfonyl)imide ($[C_4mim][NTf_2]$) and *N*-butyl-*N*-methylpyrrolidinium bis(trifluoromethylsulfonyl)imide ($[C_4mpyrr][NTf_2]$) were synthesized according to standard literature procedures[11,12] and kindly donated by the group of Professor Christopher Hardacre at Queens University, Belfast. The RTILs 1-hexyl-3-methylimidazolium trifluorotris(pentafluoroethyl)phosphate ($[C_6mim][FAP]$), 1-butyl-3-methylimidazolium hexafluorophosphate ($[C_4mim][PF_6]$) and 1-butyl-3-methylimidazolium tetrafluroborate ($[C_4mim][BF_4]$) were purchased from Merck KGaA (Kilsyth, Victoria, Australia) at ultra-high purity electrochemical grade (halide content less than 100 ppm). All RTILs were used as received. Ultra-pure water with a resistance of 18.2 MΩ cm prepared by an Ultra-pure laboratory water purification system (Millipore Pty Ltd., North Ryde, NSW, Australia) and acetonitrile (MeCN, Sigma–Aldrich, 99.8 %) were used for washing the electrodes before and after use with RTILs. Methylamine gas (1.3 and 0.2 %, nitrogen fill) was purchased from CAC gases (Auburn, NSW, Australia). High purity nitrogen gas (99.9 %) was purchased from BOC gases (North Ryde, NSW, Australia) and used as a carrier gas. Ferrocene ($Fe(C_5H_5)_2$, 98 % purity) and tetra-*N*-butylammonium perchlorate (TBAP, 98 % purity) were purchased from Sigma Aldrich.

Methylammonium chloride (CH_3NH_3Cl, for synthesis) was purchased from Merck Pty. Ltd., Australia (Kilsyth, Victoria).

4.2.2 Electrochemical Experiments

A conventional two-electrode arrangement was employed, with either a home-made platinum microelectrode (8.3 µm radius) or a home-made gold microelectrode (10.9 µm radius) as the working electrode and a 0.5 mm diameter silver wire (Sigma Aldrich) as the quasi-reference electrode. The electrode diameter was calibrated electrochemically by using a well-known redox couple, ferrocene. The steady-state voltammetry of a 2 mM ferrocene (diffusion coefficient 2.3×10^{-5} cm^2s^{-1} at 298K)[13] solution in acetonitrile with 0.1 M TBAP as the electrolyte was analysed. The electrodes were housed in a glass "T-cell"[14] designed for studying microlitre quantities (20 µL) of ionic liquids in a controlled environment, previously used to study ammonia[15] and oxygen gas.[16] Chronoamperometric transients were achieved using a sample time of 0.01s. After equilibration, the potential was stepped up from a position of zero current to a potential after the oxidation peak was observed and the current was measured for 10 s. A fit using the Shoup and Szabo equation[17] was performed using the software package Origin 6.0 (Microcal Software Inc.) after deletion of the first 2 points to obtain the diffusion coefficient (*D*) and the number of electrons multiplied by concentration (*nc*).

4.2.3 Gas Mixing Setup

A similar gas mixing setup as explained in chapter 3 was used for the experiments. The % concentration of methylamine that was introduced into the T-cell was calculated using the relative flow rates of the two flow meters. A digital flowmeter (0-1.2 L/min, John Morris Scientific, NSW, Australia) was used for the nitrogen gas and an analogue flowmeter (0-60 cm^3/min, Dwyer, NSW, Australia) was used for the

methylamine gas (please see table 3.1 for calculations of concentrations). It took approximately 80 minutes for saturation to occur in the least viscous ionic liquids and the time taken between each concentration change was 45 minutes.

4.3 Results and Discussion

The electrochemistry of methylamine has been investigated in six different RTILs, $[C_2mim][NTf_2]$, $[C_4mim][NTf_2]$, $[C_6mim][FAP]$ $[C_4mpyrr][NTf_2]$, $[C_4mim][BF_4]$, and $[C_4mim][PF_6]$ on a Pt microelectrode. Experiments were also performed on a Au micro electrode in $[C_4mpyrr][NTf_2]$.

4.3.1 Electrochemical Response of Methylamine Gas in $[C_4mpyrr][NTf_2]$ on a Pt Microelectrode.

Figure 4.1 shows typical cyclic voltammetry (CV) of 1.3 % methylamine (nitrogen fill) in the RTIL $[C_4mpyrr][NTf_2]$ at a scan rate of 0.1 V/s when scanned from 0.2 V to 3.2 V to -1.5 V and back to 0.2 V. The response in the absence of methylamine is shown as the dotted line. It can be seen that there is a single broad oxidation wave, process I, at approximately 3 V followed by two reduction peaks at 0.1 V and -0.3 V (peaks II and III). It can also be seen that there is an oxidation feature (peak IV) at -0.06 V. The absence of peaks II, III and IV when scanned negative first indicates that they are a direct consequence of process I, and likely to be peaks from products formed after methylamine oxidation.

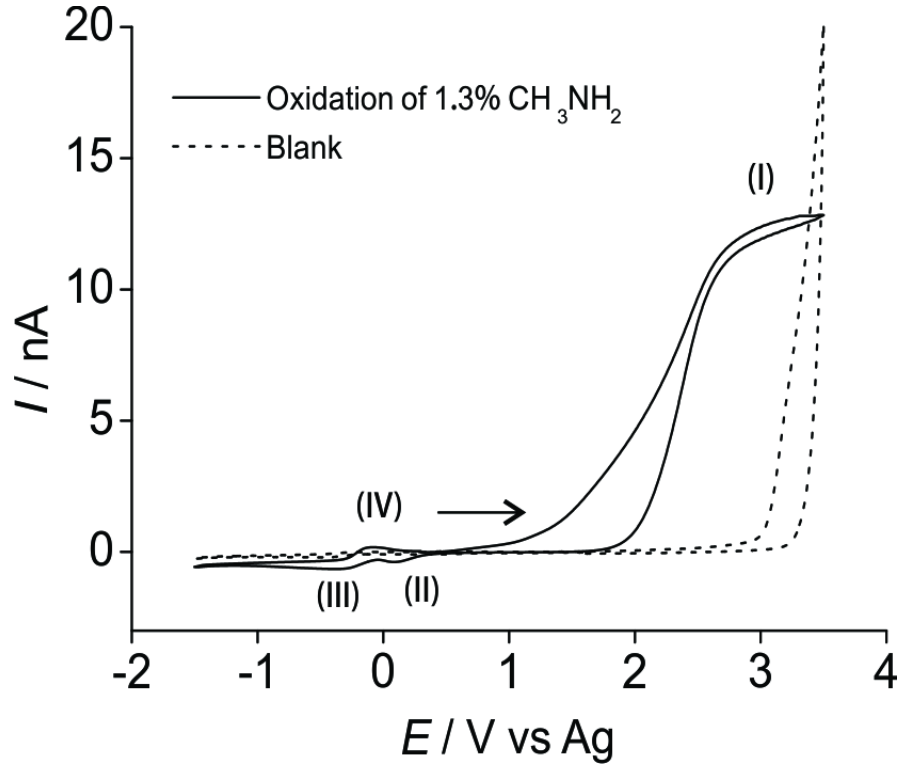

Figure 4.1: CV for the oxidation of 1.3% Methylamine (nitrogen fill) on a 8.3 µm radius Pt electrode in [C_4mpyrr][NTf_2] at a scan rate of 0.1 V/s. Dotted line is the response in the absence of methylamine

It is also important to point out that the CV looks very similar to that seen of the electrochemical oxidation of ammonia in RTILs where four process are also present.[15] The peaks for ammonia oxidation were assigned to the following reactions:

Peak (I) $$\mathrm{NH_3(g) + 3A^- \longrightarrow \frac{1}{2}N_2(g) + 3HA + 3e^-} \quad (4.1)$$

where A^- is the anion of the RTIL ($[NTf_2]^-$). HA can then transfer its proton to an ammonia molecule in the following equilibrium reaction:

$$\mathrm{HA + NH_3(g) \rightleftharpoons NH_4^+ + A^-} \quad (4.2)$$

Therefore, there are two species that can undergo reduction: the solvated proton, HA, (eq. 4.3) and ammonium ion, NH_4^+, (eq. 4.4):[15]

Peak (II) $$\mathrm{HA + e^- \longrightarrow A^- + H(ads)} \quad (4.3)$$

Peak (III) $$NH_4^+ + e^- \longrightarrow NH_3(g) + H(ads) \quad (4.4)$$

In both of these reactions, adsorbed hydrogen/protons are formed on the surface, which are then oxidised in peak IV.

In the case of methylamine, the oxidation mechanism is thought to be much more complex. Barnes and Mann[10] proposed that that the electrochemical oxidation of liquid methylamine produces ammonia gas and other by-products. The reaction is summarised below;

$$CH_3NH_2 \longrightarrow CH_3\dot{N}H_2{}^+(\text{cation radical}) + e^- \quad (4.5)$$

$$CH_3\dot{N}H_2{}^+ \longrightarrow CH_2\dot{N}H_2 + H^+ \quad (4.6)$$

$$CH_2\dot{N}H_2 \longrightarrow CH_2NH_2(\text{iminium}) + e^- \quad (4.7)$$

$$CH_2NH_2(\text{iminium}) \xrightarrow{-H^+/+H_2O} NH_3 + CH_2O \quad (4.8)$$

where methylamine gets oxidised to form a cation radical by one electron followed by a deprotonation and then another oxidation to form an iminium which then hydrolyses to form ammonia and an aldehyde. In our system the experiments are performed using RTILs and gaseous methylamine, unlike acetonitrile and liquid methylamine (methylamine dissolved in water) used in experiments conducted by Barns and Mann.[10] Therefore there will be no water present for the hydrolysation reaction however methylamine itself is a good nucleophile[18] and can replace water as the nucleophile therefore we believe reaction 4.8 can be rewritten as;

$$CH_2NH_2(\text{iminium}) \xrightarrow{-H^+/+2CH_3NH_2} NH_3 + CH_2(NHCH_3)_2 \quad (4.9)$$

This still maintains the two electron oxidation of methylamine proposed by Barnes and Mann[10] at high potentials. As ammonia is already at a potential where it can be

oxidised, it is instantly oxidised and the current is added to that of the methylamine oxidation current. Therefore we believe that process I in figure 4.1 is a result of a combination of methylamine (eq. 4.5 to 4.9) and ammonia (eq. 4.1) oxidation, likely following an overall 5-electron process. It is believed that peaks II and III in the CVs follow the same mechanism as depicted in equations 4.3 and 4.4. To rule out any possibility that peak III could be due to the reduction of the methylammonium ion instead of the ammonium ion, methylammonium chloride was dissolved in $[C_4mpyrr][NTf_2]$ and scanned negative from 0.4 V to -2 V. The absence of any peaks suggests that peaks II and III are not from the reduction of the methylammonium ion. Peak IV for methylamine in figure 4.1 is therefore likely to be due the oxidation of adsorbed hydrogen as in the case of ammonia.

To further support this mechanism ammonia gas was introduced into the system after the RTIL was saturated with methylamine gas. As expected additive behaviour was seen (figure 4.2). There was a pre peak at 1.2 V which is attributed to the oxidation of ammonia gas. The absence of other peaks on the reverse sweep also suggests that it is indeed the ammonium ion undergoing reduction and not methylammonium.

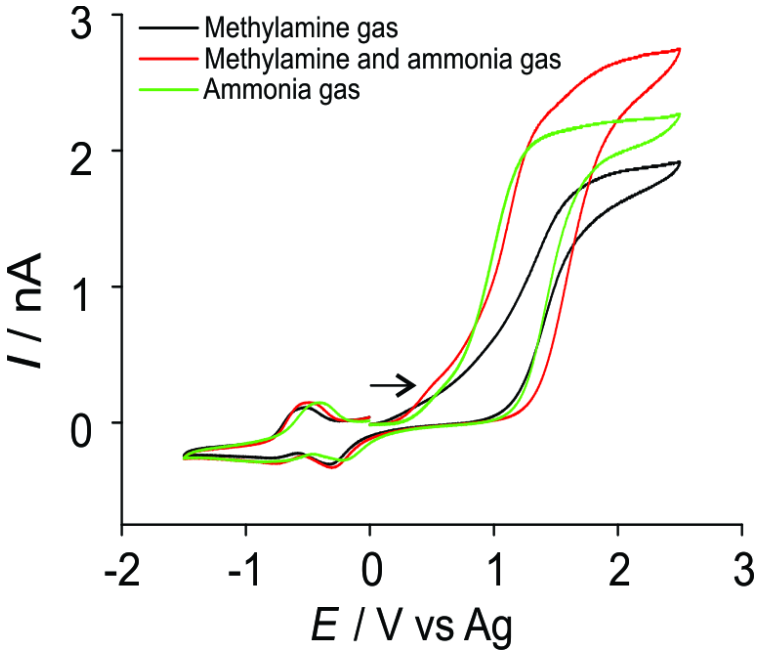

Figure 4.2: (-) CV for the oxidation of methylamine gas, (-) the oxidation of methylamine and ammonia gas combined and (-) the oxidation of ammonia gas on a 8.3 µm radius Pt electrode at a scan rate of 0.1 V/s in $[C_4mpyrr][NTf_2]$. Note the concentrations are not fixed due to the difficulties in mixing the two toxic gases safely. This is purely to show additive behaviour.

The reasonably high currents obtained at concentrations of 1.3 % methylamine in the gas phase (nitrogen fill) shows the high solubility of methylamine in $[C_4mpyrr][NTf_2]$ which is very advantageous for sensing applications and will be explored later in section 4.3.4

4.3.2 Electrochemical Response of Methylamine Gas in $[C_4mpyrr][NTf_2]$ on a Au Microelectrode

Figure 4.3 shows the CV scans obtained at varying scan rates between 0.01 V/s and 4 V/s for the oxidation of 1.3 % methylamine gas on a Au electrode in $[C_4mpyrr][NTf_2]$. It can be seen that the behaviour is very similar to that of a Pt electrode except for the prepeak seen at approximately 1.1 V which could be due to the formation of gold oxides. This additional peak resulted in all further experiments being conducted only on the Pt surface, since the peak current for process I is a

combination of the two processes. The magnitude of peak IV is much smaller on the Au surface as compared to the Pt surface and this further suggests that peak IV is due to the oxidation of adsorbed hydrogens which is more evident on Pt surfaces.

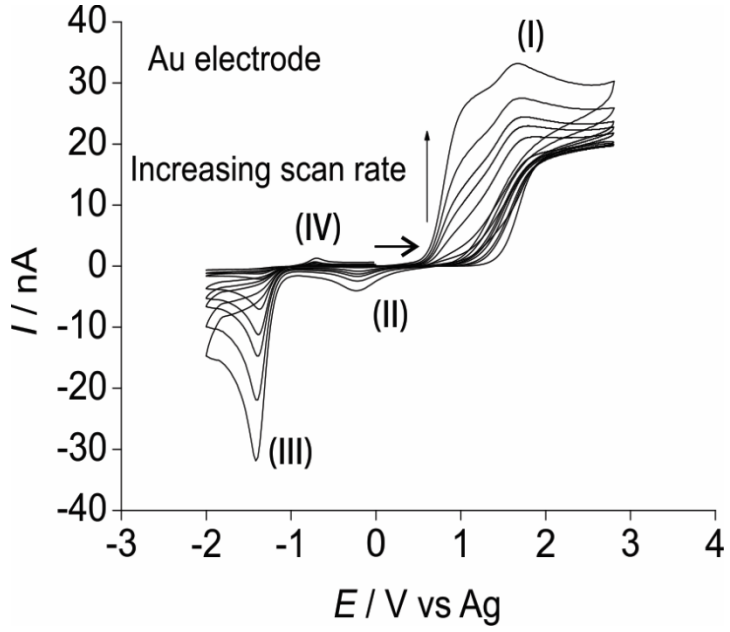

Figure 4.3: CV for the oxidation of 1.3 % methylamine on a 10.9 µm radius Au electrode in $[C_4mpyrr][NTf_2]$ at varying scan rates from 0.01 V/s to 4 V/s.

4.3.3 Electrochemical Study of Methylamine Gas on a Pt microelectrode in Different RTILs

In order to investigate the electrochemical behaviour of methylamine in different RTILs, the electrochemical oxidation at a range of scan rates from 0.01 V/s to 4 V/s was performed in six different RTILs with varying cations and anions, namely, $[C_2mim][NTf_2]$, $[C_4mim][NTf_2]$, $[C_6mim][FAP]$ $[C_4mpyrr][NTf_2]$, $[C_4mim][BF_4]$, and $[C_4mim][PF_6]$. Figure 4.4 shows typical CVs obtained and all are highly reproducible on consecutive days. It can be seen clearly that the voltammograms exhibit a very similar behaviour with the presence of four processes (I to IV) as described in section 4.3.1. However, the voltammetry in the $[FAP]^-$ ionic liquid shows a double wave for the oxidation, suggesting that this RTIL may not be the

most suitable for further analytical studies. In all the six RTILs, peak II becomes relatively smaller at higher scan rates which is analagous to that reported for ammonia oxidation in RTILs.[15]

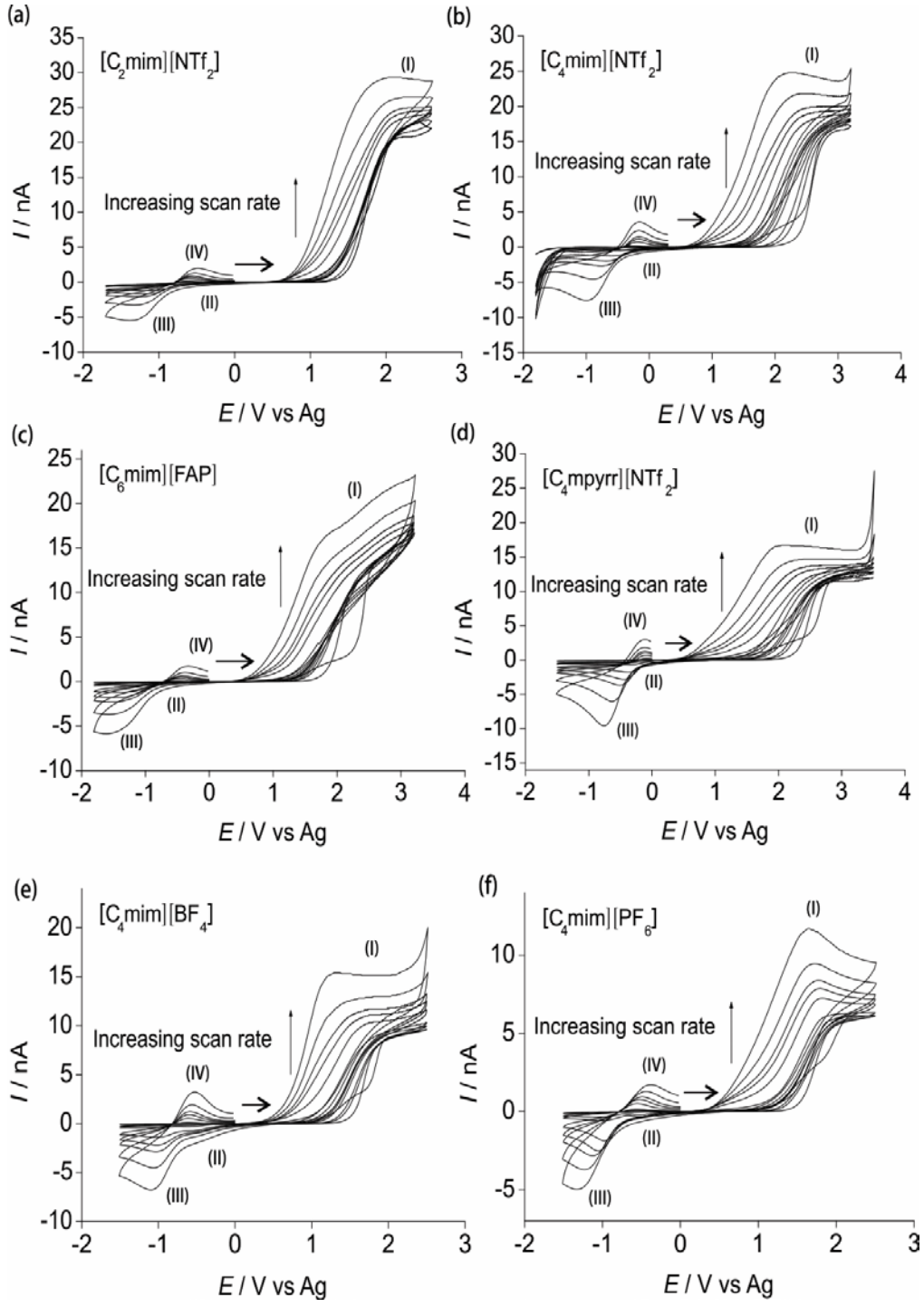

Figure 4.4: CV for the oxidation of 1.3 % methylamine on a 8.3 µm radius Pt electrode in a) $[C_2mim][NTf_2]$, b) $[C_4mim][NTf_2]$, c) $[C_6mim][FAP]$, d) $[C_4mpyrr][NTf_2]$, e) $[C_4mim][BF_4]$, f) $[C_4mim][PF_6]$ at varying scan rates from 0.01 V/s to 4 V/s.

The potential separation of peaks I and peak III are very similar (at higher scan rates) on both the Au and the Pt surfaces, however on the Pt surface the peaks are much closer at lower scan rates compared to Au. It is also clear from figure 4.4 that at high scan rates peak III becomes more obvious and at low scan rates peak II is more obvious which suggests that the equilibrium in equation 4.2 is shifted to the right which suggests that at short timescale more of the ammonium ions are present for the reduction. The current obtained for the oxidative process I for the six RTILs at the various scan rates was plotted against the square root of scan rate and a linear response (R^2 value=0.99, see figure 4.5) was obtained for all the RTILs, which suggests that the electrochemical process occurring is most likely diffusion controlled. The peak potential of this wave becomes more negative as the scan rate is increased which indicates electrochemical irreversibility.[19,20]

However, the fact that the plots do not go through the origin is a well-known feature of voltammetry at microelectrodes in RTILs, where the behaviour is somewhere in-between pure microelectrode (radial diffusion) and pure macroelectrode (linear diffusion). Voltammetry at microelectrodes in RTILs is known to give rise to behaviour somewhere in-between pure microelectrode (radial diffusion) and pure macroelectrode (linear diffusion).[21] For true steady-state behaviour to apply, the following inequality must be met:

$$v \ll \frac{RTD}{nFr_d^2} \tag{4.10}$$

Where v is the scan rate, R is the universal gas constant, and T is the absolute temperature, D is the diffusion coefficient, n is the number of electrons, F is Faraday's constant and r is the radius of the disk. In this work, if we take r to be 8.3 μm and D to be 4.5×10^{-10} m^2s^{-1} for methylamine/ammonia in $[C_2mim][NTf_2]$, the

scan rate must be less than 75 mVs^{-1} for true steady-state behaviour. Since the range of scan rates employed in this work is 10-4,000 mVs^{-1}, this is in the intermediate range for pure micro- or pure macro-electrode behaviour, and the plots of current vs square root scan rate do not pass through the origin.

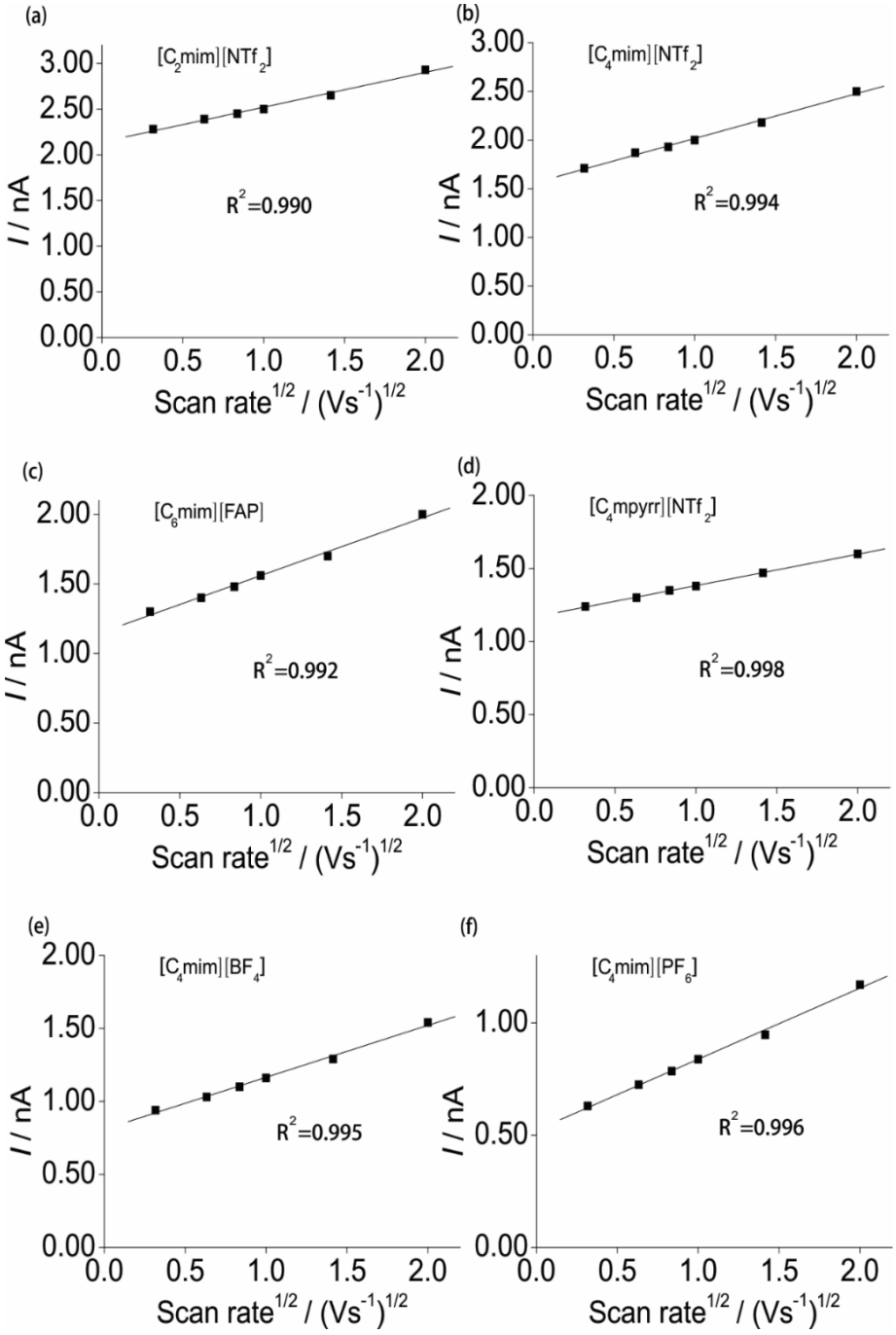

Figure 4.5: Plot of 1.3 % methylamine oxidation currents vs square root of scan rates in the six RTILs, a) $[C_2mim][NTf_2]$, b) $[C_4mim][NTf_2]$, c) $[C_6mim][FAP]$, d) $[C_4mpyrr][NTf_2]$, e) $[C_4mim][BF_4]$, and f) $[C_4mim][PF_6]$ on a Pt microelectrode (diameter 8.3 µm)

Chronoamperometric transients were performed on 1.3 % methylamine in the RTILs and an example is shown in figure 4.6 for 1.3 % methylamine in $[C_2mim][NTf_2]$. The experimental data was fitted with the Shoup and Szabo[17] expression and diffusion coefficients between ca. 1 to 4.5 × 10^{-10} m^2s^{-1} were obtained for the various RTILs which follow approximately the Stokes Einstein relationship where the diffusion coefficient is inversely proportional to solvent viscosity.[22] The fitting also gave *nc* values in all the RTILs between 15-25 mM assuming a five electron process (see Barnes and Mann),[10] which gives a concentration of approximately 3-5 mM for 1.3 % methylamine. This suggests that the saturated concentration (100 %) methylamine (assuming a linear increase at higher concentrations) will be approximately 230-400 mM which is relatively high and this is extremely favourable for sensing purposes. This compares to 2-4 mM for oxygen gas,[16] ~3-10 mM for hydrogen gas,[23] ~200-1600 mM for sulphur dioxide gas[24] and ~200-500 mM for hydrogen sulphide gas.[25]

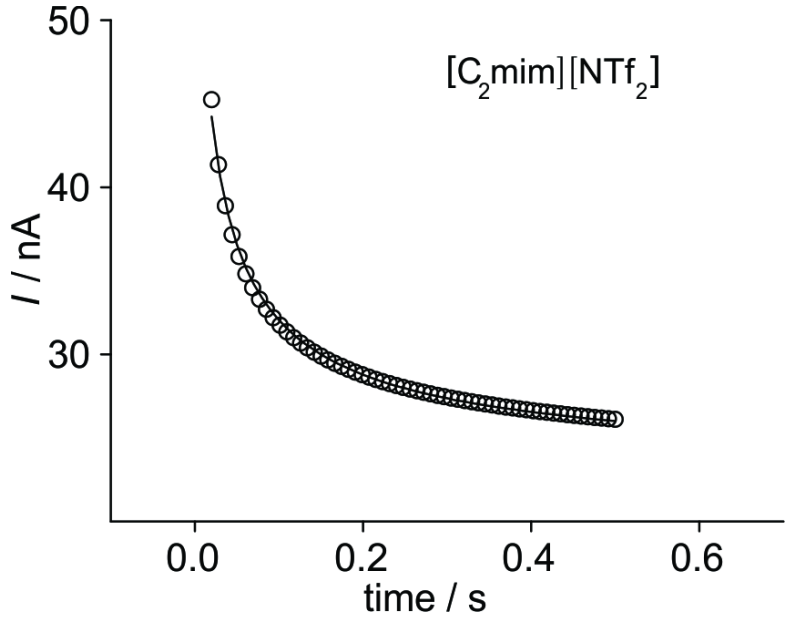

Figure 4.6: Chronoamperometric transient for the oxidation of 1.3 % methylamine gas in the RTIL $[C_2mim][NTf_2]$. The potential was stepped from 0 V to +2.6 V. Experimental (-) and fitted theoretical (o) data following the Shoup and Szabo expression.[17]

4.3.4 Analytical Utility of Methylamine in $[C_2mim][NTf_2]$ and $[C_4mpyrr][NTf_2]$

Once the fundamental behaviour was understood, the analytical utility of methylamine was studied in two RTILs $[C_2mim][NTf_2]$ and $[C_4mpyrr][NTf_2]$. $[C_4mpyrr][NTf_2]$ was chosen due to all four processes being clearly defined and $[C_2mim][NTf_2]$ was chosen due to the fastest gas saturation time as it is the least viscous RTIL. Voltammetry was recorded at a scan rate of 0.1 V/s. Figure 4.7 shows typical CVs of six different concentrations of methylamine on a Pt microelectrode. On both graphs it can be seen that as the concentration increases, the currents of all four processes (I to IV) increases.

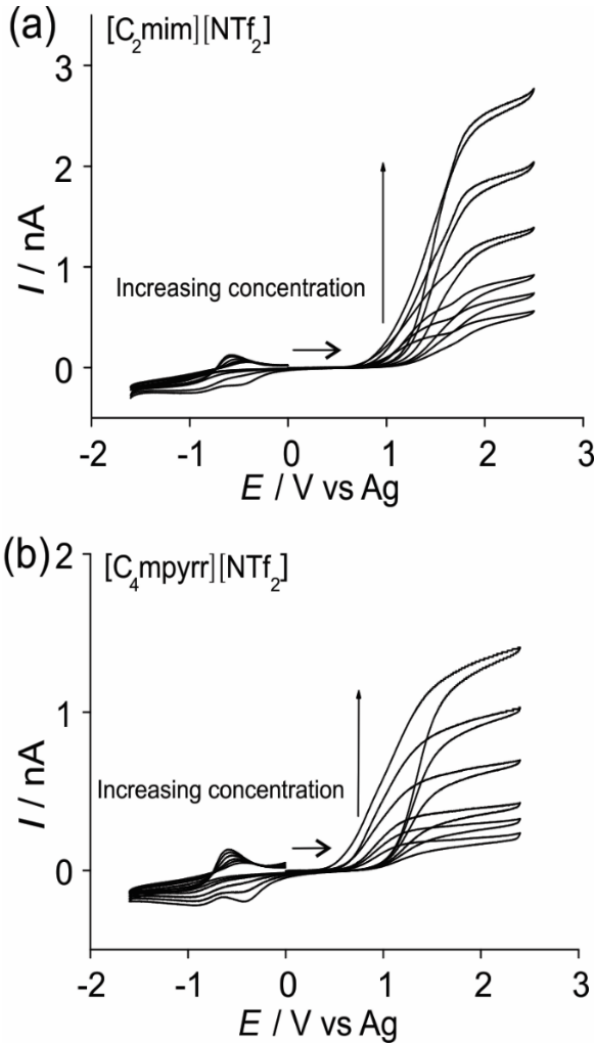

Figure 4.7: CV for the oxidation of different concentrations of methylamine on a 8.3 µm radius Pt electrode in a) $[C_2mim][NTf_2]$ and b) $[C_4mpyrr][NTf_2]$ at a scan rate 0.1 V/s.

Figure 4.8 shows the corresponding calibration graphs (plots of current for process I vs gas phase concentration). It can be seen that for both the ionic liquids a linear behaviour is observed with R^2 values of > 0.99, and sensitivities/gradients of 3.03×10^{-18} and 1.24×10^{-12} A/ppm in $[C_2mim][NTf_2]$ and $[C_4mpyrr][NTf_2]$, respectively. Due to the complicated oxidation mechanism, it was originally unclear if the calibration curves would be linear, however, excellent linearity was observed which is very important for sensing applications. Limit of detections (LODs) (3σ) of 34 and 33 ppm were obtained for $[C_2mim][NTf_2]$ and $[C_4mpyrr][NTf_2]$, respectively, which clearly shows that RTILs can be used as a solvent for the electrochemical detection of low concentrations of methylamine gas.

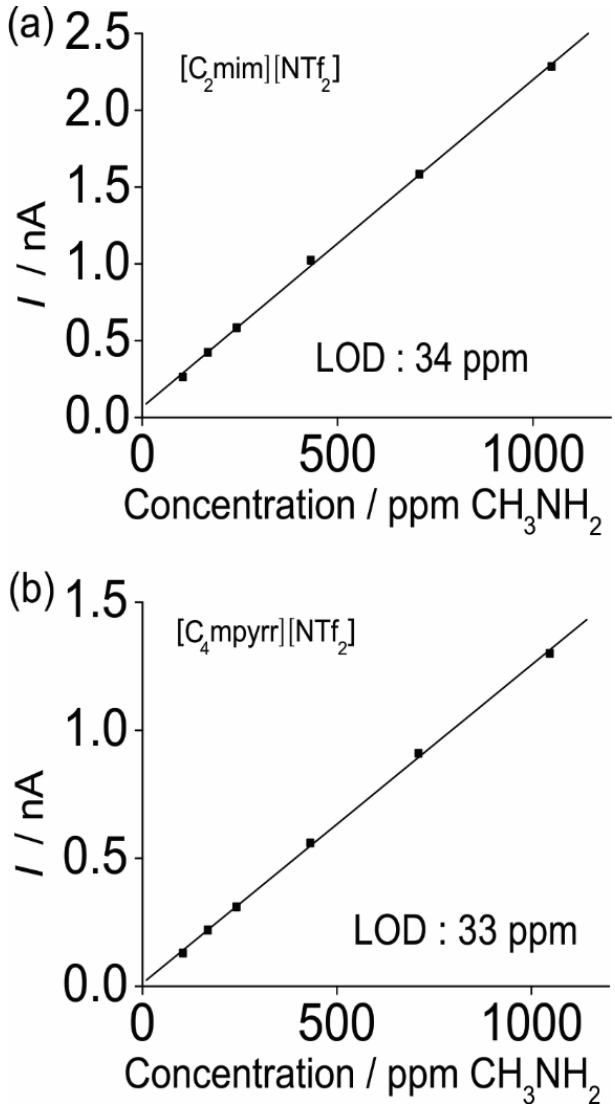

Figure 4.8: Calibration graph of peak current for process I vs gas phase concentration obtained from the CVs for the oxidation of different concentrations of methylamine on a 8.3 µm radius Pt electrode in a) $[C_2mim][NTf_2]$, b) $[C_4mpyrr][NTf_2]$.

4.4 Conclusions

The electrochemical oxidation of methylamine gas has been studied in various RTILs for the first time. In all the RTILs, similar behaviour is observed where one broad oxidative wave and two reduction peaks are seen, followed by another oxidation peak. The mechanism is believed to be highly complex, involving the formation of ammonia as a by-product which is itself instantly oxidised. A high solubility of several hundred mM in the RTIL phase is estimated from chronoamperometric

fitting. The analytical utility of methylamine was then studied in $[C_2mim][NTf_2]$ and $[C_4mpyrr][NTf_2]$ and the calibration graphs obtained were linear with LODs of 34 and 33 ppm respectively which suggests that RTILs can be used as a favourable solvent for the electrochemical sensing of methylamine gas.

4.5 References

(1) Association, C. G.: *Handbook of compressed gases*; Springer US, 1999.
(2) Corbin, D. R.; Schwarz, S.; Sonnichsen, G. C. Methylamines synthesis: A review. *Catal. Today* **1997**, *37*, 71-102.
(3) Miron, Y. Thermal decomposition of monomethylamine nitrate. *J. Hazard. Mater.* **1980**, *3*, 301-321.
(4) Zhang, K.; Hawrylak, B.; Palepu, R.; Tremaine, P. R. Thermodynamics of aqueous amines: excess molar heat capacities, volumes, and expansibilities of {water + methyldiethanolamine (MDEA)} and {water + 2-amino-2-methyl-1-propanol (AMP)}. *J. Chem. Thermodyn.* **2002**, *34*, 679-710.
(5) Jou, F.-Y.; Otto, F. D.; Mather, A. E. Vapor-liquid equilibrium of carbon dioxide in aqueous mixtures of monoethanolamine and methyldiethanolamine. *Ind. Eng. Chem. Res.* **1994**, *33*, 2002-2005.
(6) Turkington, R.: *Chemicals used for illegal purposes*; Wiley, 2009.
(7) Sigrist, M. W.; Bartlome, R.; Marinov, D.; Rey, J. M.; Vogler, D. E.; Wächter, H. Trace gas monitoring with infrared laser-based detection schemes. *Appl. Phys. B* **2008**, *90*, 289-300.
(8) Huerta, F.; Morallón, E.; Pérez, J. M.; Vázquez, J. L.; Aldaz, A. Oxidation of methylamine and ethylamine on Pt single crystal electrodes in acid medium. *J. Electroanal. Chem.* **1999**, *469*, 159-169.
(9) Łuczak, T. Activity of gold towards methylamine electrooxidation. *J. Appl. Electrochem.* **2007**, *37*, 461-466.
(10) Barnes, K. K.; Mann, C. K. Electrochemical oxidation of primary aliphatic amines. *J. Org. Chem.* **1967**, *32*, 1474-1479.
(11) Bonhôte, P.; Dias, A.-P.; Papageorgiou, N.; Kalyanasundaram, K.; Grätzel, M. Hydrophobic, highly conductive ambient-temperature molten salts. *Inorg. Chem.* **1996**, *35*, 1168-1178.
(12) MacFarlane, D. R.; Meakin, P.; Sun, J.; Amini, N.; Forsyth, M. Pyrrolidinium imides: A new family of molten salts and conductive plastic crystal phases. *J. Phys. Chem. B* **1999**, *103*, 4164-4170.
(13) Sharp, M. Determination of the charge-transfer kinetics of ferrocene at platinum and vitreous carbon electrodes by potential steps chronocoulometry. *Electrochim. Acta* **1983**, *28*, 301-308.
(14) Silvester, D. S.; Aldous, L.; Hardacre, C.; Compton, R. G. An electrochemical study of the oxidation of hydrogen at platinum electrodes in several room temperature ionic liquids. *J. Phys. Chem. B* **2007**, *111*, 5000-5007.
(15) Ji, X.; Silvester, D. S.; Aldous, L.; Hardacre, C.; Compton, R. G. Mechanistic studies of the electro-oxidation pathway of ammonia in several room-temperature ionic liquids. *J. Phys. Chem. C* **2007**, *111*, 9562-9572.

(16) Huang, X.-J.; Rogers, E. I.; Hardacre, C.; Compton, R. G. The reduction of oxygen in various room temperature ionic liquids in the temperature range 293−318 K: Exploring the applicability of the Stokes−Einstein relationship in room temperature ionic liquids. *J. Phys. Chem. B* **2009**, *113*, 8953-8959.
(17) Shoup, D.; Szabo, A. Chronoamperometric current at finite disk electrodes. *J. Electroanal. Chem. Interfacial Electrochem.* **1982**, *140*, 237-245.
(18) Fox, M. A.; Whitesell, J. K.: *Organic chemistry.*; Jones and Bartlett Publishers, 2004.
(19) Ji, X.; Banks, C. E.; Silvester, D. S.; Aldous, L.; Hardacre, C.; Compton, R. G. Electrochemical ammonia gas sensing in nonaqueous systems: A comparison of propylene carbonate with room temperature ionic liquids. *Electroanal.* **2007**, *19*, 2194-2201.
(20) Compton, R. G.; Banks, C. E.: *Understanding voltammetry*; World Scientific, 2007.
(21) Buzzeo, M. C.; Evans, R. G.; Compton, R. G. Non-haloaluminate room-temperature ionic liquids in electrochemistry—a review. *ChemPhysChem* **2004**, *5*, 1106-1120.
(22) Barrosse-Antle, L. E.; Bond, A. M.; Compton, R. G.; O'Mahony, A. M.; Rogers, E. I.; Silvester, D. S. Voltammetry in room temperature ionic liquids: comparisons and contrasts with conventional electrochemical solvents. *Chem. Asian J.* **2010**, *5*, 202-230.
(23) Silvester, D. S.; Ward, K. R.; Aldous, L.; Hardacre, C.; Compton, R. G. The electrochemical oxidation of hydrogen at activated platinum electrodes in room temperature ionic liquids as solvents. *J. Electroanal. Chem*, **2008**, *618*, 53-60.
(24) Barrosse-Antle, L. E.; Silvester, D. S.; Aldous, L.; Hardacre, C.; Compton, R. G. Electroreduction of Sulfur Dioxide in Some Room-Temperature Ionic Liquids. *J. Phys. Chem. C* **2008**, *112*, 3398-3404.
(25) O'Mahony, A. M.; Silvester, D. S.; Aldous, L.; Hardacre, C.; Compton, R. G. The Electrochemical Reduction of Hydrogen Sulfide on Platinum in Several Room Temperature Ionic Liquids. *J. Phys. Chem. C* **2008**, *112*, 7725-7730.

5. Electrochemical Reduction and Sensing of Chlorine Gas in a Room Temperature Ionic Liquid

In this chapter, the electrochemical behaviour of chlorine gas in the room temperature ionic liquid (RTIL) 1-ethyl-3-methylimidazolium bis(trifluoromethylsulfonyl)imide ([C_2mim][NTf_2]) is reported. Cyclic voltammetry (CV) and chronoamperometry (CA) on a Pt microelectrode revealed two electron reduction of Cl_2 to chloride ions. On the CV reverse sweep, an oxidation peak due to the oxidation of chloride was observed. The reduction process was diffusion controlled at the concentrations studied (≤4.5 % in the gas phase), in contrast to a previous report[1] which examined only 100 % chlorine. The diffusion-controlled currents were linear with gas phase concentration over the range 174-3333 ppm, yielding limits of detection (LOD) of 106 and 112 ppm from CV and CA, respectively. Fitting of the CA transients to the Shoup and Szabo expression gave a diffusion coefficient for chlorine in the RTIL of ca. 2.6×10^{-10} m^2s^{-1}. Furthermore, determination of the equilibrium concentration of Cl_2 in the RTIL phase as a function of gas phase concentration enabled a value of 35 to be determined for the Henry's law dimensionless volatility constant. These results suggest that RTILs can be used as solvents for chlorine detection.

5. ELECTROCHEMICAL REDUCTION AND SENSING OF CHLORINE GAS IN A ROOM TEMPERATURE IONIC LIQUID 105

5.1 Introduction 107

5.2 Experimental Section 110

5.2.1 Chemical Reagents 110

5.2.2 Electrochemical Experiments 111

5.2.3 Gas Mixing Setup 111

5.2.4 Safety Considerations 112

5.3 Results and Discussion 112

5.3.1 Electrochemical Reduction of Chlorine Gas on a Pt Microelectrode 113

5.3.2 Analytical Utility of Chlorine Gas 116

5.3.3 Chronoamperometry Analysis for the Electrochemical Reduction of Chlorine Gas 119

5.3.4 Henry's Law Constant of Chlorine Gas in $[C_2mim][NTf_2]$ 121

5.4 Conclusions 122

5.5 References 123

Work presented in this section has been published in the journal, Journal of Physical Chemistry C, titled, "Electrochemical Behaviour of Chlorine on Platinum Microdisk and Screen Printed Electrodes in a Room Temperature Ionic Liquid"

5. Electrochemical Reduction and Sensing of Chlorine Gas in a Room Temperature Ionic Liquid

5.1 Introduction

Chlorine is a diatomic yellowish green gas that is denser than air, has an intensely suffocating odour and is used in the production of other chlorine-containing compounds. Due to their very strong oxidising properties, chlorine compounds (such as sodium hypochlorite and chlorine dioxide) are used extensively throughout the world in water treatment, particularly in sewage treatment and in swimming pool disinfection.[2,3] Chlorine is also used in the bleaching of cloth and paper,[4] for the production of chlorinated organic solvents and polymers, and for applications in stabilization of packaged foods.[5,6] Due to its toxicity, chlorine has been used as a chemical warfare agent, either alone or in a mixture such as mustard gas, for example in World War I[2] and more recently in Syria.[7]

Chlorine's toxicity is due to its strong oxidising power. When chlorine is inhaled, it reacts with moisture in the mucosal surface and airways, forming HCl and HClO which causes tissue damage.[3] Damage can also occur to the eyes and skin in the presence of moisture. The current (USA) Occupational Safety and Health Administration Permissible Exposure Limit (OSHA PEL) is 1 ppm. At 30 ppm and above, dyspnea and esophageal perforation might occur. Given its high toxicity and importance in the relevant industries, it is essential to be able to monitor and detect low concentrations of chlorine. One strategy to detect toxic gases is to use

electrochemical sensors, an example of which is the AGS, where the current is monitored as a function of concentration.

Common aqueous electrolyte solutions currently employed in AGSs cannot withstand extreme conditions such as high temperature and pressure.[8,9] By replacing the solvent/electrolyte with non-volatile solvents such as room temperature ionic liquids (RTILs), more robust sensors may be created.[8] RTILs are composed entirely of ions, and possess intrinsic properties such as low volatility, high viscosity, wide electrochemical windows, tuneability and the ability to dissolve a wide range of species.[10] Before employing RTILs in AGSs, the electrochemical behaviour of chlorine in RTILs must be explored, which is the focus of this work.

The electrochemical behaviour of chlorine in acetonitrile, a conventional aprotic solvent, has been studied by Sereno et al.[11] and Huang et al.[1] on Pt electrodes, who found that it underwent a two-electron, diffusion-controlled reduction (equation 5.1).

$$Cl_{2(g)} + 2e^- \rightleftharpoons 2Cl^- \qquad (5.1)$$

The electrochemical behaviour of chlorine on platinum electrodes in several RTILs that were equilibrated with 100 % gaseous chlorine was studied by Huang et al.[1] Cyclic voltammetry (CV) revealed a broad reduction wave followed by a sharp oxidation peak. The broad reduction wave was attributed to the two electron reduction of chlorine and the reverse peak to the oxidation of chloride. However the voltammetry was highly unusual; not only was hysteresis (cross-over of forward and reverse scans) observed, but the currents were observed to *decrease* with increasing scan rate. This behaviour is rarely observed experimentally and it was suggested through theoretical modelling to be the result of non-dissociative adsorption of

chlorine on the Pt electrode surface, followed by electron transfer (equations 5.2 and 5.3).

$$Cl_{2(soln)} \rightleftharpoons Cl_{2(ads)} \quad (5.2)$$

$$Cl_{2(ads)} + 2e^- \rightleftharpoons 2Cl^- \quad (5.3)$$

In this mechanism, as chlorine gas is reduced at the electrode, the equilibrium in equation 5.2 becomes unbalanced, leading to net desorption of Cl_2. This effectively "unblocks" the electrode, leaving more of the electrode surface available for electron transfer, and resulting in an increase in current over time. At lower scan rates (longer timescale), there is more desorption of Cl_2 from the electrode surface, and hence higher currents are observed.

It is important to note here that in an AGS, the concentration in the gaseous phase is not the same as the concentration in the liquid phase. The concentration of gas molecules in the liquid phase differs from solvent to solvent and depends on the specific interactions of the gas molecules with the solvent. For a gas to be detected in an AGS, it must partition into the solvent and form an equilibrium (K_e) between the two phases (figure 5.1). Once equilibrium is established, the gas molecules are either reduced or oxidised on the electrode surface when a potential is applied, producing a current which is directly proportional to the concentration of gas in the liquid phase, and via K_e, in the gas phase.

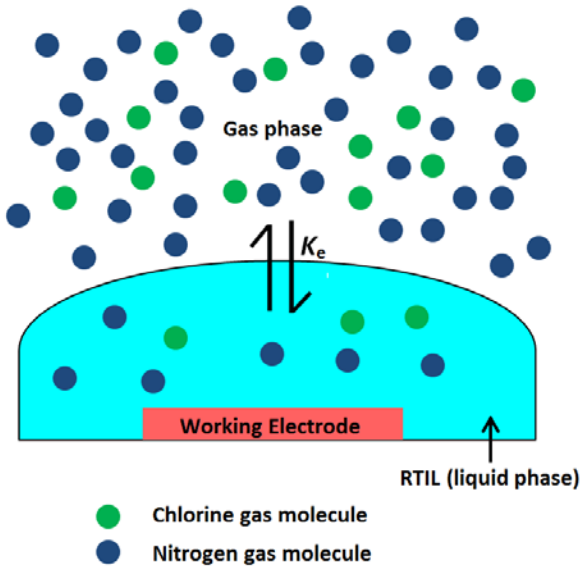

Figure 5.1: Cartoon showing the equilibrium attained between the gas molecules in the gaseous phase and RTIL phase

In this work, the focus is to explore the electrochemical behaviour of low gas-phase concentrations of chlorine (less than 4.5 % in nitrogen) in RTILs on platinum microelectrodes, in order to determine if quantification of low concentrations of chlorine is possible.

5.2 Experimental Section

5.2.1 Chemical Reagents

1-ethyl-3-methylimidazolium bis(trifluoromethylsulfonyl)imide ($[C_2mim][NTf_2]$) was synthesized according to standard literature procedures[12,13] and kindly donated by the group of Professor Christopher Hardacre at Queens University, Belfast. Ultra-pure water with a resistance of 18.2 MΩ cm prepared by an ultra-pure laboratory water purification system (Millipore Pty Ltd., North Ryde, NSW, Australia) and acetonitrile (MeCN, Sigma–Aldrich, 99.8 %) was used for making the ferrocene solution and washing the electrodes before and after use with RTILs. Chlorine gas (from two cylinders of concentrations 4.5 % and 0.2 %, the remainder being made of

nitrogen) was purchased from CAC gases (Auburn, NSW, Australia). High purity nitrogen gas (99.9 %) was purchased from BOC gases (North Ryde, NSW, Australia). Ferrocene ($Fe(C_5H_5)_2$, 98 % purity) and tetra-*N*-butylammonium perchlorate (TBAP, 98 % purity) were purchased from Sigma Aldrich.

5.2.2 Electrochemical Experiments

For experiments involving the microelectrode, a two electrode arrangement was employed with a home-made platinum microelectrode (8.3 µm radius Pt wire encased in glass) as the working electrode and a 0.5 mm diameter silver wire as a combined reference and counter electrode. The electrodes were housed in a glass "T-cell" designed for studying micro quantities (e.g. 20 µL) of ionic liquids in a controlled environment, previously used to study ammonia,[14] oxygen[15] and methylamine[16] and has been explained in experimental chapter 3. The microelectrode diameter was calibrated electrochemically by using the steady state voltammetry of a 2 mM ferrocene (diffusion coefficient 2.3×10^{-5} cm^2s^{-1} at 298 K)[17] solution in acetonitrile with 0.1 M TBAP. Chronoamperometric transients were recorded using a sample time of 0.01 s. After equilibration at 1.6 V, the potential was stepped to a potential more negative than the reduction peak and the current was measured for 10 s. After deletion of the first 10 data points, the transients were fitted to the Shoup and Szabo equation,[18] using Origin 6.0 (Microcal Software Inc.), to obtain the diffusion coefficient (*D*) and the number of electrons multiplied by concentration (*nc*).

5.2.3 Gas Mixing Setup

A similar gas mixing setup as described previously[19] and in the experimental chapter (chapter 3) of this thesis was used to obtain different concentrations of chlorine. Briefly, two gas cylinders (chlorine and nitrogen) were connected to two separate flowmeters with the aid of PTFE tubings and Swagelok fittings. These two flow

meters were then connected to a 'T joint' Swagelok fitting with PTFE tubings to allow mixing of gases before entering the T-cell. The % concentration of chlorine that was introduced into the glass cell was calculated using the relative flow rates of the two flow meters. A digital flowmeter (0-1.2 L/min, John Morris Scientific, NSW, Australia) was used for the nitrogen gas and an analogue flowmeter (0-60 cm^3/min, Dwyer, NSW, Australia) made with PTFE was used for the chlorine gas. It took approximately 90 minutes for saturation/equilibration to occur for each specific concentration. Saturation for each concentration was confirmed when two identical CVs for the same concentration were taken 15-20 minutes apart.

5.2.4 Safety Considerations

Chlorine is an extremely corrosive gas and reacts with moisture to form HCl which corrodes steel to form rust. All Swagelok fittings that were connected to the chlorine gas flowmeter were made of PTFE. Gas PTFE tape (Swagelok, WA, Australia) was wrapped three times around the threads of the metal Swagelok fittings from the chlorine gas cylinder to the regulator to ensure a tight seal and prevent leaks. A deep purge system (Chem-Master, Gas Arc Group Ltd, UK) was also added to prevent any corrosion from occurring inside the regulator and the outlet of the chlorine gas cylinder. It was connected directly to the gas cylinder and just before the regulator. The deep purge system is used to purge the system with nitrogen before and after experiments so as to remove any residual chlorine, gases or moisture that may be present on the steel surfaces of the regulator and Swagelok fittings.

5.3 Results and Discussion

The RTIL chosen for this study was $[C_2mim][NTf_2]$ because it has a wide electrochemical window (>4.5 V) and is one of the least viscous RTILs available,

making the gas equilibration time shorter than for other RTILs. In these experiments, chlorine gas is passed over the surface of the RTIL for sufficient time to enable the gas to partition into and to reach an equilibrium concentration in the RTIL phase (figure 5.1). It was shown previously[1] that chlorine can be reduced in $[C_2mim][NTf_2]$, producing a reduction wave and a corresponding oxidation peak. This RTIL was employed as the solvent in all experiments described throughout this chapter.

5.3.1 Electrochemical Reduction of Chlorine Gas on a Pt Microelectrode

Figure 5.2 shows a typical CV of $[C_2mim][NTf_2]$ equilibrated with 4.5 % chlorine gas (nitrogen fill) at a scan rate of 0.1 V/s when scanned from 1.5 V to -0.4 V and back to 1.5 V. The response in the absence of chlorine is shown as the dotted line. It can be seen that there is a steady state reduction wave and a peak shaped oxidation. These reactions correspond to the two electron reduction of chlorine to chloride and the oxidation of chloride to chlorine. The absence of the oxidation peak when the potential is initially scanned in the positive direction indicates that it is a direct consequence of the reduction process.

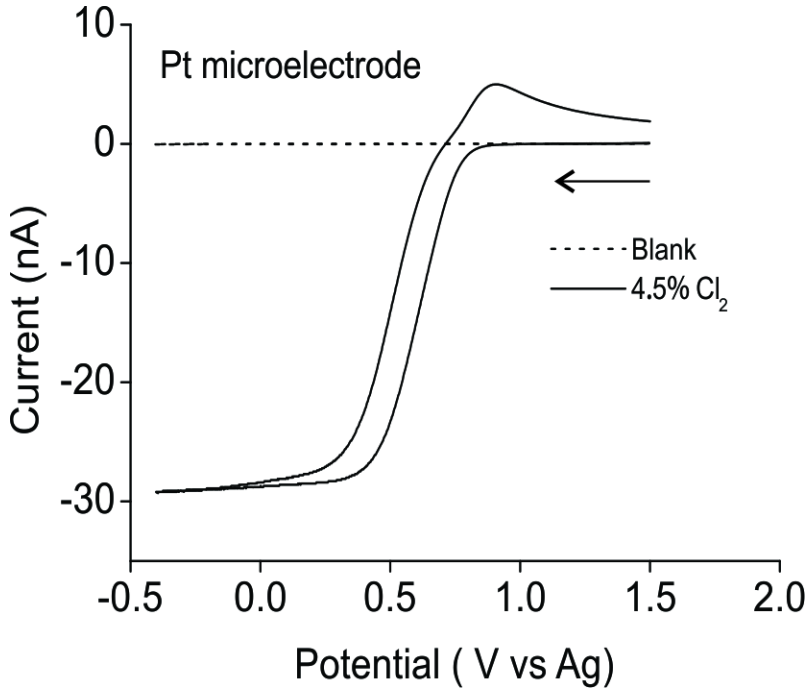

Figure 5.2: CV for the reduction of 4.5 % (4,500 ppm) chlorine gas (nitrogen fill) on a 8.3 µm radius Pt electrode in [C_2mim][NTf_2] A) at a scan rate of 0.1 V/s . Dashed line is the response in the absence of chlorine.

It is important to note here that due to the high viscosity of RTILs, when they are with a microelectrode, steady state current seen on a cyclic voltammogram cannot be taken as the true steady state limiting current. True steady state behaviour is only seen at either very slow scan rates of 10 mVs^{-1} or electrodes with a radius of 5 µm and follows the inequality;[20]

$$v \ll \frac{RTD}{nFr_d^2} \tag{5.4}$$

Where v is the scan rat, R is the universal gas constant, T is the absolute temperature, F is the faraday constant, D is the diffusion coefficient and r_d is the radius of the electrode. This behaviour in RTILs was very well shown in the work done by Evans et al.[21]. Using the values of R as 8.31 J/Kmol, T as 293 K, D as 2.6×10^{-10} m^2s^{-1} (calculated in the later sections), n as 2, F as 96485 sA/mol and r as 8.3×10^{-6} m a value of 0.048 V/s for the scan rate is required for true steady state behaviour. This is

demonstrated by the CVs in figure 5.3, where at a scan rate of 0.05 V/s steady state behaviour is seen and at progressively higher scan rates, the steady state current changes to peak-shaped. However for the reverse peak (chloride oxidation) the process is peak-shaped at all scan rates studied, due to the slower diffusion coefficient of chloride ($\sim 10^{-11}$ m^2s^{-1})[22] compared to chlorine ($\sim 10^{-10}$ m^2s^{-1}). The high currents obtained for the reduction indicates that chlorine has a high solubility in $[C_2mim][NTf_2]$ which was also reported previously by Huang et al.[1]

Figure 5.3 shows the electrochemical reduction of 4.5 % chlorine gas at various scan rates from 0.05 V/s to 3 V/s. The voltammetry goes from steady state at low scan rates to transient at high scan rates, as is often observed for gases in RTILs on microelectrodes and described by the inequality in equation 5.4. The maximum current obtained for the reductive process at various scan rates was plotted against the square root of scan rate and a linear response was obtained, suggesting that it is a one-dimensional diffusion controlled process at these scan rates (inset, figure 5.3). This is in contrast to that observed by Huang et al.[1] for 100 % Cl_2 in the gas phase. It is thought that the difference in behaviour is due to the different concentrations employed. In the present experiments, 4.5 % chlorine gas is used which is >20× less than that used by Huang et al[1] (100 %), assuming partitioning between the gas and RTIL phases is linear. This means that there is less (or no) opportunity for adsorption of Cl_2 (equation 5.2) onto the electrode surface at the lower concentrations employed here. It is likely that the Cl_2 molecules are freely diffusing in solution as indicated by the diffusion dependent reduction current. This is very important as it signifies that chlorine behaves differently at lower concentrations and indicates that this electrochemical process may be of analytical interest. It is also worthwhile to note that the CVs (figure 5.2) did not display any pre-wave or post-wave peaks, which are

useful indicators of adsorption processes accompanying electron transfer reactions. The reverse peak, which is due to the oxidation of chloride, also increases with increasing scan rates and is found to be a diffusion controlled process as a plot of current vs square root of scan rate produced a linear response ($R^2 > 0.99$).

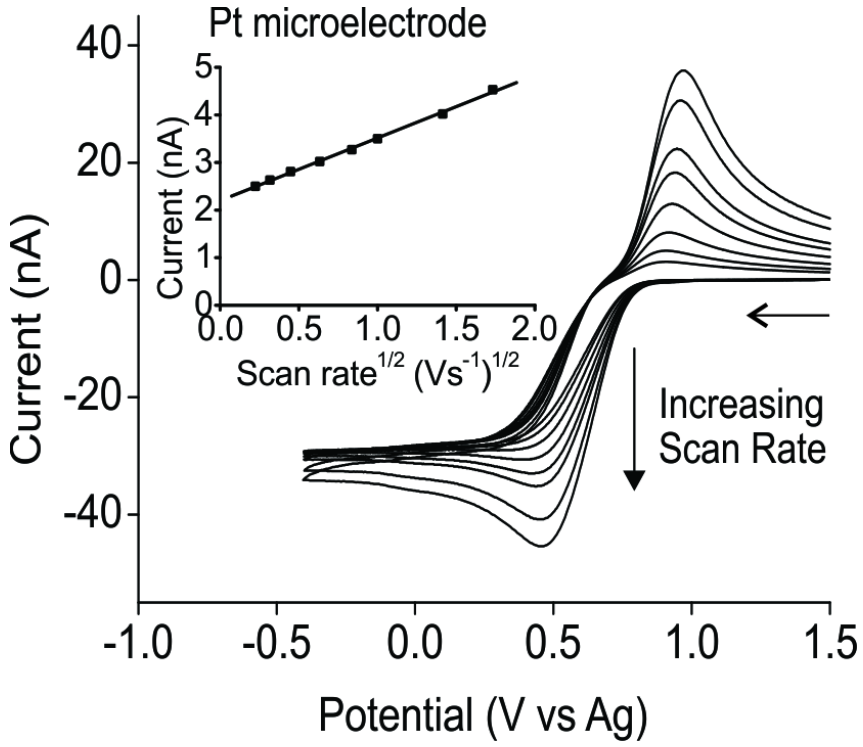

Figure 5.3: CV for the reduction of 4.5 % (4,500 ppm) chlorine gas (nitrogen fill) on a 8.3 µm radius Pt electrode in [C_2mim][NTf_2] at varying scan rates between 0.05-3 V/s. The inset shows the plot of current vs square root of scan rate

5.3.2 Analytical Utility of Chlorine Gas

Once the mechanistic studies were performed the analytical utility of chlorine gas in [C_2mim][NTf_2] was studied. Figure 5.4 shows the CVs of five different concentrations (174 ppm to 1583 ppm) of Cl_2 in [C_2mim][NTf_2] on a Pt microdisk electrode. It can be seen that as the concentration of the Cl_2 gas increases, the current for both the reduction and oxidation processes increase. Figure 5.5 shows the chronoamperometric transients obtained for ten different concentrations of chlorine gas (174 to 3333 ppm) after the potential was stepped from 1.6 V to 0.1 V after a 20 s equilibration time at 1.6 V.

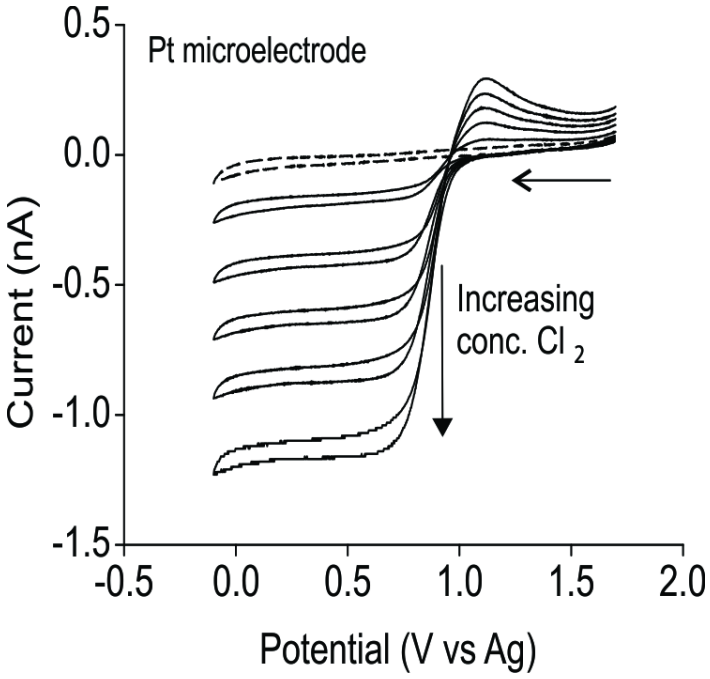

Figure 5.4: CVs for the reduction of chlorine gas (174 -1583 ppm) on a 8.3 µm radius Pt electrode in $[C_2mim][NTf_2]$ at a scan rate of 0.1 V/s. Dashed line is the response in the absence of chlorine

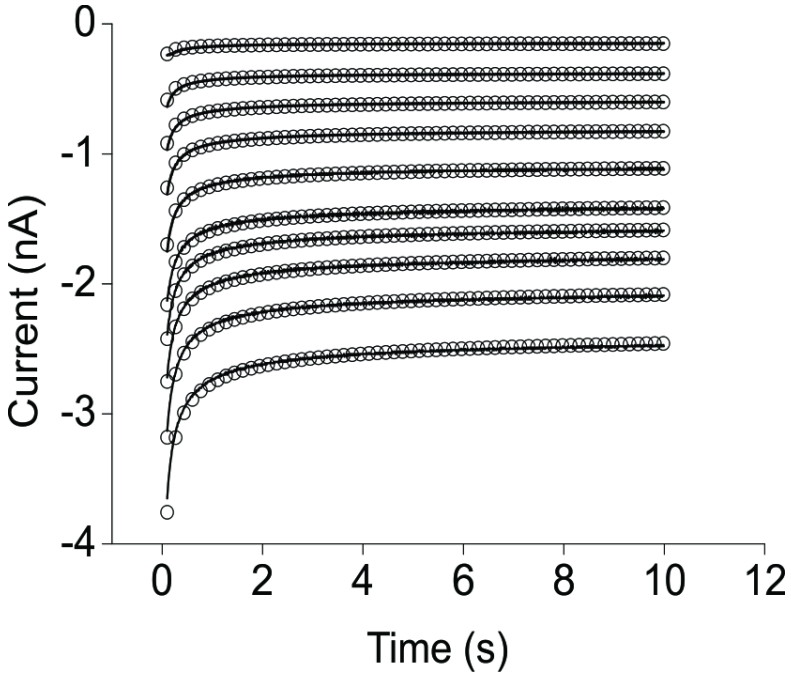

Figure 5.5: Chronoamperometric transient for the reduction of ten different concentrations of chlorine gas (174 -3333 ppm) in the RTIL $[C_2mim][NTf_2]$. The potential was stepped from 1.6 V to -0.1 V. Experimental (-) and fitted (using 2.6×10^{-10} m^2s^{-1} as *D*) theoretical (o) data following the Shoup and Szabo expression

Plots of current versus concentration for both the CV (steady-state reduction current) and chronoamperometry (reduction current at 10 s) experiments are shown in figure 5.6, which display excellent linear response behaviour (R^2 >0.99). The limits of detection (LODs) (3σ) were then obtained for the CV and chronoamperometry methods based on three times the standard deviation of the line of best fit. Values for the LOD of 106 ppm from CV and 112 ppm from chronoamperometry were obtained. Additionally, from the slopes of the graphs, the sensitivity was determined to be 6.8×10^{-13} A/ppm from CV and 7.2×10^{-13} A/ppm from chronoamperometry. The LODs obtained, together with the high solubility, suggest that this RTIL may be a suitable solvent for the electrochemical detection of chlorine.

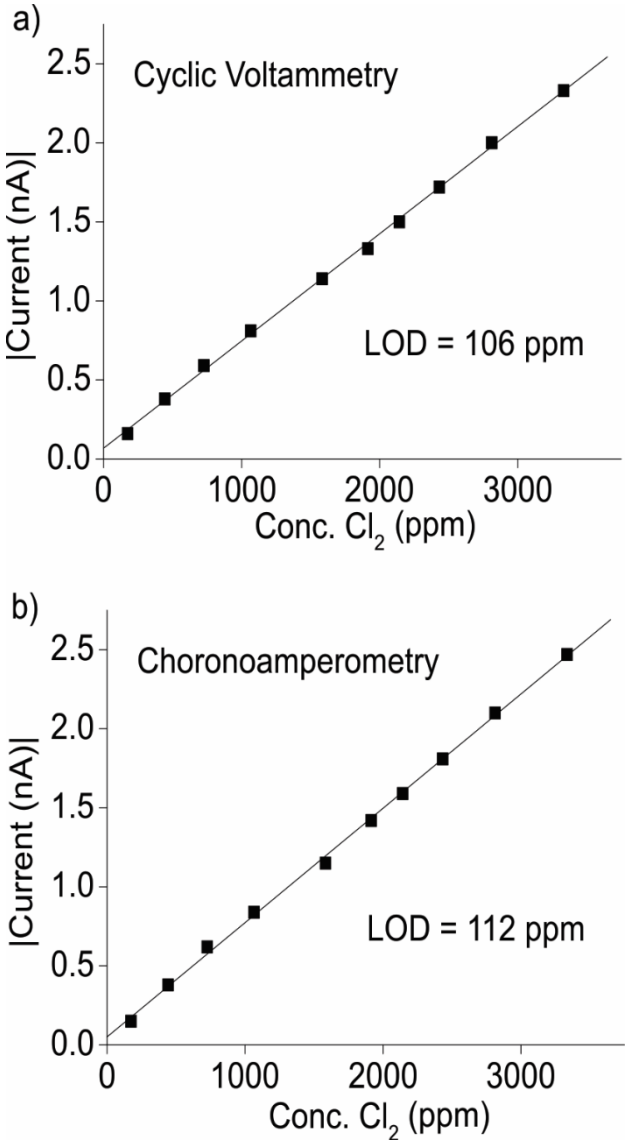

Figure 5.6: Calibration plots (current vs concentration) for the reduction of chlorine gas (174 -3333 ppm) obtained from the a) CV and b) chronoamperometric method.

5.3.3 Chronoamperometry Analysis for the Electrochemical Reduction of Chlorine Gas

The experimentally obtained chronoamperometric transients were fitted with the Shoup and Szabo[18] expression and ten different diffusion coefficient (*D*) values between 1.4×10^{-10} m^2s^{-1} and 3.2×10^{-10} m^2s^{-1} were obtained for the various concentrations. Slight variations in the 'best fit' diffusion coefficients using the Shoup and Szabo[18] expression are possible, as reported by Xiong et al.[23] In order to ascertain which *D* value is the most accurate for Cl_2 gas, each of the ten *D* values

were fixed, and the ten experimental chronoamperometric transients were refitted to the Shoup and Szabo expression (100 fits in total). The best fit (measured using the highest total R^2 values) was found for a diffusion coefficient of 2.6×10^{-10} m^2s^{-1} (also the midpoint of the *D*s obtained from the original fittings). Figure 5.5 shows the fits for all ten concentrations using this *D* value (solid line = experimental; circles = theoretical fit to the Shoup and Szabo expression). Diffusion coefficients of the order 10^{-10} m^2s^{-1} are commonly observed for gases in RTILs,[24] suggesting that this is a reasonable estimate for chlorine gas in RTILs. The fitting also gave *nc* values for all ten concentrations. Assuming a 2-electron process, concentration values between 0.09 and 1.38 mM in $[C_2mim][NTf_2]$ were obtained (see table 5.1). If the concentration scales linearly with the gas-phase concentration, a solubility of approximately 405 mM for chlorine in $[C_2mim][NTf_2]$ is estimated, which can be compared to other gas solubilities in RTILs, e.g. hydrogen (4.2 mM),[25] sulfur dioxide (230 mM)[26] and hydrogen sulphide (529 mM),[27] as well as the estimate of 1-10 M for Cl_2 that was predicted by Huang et al.[1]

Conc. Of Cl_2 in gas phase (ppm)	Conc. Of Cl_2 in RTIL phase (mM)	R^2 Values for fitting
174	0.09	0.91
444	0.22	0.97
726	0.34	0.99
1065	0.47	0.99
1583	0.63	0.99
1915	0.80	0.99
2143	0.89	0.99
2432	1.01	0.99
2813	1.17	0.99
3333	1.38	0.99

Table 5.1: Concentration of chlorine gas in the RTIL phase obtained by fitting chronoamperometric transients from figure 5.5

5.3.4 Henry's Law Constant of Chlorine Gas in [C_2mim] [NTf_2]

The partitioning constant is the ratio of the concentrations of a compound between two phases in equilibrium and it gives information such as the solubility of the gas with respect to its environment. Using the concentration values obtained via the chronoamperometric analysis, the partition coefficient of Cl_2 gas between the gas phase and [C_2mim] [NTf_2] can be obtained. This is also known as the Henry's law dimensionless "volatility constant" (H^{cc} equation 5.5).[28-30] The Henry's law dimensionless volatility constant is a measure of the ability of the gas to escape from the liquid phase.

$$H^{cc} = \frac{\text{concentration of gas in the gas phase}}{\text{concentration of gas in the liquid phase}} \quad (5.5)$$

Figure 5.7 shows the relationship between the concentration of chlorine in the gas phase and the ionic liquid phase. The concentration of chlorine in the gas phase was determined by the relative flow rates of gas from the chlorine and nitrogen gas cylinders. The concentration of the gas in the RTIL phase was determined by fitting the chronoamperometric transients to the Shoup and Szabo expression (see table 5.1) and then converting to units of ppm. It was highly encouraging that excellent linearity was obtained. Since the plot in figure 5.7 was obtained using two different cylinders (lower 5 concentrations from a 2000 ppm Cl_2 cylinder and higher 5 concentrations from a 4.5 % Cl_2 cylinder), this confirms the validity of our gas mixing system for dilution with nitrogen gas. The slope of the line from this relationship also provides Henry's law dimensionless "volatility constant".[29] A value of 35 was obtained for the Henry's law dimensionless "volatility constant", which means that the concentration of chlorine is 35 times higher in the gas phase than in the RTIL phase. Although the solubility values for various gases in RTILs have been

reported in the review by Lei et al.,[31] an experimental Henry's constant value for chlorine gas in RTILs was not reported. Hence, it is believed that this is the first time such a value is reported. Using the values obtained from a previous study[24] for oxygen where it was determined that the concentration of oxygen in the RTIL phase was 3.9 mM for 100 % oxygen in the gaseous phase and assuming a linear correlation of oxygen gas in the two phases a value of 8012 will be obtained for the Henry's law dimensionless constant using this method, which shows that there is much more oxygen in the gas phase then the liquid phase as compared to chlorine. This electrochemical method provides a relatively simple way to measure Henry's constants for highly toxic gases.

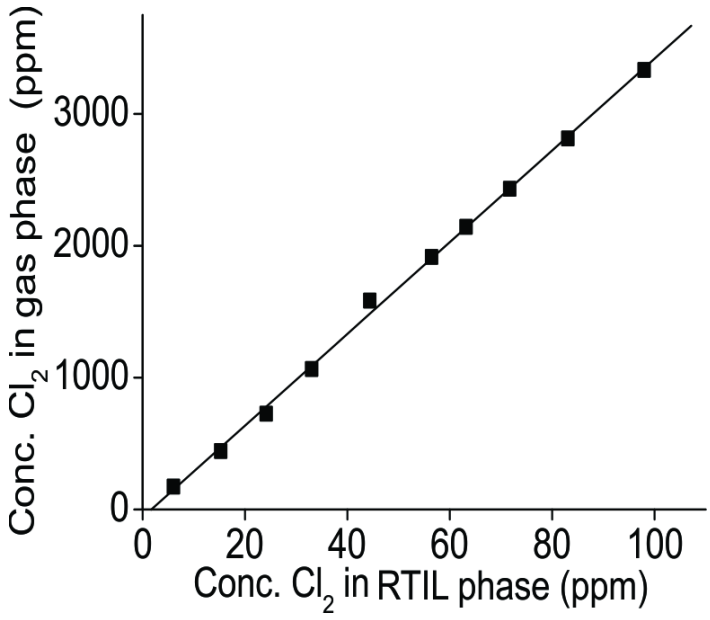

Figure 5.7: A plot of the concentration (ppm) of chlorine in the gas phase vs the RTIL phase (ppm)

5.4 Conclusions

The electrochemical behaviour of chlorine gas has been studied on Pt electrodes. On a Pt microdisk electrode, a high current for the reduction of chlorine suggests a very high solubility in the RTIL. CVs at lower concentrations (< 4.5% in the gas phase) showed no unusual scan rate dependence, as was observed previously at higher

concentrations of chlorine.[1] This is encouraging for sensing applications, and prompted the investigation of linear calibration behaviour and determination of LODs. LODs of 106 and 112 ppm were obtained from CV and chronoamperometric methods, respectively, while the responses were linear between 174 ppm to 3333 ppm. Chronoamperometric transients were fitted with the Shoup and Szabo[18] expression to yield a diffusion coefficient of 2.6×10^{-10} m^2s^{-1} and equilibrated concentrations in the liquid phase. Comparison of these liquid-phase concentrations with their corresponding gas-phase concentrations enabled the determination of the Henry's law dimensionless "volatility constant" for chlorine, which has not been reported before. These results suggest that RTILs can be utilised for chlorine gas sensing. The ability to use non-volatile RTILs to detect chlorine gas is a major advantage as it will allow more robust sensors that are able to perform in harsh conditions such as high temperature and high pressures.

5.5 References

(1) Huang, X.-J.; Silvester, D. S.; Streeter, I.; Aldous, L.; Hardacre, C.; Compton, R. G. Electroreduction of chlorine gas at platinum electrodes in several room temperature ionic liquids: Evidence of strong adsorption on the electrode surface revealed by unusual voltammetry in which currents decrease with increasing voltage scan rates. *J. Phys. Chem. C* **2008**, *112*, 19477-19483.
(2) Das, R.; Blanc, P. D. Chlorine Gas Exposure and the lung: A review. *Toxicol. Ind. Health* **1993**, *9*, 439-455.
(3) White, C. W.; Martin, J. G. Chlorine gas inhalation. *Proceed Am. Thorac. Soc.* **2010**, *7*, 257-263.
(4) Hedges, J. R.; Morrissey, W. L. Acute chlorine gas exposure. *J. Am. Coll. Emerg. Phys.* **1979**, *8*, 59-63.
(5) Zoffoli, J. P.; Latorre, B. A.; Rodrguez, E. J.; Aldunce, P. Modified atmosphere packaging using chlorine gas generators to prevent Botrytis cinerea on table grapes. *Postharvest Bio. Tech.* **1999**, *15*, 135-142.
(6) Lee, S.-Y.; Costello, M.; Kang, D.-H. Efficacy of chlorine dioxide gas as a sanitizer of lettuce leaves. *J. Food Protect.* **2004**, *67*, 1371-1376.
(7) Sparrow, A. Syria: Death from Assad's chlorine. *New York Rev. Books* **2015**, *62*, 40-42.
(8) Buzzeo, M. C.; Hardacre, C.; Compton, R. G. Use of room temperature ionic liquids in gas sensor design. *Anal. Chem.* **2004**, *76*, 4583-4588.

(9) Plechkova, N. V.; Seddon, K. R. Applications of ionic liquids in the chemical industry. *Chem. Soc. Rev.* **2008**, *37*, 123-150.
(10) Silvester, D. S.; Compton, R. G. Electrochemistry in room temperature ionic liquids: A review and some possible applications. *Z. Phys. Chem.* **2006**, *220*, 1247-1274.
(11) Sereno, L.; Macagno, V. A.; Giordano, M. C. Electrochemical behaviour of the chloride/chlorine system at platinum electrodes in acetonitrile solutions. *Electrochim. Acta* **1972**, *17*, 561-575.
(12) Bonhôte, P.; Dias, A.-P.; Papageorgiou, N.; Kalyanasundaram, K.; Grätzel, M. Hydrophobic, highly conductive ambient-temperature molten salts. *Inorg. Chem.* **1996**, *35*, 1168-1178.
(13) MacFarlane, D. R.; Meakin, P.; Sun, J.; Amini, N.; Forsyth, M. Pyrrolidinium imides: A new family of molten salts and conductive plastic crystal phases. *J. Phys. Chem. B* **1999**, *103*, 4164-4170.
(14) Ji, X.; Silvester, D. S.; Aldous, L.; Hardacre, C.; Compton, R. G. Mechanistic studies of the electro-oxidation pathway of ammonia in several room-temperature ionic liquids. *J. Phys. Chem. C* **2007**, *111*, 9562-9572.
(15) Huang, X.-J.; Rogers, E. I.; Hardacre, C.; Compton, R. G. The reduction of oxygen in various room temperature ionic liquids in the temperature range 293−318 K: Exploring the applicability of the Stokes−Einstein relationship in room temperature ionic liquids. *J. Phys. Chem. B* **2009**, *113*, 8953-8959.
(16) Murugappan, K.; Kang, C.; Silvester, D. S. Electrochemical oxidation and sensing of methylamine gas in room temperature ionic liquids. *J. Phys. Chem. C* **2014**, *118*, 19232-19237.
(17) Sharp, M. Determination of the charge-transfer kinetics of ferrocene at platinum and vitreous carbon electrodes by potential steps chronocoulometry. *Electrochim. Acta* **1983**, *28*, 301-308.
(18) Shoup, D.; Szabo, A. Chronoamperometric current at finite disk electrodes. *J. Electroanal. Chem. Interfacial Electrochem.* **1982**, *140*, 237-245.
(19) Lee, J.; Murugappan, K.; Arrigan, D. W. M.; Silvester, D. S. Oxygen reduction voltammetry on platinum macrodisk and screen-printed electrodes in ionic liquids: Reaction of the electrogenerated superoxide species with compounds used in the paste of Pt screen-printed electrodes? *Electrochim. Acta* **2013**, *101*, 158-168.
(20) Buzzeo, M. C.; Evans, R. G.; Compton, R. G. Non-haloaluminate room-temperature ionic liquids in electrochemistry—a review. *ChemPhysChem* **2004**, *5*, 1106-1120.
(21) Evans, R. G.; Klymenko, O. V.; Saddoughi, S. A.; Hardacre, C.; Compton, R. G. Electroreduction of oxygen in a series of room temperature ionic liquids composed of group 15-centered cations and anions. *J. Phys. Chem. B* **2004**, *108*, 7878-7886.
(22) Villagrán, C.; Banks, C. E.; Hardacre, C.; Compton, R. G. Electroanalytical determination of trace chloride in room-temperature ionic liquids. *Anal. Chem.* **2004**, *76*, 1998-2003.
(23) Xiong, L.; Aldous, L.; Henstridge, M. C.; Compton, R. G. Investigation of the optimal transient times for chronoamperometric analysis of diffusion coefficients and concentrations in non-aqueous solvents and ionic liquids. *Anal. Meth.* **2012**, *4*, 371-376.
(24) Rogers, E. I.; O'Mahony, A. M.; Aldous, L.; Compton, R. G. (Invited) Amperometric Gas Detection Using Room Temperature Ionic Liquid Solvents. *ECS Trans.* **2010**, *33*, 473-502.

(25) Silvester, D. S.; Ward, K. R.; Aldous, L.; Hardacre, C.; Compton, R. G. The electrochemical oxidation of hydrogen at activated platinum electrodes in room temperature ionic liquids as solvents. *J. Electroanal. Chem.* **2008**, *618*, 53-60.
(26) Barrosse-Antle, L. E.; Silvester, D. S.; Aldous, L.; Hardacre, C.; Compton, R. G. Electroreduction of sulfur dioxide in some room-temperature ionic liquids. *J. Phys. Chem. C* **2008**, *112*, 3398-3404.
(27) O'Mahony, A. M.; Silvester, D. S.; Aldous, L.; Hardacre, C.; Compton, R. G. The electrochemical reduction of hydrogen sulfide on platinum in several room temperature ionic liquids. *J. Phys. Chem. C* **2008**, *112*, 7725-7730.
(28) Oliferenko, A. A.; Oliferenko, P. V.; Seddon, K. R.; Torrecilla, J. S. Prediction of gas solubilities in ionic liquids. *Phys. Chem. Chem. Phys.* **2011**, *13*, 17262-17272.
(29) Sander, R. Compilation of Henry's law constants, version 3.99. *Atmos. Chem. Phys. Discuss.* **2014**, *14*, 29615-30521.
(30) Smith, F. L.; Harvey, A. H. Avoid common pitfalls when using Henry's law. *Chem. Eng. Prog* **2007**, *103*, 33-39.
(31) Lei, Z.; Dai, C.; Chen, B. Gas solubility in ionic liquids. *Chem. Rev.* **2013**, *114*, 1289-1326.

6. Electrochemical Oxidation and Sensing of Hydrogen Chloride Gas in Room Temperature Ionic Liquids

The electrochemical behaviour of hydrogen chloride (HCl) gas has been investigated in several RTILs, namely [C_2mim][NTf_2], [C_4mim][NTf_2], [C_6mim][FAP] [C_4mpyrr][NTf_2], [C_4mim][BF_4] and [C_4mim][PF_6] on a Pt microelectrode using cyclic voltammetry. In four RTILs, similar behaviour was seen where there is a complex mechanism. HCl gas is thought to be in its dissociated form of H^+ and $[HCl_2]^-$ in RTILs. When scanned positively from 0 V there was first an oxidation peak at ~2.1 V which was attributed to the oxidation of $[HCl_2]^-$ to form Cl_2 and H^+ which both get reduced at ~ 0.5 V and -0.5 V respectively to form H_2 and Cl^-. The formed H_2 and Cl^- then get oxidised back to H^+ and Cl_2 in the reverse reaction. In the RTILs [C_4mim][BF_4] and [C_4mim][PF_6], CVs indicated a reaction of the RTIL with the analyte/electrogenerated products and therefore might not be suitable solvents for the detection of HCl gas. This was supported by NMR spectrometry, which showed that [C_4mim][PF_6] underwent structural changes after HCl gas experiments. The analytical utility was then studied in [C_2mim][NTf_2] by utilising both peaks (oxidation of $[HCl_2]^-$ and reduction of protons) and linear calibration graphs (R^2 value of 0.99) with limit of detections (LODs) of 102 and 69 ppm obtained, for the two processes respectively. This suggests that the reduction of protons might be a better alternative than the oxidation of $[HCl_2]^-$, for sensing HCl gas. Preliminary results using differential pulse voltammetry gave a slightly lower LOD of 71 ppm for the oxidation of $[HCl_2]^-$.

6. ELECTROCHEMICAL OXIDATION AND SENSING OF HYDROGEN CHLORIDE GAS IN ROOM TEMPERATURE IONIC LIQUIDS 127

6.1 Introduction 129

6.2 Experimental Section 131

6.2.1 Chemical Reagents 131

6.2.2 Electrochemical Experiments 132

6.2.3 Gas Mixing Setup 132

6.2.4 Nuclear Magnetic Resonance Experiments 133

6.3 Results and Discussion 133

6.3.1 Electrochemical Behaviour of Hydrogen Chloride Gas in Various RTILs on a Pt Microelectrode 133

6.3.2 Electrochemical Oxidation of Hydrogen Chloride Gas in RTILs at Various Scan Rates on a Pt Microelectrode 140

6.3.3 Analytical Utility of HCl Gas in $[C_2mim][NTf_2]$ 151

6.4 Conclusions 155

6.5 References 156

Work presented in this section has been submitted to the Journal, Physical Chemistry Chemical Physics, titled, "Electrochemical Studies of Hydrogen Chloride Gas in Several Room Temperature Ionic Liquids: Mechanism and Sensing"

6. Electrochemical Oxidation and Sensing of Hydrogen Chloride Gas in Room Temperature Ionic Liquids

6.1 Introduction

Hydrogen chloride (HCl) gas is a colourless toxic gas with a strong pungent odour. The current USA Occupational Safety and Health Administration Permissible Exposure Limit (OSHA PEL) of HCl is 5 ppm in the gas phase. There are several ways to prepare hydrogen chloride gas such as reacting sulphuric acid with sodium chloride or by reacting chlorine with hydrogen at temperatures above 250^{o}C.[1,2] HCl is used in the gasoline industry as a precursor for the formation of aluminium chloride catalyst which converts n-butane to isobutane.[2] HCl is also used in the electronic industry as an etchant for semiconductor materials.[2] In the textile industry, HCl gas is used to disinfect cotton seeds and also to decompose vegetable fibres in wool so that they can be reclaimed for use in fabrics.[2] In the metal industry it is used to clean metals due to its strong disinfectant properties.[2]

HCl is highly corrosive and in the presence of moisture it forms hydrochloric acid which can cause burns and irritation to the skin, as well as causing corrosion to metals (e.g. iron).[3] HCl gas is denser than air and therefore sinks to the bottom of spaces. Ulceration of the nose, throat and larynx can occur upon excess inhalation[2] and frequent exposure can cause dermatitis.[2] HCl is also corrosive to the eyes and mucous membranes.[3,4] Concentrations above 15,000 ppm are deadly to humans and contact for more than 1 hour should be avoided at concentrations of 50 ppm and

above.[2] Due to its high toxicity and uses in many industries, it is essential to be able to detect and monitor hydrogen chloride gas.

The electrochemical behaviour of a saturated solution of hydrogen chloride in the RTIL, $[C_4mim][NTf_2]$ has been briefly studied on a Pt macroelectrode by Aldous et al.[5] who obtained four peaks (two oxidation and two reduction) in the first scan and five peaks (three oxidation and two reduction) in the second scan (all processes were diffusion controlled) and proposed a highly complicated mechanism. It is believed that HCl is in its dissociated form of $[HCl_2]^-$ and H^+ in the RTIL (equation 6.1).[5]

$$2HCl_{gas} \rightleftharpoons H^+ + [HCl_2]^- \quad (6.1)$$

The first oxidation peak that occurred while scanning from 0 to 2 V was attributed to the oxidation of $[HCl_2]^-$ to form protons (H^+_{IL}) and chlorine gas (equation 6.2).

$$[HCl_2]^- \rightleftharpoons H^+_{IL} + Cl_2 + 2e^- \quad (6.2)$$

When the scan was reversed there were two reduction peaks. The first was due to the reduction of the chlorine, which was produced in equation 6.2, to form chloride ions (equation 6.3). The second peak was due to the reduction of protons (equation 6.4-6.6).

$$Cl_{2_{gas}} + 2e^- \rightleftharpoons 2Cl^- \quad (6.3)$$

$$H^+_{IL} + e^- \rightleftharpoons H_{ads} \quad (6.4)$$

$$2H_{ads} \rightleftharpoons H_{2_{gas}} \quad (6.5)$$

$$H_{ads} + H^+_{IL} + e^- \rightleftharpoons H_{2_{gas}} \quad (6.6)$$

This second reduction peak is followed by an oxidation peak which is attributed to the oxidation of hydrogen gas to form protons, reverse of equation 6.4-6.6.

Continuing on the scan for a second cycle reveals another oxidation peak which was not seen on the first scan and this is attributed to the oxidation of chloride ions (reverse of equation 6.3) which was formed during the first reduction peak. It was reported that in these experiments there was difficulty in controlling the concentration of HCl in the RTIL. This could have been due to the nature of the experiments where HCl was bubbled directly into the RTIL and the cell was not at a constant atmosphere of HCl. Therefore rapid desorption of HCl was observed from the RTILs, which didn't allow further mechanistic or analytical studies to be performed.

In this chapter the electrochemical behaviour of hydrogen chloride gas will be investigated in several room temperature ionic liquids to expand the knowledge of the mechanism in different RTILs on a Pt microelectrode. The analytical utility will also be investigated opening up possibilities for using RTILs in amperometric gas sensors to detect hydrogen chloride gas.

6.2 Experimental Section

6.2.1 Chemical Reagents

The RTILs 1-ethyl-3-methylimidazolium bis(trifluoromethylsulfonyl)imide ([C_2mim][NTf_2]), 1-butyl-3-methylimidazolium bis(trifluoromethylsulfonyl)imide ([C_4mim][NTf_2]) and *N*-butyl-*N*-methylpyrrolidinium bis(trifluoromethylsulfonyl)imide ([C_4mpyrr][NTf_2]) were synthesized according to standard literature procedures[6,7] and kindly donated by the group of Professor Christopher Hardacre at Queens University, Belfast. The RTILs 1-hexyl-3-methylimidazolium trifluorotris(pentafluoroethyl)phosphate ([C_6mim][FAP]), 1-butyl-3-methylimidazolium hexafluorophosphate ([C_4mim][PF_6]) and 1-butyl-3-methylimidazolium tetrafluroborate ([C_4mim][BF_4]) were purchased from Merck

KGaA (Kilsyth, Victoria, Australia) at ultra-high purity electrochemical grade (halide content less than 100 ppm). Ultra-pure water with a resistance of 18.2 MΩ cm prepared by an ultra-pure laboratory water purification system (Millipore Pty Ltd., North Ryde, NSW, Australia) and acetonitrile (MeCN, Sigma–Aldrich, 99.8%) was used for washing the electrodes before and after use with RTILs. HCl gas (from two cylinders of concentrations 5 % and 0.2 %, the remainder being made of nitrogen) was purchased from CAC gases (Auburn, NSW, Australia). High purity nitrogen gas (99.9 %) was purchased from BOC gases (North Ryde, NSW, Australia). Ferrocene ($Fe(C_5H_5)_2$, 98 % purity) and tetra-*N*-butylammonium perchlorate (TBAP, 98 % purity) were purchased from Sigma Aldrich.

6.2.2 Electrochemical Experiments

A conventional two-electrode arrangement was employed, with a home-made platinum microelectrode (8.3 µm radius) as the working electrode and a 0.5 mm diameter silver wire (Sigma Aldrich) as the quasi-reference electrode as explained in the experimental chapter. The steady-state voltammetry of a 2 mM ferrocene (diffusion coefficient 2.3×10^{-5} cm^2s^{-1} at 298K)[8] solution in acetonitrile with 0.1 M TBAP as the electrolyte was analysed to calibrate the electrode diameter. The electrodes were housed in a glass "T-cell"[5] designed for studying microlitre quantities (20 µL) of ionic liquids in a controlled environment, previously used to study ammonia[9], methylamine,[10] oxygen[11] and used in previous chapters.

6.2.3 Gas Mixing Setup

A similar gas mixing setup as explained in chapter 3 was used for the experiments. The % concentration of hydrogen chloride that was introduced into the T-cell was calculated using the relative flow rates of the two flow meters. A digital flowmeter (0-1.2 L/min, John Morris Scientific, NSW, Australia) was used for the nitrogen gas

and an analogue flowmeter (0-60 cm^3/min, Dwyer, NSW, Australia) was used for the hydrogen chloride gas. It took approximately 90 minutes for saturation to occur in most of the ionic liquids and the time taken between each concentration change was 45 minutes.

6.2.4 Nuclear Magnetic Resonance Experiments

Nuclear magnetic resonance (NMR) spectra were recorded using a Bruker Advance 400 spectrometer. 1 mL of deuterated chloroform ($CDCl_3$) was used to dissolved 5 µL of RTIL ([C_2mim][NTf_2] [C_4mim][BF_4] and [C_4mim][PF_6]) in a NMR sample tube and experiments were conducted on the RTILs before and after electrochemical experiments with HCl. For the RTIL [C_2mim][NTf_2], ^{13}C and ^{1}H spectrum were obtained. For the RTIL [C_4mim][PF_6], ^{13}C, ^{1}H, ^{31}P and ^{19}F spectra were obtained. For the RTIL, [C_4mim][BF_4] ^{13}C, ^{1}H, ^{11}B and ^{19}F spectra were obtained.

6.3 Results and Discussion

6.3.1 Electrochemical Behaviour of Hydrogen Chloride Gas in Various RTILs on a Pt Microelectrode

Figure 6.1 shows the cyclic voltammograms (CVs) obtained for the behaviour of 2.56 % hydrogen chloride gas (nitrogen fill) in six different RTILs, [C_2mim][NTf_2], [C_4mim][NTf_2], [C_6mim][FAP], [C_4mpyrr][NTf_2], [C_4mim][BF_4], and [C_4mim][PF_6] on a Pt microelectrode at a scan rate 0.1 V/s when scanned from 0 to 2.3 V (3 V in the case of [C_6mim][FAP]) to -1.8 V and back to 0 V. The red line shows the first scan and the blue line shows the second scan. The response in the absence of hydrogen chloride is shown as the black line. It can be seen that in all the RTILs on the first scan there is a broad oxidation peak (I) at approximately 2 V and this is attributed to equation 6.1 where $[HCl_2]^-$ is oxidised to form protons and

chlorine gas. When the scan is reversed at 2.3 V there is a steady state reduction wave (III) at -1 V which is due to the reduction of the protons and follows equation 6.4-6.6.

It is important to note here that process II (reduction of the formed chlorine) from peak I and process IV (oxidation of the hydrogen gas formed from peak III) are not easily visible due to the much smaller electrode used in our experiments as compared to the work performed by Aldous et al.[5] However these peaks do become visible at higher scan rates, as will be discussed in the next section.

On the second scan (blue line in figure 6.1) there is an additional peak (V) at ~1.2 V that is not present on the first scan. The appearance of this peak which causes peak I to have a higher peak current on the second scan as compared to the first scan. This pre peak is attributed to the oxidation of the chloride ions (reverse of equation 6.3 which are formed as a result of process II). This peak (V) is not present on the first scan as chlorine gas has to be formed (peak I) first and then undergo oxidation to form chloride ions (process II) which then gets oxidised (peak V). It is also important to note that the current produced for process III does not change in the second scan which suggests that the concentration is stable. Table 6.1 summarises all the reactions for each peak.

Although the behaviour in all the RTILs is very similar there are some differences in certain ionic liquids. In the RTIL $[C_6mim][FAP]$, the oxidation peak I is not very evident as compared to other peaks which suggests that HCl may not be very soluble in this RTIL, which might not be advantageous from a sensing point of view.

In $[C_4mim][BF_4]$, the potential separation between peaks I and V is the smallest for all six RTILs and in the first scan it looks like there is a combination of two

processes occurring which suggests that the mechanism might be slightly different in this RTIL. In the RTIL $[C_4mim][PF_6]$ there are some major differences where in the negative scan it is complicated by many impurity peaks. Furthermore the second scan records a smaller current then the first scan and also peak V is not evident in the second scan which again suggests that there might be complications in the mechanism, probably reactions with the RTIL itself. PF_6^- and BF_4^- anions have been known to dissociate to produce HF in very acidic environments and will be investigated next.[12,13]

Peaks	Equation	Reactions
I	6.2	$[HCl_2]^- \rightleftharpoons H_{IL}^+ + Cl_2 + 2e^-$
II	6.3	$Cl_{2\,gas} + 2e^- \rightleftharpoons 2Cl^-$
III	6.4	$H_{IL}^+ + e^- \rightleftharpoons H_{ads}$
	6.5	$2H_{ads} \rightleftharpoons H_{2\,gas}$
	6.6	$H_{ads} + H_{IL}^+ + e^- \rightleftharpoons H_{2\,gas}$
IV	6.7	Reverse of Peak III
V	6.8	Reverse of Peak II

Table 6.1: Summary of proposed reactions and peak assignments

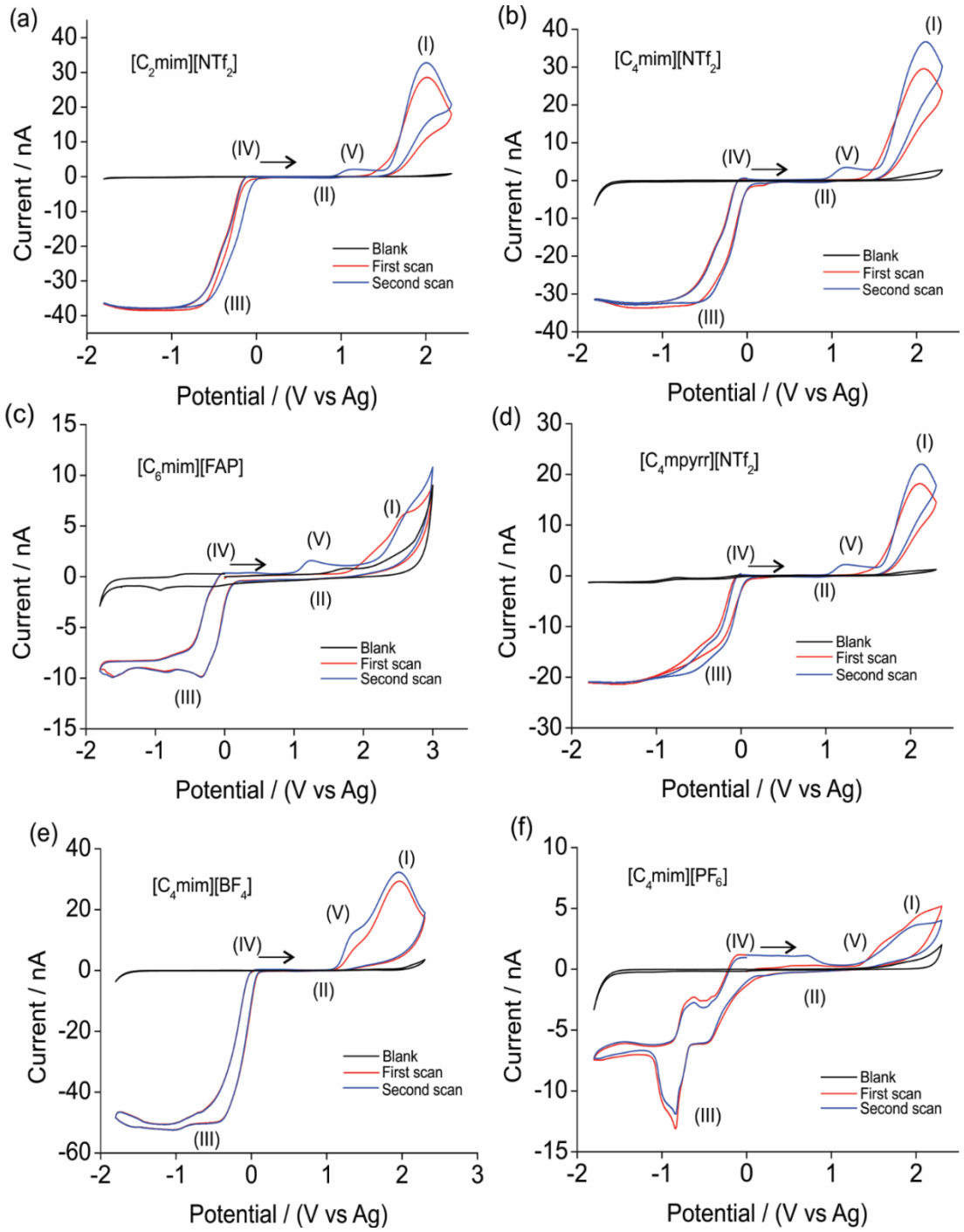

Figure 6.1: CV for the oxidation of 2.56 % hydrogen chloride gas on a 8.3 µm radius Pt electrode in a) $[C_2mim][NTf_2]$, b) $[C_4mim][NTf_2]$, c) $[C_6mim][FAP]$, d) $[C_4mpyrr][NTf_2]$, e) $[C_4mim][BF_4]$, f) $[C_4mim][PF_6]$ at a scan rate 0.1 V/s. Red line indicates first scan, blue line indicates second scan and the black line is the blank (response in the absence of hydrogen chloride gas).

Another important finding is shown in figure 6.2 where in the RTILs $[C_4mim][BF_4]$ and $[C_4mim][PF_6]$ it was not possible to obtain featureless blanks after HCl gas

experiments were performed. The blanks after the HCl gas experiments were obtained by flushing the system with nitrogen. This suggests that the RTILs have undergone a change which could explain the difference in behaviour seen in those two RTILs for the oxidation of HCl gas. This was not seen in the other four ionic liquids. In figure 6.2, the first scan for the electrochemical oxidation of 2.56 % HCl gas is also shown. It can be seen that in $[C_4mim][PF_6]$ the blank scan has peaks at -1 V and between 0 and -0.8 V which have much higher currents then the currents produced for the oxidation of HCl gas. These peaks could be due to the by-products of the 'destroyed' RTIL present in the RTIL after experiments with HCl gas.

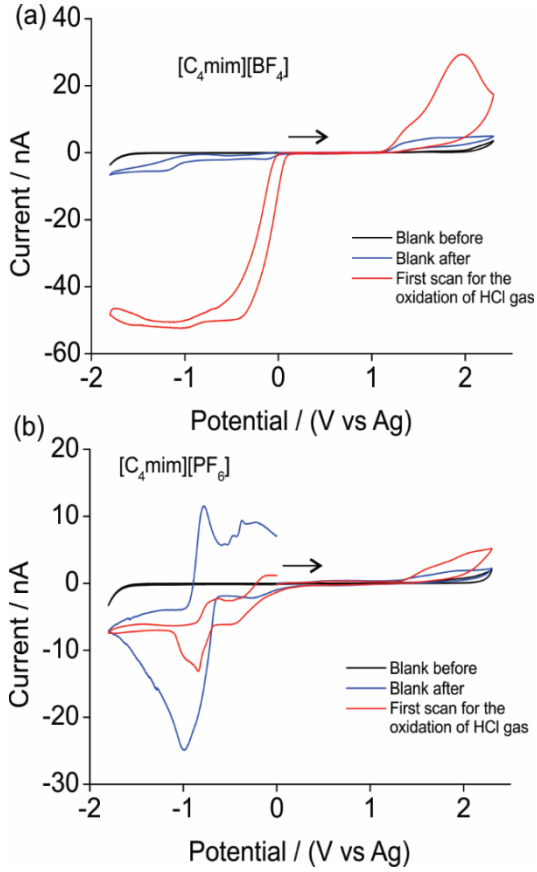

Figure 6.2: CV showing changes in blank scans for the oxidation of 2.56 % hydrogen chloride gas on a 8.3 µm radius Pt electrode in a) $[C_4mim][BF_4]$ and b) $[C_4mim][PF_6]$ at a scan rate 0.1 V/s. Black line is the blank scan before HCl gas was introduced into the T-cell and the blue line is blank scan after HCl gas experiments.

It has been reported that in the RTIL $[C_4mim][PF_6]$, acid catalysed decomposition of the anion is possible forming HF.[12,13] In the present work there are free H^+ ions that could possibly remove a fluorine atom from $[PF_6]^-$. Similar behaviour was observed in $[C_4mim][BF_4]$ due to the $[BF_4]^-$ anion but to a lesser extent. In order to further characterise the RTILs before and after experiments, nuclear magnetic resonance (NMR) spectroscopy was performed in an attempt to see structural changes in the RTILs. The NMR spectroscopy of $[C_4mim][PF_6]$ for ^{13}C, ^{1}H, ^{31}P and ^{19}F were performed and figure 6.3 shows the NMR spectra for ^{1}H, ^{31}P and ^{19}F (for full spectrum of these 3 elements and the spectrum for ^{13}C please see appendix A) before and after the electrochemical experiments. From the ^{1}H spectrum (chemical shift between 9 and 11.5) in figure 6.3b it can be seen that there are no features in the RTIL before experiments. However after electrochemical experiments with HCl it can be seen that at δ=11.5 ppm there are some features which can be attributed to hydrogen bonding.[14] Previous work performed by Shenderovich et al.[14] on HF and tetrabutylammonium fluoride attributed features between δ=10 and δ=17 to hydrogen bonding between a fluoride anion and the HF molecule. They also attributed the number of hydrogen bonds to decrease from 4 to 1 as the chemical shift increases from δ=10 to δ=17. In our case it is possible that there are up to 4 hydrogen bonds between the fluoride in $[PF_6]^-$ and an HF. For there to be HF molecules, H^+ ions needed to have removed fluorine from the $[PF_6]^-$. This was further supported by the NMR spectra of ^{31}P and ^{19}F (Figure 6.3a and c) where the ratio of the peaks before and after experiments were not the same, which suggests that PF_6 has become PF_{6-n} (where n is less than or equal to 5). This supports the suggestion that $[C_4mim][PF_6]$ has undergone a structural change and might not be suitable for HCl gas sensing

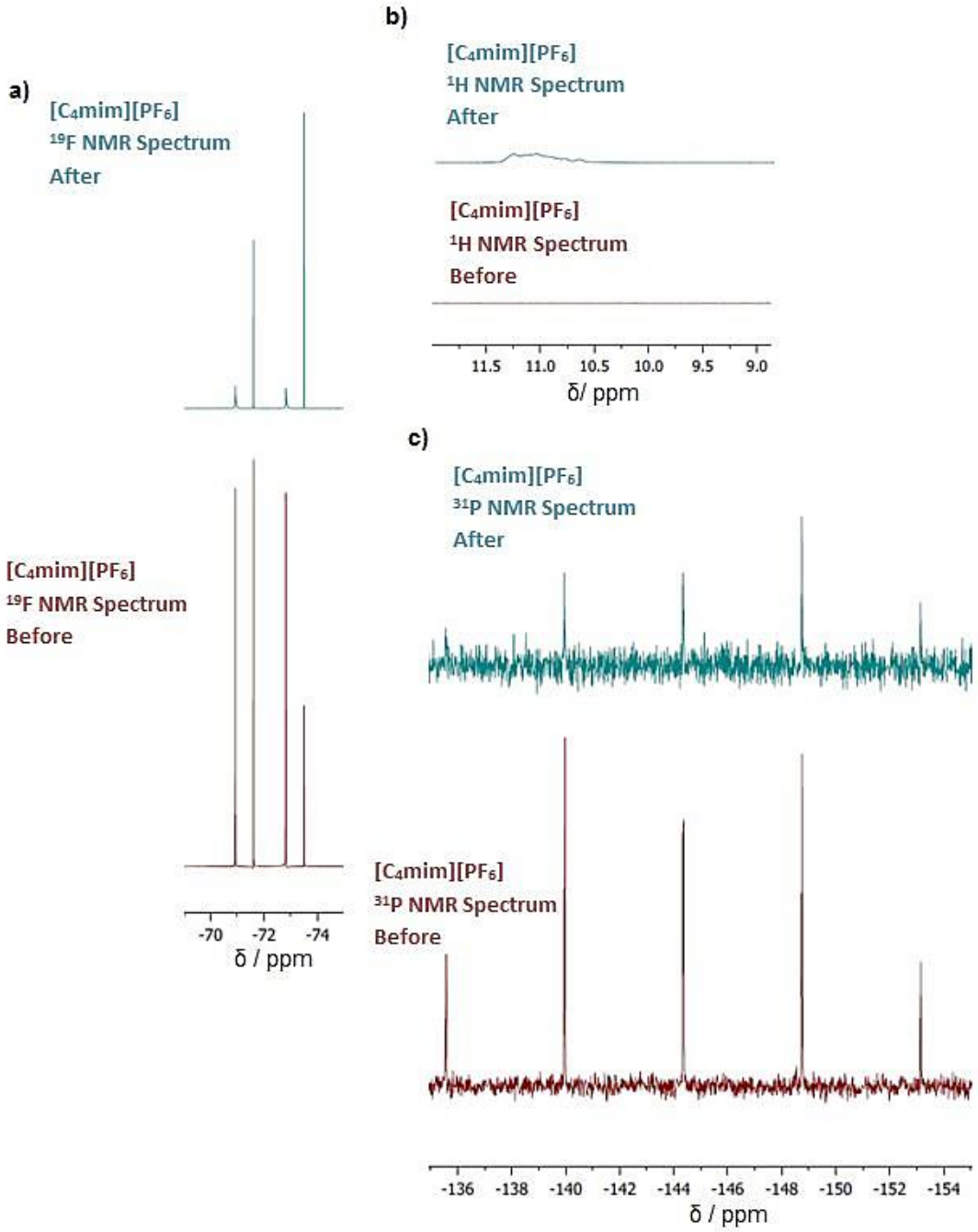

Figure 6.3: NMR signals for a) ^{19}F, b) ^{1}H and c) ^{31}P in the RTIL, $[C_4mim][PF_6]$ before and after experiments with HCl

The NMR spectra of ^{13}C, ^{1}H, ^{11}B and ^{19}F were obtained for $[C_4mim][BF_4]$ before and after experiments and there were no noticeable changes in the spectra which suggests that the NMR was not sensitive to pick up the signals if there were any changes to the structure of the RTIL. There were also no changes in the ^{13}C and ^{1}H

spectrum of $[C_2mim][NTf_2]$ before and after the experiments. This further supports the electrochemistry results that suggest that $[C_2mim][NTf_2]$ has not undergone a structural change after experiments with HCl gas.

6.3.2 Electrochemical Oxidation of Hydrogen Chloride Gas in RTILs at Various Scan Rates on a Pt Microelectrode

The behaviour of HCl gas in the RTILs follows a CE mechanism with a chemical step (C, dissociation of 2HCl to H^+ and $[HCl_2]^-$) followed by an electrochemical step (E). The CE process gives rise to the oxidation (peak I).

The reasonably high currents obtained at concentrations of 2.56 % in the gas phase (nitrogen fill) suggests high solubility of hydrogen chloride in $[C_2mim][NTf_2]$, $[C_4mim][NTf_2]$, and $[C_4mpyrr][NTf_2]$ (as seen for MA in chapter 4 and chlorine in chapter 5), which is very advantageous for sensing applications and will be explored later in section 6.3.4

To further investigate the electrochemical oxidation of HCl gas, scan rates study was performed in all the six RTILs for the first scan (figure 6.4) at a range of scan rates from 0.05 V/s to 2 V/s. It can be seen clearly that in all the voltammograms as the scan rates increase, the currents for all processes increases. Peaks II and IV, which were not very evident in figure 6.1 due to the lower scan rate used, became more evident at higher scan rates as shown in figure 6.4.

It can be seen that in the RTILs $[C_4mim][BF_4]$ and $[C_4mim][PF_6]$ process III is very different to the other RTILs. Process III is due to reduction of the protons and it has been mentioned by Silvester et al[13] that the stability of this process is based on various factors including the stability of the protonated anion and they did see slightly different behaviour in both of these RTILs. The scan rates study further

proves that the RTIL has undergone a change and therefore will not be discussed from a mechanistic point of view. These detrimental changes to both these RTILs suggest that they will not be ideal for solvents for the detection of HCl gas.

In the RTILs $[C_2mim][NTf_2]$, $[C_4mim][NTf_2]$, $[C_6mim][FAP]$ and $[C_4mpyrr][NTf_2]$ it can be clearly seen that process III splits into two peaks at high scan rates. This process is due to the reduction of the protons to form hydrogen gas (equation 6.4-6.6 6.6). This was clearly seen by Silvester et al.[13] and Aldous et al.[5] where the splitting was attributed to the two competing reactions (equations 6.4 and 6.6).

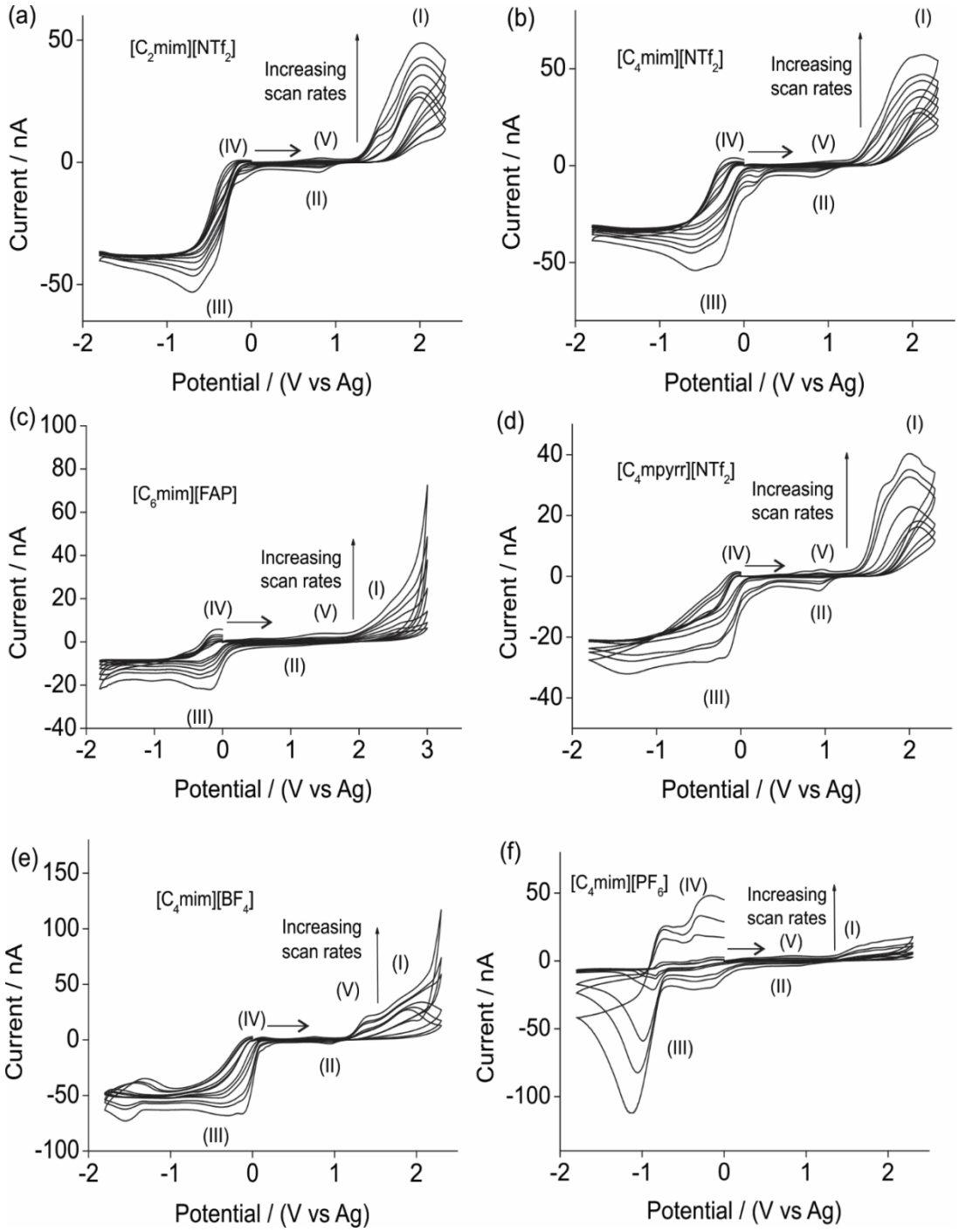

Figure 6.4: CVs for the oxidation (first scan) of 2.56 % hydrogen chloride gas on a 8.3 µm radius Pt electrode in a) $[C_2mim][NTf_2]$, b) $[C_4mim][NTf_2]$, c) $[C_6mim][FAP]$, d) $[C_4mpyrr][NTf_2]$, e) $[C_4mim][BF_4]$ and f) $[C_4mim][PF_6]$ at various scan rates between 0.05-2 V/s.

Figure 6.5 shows the electrochemical oxidation of HCl gas at various scan rates from 0.05 V/s to 2 V/s but this time for the second scan. Peak V which is due to the oxidation of the electrogenerated chloride, becomes clear in the second scan as mentioned in section 6.3.1. This process, together with all the other four processes, increases in current with increasing scan rates. Another point to note is that at higher scan rates (> 0.2 V/s) there is the appearance of a shoulder for peak I which is evident in the RTILs $[C_2mim][NTf_2]$, $[C_4mim][NTf_2]$ and $[C_4mpyrr][NTf_2]$ in the first scan (figure 6.1 a, b and d) which does not appear in the second scan. This could be due to process I (two electron oxidation of $[HCl_2]^-$), splitting into two one electron steps thereby forming an intermediate that undergoes an oxidation at higher potentials. All other features are the same in both the first and scan scans at varying scan rates.

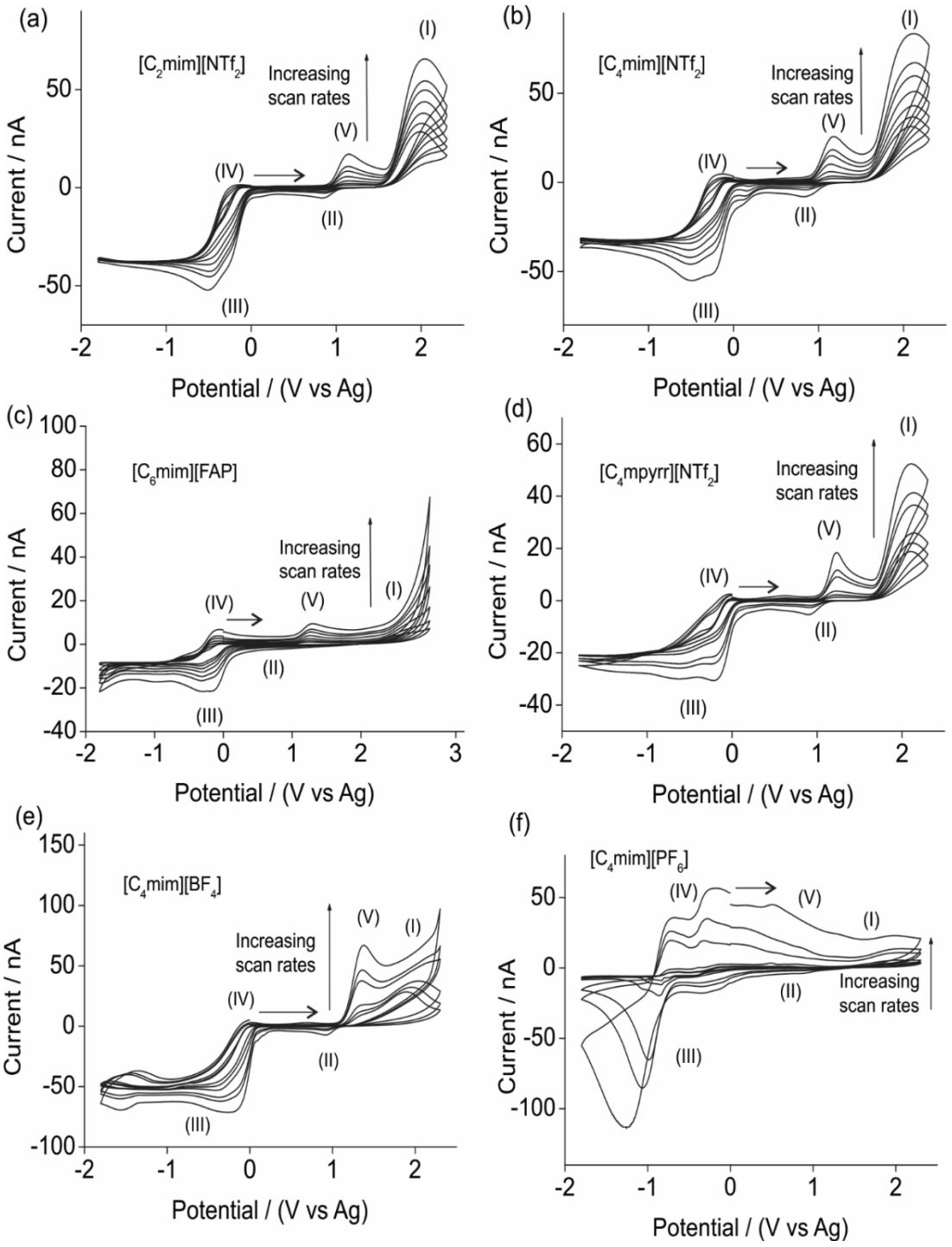

Figure 6.5: CV for the oxidation (second scan) of 2.56 % hydrogen chloride gas on a 8.3 µm radius Pt electrode in a) $[C_2mim][NTf_2]$, b) $[C_4mim][NTf_2]$, c) $[C_6mim][FAP]$, d) $[C_4mpyrr][NTf_2]$, e) $[C_4mim][BF_4]$ and f) $[C_4mim][PF_6]$ at various scan rates between 0.05-2 V/s.

Due to clear peaks being present in three of the RTILs ([C_2mim][NTf_2], [C_4mim][NTf_2] and [C_4mpyrr][NTf_2]), further mechanistic studies were only performed on them. The current obtained for oxidative process I (first scan and second scan), oxidative process V (second scan) and reductive process III (first scan) for the three RTILs ([C_2mim][NTf_2] (figure 6.6), [C_4mim][NTf_2] (figure 6.7) and [C_4mpyrr][NTf_2] (figure 6.8)) at the various scan rates was plotted against the square root of scan rate. In all figures it can be seen clearly seen that the plots do not go through zero. This is a common feature of voltammetry at microelectrodes in RTILs.[15]

It can be seen that the plot of $[HCl_2]^-$ oxidation peak currents for the second scan (b) have a higher R^2 value for the line of best fit as compared to the first scan (a) for all three ionic liquids . This is probably due to the onset of the pre peak just before peak I, at higher scan rates which is only evident at the first scan, which is influencing the peak current. This pre peak is very much more obvious in the RTIL [C_4mpyrr][NTf_2] (figure 6.4) and it shows in the plot of current vs square root of scan rate (figure 6.8a) where the line of best fit had the lowest R^2 value.

In all three figures it can be seen that good linearity is achieved with R^2 values of approximately 0.99 (except in the case of figure 6.8a), suggesting that the electrochemical processes occurring are most likely diffusion controlled (plots of peak current vs scan rate (not shown) showed lesser linearity (lower R^2 values)). It is important to mention here that due to the many processes occurring on the electrode surface the currents produced for each process are heavily influenced by the other processes.

Chronoamperometric transients were performed on 0.15 % HCl gas in the RTIL $[C_2mim][NTf_2]$ by stepping up from 0 V to 2.3 V and the experimental data was attempted to be fitted with the Shoup and Szabo[16] expression but as expected fitting was not possible due to the complexity of the processes occurring and the dependence of the current on other processes.

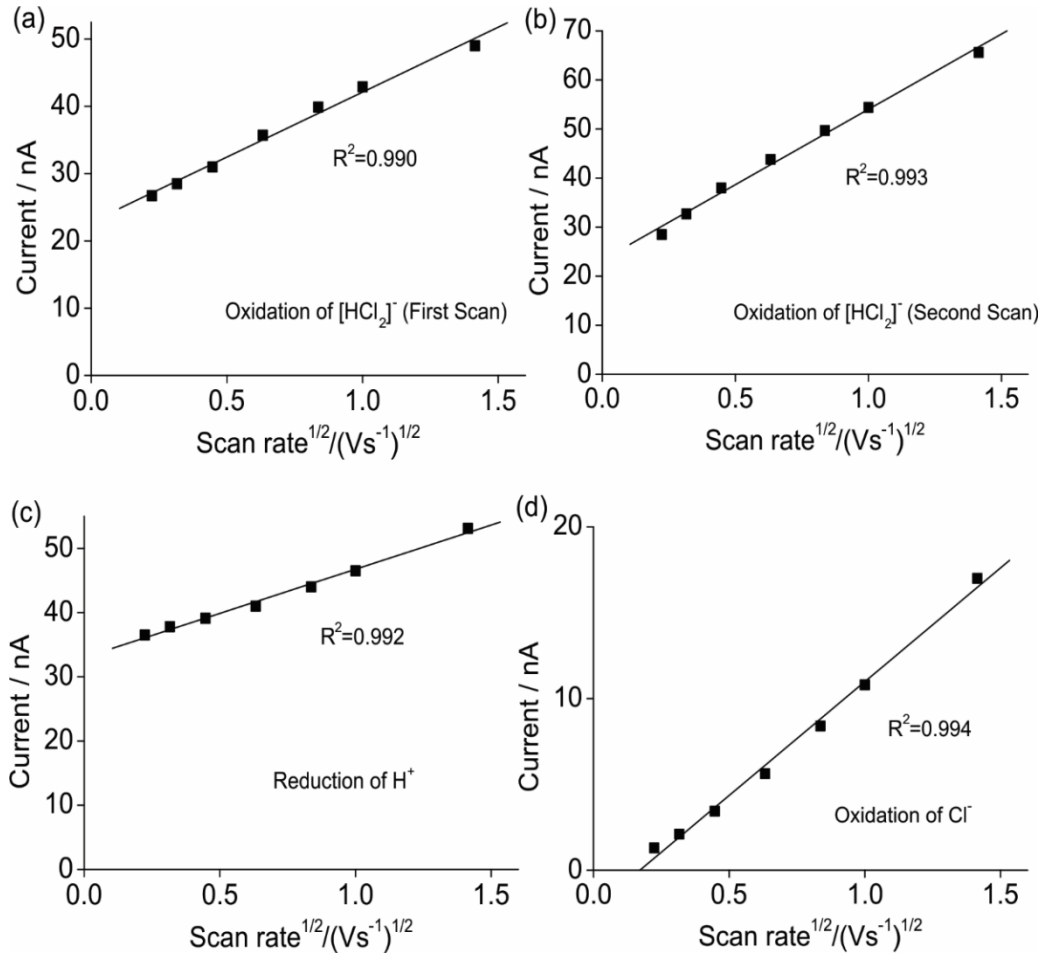

Figure 6.6: Plot of currents vs square root of scan rates in $[C_2mim][NTf_2]$ on a Pt microelectrode (diameter 8.3 µm) for a) $[HCl_2]^-$ oxidation during first scan, b) $[HCl_2]^-$ oxidation during second scan, c) H^+ reduction and d) Cl^- oxidation

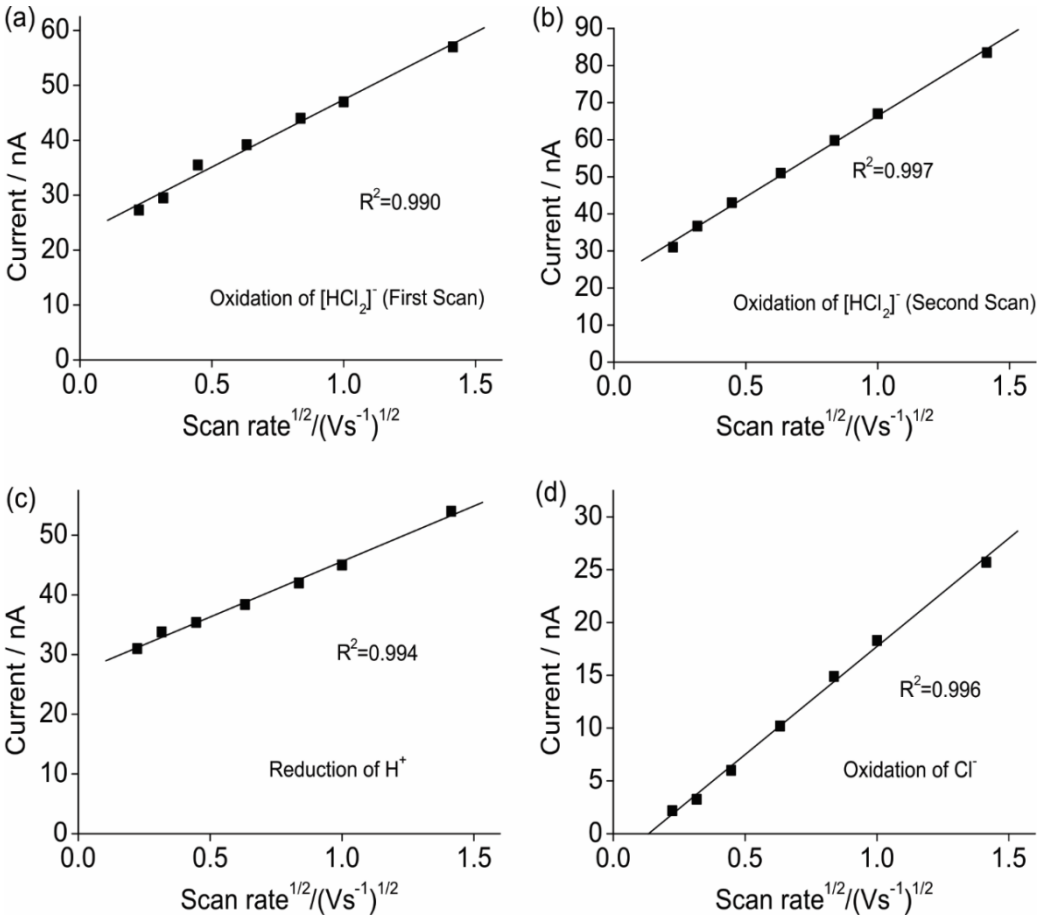

Figure 6.7: Plot of currents vs square root of scan rates in $[C_4mim][NTf_2]$ on a Pt microelectrode (diameter 8.3 µm) for a) $[HCl_2]^-$ oxidation during first scan, b) $[HCl_2]^-$ oxidation during second scan, c) H^+ reduction and d) Cl^- oxidation

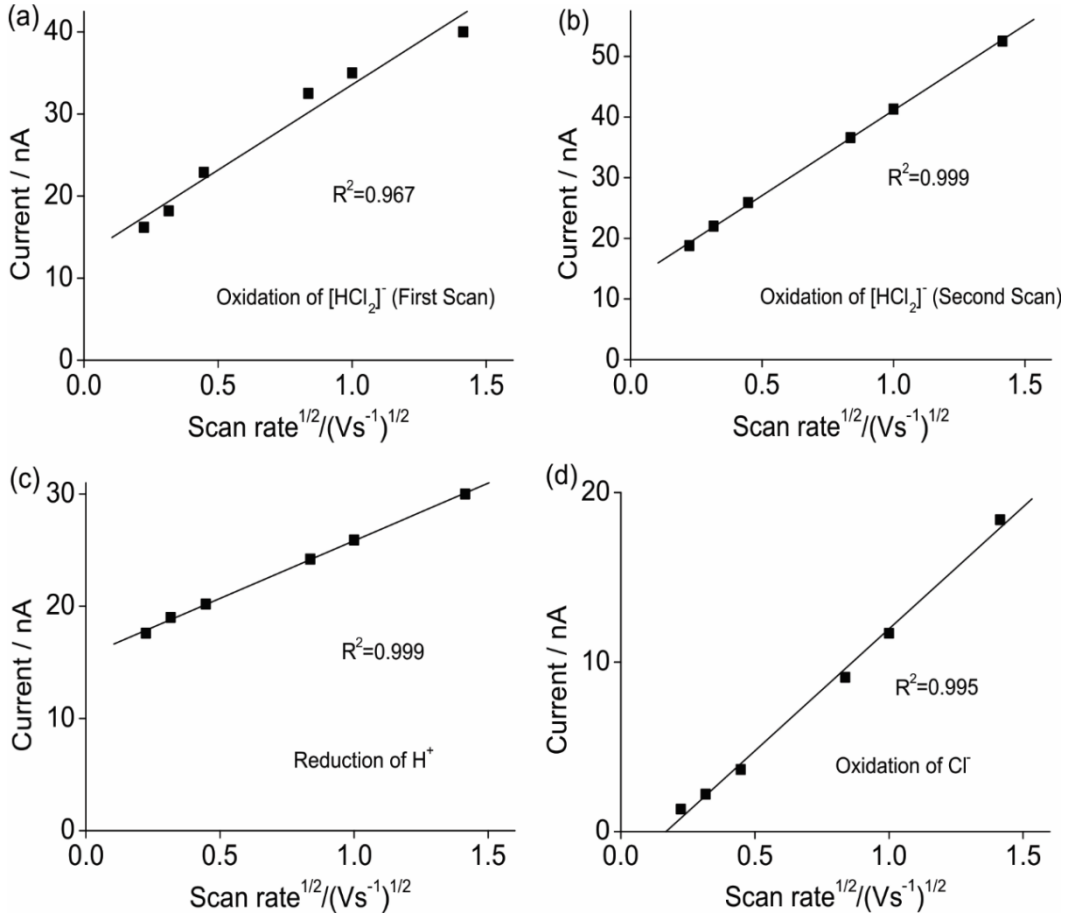

Figure 6.8: Plot of currents vs square root of scan rates in $[C_4mpyrr][NTf_2]$ on a Pt microelectrode (diameter 8.3 µm) for a) $[HCl_2]^-$ oxidation during first scan, b) $[HCl_2]^-$ oxidation during second scan, c) H^+ reduction and d) Cl^- oxidation

As mentioned previously, in RTILs HCl gas is thought to be in its dissociated form of H^+ and $[HCl_2]^-$. Therefore, when initially scanned in a negative direction, H^+ ions which are already present in the RTIL should get reduced. Experiments at different scan rates were performed in $[C_2mim][NTf_2]$ where the CVs were obtained by scanning negative first (figure 6.9) followed by a full scan (0.4 V to -1.8 V to 2.3 to -1.8 and to 0 V). As predicted, there are free H^+ ions which get reduced (red scan figure 6.9) first and then the CV looks very similar to the CV in figure 6.1a where all the processes are clear and well defined. However by scanning up to 2.3 V, more H^+ ions are being produced (Equation 6.2) therefore it would be expected that the 2nd reduction scan (black) would produce a higher current compared to the first scan (red

scan) but this was only evident at the higher scan rates (0.7 V/s to 4 V/s). Figure 6.10 shows a plot of the normalised current (current for 2nd process (black line) divided by current for the 1st process (red line)) vs the scan rate. From the plot it can be seen that the normalised current is negligible at low scan rates. This behaviour could be explained by the fact that at low scan rates the timescale of the experiment is much longer, therefore the H^+ species that were produced in the oxidation peak I (black scan) have diffused away from the electrode and are not visible when scanned negative. However at high scan rates, since the timescale of the experiment is much shorter, there is insufficient time for the diffusion of the species, therefore higher currents are produced in the 2nd scan to show the reduction of more H^+ ions (addition of both currents produced from the protons already present in the RTIL and the protons produced as a result of process I).

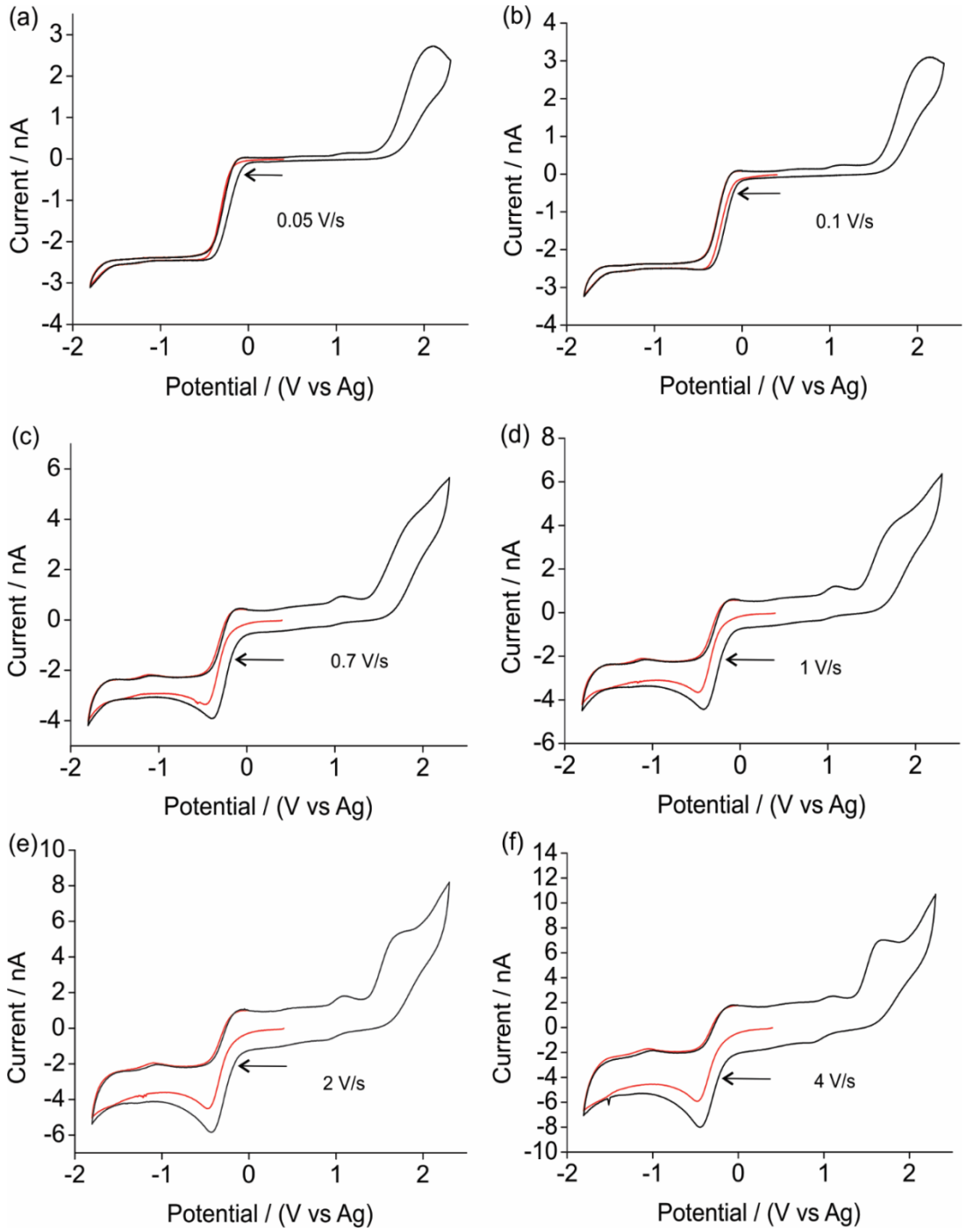

Figure 6.9: CV for the oxidation (second scan) of 0.15 % HCl gas on a 8.3 µm radius Pt electrode in $[C_2mim][NTf_2]$ at various scan rates of a) 0.05 V/s, b) 0.1 V/s, c) 0.7 V/s, d) 1 V/s, e) 2 V/s and f) 4 V/s. Red CV shows scanning negative first (0.4 V to -1.8 V to 0 V). The black CV shows the continuation of the scan (0 V to 2.3 V to -1.8 V and to 0 V).

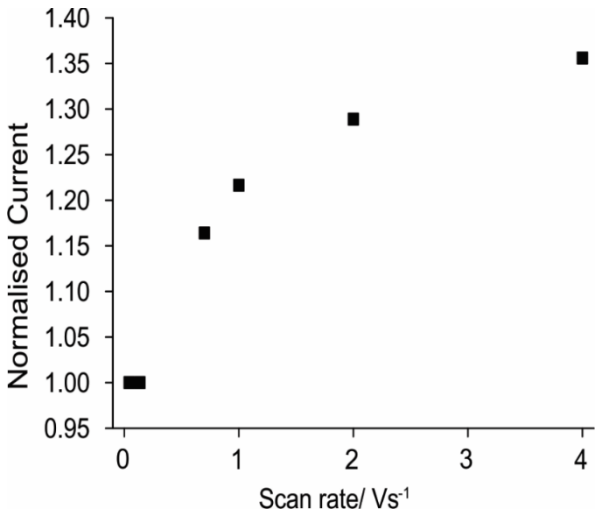

Figure 6.10: Plot of normalised current (absolute current for peak III, first scan (black scan)/absolute current for peak III, second scan (red scan)) vs the scan rate obtained from figure 6.9

6.3.3 Analytical Utility of HCl Gas in $[C_2mim][NTf_2]$

Once the fundamental behaviour was understood, the analytical utility of hydrogen chloride was studied in one RTIL $[C_2mim][NTf_2]$ due to all redox processes being clearly defined and also due to the fastest gas saturation time as it is the least viscous RTIL. Voltammetry was recorded at a scan rate of 0.1 V/s. Figure 6.11 shows typical CVs of six different concentrations of hydrogen chloride on a Pt microelectrode for both the first and second scan for each concentration. It can be seen that on the second scan there is a slight increase in the peak current for process I and this is due to the contribution of the oxidation of chloride (process V). On both graphs it can be seen that as the concentration increases, the currents of all processes increases. However a measurable increase is seen only for process I (oxidation of $[HCl_2]^-$) and III (reduction of protons). Therefore a calibration graph was obtained for both these two processes (for process I the current for the first scan was taken) and they are shown in figure 6.12. It can be seen that a linear behaviour is observed with R^2 values of > 0.99, and sensitivities/gradients of 1.99×10^{-12} and 1.75×10^{-12} A/ppm, for process I and process III respectively. Due to the complicated oxidation

mechanism, it was originally unclear if the calibration plots would be linear, however, excellent linearity was observed which is very important for sensing applications. Limit of detections (LODs) (3σ) of 102 and 69 ppm were obtained for process I and process III, respectively, which clearly shows that RTILs can be used as a solvent for the electrochemical detection of low concentrations hydrogen chloride. However at low concentrations (104, 168 ppm and 242 ppm) it was very hard to determine the peak current for process I as a clear well defined peak was not observed but there were no such issues with process III. This together with the LODs obtained suggests that to determine the concentrations of HCl using the currents obtained from the reduction of protons might be a better alternative. Furthermore there was also some curvature for process I which could be due to the difficulties in measuring the peak current and that will increase the LOD as compared to a straight line.

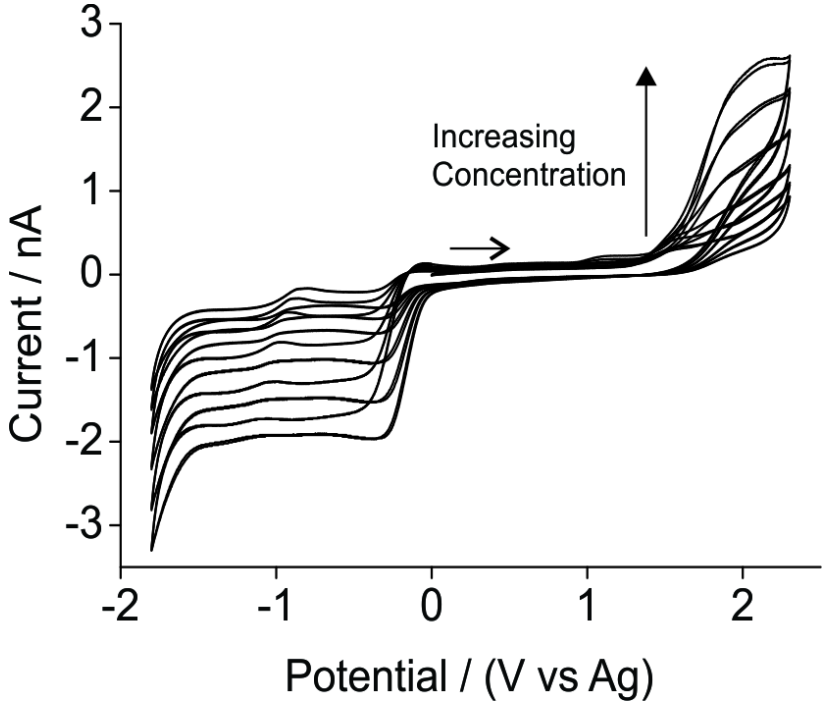

Figure 6.11: CV (first and second scan) for the oxidation of different concentrations (104, 168, 242, 431, 710 and 1048 ppm) of HCl gas on a 8.3 µm radius Pt electrode in $[C_2mim][NTf_2]$at a scan rate 0.1 V/s.

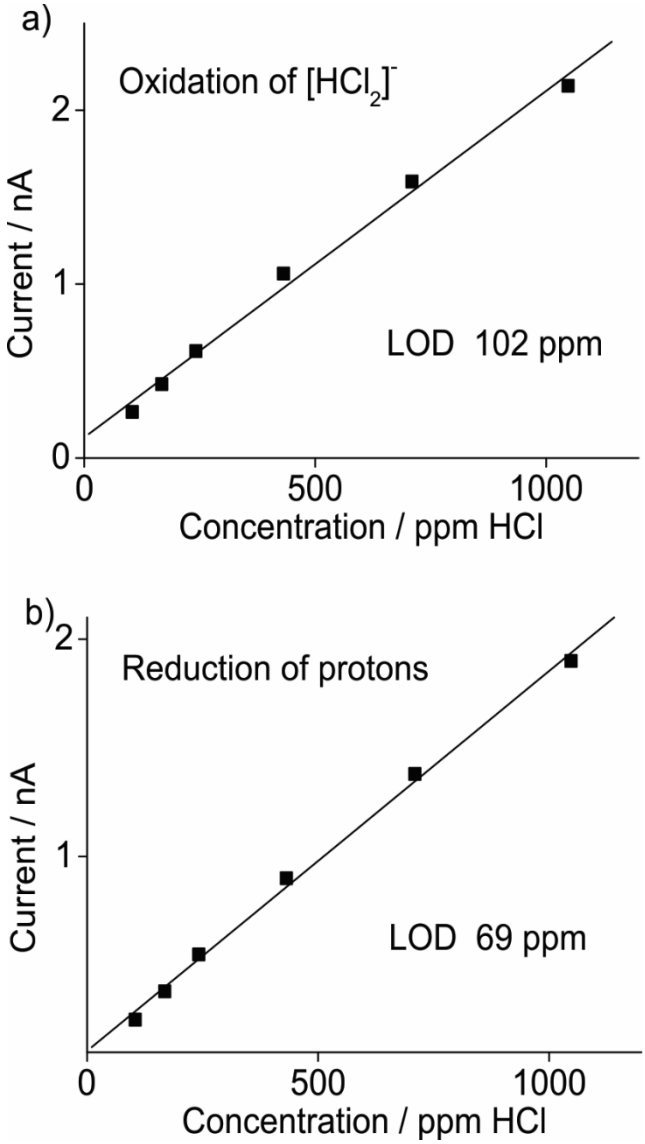

Figure 6.12: Calibration graph of peak current for a) process I (first scan) and b) process III vs gas phase concentration obtained from the CVs for the oxidation of different concentrations (104, 168, 242, 431, 710 and 1048 ppm) of HCl gas on a 8.3 µm radius Pt electrode in $[C_2mim][NTf_2]$.

Due to the difficulties in measuring the peak current for process I at low concentrations, differential pulse voltammetry (DPV), which is a more sensitive technique compared to cyclic voltammetry, was used to obtain a calibration graph. DPV is a technique where a series of potential pulses of fixed amplitude is applied and the current is measured at two points for each pulse, one just before the pulse is applied and the other at the end of the pulse which allows for the decay of the non-

Faradaic current. This difference in current is plotted against the potential. The major advantage of using DPV is to lower the impact of the charging current thereby increasing the sensitivity of the Faradaic current due to the analyte. Figure 6.13a shows DPVs for process I (oxidation of $[HCl_2]^-$) for the same six concentrations as used in figure 6.11. The optimised parameters for the DPV were amplitude of 0.075 V with a modulation time of 0.025 s and an interval time of 0.05 s. The initial potential was 1 V and the end potential was 2.3 V. It can be seen from figure 6.13a that one clear peak at approximately 1.8 V is seen and its current increases with an increase in concentration. The peak is very well defined as compared to the CV method, which was expected due to reduction of the capacitive charging current. The peak current was then plotted with respect to the concentration to obtain a calibration graph as shown in figure 6.11b. Excellent linearity was observed and a LOD (3σ) of 71 ppm was obtained with a sensitivity of 4.95×10^{-13} A/ppm. The improved LOD (as compared to the CV) obtained suggests that DPV might be a better technique to investigate the oxidation of $[HCl_2]^-$ for analytical purposes.

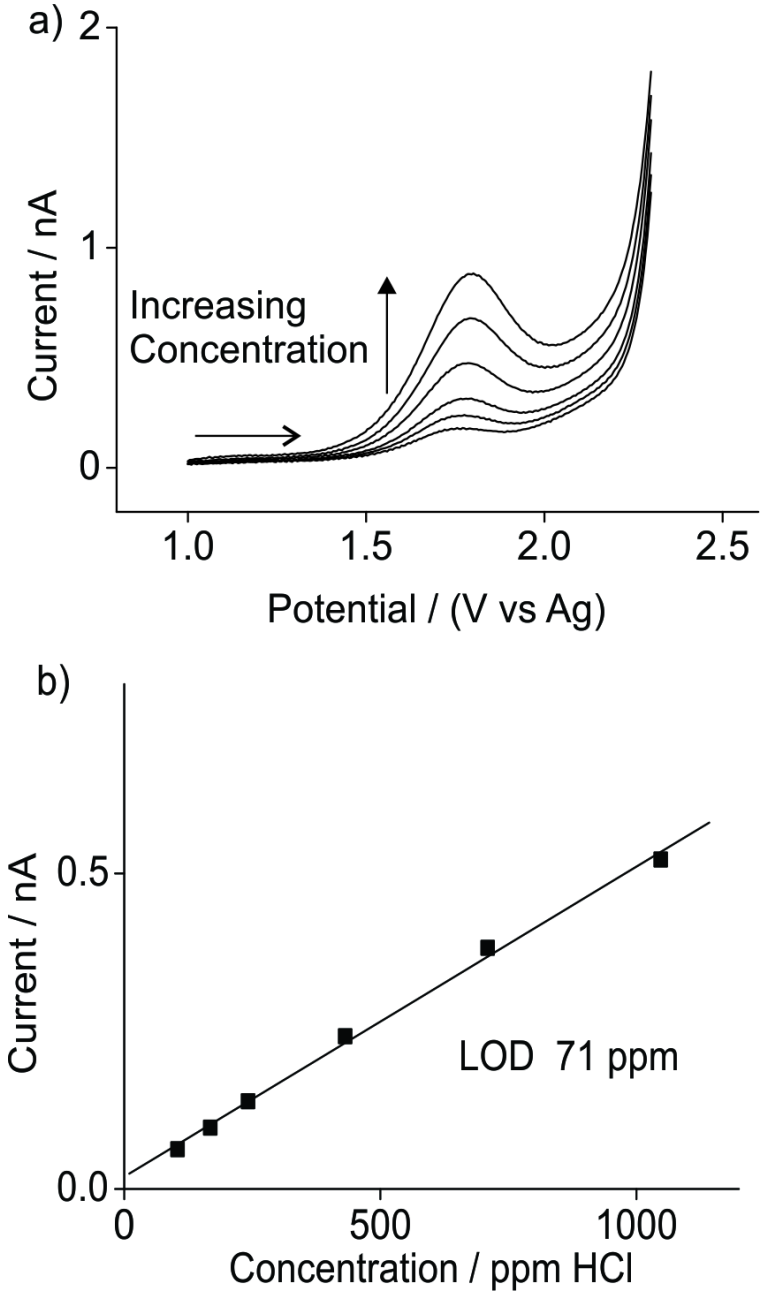

Figure 6.13: a) DPV and b) calibration graph of peak current for process I vs gas phase concentration obtained from the DPVs for the oxidation of different concentrations (104, 168, 242, 431, 710 and 1048 ppm) of hydrogen chloride gas on a 8.3 µm radius Pt electrode in $[C_2mim][NTf_2]$

6.4 Conclusions

The electrochemical behaviour of hydrogen chloride gas has been studied in various RTILs. In some RTILs a similar behaviour is observed where in the first CV scan four peaks were present and in the second scan five peaks are present. Due to the

complicated mechanism, where there is a chemical step before the electrochemical step chronoamperometric analysis/fitting was not possible. Three of the RTILs were deemed not suitable for HCl gas sensing; $[C_6mim][FAP]$ due to the oxidation peak not being clear, $[C_4mim][BF_4]$ and $[C_4mim][PF_6]$ because of possible reaction of HCl (or its reaction by-products) with the RTIL. NMR spectroscopy confirmed that $[C_4mim][PF_6]$ underwent structural changes after HCl electrochemical experiments.

The analytical utility was studied in $[C_2mim][NTf_2]$. Linear calibration graphs were obtained and a LOD of 102 ppm was obtained when the currents were acquired from the oxidation of $[HCl_2]^-$. At low concentrations it was hard to differentiate the oxidation peak using CVs therefore DPV was employed and a lower LOD of 71 ppm was obtained which suggests that DPV could be used as another analytical tool to sense HCl. An alternative method of sensing HCl gas has also been proposed where the reduction of protons were analysed and a LOD of 69 ppm was obtained when this method was used. This could be a more viable method to detect HCl gas due to the oxidation of $[HCl_2]^-$ being at very high potentials and very complicated where there are numerous processes occurring on the electrode surface.

6.5 References

(1) Arnáiz, F. J. A Convenient way to generate hydrogen chloride in the freshman lab. *J. Chem. Educ.* **1995**, *72*, 1139.
(2) Association, C. G.: *Handbook of compressed gases*; Springer US, 1999.
(3) Pohanish, R. P.: *Sittig's handbook of toxic and hazardous chemicals and carcinogens: A-K*; Elsevier, 2012.
(4) O'Neil, M. J.: *The Merck index: An encyclopedia of chemicals, drugs, and biologicals*; Royal Society of Chemistry, 2013.
(5) Aldous, L.; Silvester, D. S.; Pitner, W. R.; Compton, R. G.; Lagunas, M. C.; Hardacre, C. Voltammetric studies of gold, protons, and $[HCl_2]^-$ in ionic liquids. *J. Phys. Chem. C* **2007**, *111*, 8496-8503.
(6) Bonhôte, P.; Dias, A.-P.; Papageorgiou, N.; Kalyanasundaram, K.; Grätzel, M. Hydrophobic, highly conductive ambient-temperature molten salts. *Inorg. Chem.* **1996**, *35*, 1168-1178.

(7) MacFarlane, D. R.; Meakin, P.; Sun, J.; Amini, N.; Forsyth, M. Pyrrolidinium imides: A new family of molten salts and conductive plastic crystal phases. *J. Phys. Chem. B* **1999**, *103*, 4164-4170.
(8) Sharp, M. Determination of the charge-transfer kinetics of ferrocene at platinum and vitreous carbon electrodes by potential steps chronocoulometry. *Electrochim. Acta* **1983**, *28*, 301-308.
(9) Ji, X.; Silvester, D. S.; Aldous, L.; Hardacre, C.; Compton, R. G. Mechanistic studies of the electro-oxidation pathway of ammonia in several room-temperature ionic liquids. *J. Phys. Chem. C* **2007**, *111*, 9562-9572.
(10) Murugappan, K.; Kang, C.; Silvester, D. S. Electrochemical oxidation and sensing of methylamine gas in room temperature ionic liquids. *J. Phys. Chem. C* **2014**, *118*, 19232-19237.
(11) Huang, X.-J.; Rogers, E. I.; Hardacre, C.; Compton, R. G. The reduction of oxygen in various room temperature ionic liquids in the temperature range 293−318 K: Exploring the applicability of the Stokes−Einstein relationship in room temperature ionic liquids. *J. Phys. Chem. B* **2009**, *113*, 8953-8959.
(12) Swatloski, R. P.; Holbrey, J. D.; Rogers, R. D. Ionic liquids are not always green: hydrolysis of 1-butyl-3-methylimidazolium hexafluorophosphate. *Green Chem.* **2003**, *5*, 361-363.
(13) Silvester, D. S.; Aldous, L.; Hardacre, C.; Compton, R. G. An electrochemical study of the oxidation of hydrogen at platinum electrodes in several room temperature ionic liquids. *J. Phys. Chem. B* **2007**, *111*, 5000-5007.
(14) Shenderovich, I. G.; Smirnov, S. N.; Denisov, G. S.; Gindin, V. A.; Golubev, N. S.; Dunger, A.; Reibke, R.; Kirpekar, S.; Malkina, O. L.; Limbach, H.-H. Nuclear magnetic resonance of hydrogen bonded clusters between F^- and $(HF)_n$: Experiment and theory. *Ber. Bunsenges. Phys. Chem* **1998**, *102*, 422-428.
(15) Buzzeo, M. C.; Evans, R. G.; Compton, R. G. Non-haloaluminate room-temperature ionic liquids in electrochemistry--a review. *ChemPhysChem* **2004**, *5*, 1106-1120.
(16) Shoup, D.; Szabo, A. Chronoamperometric current at finite disk electrodes. *J. Electroanal. Chem. Interfacial Electrochem.* **1982**, *140*, 237-245.

7. Screen Printed Electrodes for the Detection of Methylamine, Chlorine and Hydrogen Chloride Gas

Commercially available screen printed electrodes (SPEs) have been utilised in this work in order to investigate their suitability for gas detection. Physical characterisation using scanning electron microscopy (SEM) and X-ray photoelectron spectroscopy (XPS) were performed on these surfaces. SEM revealed the differences in porosity and surface roughness of the various working electrode surfaces. XPS identified some elements present on the working electrode surfaces which are likely due to the materials used in the screen printing process. The electrochemical behaviour of methylamine, chlorine and hydrogen chloride gas has been investigated in the RTIL $[C_2mim][NTf_2]$ on various screen printed electrodes (Pt, Au, C and, in the case of chlorine, carbon nanotubes and graphene modified C) using cyclic voltammetry. Among the SPEs studied, Pt SPE was found to give the best analytical response for all three toxic gases. The electrochemical behaviour of these three target gases obtained on these Pt SPEs was compared with the Pt microelectrodes (studied in chapter 4, 5 and 6) and similar behaviour was observed with comparable limit of detections, indicating that Pt SPEs could be used as cheap alternatives for amperometric gas sensing. On Au SPEs, issues such as impurity peaks and reaction with electrochemically generated products make them unattractive for the detection of these three gases. On the carbon surfaces, a large capacitance was observed which is not favourable for sensing purposes as it may swamp the favourable Faradaic (analytical) current.

7. SCREEN PRINTED ELECTRODES FOR THE DETECTION OF METHYLAMINE, CHLORINE AND HYDROGEN CHLORIDE GAS 159

7.1 Introduction 162

7.2 Experimental 164

7.2.1 Chemical Reagents 164

7.2.2 Electrochemical Experiments 164

7.2.3 Scanning Electron Microscopy Experiments 165

7.2.4 X-Ray Photoelectron Spectroscopy Experiments 165

7.2.5 Gas Mixing Setup 166

7.3 Physical Characterisation of SPEs 166

7.3.1 SEM 166

7.3.2 XPS 168

7.3.2.1 Pt SPE 168

7.3.2.2 Au SPE 172

7.3.2.3 C SPE 177

7.4 Methylamine Gas 181

7.4.1 Electrochemical Oxidation of Methylamine Gas on Pt SPEs 181

7.4.2 Analytical Utility of Methylamine Gas on Pt SPEs 183

7.4.3 Electrochemical Behaviour and Analytical Utility of Methylamine Gas on Au and C SPEs 185

7.5 Chlorine Gas 187

7.5.1 Electrochemical Reduction of Chlorine Gas on Pt SPEs 187

7.5.2 Analytical Utility of Chlorine Gas on Pt SPEs 189

7.5.3 Electrochemical Behaviour and Analytical Utility of Chlorine gas on Au, C, Graphene Modified C and Carbon Nanotubes Modified C SPEs 191

7.6 Hydrogen Chloride Gas 193

7.6.1 Electrochemical Oxidation of Hydrogen Chloride Gas on Pt SPEs 193

7.6.2 Analytical Utility of Hydrogen Chloride Gas on Pt SPEs 201

7.6.3 Electrochemical Behaviour of Hydrogen Chloride Gas on Au and C SPEs 204

7.7 Comments about the Reproducibility, Reusability and Advantages of SPEs 206

7.8 Conclusions 207

7.9 References 208

Work presented in this section has been published in the Journal of Physical Chemistry C, titled, “Electrochemical Behaviour of Chlorine on Platinum Microdisk and Screen Printed Electrodes in a Room Temperature Ionic Liquid” and also in the Journal, Sensors titled, “Sensors for Highly Toxic Gases: Methylamine and Hydrogen Chloride Detection at Low Concentrations in an Ionic Liquid on Pt Screen Printed Electrodes”.

7. Screen Printed Electrodes for the Detection of Methylamine, Chlorine and Hydrogen Chloride Gas

7.1 Introduction

Miniaturization has been the driving force for many industries and the electrochemistry industry is no different. ‘Lab-on-a-chip’ type designs have become increasingly more popular for amperometric gas sensors (AGSs). Being able to have low cost disposable portable sensors has been the motivating stimulus and screen printing technology is a platform for the fabrication of chemical sensors with those properties.[1,2] In screen printing technology a fluid containing many different substances such as graphite, carbon black and polymeric binders is squeezed through a mesh screen which defines the shape and size of the electrode.[3] Not only will the usage of screen printed electrodes (SPEs) in AGSs improve portability but it will also take a great leap towards cheaper manufacturing cost due to the smaller amount of expensive precious material/metal (e.g. Pt/Au) required by miniaturization of the solid electrode. Another advantage that can be exploited by using these SPEs is the much smaller volume of electrolyte (e.g. thin layer) needed, which would allow faster response times and greater sensitivity. Previous work on ammonia[4] and

oxygen[5] gas sensing on these SPEs have already been done and shown that reasonable limit of detections (LODs) are observed.

In the previous chapters the electrochemical behaviour of three toxic gases, namely methylamine, chlorine and hydrogen chloride, have been investigated in room temperature ionic liquids (RTILs) on conventional electrodes. In this chapter various SPEs bought from Dropsens (Oviedo, Spain) will be investigated for their suitability in detecting these gases by using RTILs as the solvent of choice. It is important to note here that RTILs are ideal solvents to be used in conjunction with SPEs. If conventional aqueous solvents are used with SPEs, due to the small amount of solvent (10 µl) that is used they will evaporate quickly over time. Therefore by using RTILs and exploiting their negligible vapour pressure property which means they don't evaporate, more robust sensors can be made. Hence it can be said that RTILs and SPEs work hand in hand in improving the robustness and cost of AGSs.

In this work, mechanistic studies will first be performed to see if the electrochemical behaviour of these toxic gases on SPEs are similar to conventional electrodes, and then their analytical utility will also be studied so that a direct comparison of LODs can be made with conventional electrodes in the RTIL $[C_2mim][NTf_2]$. It is important to note that in previous work, the reduction of oxygen on SPEs was different to that on microelectrodes in this RTIL (reaction of the reduction product with the materials in the SPE paste) and indicated that the detection of oxygen on Pt SPEs may not be feasible for long-term studies.[5] All experiments in this chapter were conducted with the RTIL $[C_2mim][NTf_2]$, which has a high intrinsic conductivity and it is one of the least viscous ionic liquid, hence a faster response can be obtained. It has also been shown in the previous chapters that on a platinum microelectrode a linear current response can be obtained for all three toxic gases in $[C_2mim][NTf_2]$.

The SPEs will be first characterised using two well-known characterisation techniques, scanning electron microscopy (SEM) and X-ray photoelectron spectroscopy (XPS).

7.2 Experimental

7.2.1 Chemical Reagents

1-ethyl-3-methylimidazolium bis(trifluoromethylsulfonyl)imide ($[C_2mim][NTf_2]$) was synthesized according to standard literature procedures[6,7] and kindly donated by the group of Professor Christopher Hardacre at Queens University, Belfast and was used as received. Ultra-pure water with a resistance of 18.2 MΩ cm prepared by an ultra-pure laboratory water purification system (Millipore Pty Ltd., North Ryde, NSW, Australia) and acetonitrile (MeCN, Sigma–Aldrich, 99.8 %) were used for washing the electrodes after use with RTILs. Methylamine (0.2 % nitrogen fill), chlorine gas (0.2 % and 4.5 %, nitrogen fill) and hydrogen chloride gas (0.2 % nitrogen fill) was purchased from CAC gases (Auburn, NSW, Australia). High purity nitrogen gas (99.9 %) was purchased from BOC gases (North Ryde, NSW, Australia) and used as a carrier gas.

7.2.2 Electrochemical Experiments

Five SPEs employed in this study were purchased from DropSens (DRP-110, DRP-550, DRP-220AT, DRP-110CNT, DRP-110GPH, Oviedo, Spain). The SPEs consists of a three electrode set-up with a working, counter and reference electrodes. The working electrode (WE) surfaces employed in this study were platinum, gold, carbon and carbon modified with carbon nanotubes and graphene. A silver quasi-reference electrode was used in all the five SPEs. The counter electrode (CE) was typically made from the same material as the WE surface (e.g Pt for Pt SPEs, Au for Au SPEs and C for C and C-modified SPEs). The SPEs were housed in a glass “T-cell”

previously used to study ammonia[4] and oxygen[5] and have been described in the experimental chapter (chapter 3). The SPEs were used as is without any activation/precleaning as this represents the conditions required in the real world.

7.2.3 Scanning Electron Microscopy Experiments

SEM characterisation of the SPEs employed in this work was performed using a Tescan Mira3 FESEM. An accelerating voltage of 5 kV and working distance of ~ 5 mm was used at different magnifications. The SPEs were placed in the sample holder without any sample preparation (e.g. platinum coating) since the surfaces were sufficiently conductive.

7.2.4 X-Ray Photoelectron Spectroscopy Experiments

All XPS experiments were performed with Dr Kane O'Donnell from the Department of Physics, Astronomy and Medical Radiation Science, Curtin University. XPS analysis was performed on a Kratos AXIS Ultra DLD using Al K α radiation as the X-Ray source. The SPEs were first cut into smaller pieces to reveal only the working electrode surfaces and a small section of the polymer that is coated on top of the silver leads. The polymer was then scratched to reveal the silver leads. The prepared electrode was mounted onto the sample stage using conductive carbon tape. Silver conducting paint was used to make electrical contact from the silver leads to the sample stage. Scans for the full spectrum were performed between 0 and 1200 eV binding energy. Once elements were identified using the wide spectrum, high resolution elemental scans were performed to obtain more information on the behaviour of these elements. CasaXPS, a commonly used software program to analyse XPS data, was then used to plot and analyse the peaks. Fingerprinting of

peaks was performed using the National Institute of Standards and Technology (NIST) X-ray photoelectron spectroscopy database.

7.2.5 Gas Mixing Setup

Please see previous chapters (chapter 3, 4, 5 and 6) for the gas mixing setup used for each gas.

7.3 Physical Characterisation of SPEs

7.3.1 SEM

SEM provides high resolution imaging of the topography of the SPE electrode surfaces and also size and distribution of particles on the surface. Figures 7.1 and 7.2 show topographic images of the working electrode surfaces of the different SPEs (Pt, Au, C, C-Graphene and C-CNTs,) at magnifications of 2000 × and 10000 ×. On the platinum surface (figures 7.1a and 7.2a) the dark patches are the holes and the white patches are the Pt particles. It can be seen that the Pt surface is very porous and rough. On the Au surface (figure 7.1b and 7.2b) there are tiny crystalline structures that correspond to gold crystals. On the C and the CNT modified C surface (figure 7.1 c and e and 7.2 c and e) it can be seen clearly that the surface is very flaky and suggests that there might not be good adhesiveness to the substrate. The unique difference between these two surfaces is that the CNT modified surfaces look more ‘fibrous’ which is due the presence of the carbon nanotubes. On the graphene modified carbon surface (figure 7.1d and 7.2d) there are numerous flaky graphene particles that are covering the whole carbon surface. It is obvious from these images that the porosity and roughness of the working electrode surfaces are different for each SPE and this might have an impact on the electrochemistry.

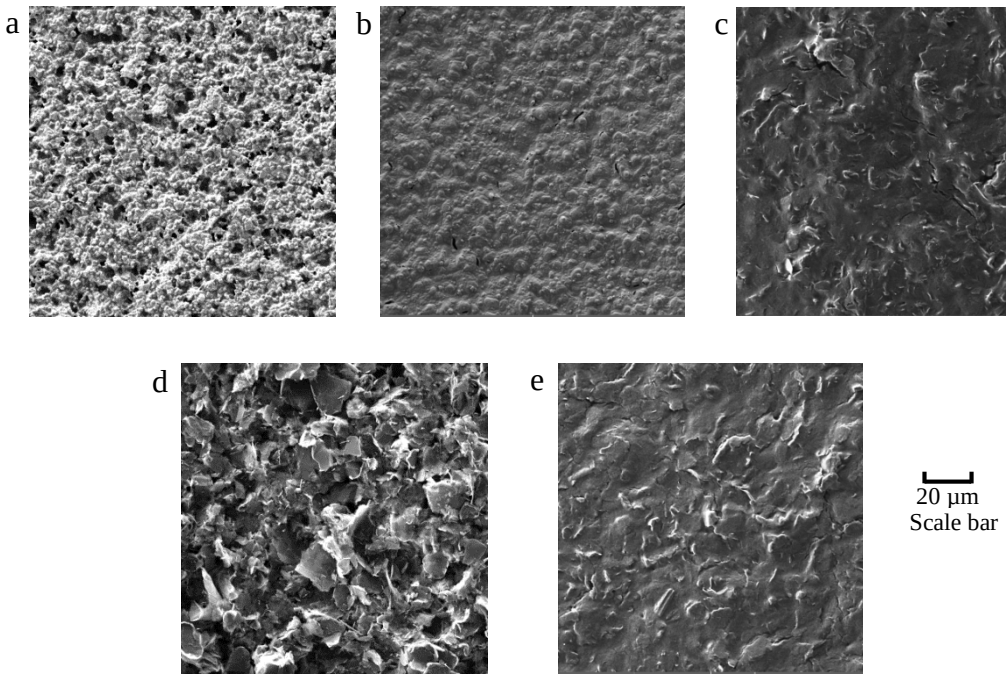

Figure 7.1: SEM images of a) platinum, b) gold, c) carbon, d) graphene modified carbon and e) CNT modified carbon at 2000 × magnification. The scale bar applies to all the images.

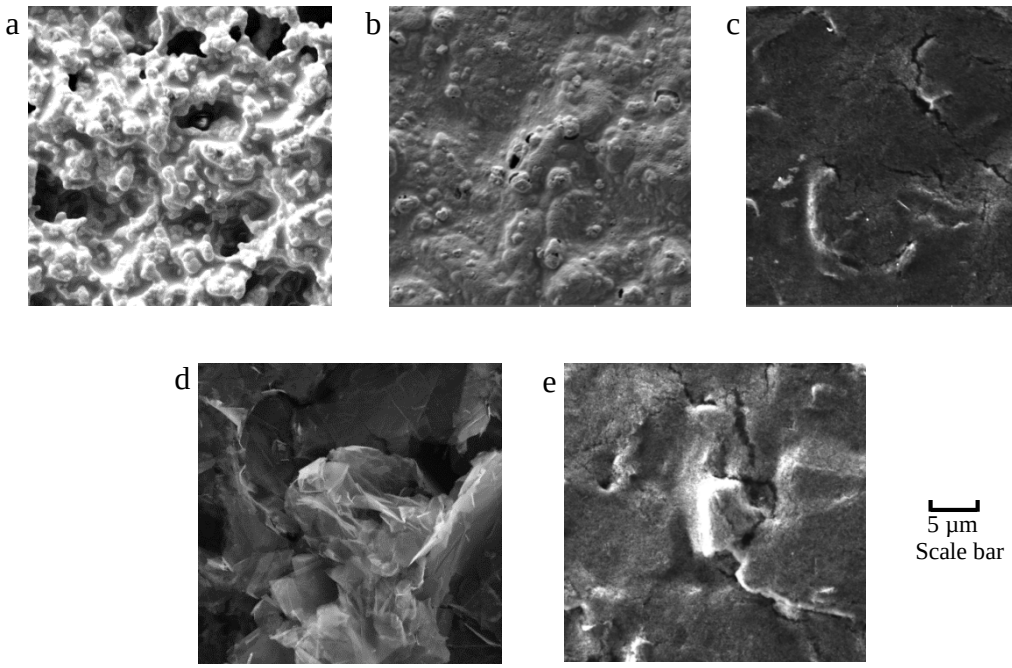

Figure 7.2: SEM images of a) platinum, b) gold, c) carbon, d) graphene modified carbon and e) CNT modified carbon at 10 000 × magnification. The scale bar applies to all the images.

7.3.2 XPS

XPS was used as a characterisation tool to investigate the chemical elements present on the working electrode surfaces of the three main SPEs, Pt, Au and C. The SPEs were characterised out of the box (bare) and also after they were exposed to the RTIL (RTIL Exposed). The SPE exposed to the RTIL was washed with acetonitrile before XPS experiments. The NIST X-ray photoelectron spectroscopy database was used as the tool to fingerprint the peaks. In all cases a full wide spectrum was first obtained followed by a high resolution spectrum.

7.3.2.1 Pt SPE

Figure 7.3 shows a survey spectra between 0 and 1200 eV for both the bare and RTIL-exposed Pt SPEs. The full survey identified Pt 4f, Pb 4f, C 1s and O 1s on the bare Pt SPE and on the RTIL exposed Pt SPE, together with the elements found on the bare, S 2s, Ag 3d and F 1s were also identified.

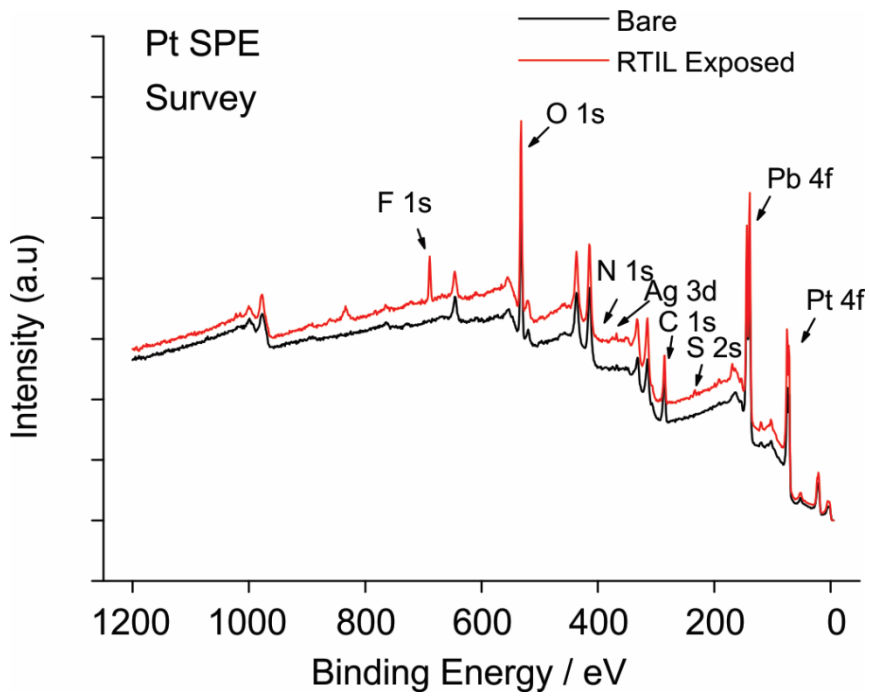

Figure 7.3: XPS survey spectra of Pt SPEs for B.E. between 0 and 1200 eV

Once the peaks were identified using the survey and NIST X-ray photoelectron spectroscopy database, elemental analysis was performed on all the peaks to obtain high resolution data. Figure 7.4 shows the comparison between the Pt 4f, Pb 4f, C 1s and O 1s on the bare and the RTIL exposed Pt SPE. On the Pt 4f spectrum (figure 7.4a), two peaks are evident at 74.6 eV and 71.1 eV which are due to the 4f 5/2 and 4f 7/2 spin orbit coupling and due to the binding energies (B.Es) that are attributed to Pt metal. Unexpectedly, lead (figure 7.4b) was also found on the surface of these SPEs. The peaks at 139.7 eV/139.4 eV and 144.5 eV/144.2 eV are again due to the 4f 5/2 and 4f 7/2 spin orbit coupling. The binding energies of 139.7 eV/139.4 eV are slightly higher than 136.8 eV for Pb metal, suggesting that the compound present is most likely $Pb(NO_3)_2$. This maybe present as a result of the screen printing process, where $Pb(NO_3)_2$ can be used as a mordant.[8,9] The O spectrum (figure 7.4d) shows a broad peak at 532.5 eV/532 eV. The O 1s region cannot be interpreted easily due to the overlap of many species at the same region. However the absence of a peak between 529-530 eV suggests that no metal oxides are present.

Figure 7.4c shows the C 1s region for both types of SPEs. Due to adventitious carbon (adsorbed carbon contaminants from the atmospheric exposure) it is difficult to interpret the carbon spectra. The adventitious carbon could be due to both C-C and C-O bonds, but due to the slightly higher B.E. of 286.6 eV there are more C-O bonds as compared to C-C bonds. This feature, when present on the bare electrodes, suggests that the binder in these electrodes has a high concentration of C-O bonding. This is further backed up by the O 1s spectrum where the consistent presence of O 1s peak could be due to the C-O bonds. However there are some distinct differences between the bare (black line) and RTIL exposed (red line) samples. The extra peaks present at 290 eV and 294 eV on the RTIL exposed SPE can be attributed to the

RTIL. Due to the negligible vapour pressure of RTILs, they have been used in various XPS studies as liquids.[10-12] Ikari et al.[13] have reported the XPS characterisation of $[C_2mim][NTf_2]$ and have attributed the peak at 294 eV to the carbon in the anion $[NTf_2]^-$ and the reason the peak is shifted to a higher B.E is because it is attached to F which is very electronegative causing the carbon to have a withdrawal of valence electron charge. The shoulder at 290 eV is due to the single carbon connected directly to the 2 Ns in the imidazolium ring in the cation part of the RTIL.[13] The other carbons present in the RTIL are masked with adventitious carbon under the peak at approximately 286 eV. Both of these peaks are not present on the bare surface which suggests that even after washing the SPE with acetonitrile some RTIL has remained on the surface.

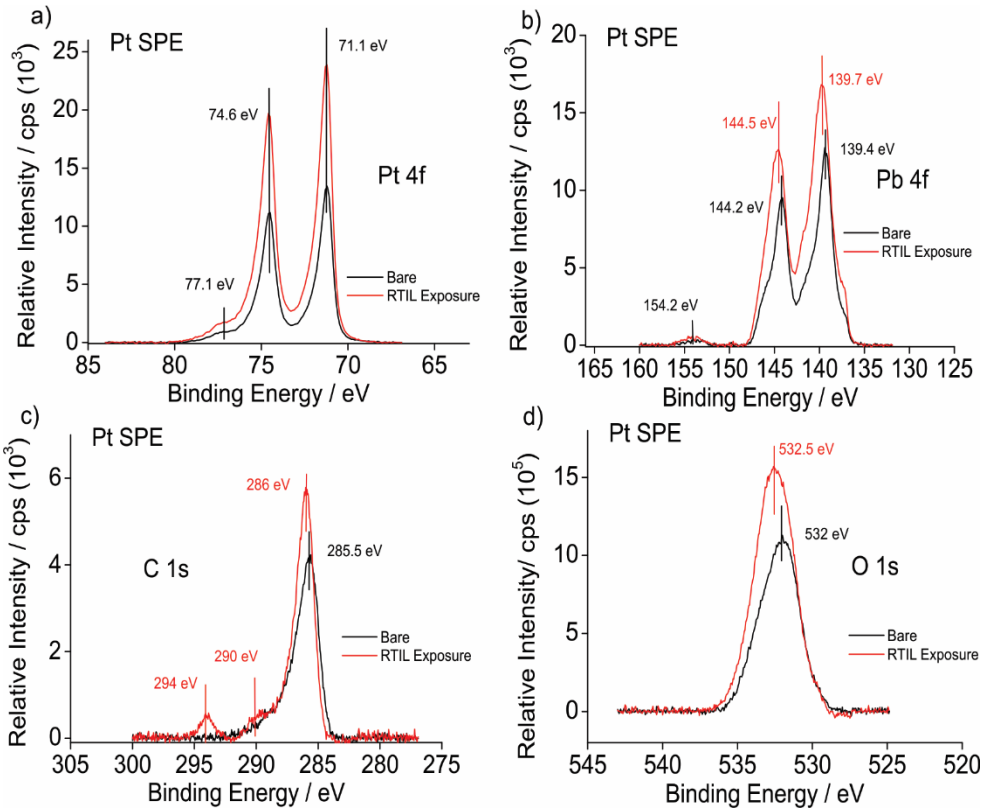

Figure 7.4: XPS spectra of Pt SPEs for a) Pt 4f region, b) Pb 4f region, c) C 1s region and d) O 1s region. Black line shows bare Pt SPE and red line shows Pt SPEs exposed to the RTIL $[C_2mim][NTf_2]$.

This was further supported by the spectra for S 2s, N 1s and F 1s (figure 7.5). A peak at 689.8 eV was observed for F 1s, attributed to an organic fluoride, most likely the fluorine in the $[NTf_2]^-$ anion and not metal fluoride (684-685.5 eV). The peak at 234.1 eV for S 2s is also identified to be from the $[NTf_2]^-$ anion. On the N 1s spectrum the resolution is poor, however a double peak can be seen at approximately 401 eV which is due to the nitrogens in the RTIL. The peak at the slightly higher B.E. is due to the $[C_2mim]^+$ cation and the peak at the slightly lower B.E is from the $[NTf_2]^-$ anion.[13] These peaks are clearer on the Au SPE and will be discussed in greater detail in the Au SPE section. Interestingly Ag 3d peaks were also observed on the RTIL exposed Pt SPEs. The doublet is due to the spin coupling of the 3d 5/2 and 3d 7/2 orbits. The slightly lower B.E of 367.7 eV (368.2 eV is seen for Ag metal) seen for Ag 3d 5/2 suggests that it could be in its oxidised form of Ag_2O.[14] The presence of Ag could be due to the silver reference electrode. During the washing process with acetonitrile, after exposure with RTIL, the silver oxide from the reference electrode on the SPE could have been transferred to the working electrode surface.

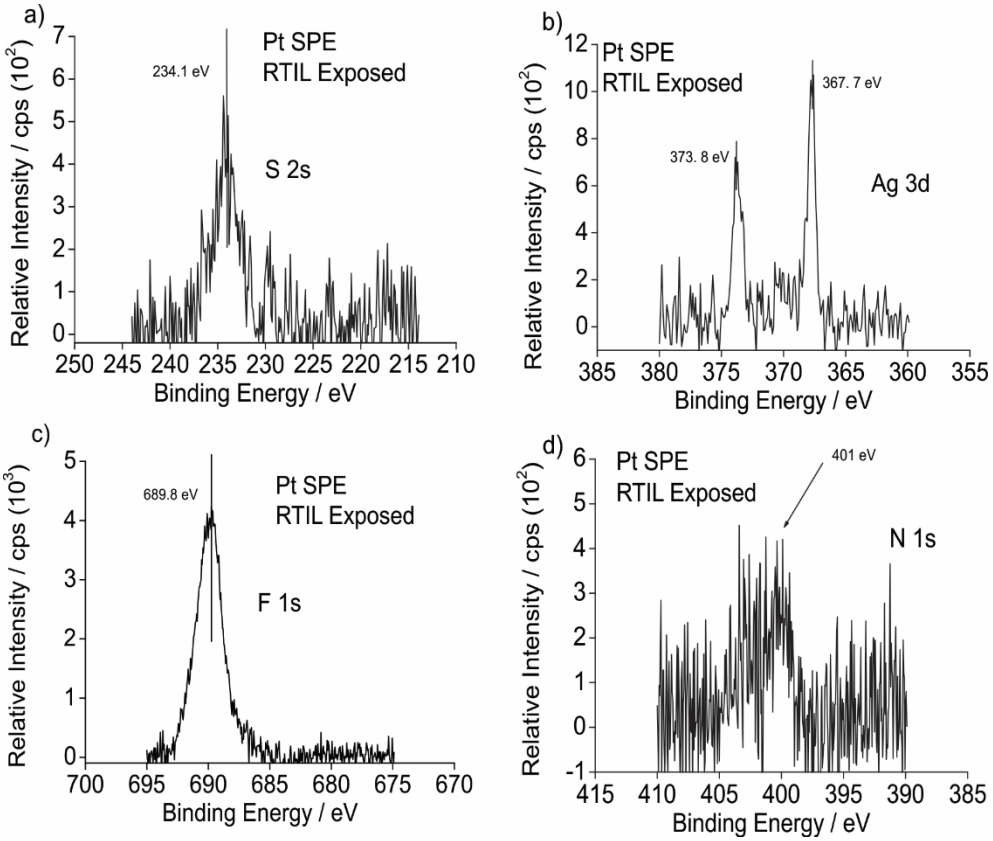

Figure 7.5: XPS spectra of Pt SPEs for a) S 2s region, b) Ag 3d region, c) F 1s region and d) N 1s region after exposed to the RTIL $[C_2mim][NTf_2]$

7.3.2.2 Au SPE

Figure 7.6 shows the full survey spectra of the working electrode of a Au SPE and peaks for Au 4f, Bi 4f, C 1s, Rh 3d, O 1s and F 1s were identified on the bare Au SPE. On the RTIL exposed SPE, together with those peaks, peaks for N 1s, Ag 3d and S 2s were also obtained. Again, the NIST X-ray Photoelectron Spectroscopy Database was used to perform elemental analysis.

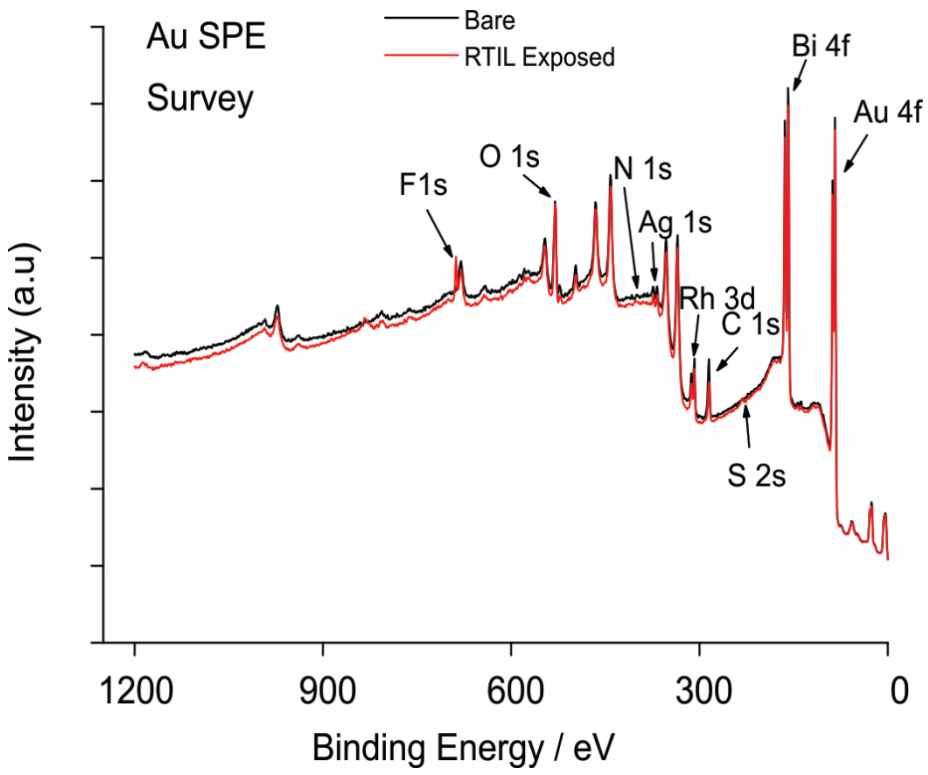

Figure 7.6: XPS survey spectra of Au SPEs for B.E. between 0 and 1200 eV

Figure 7.7 shows the spectra for Au 4f, Bi 4f, C 1s, Rh 3d, O 1s and F 1s for both the bare (black line) and the RTIL exposed (red line) Au SPE. B.Es of 84.2 eV and 87.8 eV for the 4f 7/2 and 4f 5/2 spin orbit couplings (figure 7.7a) suggest that Au is in its pure metallic form.[15] Two additional metals were also identified on the Au SPE, namely Bi and Rh. Figure 7.7b shows the Bi 4f XPS spectrum for both the bare and the RTIL exposed SPE and B.Es of 158.5/158.7 eV and 163.8/164 eV suggest that the Bismuth is in its oxidised form of Bi_2O_3.[16,17] Bismuth oxide is used as a yellow pigment[18] and could be used in the screen printing process to make the Au working electrode surface look yellow and brighter. It is also said to have good qualities as a binder[19,20] which suggest that it could be present in the paste during the screen printing process.

The presence of Rh 3d peaks (figure 7.7d) at 308.2 eV (3d 5/2) and 313.1 eV (3d 7/2) suggest that Rhodium oxide is also present.[21] Rhodium oxide is transparent and

conductive and has a higher work function then indium tin oxide (ITO) and therefore has been used to coat ITO to enhance the work function of organic light emitting diodes.[22] It is possible that Rhodium oxide is used on Au SPEs to increase the conductivity. On the O 1s spectrum two clear peaks are present on the Au SPEs unlike the Pt surface. On the Au SPE there is an O 1s peak at 529.5/529.7 eV and 531.4/532 eV. The peak at 531.4/532 eV is due to many overlapping regions, which is hard to interpret and was seen on the Pt surface. However the peak at 529.5/529.7 eV was not seen on the Pt surface and is probably due to the presence of metal oxides (rhodium or bismuth oxide). On the C 1s spectrum, just like the Pt surface, the bare and the RTIL exposed Au SPEs look different. The presence of the peak at 292.6 eV is due to C in the $[NTf_2]^-$ anion and the shoulder at 288.1 eV is due to the single carbon connected directly to the 2 Ns in the cation of the RTIL and they have been discussed in greater detail in the previous section.

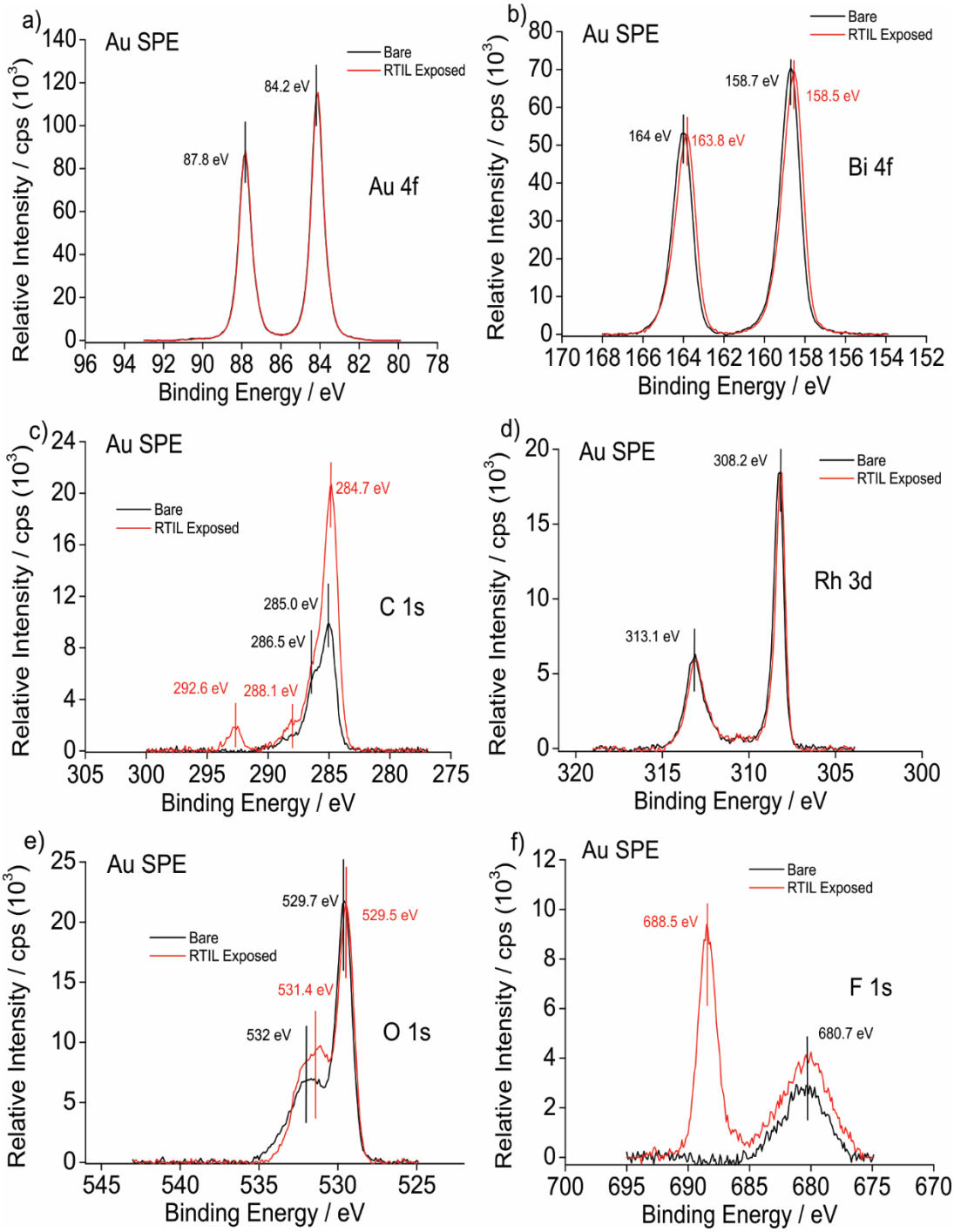

Figure 7.7: XPS spectra of Au SPEs for a) Au 4f region, b) Bi 4f region, c) C 1s region, d) Rh 3d region, e) O 1s region and f) F 1s region. Black line shows bare Au SPE and red line shows RTIL exposed Au SPEs

The presence of additional peaks characteristic of the RTIL are also seen on the Au surface, F 1s (Figure 7.7f), S 2s (Figure 7.8a) and N 1s (Figure 7.8c). In the F 1s spectrum there is also a broad feature at 630 eV on both surfaces identified as Au 4 p1/2. The spectrum for N 1s (figure 7.8c) shows two peaks, one at 399.2 eV which is due to the $[NTf_2]^-$ anion and the other at 401.5 eV is due to the $[C_2mim]^+$ cation.[13] In the $[NTf_2]^-$ anion the nitrogen has a negative charge and therefore has a lower B.E as compared to the nitrogens in the $[C_2mim]^+$ cation. There are two nitrogens in the $[C_2mim]^+$ cation and one nitrogen in the $[NTf_2]^-$ anion therefore it should be expected that the ratio of the peaks should be 2:1 as shown by Ikari et al.[13]. However this was not the case which suggest that the $[NTf_2]^-$ anion adsorbs more readily than the $[C_2mim]^+$ cation onto the SPE surfaces. Another important comparison that can be made between the Au and Pt surfaces is that on the Au surfaces the relative intensity of all the RTIL peaks are much higher which suggests that the RTIL adsorbs more onto the Au surface then the Pt surface. This increase in wettability of the Au SPE could explain why for the same concentrations of gas the Au surface always gives a slightly higher current as compared to the Pt surface (discussed in greater detail in section 7.4 Methylamine Gas). In figure 7.8b the spectrum for Ag 3d is shown and, similar to the Pt SPE, two peaks are present. Peaks at 367.7 eV and 373.5 eV suggest the presence of AgO[14] which could be due to contamination from the Ag reference electrode.

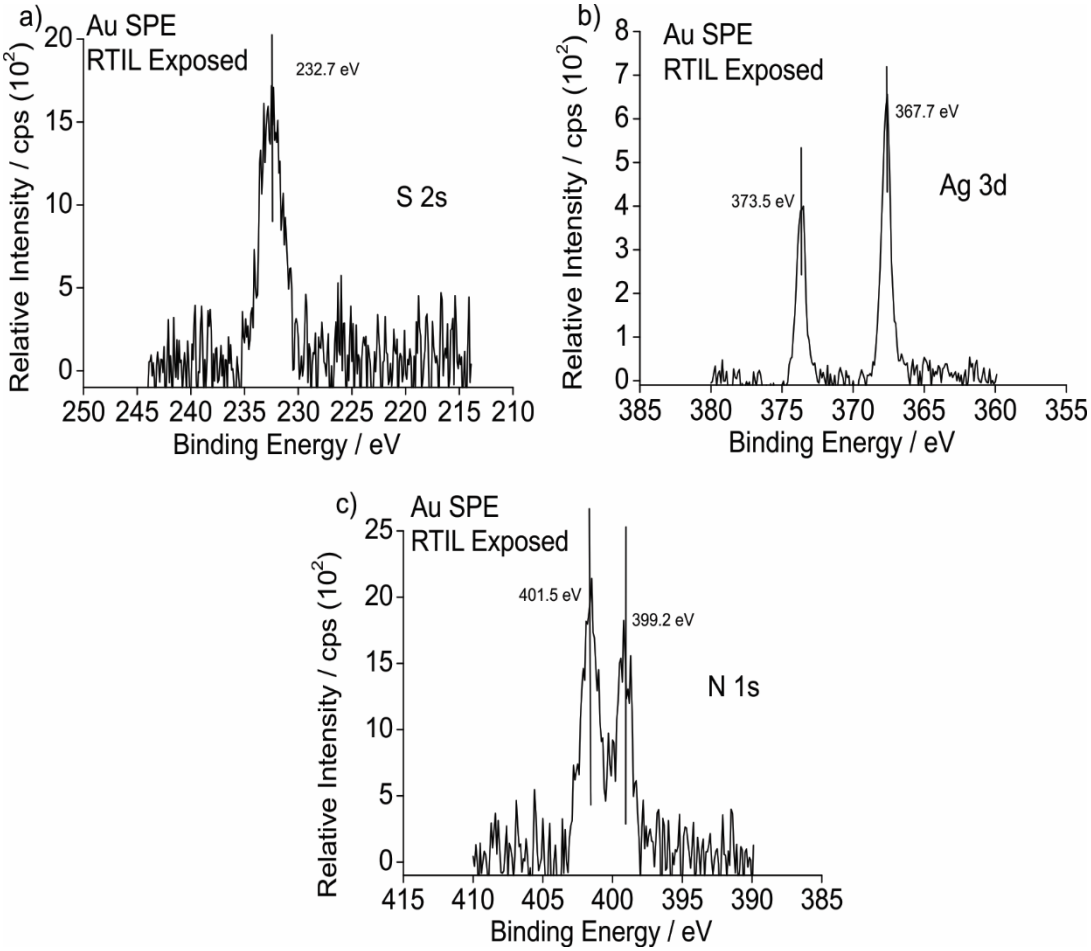

Figure 7.8: XPS spectra of Au SPEs for a) S 2s region, b) Ag 3d region and c) N 1s region after exposed to the RTIL $[C_2mim][NTf_2]$

7.3.2.3 C SPE

Figure 7.9 shows the full survey spectra obtained on both the bare (black) and RTIL exposed (red) C SPE. On the bare SPE Cl 2p, C 1s and O 1s were identified and on the RTIL exposed SPE N 1s, F 1s and S 2s were also present.

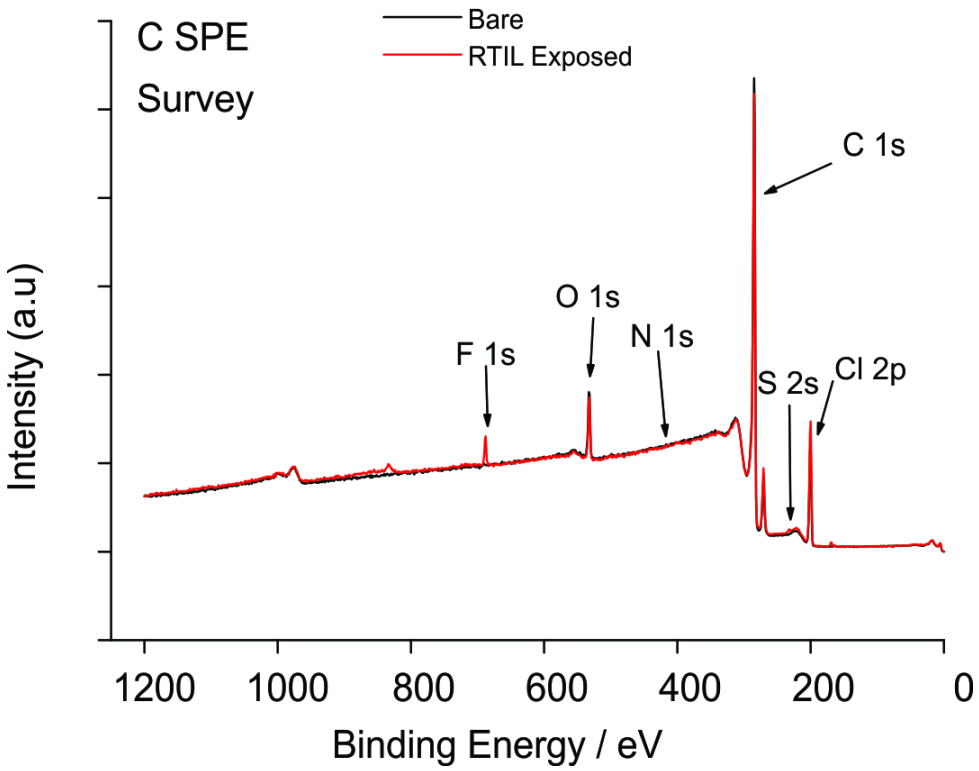

Figure 7.9: XPS survey spectra of C SPEs for B.Es between 0 and 1200 eV

Figure 7.10 shows the elemental analysis of Cl 2p, C 1s and O 1s that were present on both types of SPEs. The presence of O 1s at 532.5 eV could be explained by the overlap of many peaks such as C-O, C=O or even SiO_2 and is hard to interpret accurately. Just like the O 1s peak the C 1s peak is difficult to interpret due to adventitious carbon. The presence of chlorine was confirmed by the Cl 2p peak (Figure 7.10a). Two peaks at 200/200.1 eV and 201.6/201.7 eV was attributed to Cl 2p 3/2 and Cl 2p 1/2 respectively. The Cl 2p 3/2 peak for metallic chloride is usually between 198.5 and 199 eV and organic chloride is at approximately 200 eV. The Cl 2p 3/2 peak at 200.1 eV has been reported previously to be due to the halogenated polymer poly(vinyl chloride).[23] Plastisol is a poly(vinyl chloride) ink that is used for screen printing and very likely also used in the screen printing of Dropsens carbon SPEs.[24] Figure 7.11 shows the spectra for the RTIL exposed C SPE for S 2s, N1s and F 1s. All three spectrums show that the RTIL adsorbs on the Carbon SPE. On the S

2s spectrum there is a peak at 220.5 eV and this is most likely due to the plasmon resonance peak of the Cl 2p peak. This broad peak also sometimes referred to as the 'step' occurs when there is an abundance of a material like Cl and C (in this case). This feature is also seen for C at approximately 310 eV which can be seen on the survey spectrum (figure 7.9) just before the large C 1s peak. However on the C 1s spectrum (figure 7.10b) the characteristic peak for the C in the $[NTf_2]^-$ anion that was seen on both the Pt and Au SPE was not present on the C surface.

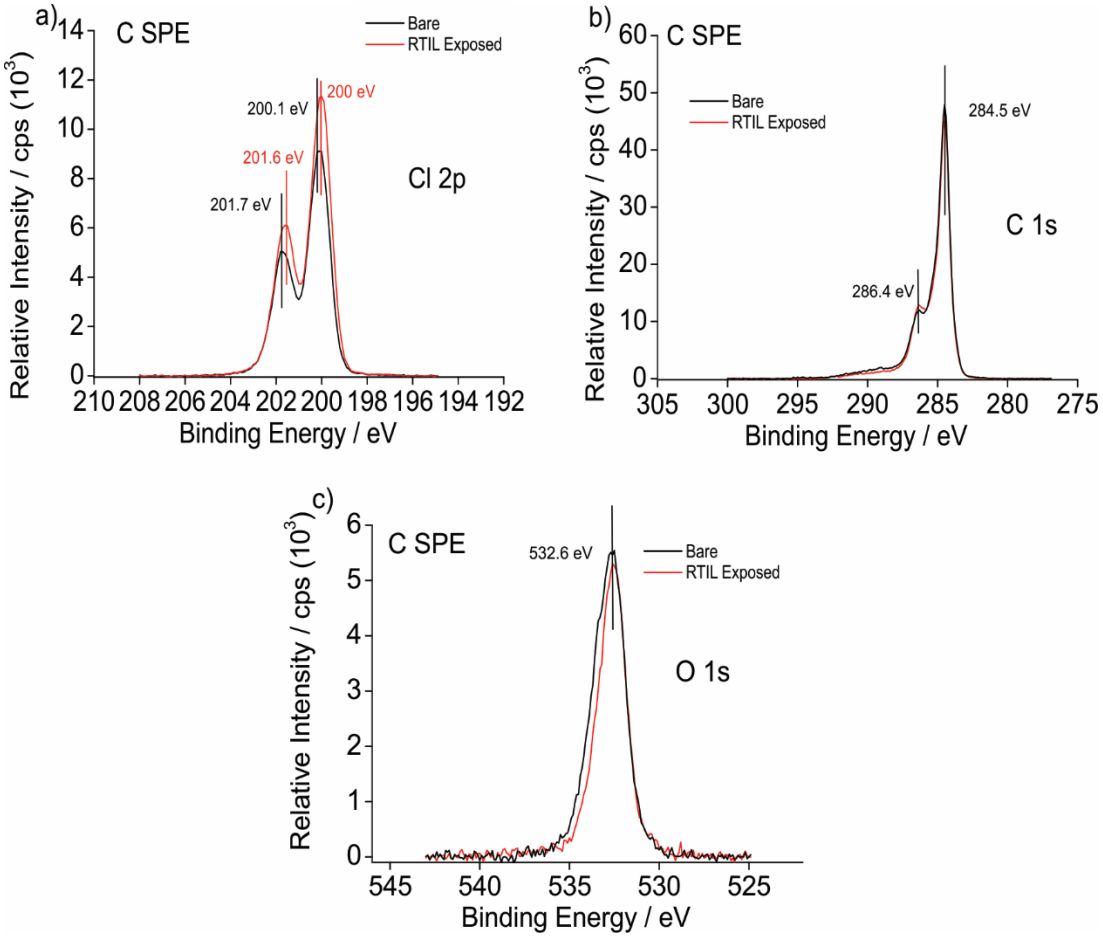

Figure 7.10: XPS spectrum of C SPEs for a) Cl 2p region, b) C 1s region and c) O 1s region. Black line shows bare Pt SPE and red line shows Pt SPEs exposed to RTIL

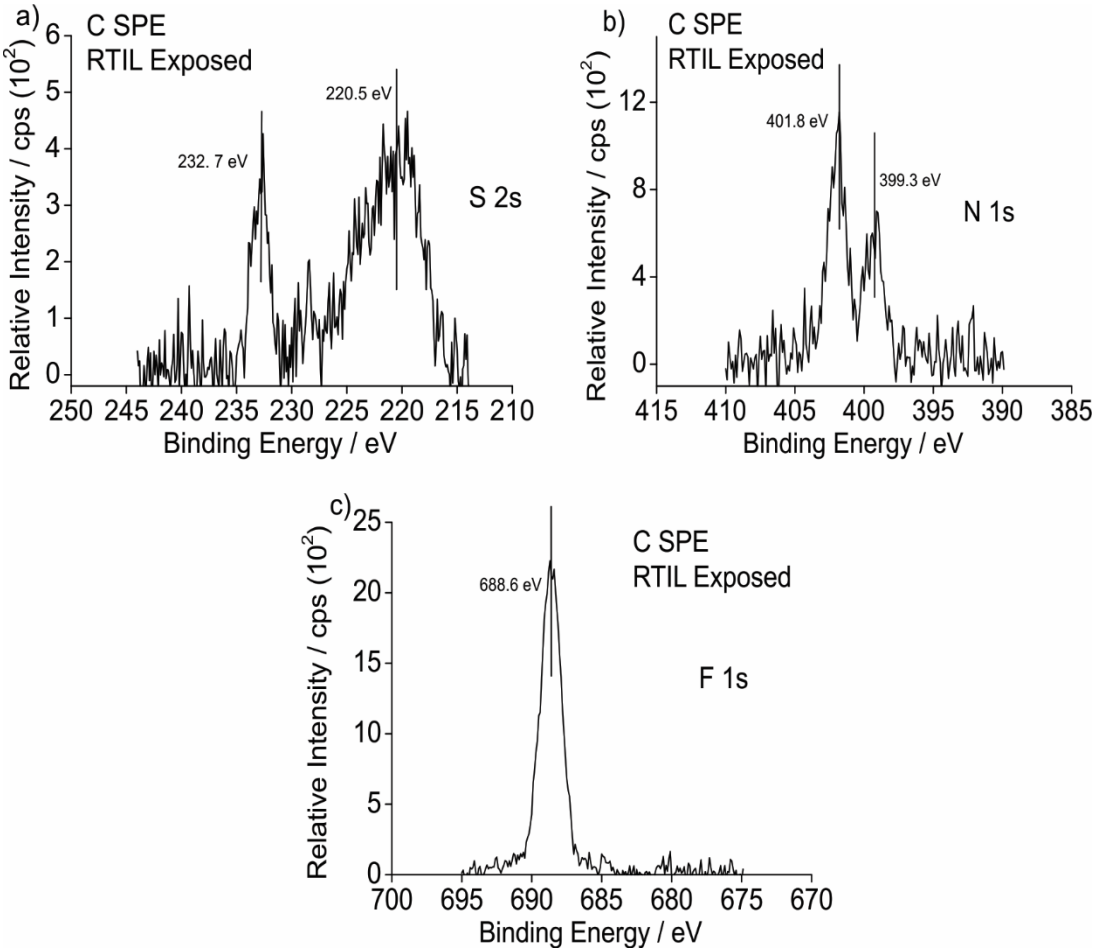

Figure 7.11: XPS spectra of C SPEs for a) S 2s region, b) N 1s region and c) F 1s region after exposed to the RTIL $[C_2mim][NTf_2]$

This concludes the physical characterisation of these SPE surfaces. SEM showed that the surfaces vary in terms of roughness and porosity which could affect the electrochemical response. XPS characterisation revealed the presence of some impurity peaks during the screen printing process which could be detrimental to the electrochemical behaviour of the gases on these surfaces. From the strength of the signals obtained from the XPS spectrum it can be said that on the Pt SPE the quantity of platinum to lead is in a 55 to 45 ratio and in the case of the Au SPE the quantity of gold to bismuth is in a 60 to 40 ratio. In the next few sections the electrochemical behaviour of the three target gases will be investigated on these SPEs.

7.4 Methylamine Gas

7.4.1 Electrochemical Oxidation of Methylamine Gas on Pt SPEs

Figure 7.12 shows the electrochemical oxidation of 0.15 % methylamine gas on a platinum SPE in the RTIL [C_2mim][NTf_2]. Similar to the platinum microelectrode, there are 4 peaks present.[25] There is first an oxidation peak (I) at approximately 1.5 V followed by two reduction peaks (II and III) at -0.1 V and -0.8 V and then finally another oxidation peak (IV) at -0.2 V. Peak II, III and IV were absent when scanned negative first which specifies that they are a result of the products formed after the oxidation peak (I). The mechanism of the reaction has been elucidated in our previous work[25] and in chapter 4 and therefore will not be explained in detail here. In brief, methylamine is oxidised to form ammonia which itself undergoes oxidation as it is already at a potential that can be oxidised. The combination of these two processes produces the oxidation peak (I) which will be used as our analytical response.

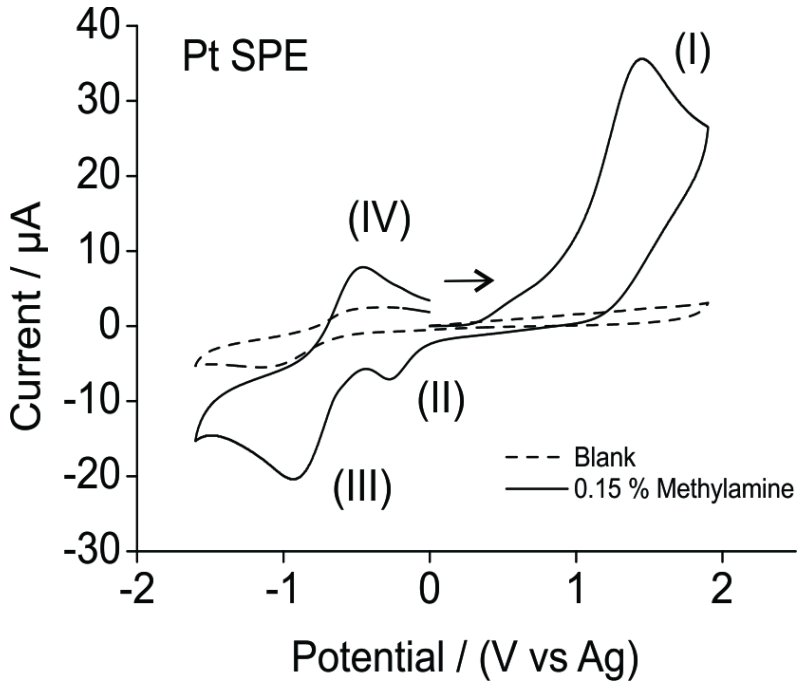

Figure 7.12: CV for the oxidation of 0.15 % methylamine gas on a Pt SPE in [C_2mim][NTf_2] at a scan rate of 0.1 V/s. Dotted line is the response in the absence of methylamine.

Figure 7.13 shows cyclic voltammetry for the oxidation of 0.15 % methylamine at varying scan rates from 0.05 V/s to 1 V/s when scanned from 0 to 2 V and back to -1.8 V. It can be seen that as the scan rates increase the peak currents for all four peaks increases. There is also the presence of a pre peak before peak I (more visible at higher scan rates) and this could be attributed to the splitting of the two process (ammonia oxidation and methylamine oxidation).[25] The inset in figure 7.13 shows a plot of the peak current for the oxidation peak (I) vs the square root of scan rate. A linear response was obtained which signifies that the process occurring is diffusion controlled such as suggested previously on a Pt microelectrode (chapter 4). These results are encouraging as it shows that the behaviour on a Pt SPE is very similar to a Pt microelectrode. It has been shown previously that oxygen voltammetry on SPEs in some RTILs[5] is not ideal and that the behaviour on a microelectrode is not the same as on a SPE which signifies that SPEs might not be suitable for oxygen gas detection. In our case, it has been established that the behaviour on a SPE is similar of that on a microelectrode, so next step is to study the analytical utility of methylamine gas on SPEs.

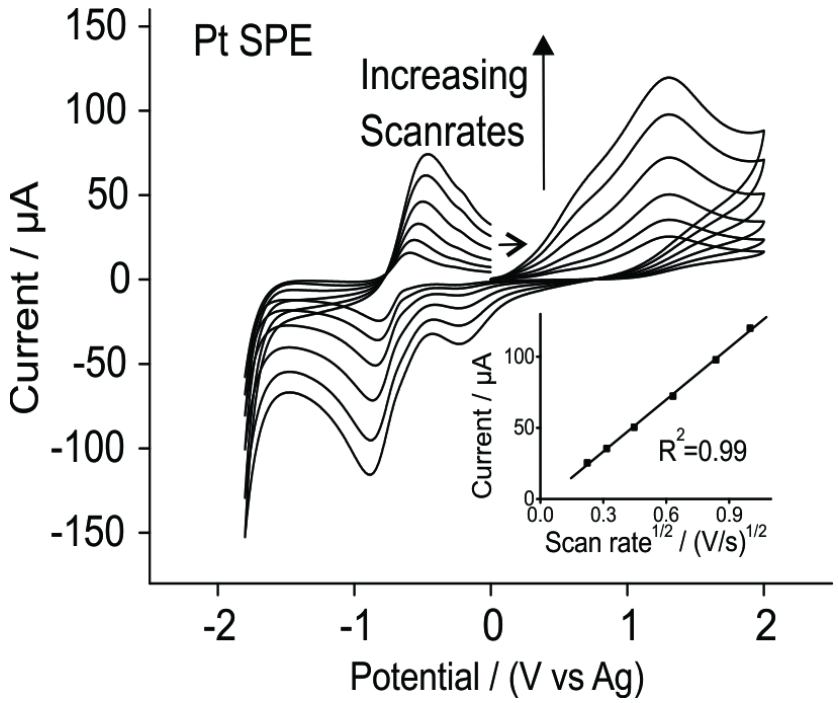

Figure 7.13: CV for the oxidation of 0.15 % methylamine gas on a Pt SPE in $[C_2mim][NTf_2]$ at varying scan rates between 0.05-2 V/s. The inset shows the plot of current vs square root of scan rate for process I.

7.4.2 Analytical Utility of Methylamine Gas on Pt SPEs

To study the analytical utility much lower concentrations of methylamine gas was used. Figure 7.14 shows the oxidation of methylamine gas at six different concentrations (from 104 to 710 ppm) on a Pt SPE in $[C_2mim][NTf_2]$ at a scan rate of 0.1 V/s. It can be seen that as the concentration of methylamine increases the current for all four peaks increases. For analytical purposes, the oxidation peak current was plotted against the respective concentrations to obtain the calibration graph (figure 7.15). Excellent linearity with a sensitivity of 2.42×10^{-8} A/ppm was obtained for the range of concentrations studied. A LOD (3σ) of 53 ppm was obtained which is similar to the LOD of 34 ppm obtained on a Pt microelectrode (chapter 4), which is highly encouraging and shows that Pt SPEs can be used for methylamine gas detection, allowing for a cheaper and a more miniaturised AGSs for methylamine using SPEs and RTILs.

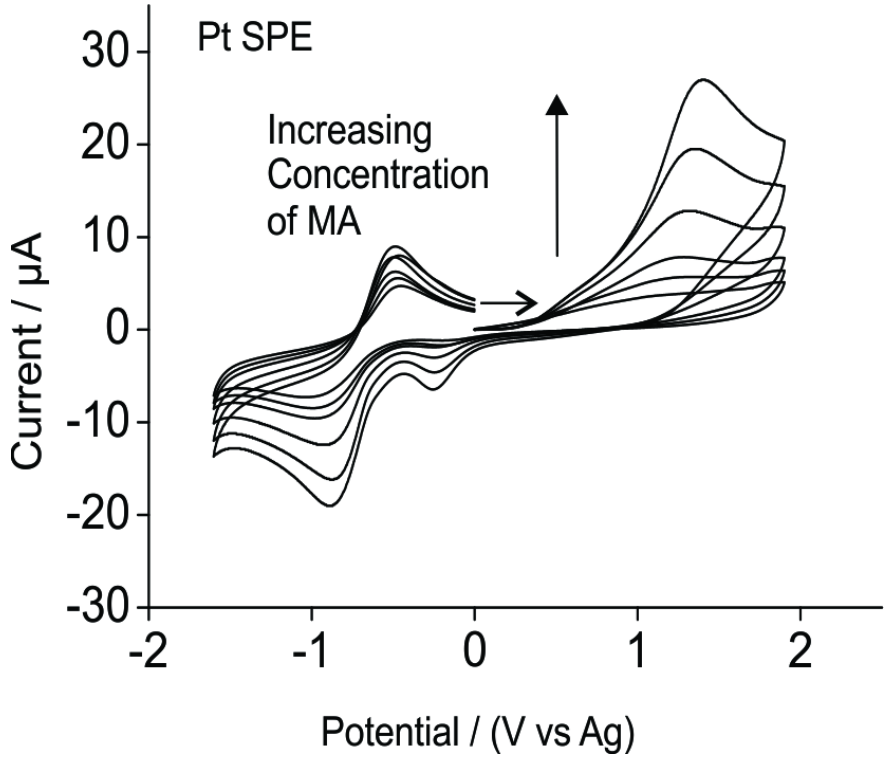

Figure 7.14: CVs for the oxidation of methylamine gas (104 -710 ppm) on a Pt SPE in $[C_2mim][NTf_2]$ at a scan rate of 0.1V/s.

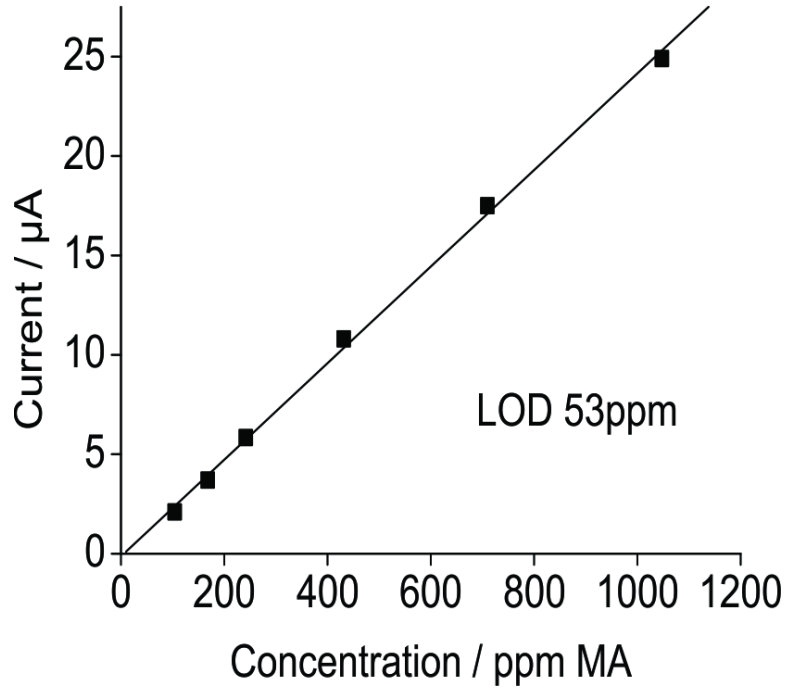

Figure 7.15: Calibration plot obtained for the oxidation of methylamine gas (104-710 ppm) using the oxidation peak current from figure 7.14

7.4.3 Electrochemical Behaviour and Analytical Utility of Methylamine Gas on Au and C SPEs

The analytical utility was also investigated on both gold and carbon SPEs to give a comparison to the Pt SPE. Figures 7.16 and 7.17 show the cyclic voltammograms obtained for the oxidation of methylamine on a gold and carbon SPE respectively for the same six concentrations as on a Pt SPE (104 to 710 ppm). Similar to the Pt SPE, on the gold surface clear peaks were observed. However it can be seen that on the gold surface the voltammetry is complicated by other small impurity peaks. This was also observed previously when gold SPEs were used for sensing of ammonia gas and they were attributed to the presence of water impurities.[4] The additional processes was also seen for the oxidation of methylamine on a gold microelectrode[25] and they were attributed to the formation of gold oxide or water impurities. Despite these additional peaks, the oxidation peak current was not affected so a calibration graph of current vs concentration was plotted. Good linearity was achieved with a LOD (3σ) of 101 ppm. An important point to note here is that the currents obtained on the gold SPE were slightly higher than the currents obtained for a Pt SPE on the same sized working electrode, resulting in a higher sensitivity on the Au SPE (2.54×10^{-8} A/ppm). This is further supported by the results obtained from the XPS characterisation, as the intensity of the RTIL XPS peaks are much higher on the Au surface then the Pt surface. This suggests that the RTIL adsorbs more readily onto the Au surfaces. The increase in wettability of the Au electrode results in a higher sensitivity. Carter et al.[26] reported that choosing an RTIL that wets the electrode surface better will increase the sensitivity and performance of a AGS. Although the sensitivity is slightly higher on the Au surface, the presence of the impurity peaks could affect the analytical response.

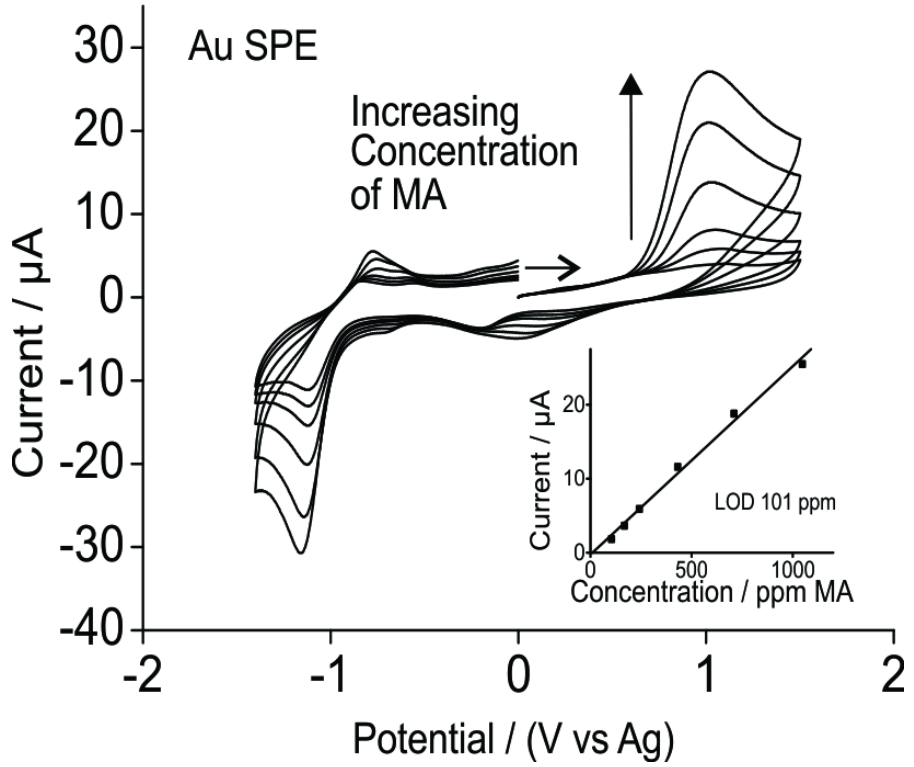

Figure 7.16: CVs for the reduction of methylamine gas (104 -710 ppm) on Au SPE in $[C_2mim][NTf_2]$ at a scan rate of 0.1V/s. Inset is the calibration plot obtained for the oxidation of methylamine gas (104-710 ppm) using the peak current.

On the carbon surfaces there are no distinct differences in the voltammetry obtained for the six different concentrations (figure 7.17). It is possible that the electrochemical oxidation of methylamine gas is not active on carbon within the available potential window which was seen previously for ammonia[4] on these SPEs. There is also a very high capacitance observed on these carbon surfaces which could swamp the Faradaic current. The non-Faradaic capacitive current observed is not ideal and it makes carbon SPEs not suitable for gas sensing utilizing ionic liquids as the electrolyte/solvent. Experiments were not performed on carbon modified surfaces (like in the case of chlorine- see next section) as no analytical response could be obtained for the concentration of methylamine gas investigated.

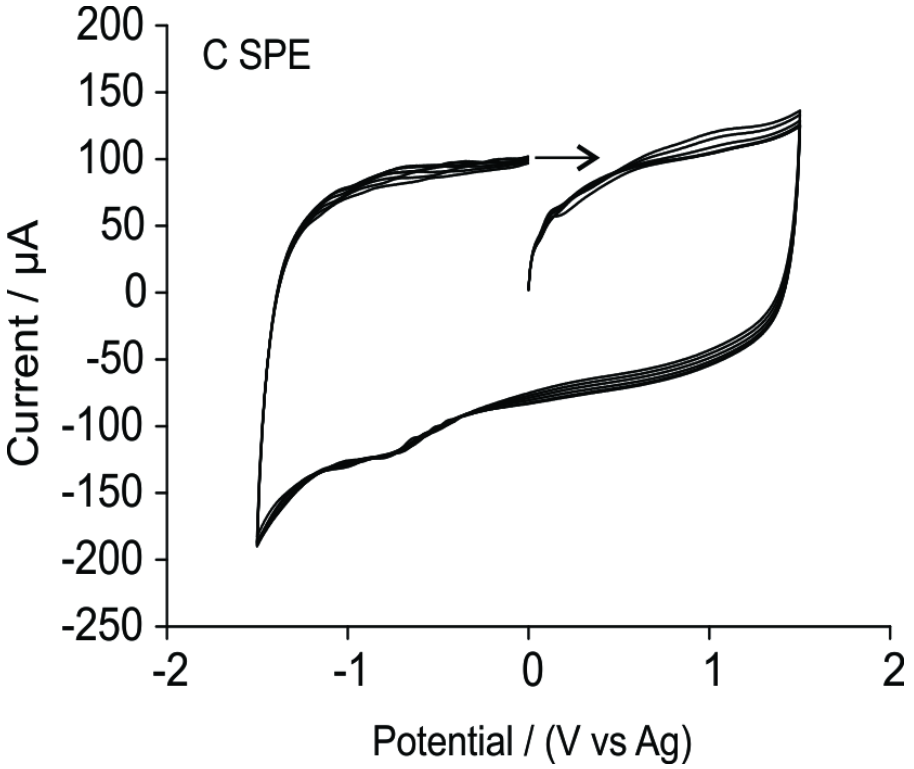

Figure 7.17: CVs for the oxidation of methylamine gas (104 -710 ppm) on a C SPE in $[C_2mim][NTf_2]$ at a scan rate of 0.1 V/s.

7.5 Chlorine Gas

7.5.1 Electrochemical Reduction of Chlorine Gas on Pt SPEs

Figure 7.18 shows the electrochemical reduction of 4.5 % chlorine gas on a Pt SPE at 100 mV/s. It can be seen that there is a reduction peak (chlorine gas to chloride ions) at 0.34 V and an oxidation peak (chloride to chlorine gas) at 0.72 V with a peak to peak separation of 0.38 V suggesting the reaction is not completely reversible. The reduction process on the SPE is peak-shaped (in contrast to steady state on the microelectrode) due to the contribution of linear diffusion on the larger SPE working electrode (diameter 4 mm).

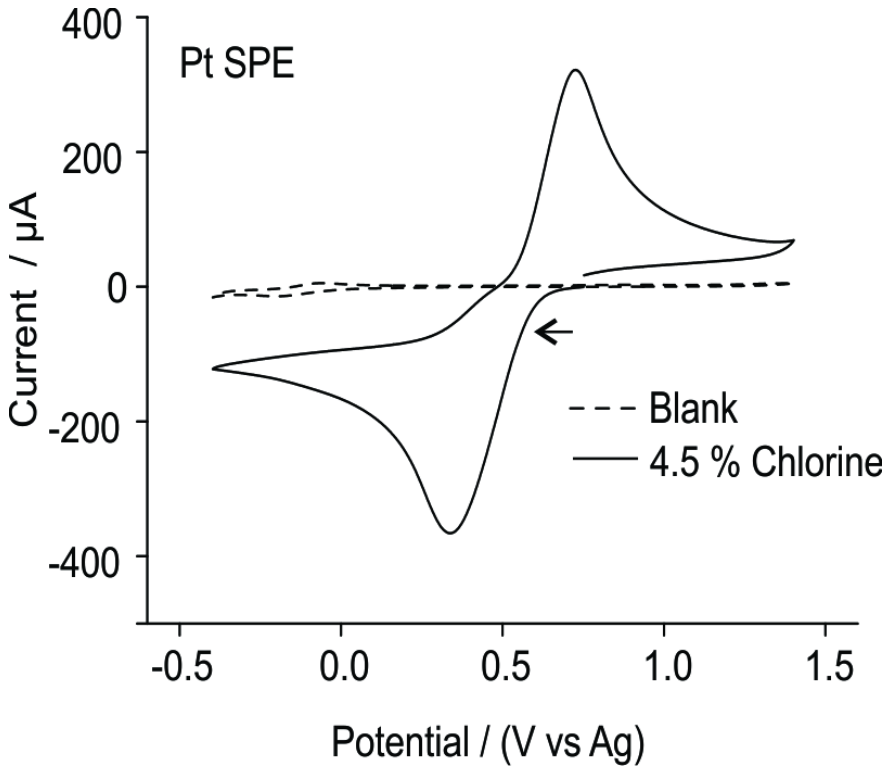

Figure 7.18: CV for the reduction of 4.5 % chlorine gas (nitrogen fill) on a Pt SPE in $[C_2mim][NTf_2]$ at a scan rate of 0.1 V/s Dotted line is the response in the absence of chlorine.

Figure 7.19 shows the electrochemical reduction of 4.5 % chlorine gas at various scan rates from 0.05 V/s to 3 V/s. The current obtained for the reductive process at the various scan rates was plotted against the square root of scan rate, and similar to the microelectrode, a linear response was obtained (see inset Figure 7.19) which suggests that the process is also diffusion controlled. The similar electrochemical behaviour seen on both the SPE and the microelectrode suggests that the mechanism for the reduction of chlorine gas is the same, which is encouraging for sensing purposes.

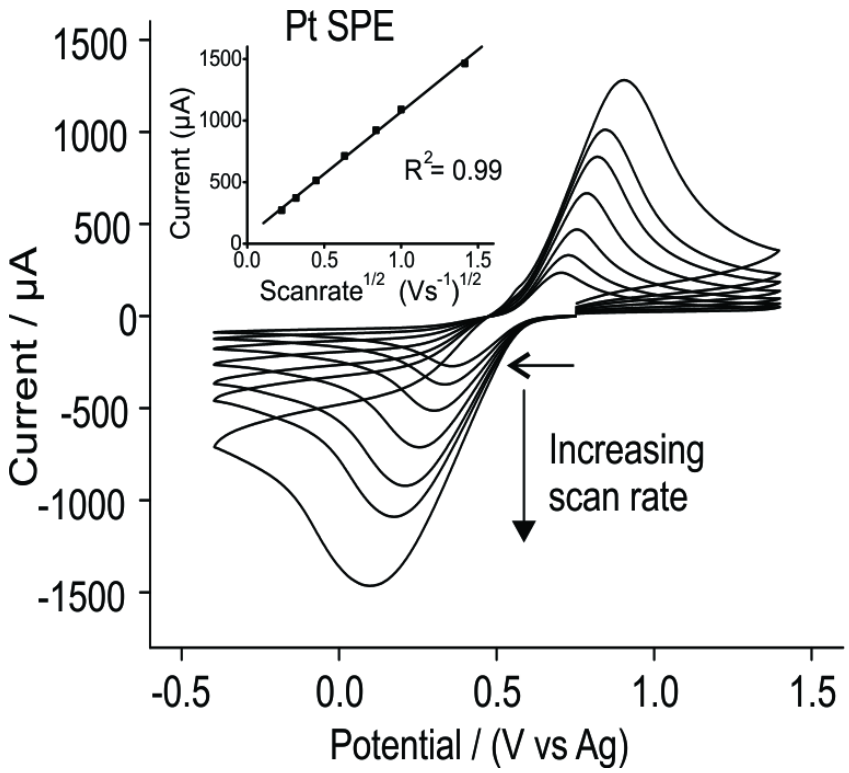

Figure 7.19: CV for the reduction of 4.5 % chlorine gas (nitrogen fill) on a Pt SPE in $[C_2mim][NTf_2]$ at varying scan rates between 0.05-3 V/s. The inset shows the plot of current vs square root of scan rate.

7.5.2 Analytical Utility of Chlorine Gas on Pt SPEs

The analytical utility was studied in much lower concentration of chlorine gas then above. Figure 7.20 shows typical CVs of five different concentrations of chlorine gas (173 to 1583 ppm) on a Pt SPE. It can be seen that the concentration of both the reduction and the oxidation processes increases in current with the concentration of the gas. Using the reduction peak current, it is possible to obtain a calibration graph and determine the analytical utility of chlorine gas on a Pt SPE.

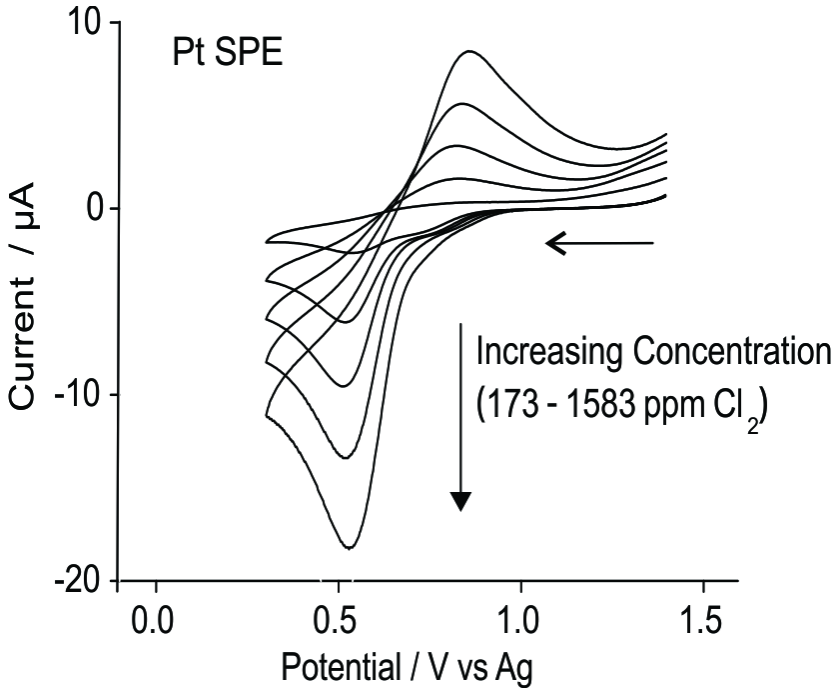

Figure 7.20: CVs for the reduction of chlorine gas (173 -1583 ppm) on a Pt SPE in $[C_2mim][NTf_2]$ at a scan rate of 0.1V/s.

Figure 7.21 shows the calibration graph obtained on a Pt SPE using the reduction peak currents for the same concentration range studied previously on a Pt microelectrode (the 10 points on the calibration graph also includes the concentration values from another cylinder). It can be seen that a linear behaviour is observed, with $R^2 > 0.99$, a sensitivity of 1.01×10^{-8} A/ppm and a LOD (3σ) of 137 ppm. While the LOD is comparable to that obtained at a microelectrode (106 ppm), the sensitivity is higher on the SPE, which is a consequence of the geometric sizes of the two electrodes. Normalizing the CV sensitivities for the geometric areas of the respective electrodes yields values of 3.15×10^{-7} A/cm^2·ppm and 8.08×10^{-8} A/cm^2·ppm for the microelectrode and SPE respectively which indicates that the microelectrode has a higher sensitivity due to the higher current density on the smaller electrode. The excellent linearity and reasonable limits of detection obtained show that Pt SPEs may be useful low-cost platforms for the detection of chlorine.

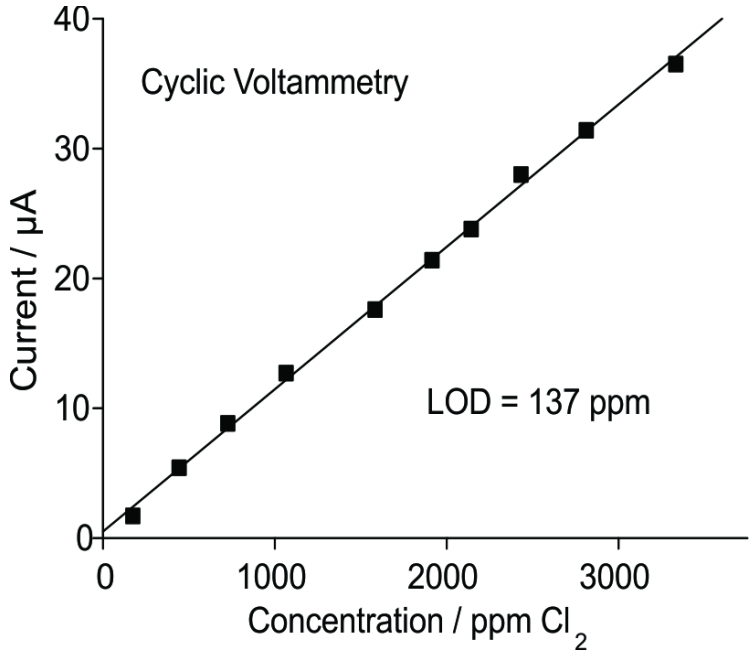

Figure 7.21: Calibration plot obtained for the reduction of chlorine gas (173 -3333 ppm) using the limiting/peak current on a Pt SPE. The lower 5 concentration points are from a 0.2 % chlorine cylinder (CVs shown in figure 7.20) while the other 5 higher concentrations are from a 4.5 % cylinder (CVs not shown).

7.5.3 Electrochemical Behaviour and Analytical Utility of Chlorine gas on Au, C, Graphene Modified C and Carbon Nanotubes Modified C SPEs

The electrochemical behaviour of chlorine gas was also investigated on various other SPEs from Dropsens. Figure 7.22 shows the typical CVs obtained for five concentrations of chlorine gas on Au, C, graphene modified C and carbon nanotubes modified C SPEs. It can be seen that on all surfaces that the peak currents for the reduction increase with concentration. The insets to the figure shows the calibration graphs obtained from the reduction peak currents in the CVs.

On the gold surface a very high LOD (3σ) is obtained (411 pm, approximately 4 times more than the Pt surface). It can be seen from the CVs that there is a complex process occurring on the working electrode surface. The loss of the oxidation peak suggests that the electro generated chloride reacts with gold to form gold chloride

species, which is not unexpected. Together with the high LOD obtained it can be said that Au SPEs are not suitable for the detection of chlorine gas sensing in RTILs. Au SPEs were also deemed not suitable for ammonia gas sensing in a previous study due to impurity peaks[4] and also in section 7.4.3, for methylamine sensing.

It can be seen that on all the carbon and carbon modified surfaces there is one reduction peak and one oxidation peak. It is believed that this is the two electron reversible reduction of chlorine to chloride. The peak to peak separation on the carbon surfaces are between 0.25-0.29 V which suggests that the kinetics of the reaction is slightly faster than the platinum surfaces however there is a very large capacitive current that is most likely due to the non-conductive carbon deposits on the working electrode surface together with the use of RTILs which was seen previously for the oxidation of ammonia gas.[4] The non-Faradaic charging currents that are observed on all the carbon and carbon modified surfaces are not ideal for sensing purposes as it may swamp the Faradaic current that is produced from the analyte species. We are however able to see changes in the CVs for each concentrations. After obtaining calibration graphs for the 3 carbon surfaces it can be seen that the graphene and carbon nanotubes modified surfaces have a slightly better LOD (3σ) of 173 and 174 ppm respectively as compared to carbon's 208 ppm. However due to the limitations, of not being able to go down to much lower concentrations, that arises from the very large capacitance, carbon and carbon modified surfaces are also deemed not suitable for chlorine gas sensing in conjunction with RTILs.

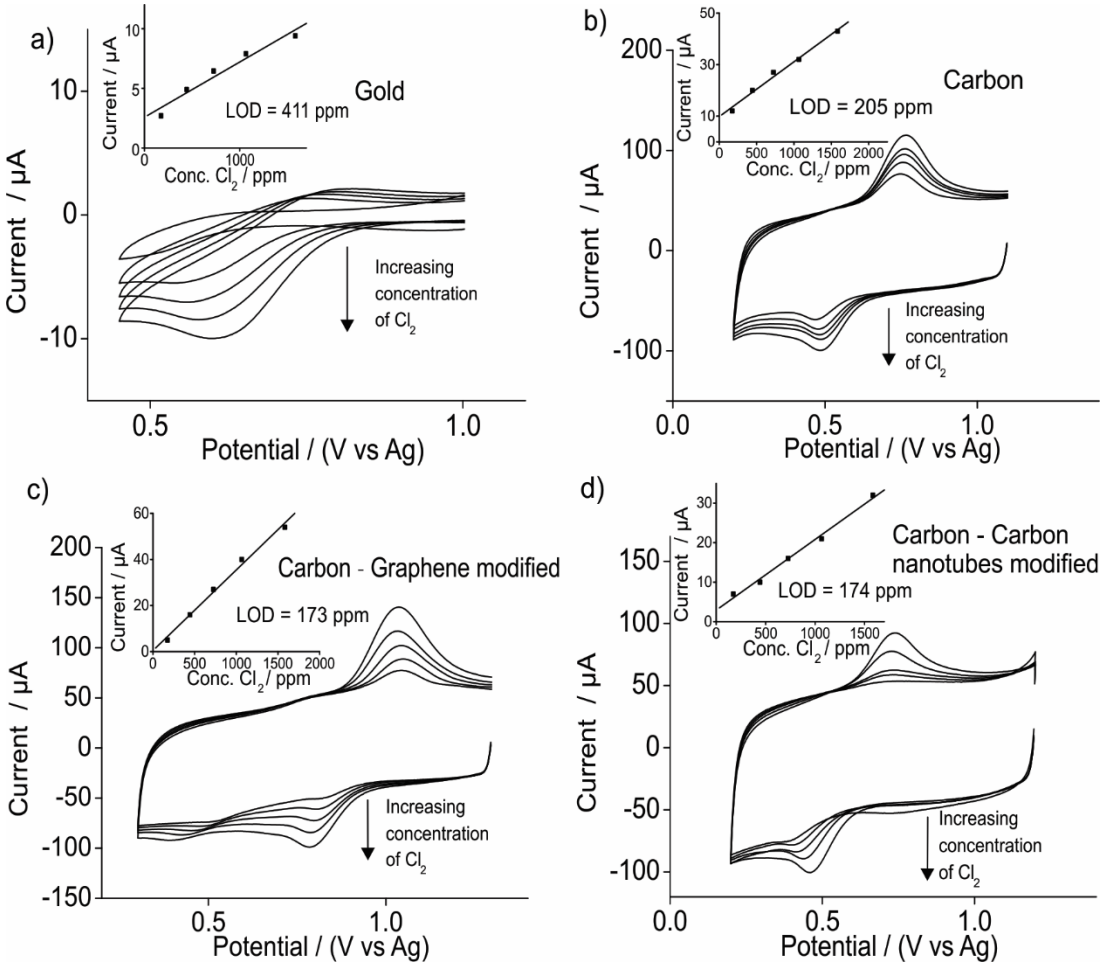

Figure 7.22: CVs for the reduction of chlorine gas (173 -1583 ppm) on a) gold, b) carbon, c) carbon - graphene modified and d) carbon - carbon nanotubes modified SPE in $[C_2mim][NTf_2]$ at a scan rate of 0.1V/s. The insets show the plots of the limiting/peak current for the reduction vs concentration.

7.6 Hydrogen Chloride Gas

7.6.1 Electrochemical Oxidation of Hydrogen Chloride Gas on Pt SPEs

The electrochemical behaviour of HCl gas is investigated on Pt SPEs. It is believed that HCl is its dissociated form of $[HCl_2]^-$ and H^+ in the RTIL. Figure 7.23 shows the electrochemical behaviour of 0.15 % hydrogen chloride gas on a Pt SPE scanned from 0 V to 2.2 V to -0.9 V and back to 0 V for two scans. It can be seen that there is a oxidation peak (I) at approximately 1.65 V which is attributed to the oxidation of $[HCl_2]^-$ by two electrons to form H^+ and Cl_2.[27] The electrogenerated chlorine is then reduced by two electrons at approximately 0.78 V (II) to form Cl^-. The formed and

already present H^+ then gets reduced (III) at -0.38 V to form H_2 which then gets oxidised (IV) at approximately 0 V. There is a pre peak before process III at approximately 0.2 V which was seen previously in the work done by Aldous et al.[27] and Silvester et al.[28] and has been attributed to the 2 competing reduction reactions of H^+. This was also seen and investigated in chapter 6 of this thesis when the behaviour of HCl gas was studied on a Pt microelectrode. Unlike the Pt microelectrode (chapter 6) the reduction process on the SPE is peak shaped. This is due to the differences in diffusion patterns, as on the SPE the working electrode is much larger (diameter 4 mm) which leads to linear diffusion of the species which in turns produces peak shaped currents whereas on a microelectrode it is dominated by radial diffusion which produces more steady state current. There are two peaks (first peak at -0.22 V (IVa) and second peak at 0.07 V (IVb)) for process IV which is the oxidation of hydrogen gas to form H^+ and this could be due to forming both adsorbed and free hydrogen ions.[28] This behaviour was not seen on the Pt microelectrode (chapter 6) where there was only one peak for the oxidation of H^+ and this could be a feature of the Pt SPE where the peaks are much clearer due to the larger area of the electrode (radial diffusion). On the second scan peak V becomes evident which is due to the oxidation of chloride species that was formed at process II and this was only present on the second scan as chlorine gas first needs to be formed (first scan).

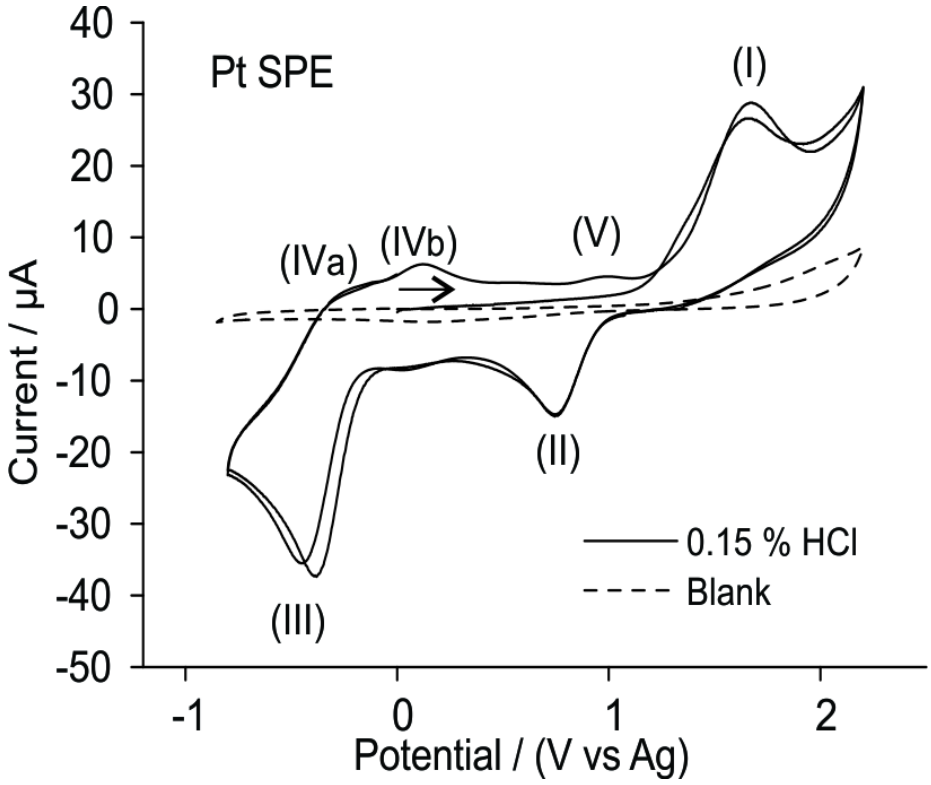

Figure 7.23: CV (2 cycles) for the oxidation of 0.15 % hydrogen chloride gas (nitrogen fill) on a Pt SPE in $[C_2mim][NTf_2]$ at a scan rate of 0.1 V/s Dotted line is the response in the absence of hydrogen chloride gas

Figure 7.24 shows CV scans for the oxidation of 0.15 % hydrogen chloride gas at varying scan rates between 0.05 V/s to 3 V/s when scanned from 0 V to 2.2 V to -0.9 V and back to 0 V (for clarity only the second scan is shown). It is evident that the peak currents for all processes increase with increasing scan rates. Therefore to study the behaviour of these processes the peak currents for all peaks (I to V) were plotted against the square root of scan rate (figure 7.25).

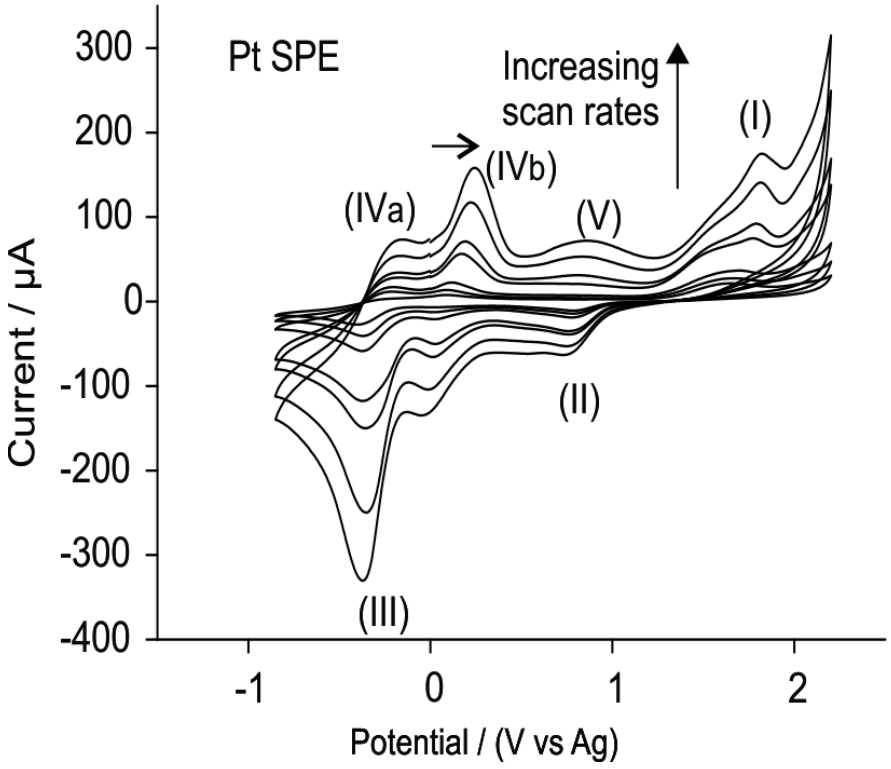

Figure 7.24: CV (second scan) for the oxidation of 0.15 % hydrogen chloride gas (nitrogen fill) on a Pt SPE in $[C_2mim][NTf_2]$ at varying scan rates between 0.05-3 V/s .

For peak I (oxidation of $[HCl_2]^-$, figure 7.25a and b) it can be seen that good linearity is achieved with plots with R^2 values of approximately 0.99 suggesting that the electrochemical process occurring is most likely diffusion controlled. From figure 7.25c it can be seen that excellent linearity is observed which tells us the reduction of Cl_2 is also diffusion controlled. The oxidation of H_2 also seems to follow a diffusion controlled process as a better fit is seen for the square root of scan rate (figure 7.25d and e) as compared to the scan rate (not shown). It is important to note here that due to the many processes occurring on the electrode surface the currents produced for each process is heavily influenced by the other processes.

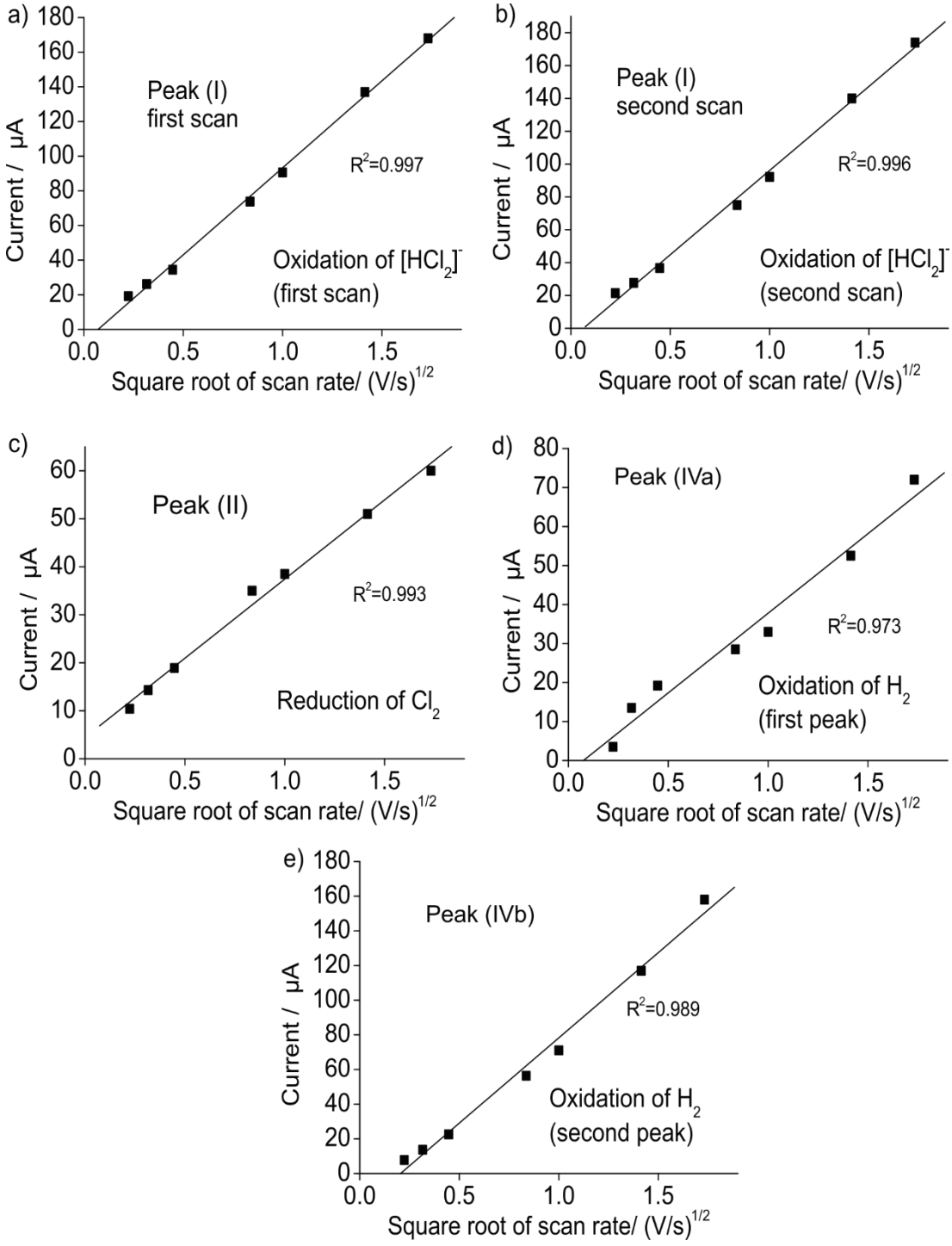

Figure 7.25: Plot of current vs square root of scan rate in $[C_2mim][NTf_2]$ on a Pt SPE for a) $[HCl_2]^-$ oxidation during first scan (peak I), b) $[HCl_2]^-$ oxidation during second scan (peak I), c) reduction of Cl_2 (peak II), d) H_2 oxidation (peak IVa) and e) H_2 oxidation (peak IVb)

However for the reduction of H^+, it was difficult to determine the nature of the process (pre peak at 0.2 V and peak at -0.38 V(process III)) as similar linearity was seen for both the scan rate (figure 7.26a and c) and square root of scan plots (figure

7.26b and d). However this deviation could be affected by the H^+ ions that are already present in the solution (in RTILs HCl exists as H^+ and $[HCl_2]^-$). When scanned negative first we already have H^+ in the solution that undergoes reduction to form H_2 which is clearly visible in figure 7.27. This process could affect the difficulty in accurately measuring the current for the reduction of protons.

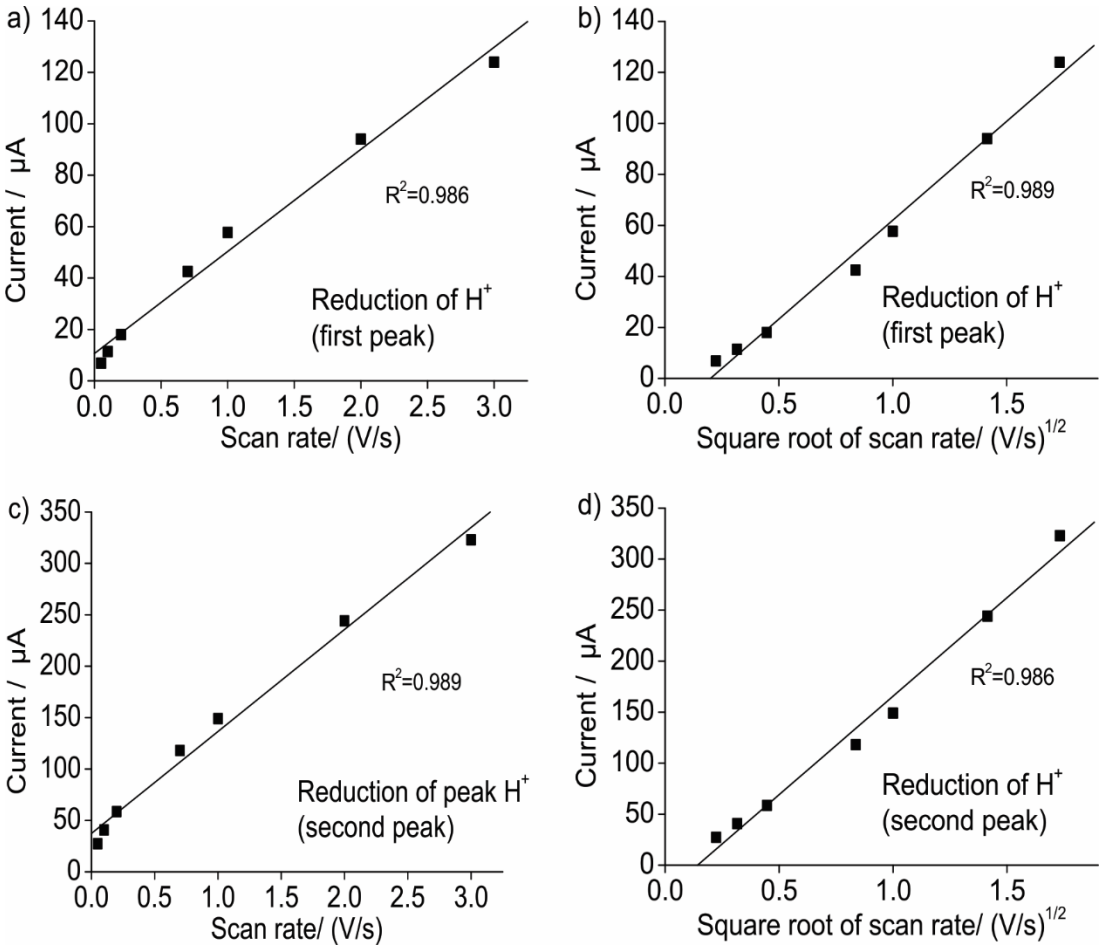

Figure 7.26: Plot of current vs scan rate in $[C_2mim][NTf_2]$ on a Pt SPE for a) H^+ reduction at -0.22 V, c) H^+ reduction at 0.07 V and plot of currents vs square root of scan rates in $[C_2mim][NTf_2]$ on a Pt SPE for b) H^+ reduction at -0.22 V and d) H^+ reduction at 0.07 V

HCl gas is thought to be in its dissociated form of H^+ and $[HCl_2]^-$ and it was shown in chapter 6 (figure 6.9) that when scanned negative before scanning positive from 0 V the H^+ that are already present in the RTIL gets reduced to H_2 which further supports the mechanism. Figure 7.27 shows the CVs at different scan rates obtained

by scanning negative first following by a full scan (0.4 V to -0.85 V to 2.2 to -0.85 V and to 0 V). Just like in the case of a microelectrode the second scan (black CV) produces a higher current as compared to the first scan (red CV). Figure 7.28 shows a plot of the normalised current (current for second process (black scan) divided by current for the first process (red scan)) vs the scan rate. The microelectrode result from chapter 6 figure 6.10 is also plotted in figure 7.28 to see the differences in the behaviour. It can be seen that on the Pt SPE even at low scan rates of 0.05 V/s and 0.1 V/s there is a significant difference in the current obtained between the first scan (red CV) and the second scan (black CV) for the reduction of H^+. This again can be explained by the differences in the size of the electrode where the SPE has a much larger area then the microelectrode therefore the H^+ that was generated from the second scan (black scan) has not diffused away from the electrode and together with the H^+ that is already in the solution undergoes the reduction to form H_2 (addition of both currents produced from the protons already present in the RTIL and the protons produced as a result of peak I). As the scan rates increase the normalised currents increase until sufficiently high enough scan rates (e.g. 2 and 4 V/s) where the timescale of the experiment is much smaller therefore not enough H^+ can be produced and this is seen clearly in figure 7.28, as the normalised current reaches a steady state.

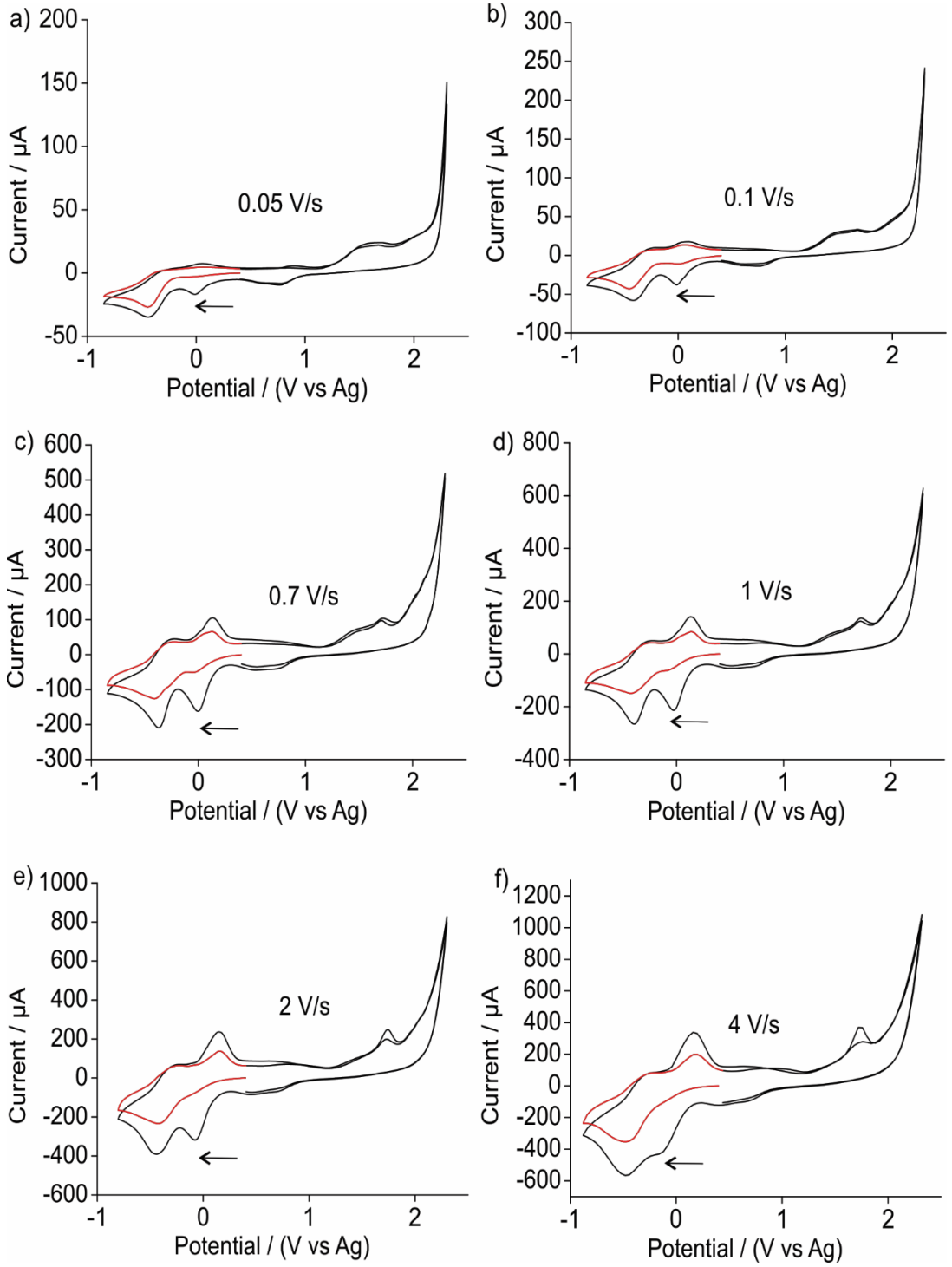

Figure 7.27: CVs for the reduction of 0.15 % hydrogen chloride gas (nitrogen fill) on a Pt SPE in $[C_2mim][NTf_2]$ at varying scan rates of a) 0.05 V/s, b) 0.1 V/s, c) 0.7 V/s, d) 1V/s, e) 2 V/s and f) 4 V/s. Red line shows CV scanning negative first (0.4 V to -0.85 V to 0.4 V). Black line shows the second CV cycle from 0.4 V to 2.2 V to -0.85 V to 2.2 V to 0.4 V.

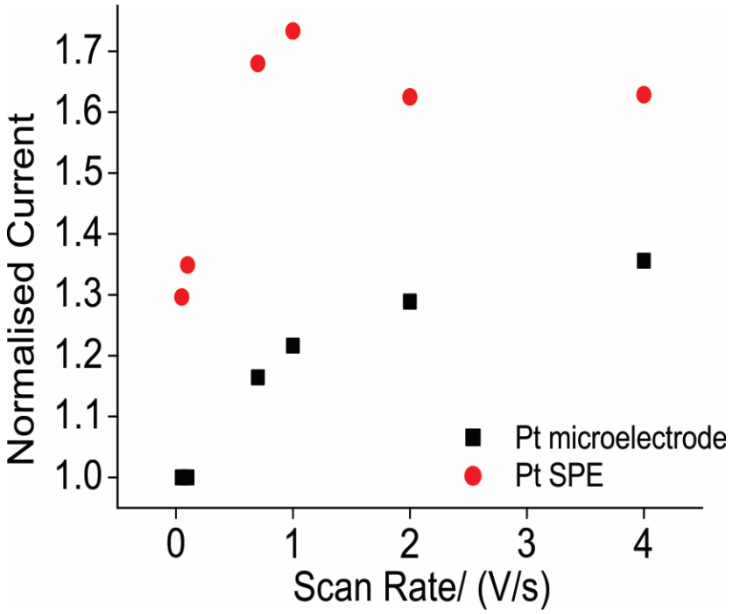

Figure 7.28: Plot of normalised current (current for second process (black scan)/current for the first process (red scan)) vs the scan rate obtained from figure 7.27 for Pt SPE (circle). The results obtained for Pt microelectrode (square) from chapter 6 figure 6.10 is also shown on this plot.

7.6.2 Analytical Utility of Hydrogen Chloride Gas on Pt SPEs

Once the electrochemical mechanistic behaviour of HCl gas was studied on a Pt SPE and compared to that of a Pt microelectrode the analytical utility of hydrogen chloride gas is studied on these Pt SPEs. Figure 7.29 shows typical CVs of six different concentrations of hydrogen chloride on a Pt SPE for both the first and second scan for each concentration. It can be seen that on the second scan there is a slight increase in the peak current for process I and this is due to the contribution of the chloride oxidation current process V. It can be seen that as the concentration increases the current increases for all peaks. Using the reduction of H^+ and the oxidation of $[HCl_2]^-$ (the current for the first scan was taken) where a measurable increase in the peak currents were obtained, a calibration graph was plotted (figure 7.30a and b).

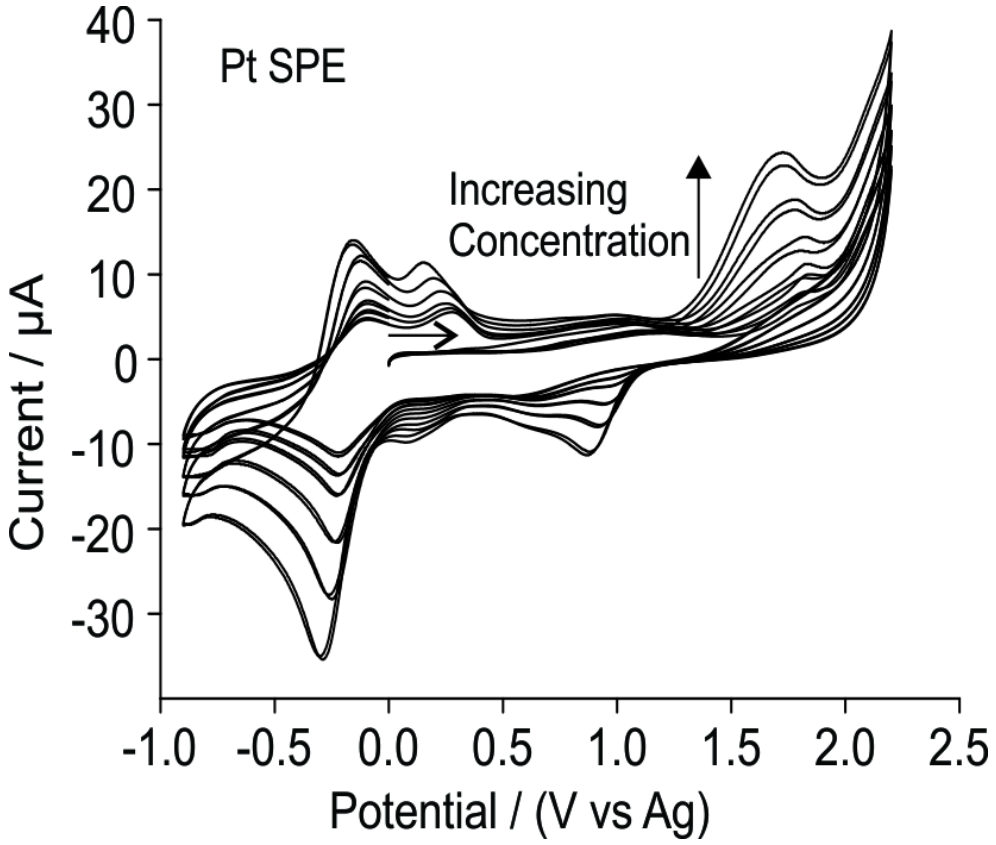

Figure 7.29: CV (first and second scan) for the oxidation of different concentrations (104, 168, 242, 431, 710 and 1048 ppm) of HCl gas on a Pt SPE in $[C_2mim][NTf_2]$ at a scan rate 0.1 V/s.

Figure 7.30 shows the calibration plots obtained from both the oxidation of $[HCl_2]^-$ (process I) and the reduction of protons (process III) and it can be seen that excellent linearity is observed with a R^2 values of > 0.99 and sensitivities/gradients of 1.73×10^{-8}A/ppm and 2.5×10^{-8} A/ppm, respectively for peak (I) and (III) respectively. Due to the amount of processes occurring at the electrode surface it was unsure if good linearity would be observed but excellent linearity was observed which is very crucial for sensing applications. LODs (3σ) of 45 ppm and 92 ppm were obtained for peak I and peak III, respectively, which clearly shows that Pt SPEs can be used in conjunction with RTILs for the electrochemical detection of low concentrations of hydrogen chloride gas.

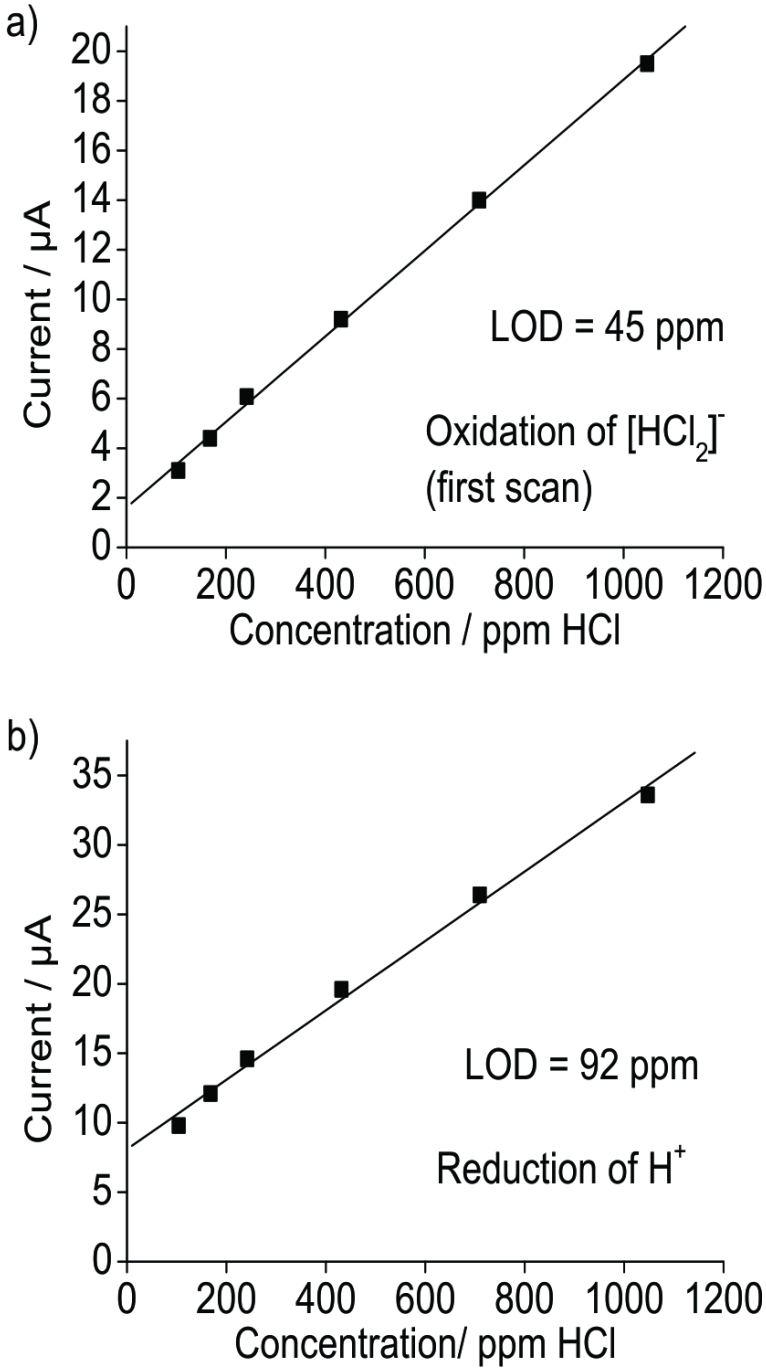

Figure 7.30: Calibration graph of peak current vs concentration for a) process I (first scan) and b) process III vs gas phase concentration obtained from the CVs for the oxidation of different concentrations (104, 168, 242, 431, 710 and 1048ppm) of hydrogen chloride gas on a Pt SPE in $[C_2mim][NTf_2]$.

7.6.3 Electrochemical Behaviour of Hydrogen Chloride Gas on Au and C SPEs

Figure 7.31 shows typical CVs obtained for the oxidation of HCl gas on Au SPE. The dotted line in the figure is the blank in the absence of HCl gas. The CV shows the second and third scan taken in the presence of HCl gas. It can be seen that there is a large stripping peak (A) at approximately 1.7 V which is masking the peak for the oxidation of $[HCl_2]^-$, and the current for the stripping peak increases at subsequent scans. It has been reported previously[27,29] that chloride impurities in RTILs can cause a chloride induced gold stripping peak at approximately 1.7 V that follows equation 7.1 on gold electrodes. It is probable that the same behaviour is seen on these Au SPEs. Process B is reported to be the reduction of dissolution by products as a result of process A.

$$Au_{surface}Cl^- \rightleftharpoons Au_{surface}Cl + e^- \qquad (7.1)$$

Using repetitive scans the “stripping peak” increases in current as more and more chloride are produced therefore increasing the amount of $Au_{surface}Cl^-$ formed. On the first scan the stripping peak was not evident as there were no free chloride present in the RTIL to form the $Au_{surface}Cl^-$ species. This instability in the surface makes Au SPEs not suitable for HCl gas sensing, particularly using the oxidation peak.

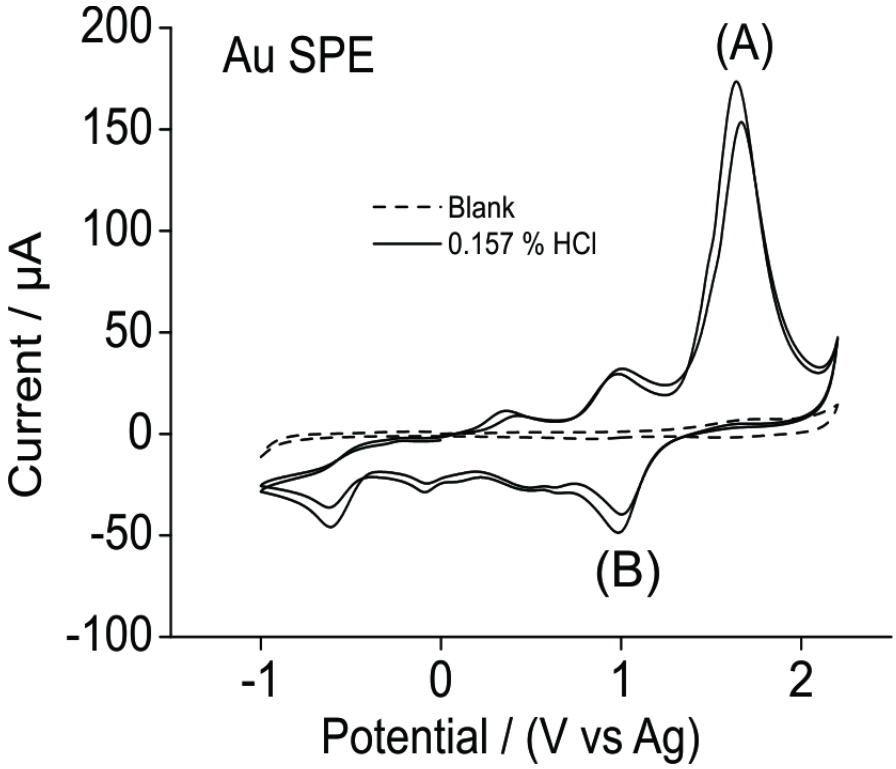

Figure 7.31: CV for the reduction of 0.15 % hydrogen chloride gas (nitrogen fill) on a Au SPE in $[C_2mim][NTf_2]$ at a scan rate of 0.1 V/s. Dotted line is the response in the absence of hydrogen chloride gas.

Figure 7.32 shows the behaviour of 0.15 % HCl gas on C SPEs. On the blank scan (dotted line) scanning up to 2 V causes a sharp increase in current. This feature has a reverse (reduction) process at approximately 1 V. This was not seen when scanned till 1.5 V (figure 7.17) and could be due to the oxidation and reduction of impurities on the carbon surface. This behaviour together with the large capacitance prevents them from being usable for the detection of hydrogen chloride gas as the analytical response is being masked. However to see the response of these electrodes in the presence of hydrogen chloride gas, 0.15 % HCl gas was allowed into the system and the response is shown in figure 7.32 (solid line). As expected no clear analytical response can be obtained for the concentration of HCl gas studied which signifies that C SPEs will also not be suitable for HCl gas sensing.

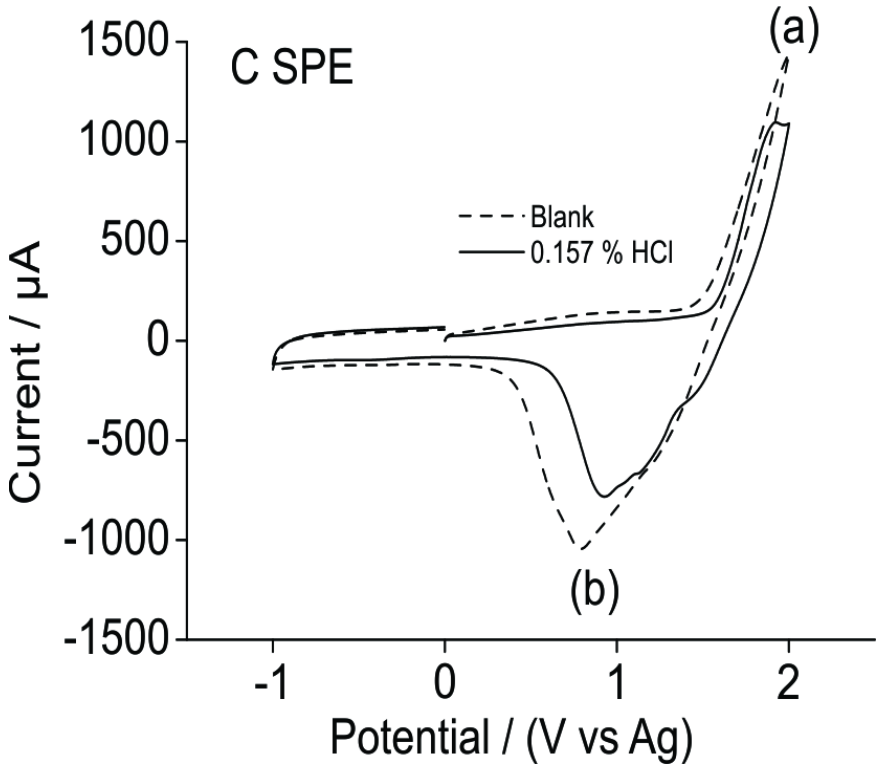

Figure 7.32: CV for the reduction of 0.15 % hydrogen chloride gas (nitrogen fill) on a C SPE in $[C_2mim][NTf_2]$ at a scan rate of 0.1 V/s Dotted line is the response in the absence of hydrogen chloride gas.

7.7 Comments about the Reproducibility, Reusability and Advantages of SPEs

It is important to note here that good reproducibility is seen within these low cost SPEs. On the SPEs the electrochemical behaviour of the gases were similar to different electrodes from the same batch which is very significant, as it suggests that these SPEs, which are usually mass produced, to cut cost, can actually be used for cheap detection of highly toxic gases. The same electrode can also be reused on multiple occasions to yield similar currents (σ of 0.7 % when SPE was used 3 days consecutively with the same solvent) for the matching concentration which suggests that these electrodes are robust and offer great reproducibility. Another main benefit is the limited shift of peak currents relative to the potential (although a quasi-reference electrode, Ag, is used). Another big advantage is the much lower response

times due to the microliter quantities of solvent used and the thin layer of solvent on top of the electrode surfaces. All these benefits that are seen on these SPEs make them attractive for cheap and portable sensors which would be ideal for untrained personnel in the field.

7.8 Conclusions

The electrochemical behaviour of methylamine, chlorine and hydrogen chloride gases has been investigated on various SPEs after physical characterisation with SEM and XPS. SEM revealed that the surfaces of these electrodes have very different porosity and roughness that could affect the voltammetry. XPS suggested that there were lead impurities on Pt, Rh and Bi impurities on Au and chloride impurities on C. These impurities are likely to be due to the screen printing process.

The electrochemical behaviour of methylamine and hydrogen chloride was investigated on Au, Pt and C surfaces while the electrochemical behaviour of chlorine gas has been investigated on Pt, Au, C, carbon nanotubes modified C and graphene modified C surfaces. Electrochemical behaviour of all three gases on the Pt SPE was very similar to the microelectrode. No unusual behaviour on the SPEs is seen which shows that the paste/polymeric binder that is used to make these Pt SPES do not react with the toxic gases in a detrimental way. The Pt SPEs proved to be the best surfaces for the detection of all three gases. On the Pt surface a LOD of 53 ppm for methylamine (Pt microelectrode 34 ppm), 137 ppm for chlorine (Pt microelectrode 106 ppm) and 45 ppm for hydrogen chloride gas (Pt microelectrode 102 ppm) was obtained.

Only methylamine gas was suitable for detection on Au SPE and a LOD of 101 ppm was obtained. The reaction of the formed chloride on the Au surface makes it not

suitable for the sensing of chlorine gas and for hydrogen chloride gas the voltammetry was complicated by chloride induced stripping peak. The carbon surfaces were deemed not suitable either due to limitations in the potential window on these surfaces or the large capacitance on these surfaces when used in conjunction with RTILs.

Results obtained so far are encouraging and suggest that low cost SPEs can be utilised for the detection of these three target gases with Pt SPEs providing the best response compared to Au and C. It is also interesting to note that the lead oxide found on Pt SPE surfaces do not seem to affect the electrochemical response. These SPEs, together with the use of small amounts of solvents, which is a huge advantage, may significantly reduce the costs of amperometric gas sensing devices. The ability to use non-volatile RTILs with SPEs is another major advantage as it will allow more robust sensors that are able to perform in harsh conditions such as high temperature and high pressures. These results suggest that low cost Pt SPEs could be used as electrode alternatives for the amperometric gas sensing of these target gases.

7.9 References

(1) Metters, J. P.; Kadara, R. O.; Banks, C. E. New directions in screen printed electroanalytical sensors: an overview of recent developments. *Analyst* **2011**, *136*, 1067-1076.
(2) Crowley, K.; O'Malley, E.; Morrin, A.; Smyth, M. R.; Killard, A. J. An aqueous ammonia sensor based on an inkjet-printed polyaniline nanoparticle-modified electrode. *Analyst* **2008**, *133*, 391-399.
(3) Choudhry, N. A.; Kampouris, D. K.; Kadara, R. O.; Jenkinson, N.; Banks, C. E. Next generation screen printed electrochemical platforms: Non-enzymatic sensing of carbohydrates using copper(ii) oxide screen printed electrodes. *Anal. Meth.* **2009**, *1*, 183-187.
(4) Murugappan, K.; Lee, J.; Silvester, D. S. Comparative study of screen printed electrodes for ammonia gas sensing in ionic liquids. *Electrochem. Commun.* **2011**, *13*, 1435-1438.
(5) Lee, J.; Murugappan, K.; Arrigan, D. W. M.; Silvester, D. S. Oxygen reduction voltammetry on platinum macrodisk and screen-printed electrodes in ionic

liquids: Reaction of the electrogenerated superoxide species with compounds used in the paste of Pt screen-printed electrodes? *Electrochim. Acta* **2013**, *101*, 158-168.
(6) Bonhôte, P.; Dias, A.-P.; Papageorgiou, N.; Kalyanasundaram, K.; Grätzel, M. Hydrophobic, highly conductive ambient-temperature molten salts†. *Inorg. Chem.* **1996**, *35*, 1168-1178.
(7) MacFarlane, D. R.; Meakin, P.; Sun, J.; Amini, N.; Forsyth, M. Pyrrolidinium imides: A new family of molten salts and conductive plastic crystal phases. *J. Phys. Chem. B* **1999**, *103*, 4164-4170.
(8) Johnson, F. M. The genetic effects of environmental lead. *Mutat. Res.* **1998**, *410*, 123-140.
(9) Berry, R. A. The manurial properties of lead nitrate. *J. Agr. Sci.* **1924**, *14*, 58-65.
(10) Höfft, O.; Bahr, S.; Himmerlich, M.; Krischok, S.; Schaefer, J.; Kempter, V. Electronic structure of the surface of the ionic liquid [EMIM][Tf_2N] studied by metastable impact electron spectroscopy (MIES), UPS, and XPS. *Langmuir* **2006**, *22*, 7120-7123.
(11) Silvester, D. S.; Broder, T. L.; Aldous, L.; Hardacre, C.; Crossley, A.; Compton, R. G. Using XPS to determine solute solubility in room temperature ionic liquids. *Analyst* **2007**, *132*, 196-198.
(12) Gottfried, J.; Maier, F.; Rossa, J.; Gerhard, D.; Schulz, P.; Wasserscheid, P.; Steinrück, H.-P. Surface studies on the ionic liquid 1-ethyl-3-methylimidazolium ethylsulfate using X-ray photoelectron spectroscopy (XPS). *Z. Phys. Chem.* **2006**, *220*, 1439-1453.
(13) Ikari, T.; Keppler, A.; Reinmöller, M.; Beenken, W. J.; Krischok, S.; Marschewski, M.; Maus-Friedrichs, W.; Höfft, O.; Endres, F. Surface electronic structure of imidazolium-based ionic liquids studied by electron spectroscopy. *Electron. J. Surf. Sci. Nanotechnol.* **2010**, *8*, 241-245.
(14) Hammond, J.; Gaarenstroom, S.; Winograd, N. X-ray photoelectron spectroscopic studies of cadmium-and silver-oxygen surfaces. *Anal. Chem.* **1975**, *47*, 2193-2199.
(15) Turner, N. H.; Single, A. M. Determination of peak positions and areas from wide-scan XPS spectra. *Surf. Interface Anal.* **1990**, *15*, 215-222.
(16) Debies, T. P.; Rabalais, J. W. X-ray photoelectron spectra and electronic structure of Bi_2X_3 (X = O, S, Se, Te). *Chem. Phys.* **1977**, *20*, 277-283.
(17) Schuhl, Y.; Baussart, H.; Delobel, R.; Le Bras, M.; Leroy, J.-M.; Gengembre, L.; Grimblot, J. Study of mixed-oxide catalysts containing bismuth, vanadium and antimony. Preparation, phase composition, spectroscopic characterization and catalytic oxidation of propene. *J. Chem. Soc. Faraday Trans. 1: Phys. Chem. Conden. Phase.* **1983**, *79*, 2055-2069.
(18) da Silva, R. M.; Kubaski, E. T.; Cava, S.; Moreira, M. L.; Sequinel, T.; Tebcherani, S. M. Development of a yellow pigment based on bismuth and molybdenum-doped TiO_2 for coloring polymers. *In. J. Appl. Ceram. Tech.* **2015**, *12*, E112-E119.
(19) Minges, M. L.; Committee, A. S. M. I. H.: *Electronic materials handbook: Packaging*; Taylor & Francis, 1989.
(20) Dumesuil, M. E.: Vitrifiable inorganic ceramic binder and silver compositions containing same. 1960.U.S Patent No.2942992
(21) Okamoto, Y.; Ishida, N.; Imanaka, T.; Teranishi, S. Active states of rhodium in rhodium exchanged Y zeolite catalysts for hydrogenation of ethylene and

acetylene and dimerization of ethylene studied with X-ray photoelectron spectroscopy. *J. Catal.* **1979**, *58*, 82-94.
(22) Kim, S. Y.; Baik, J. M.; Yu, H. K.; Kim, K. Y.; Tak, Y.-H.; Lee, J.-L. Rhodium-oxide-coated indium tin oxide for enhancement of hole injection in organic light emitting diodes. *Appl. Phys. Lett.* **2005**, *87*, 072105.
(23) Briggs, D. Handbook of X-ray Photoelectron Spectroscopy C. D. Wanger, W. M. Riggs, L. E. Davis, J. F. Moulder and G. E.Muilenberg Perkin-Elmer Corp., Physical Electronics Division, Eden Prairie, Minnesota, USA, 1979. pp. 190. *Surf. Interface Anal.* **1981**, *3*.
(24) Anderson, R. C.: Screen printing method and apparatus.1986. U.S Patent No. 4590854
(25) Murugappan, K.; Kang, C.; Silvester, D. S. Electrochemical oxidation and sensing of methylamine gas in room temperature ionic liquids. *J Phys. Chem. C* **2014**, *118*, 19232-19237.
(26) Carter, M. T.; Stetter, J. R.; Findlay, M. W.; Patel, V. Rational design of amperometric gas sensors with ionic liquid electrolytes. *ECS Trans.* **2014**, *64*, 95-103.
(27) Aldous, L.; Silvester, D. S.; Pitner, W. R.; Compton, R. G.; Lagunas, M. C.; Hardacre, C. Voltammetric studies of gold, protons, and $[HCl_2]^-$ in Ionic Liquids. *J. Phys. Chem. C* **2007**, *111*, 8496-8503.
(28) Silvester, D. S.; Aldous, L.; Hardacre, C.; Compton, R. G. An electrochemical study of the oxidation of hydrogen at platinum electrodes in several room temperature ionic liquids. *J. Phys. Chem. B* **2007**, *111*, 5000-5007.
(29) Aldous, L.; Silvester, D. S.; Villagran, C.; Pitner, W. R.; Compton, R. G.; Cristina Lagunas, M.; Hardacre, C. Electrochemical studies of gold and chloride in ionic liquids. *New J. Chem.* **2006**, *30*, 1576-1583.

8. Electrochemical Characterization of an Oleyl - Coated Magnetite Nanoparticle-modified Electrode

In this work, the electrochemical behaviour of oleyl-coated Fe_3O_4 nanoparticles synthesised via a chemical coprecipitation approach was investigated. A simple approach based on formation of a film of nanoparticles on an electrode surface was employed together with cyclic voltammetry (CV). Characterisation by SEM, confocal Raman spectroscopy and XPS showed that Fe_3O_4 nanoparticles with a particle size of 20 nm coated with oleic acid were synthesized. These nanoparticles showed superparamagnetic behaviour, and formed a homogeneous film from their solution when dried in air. The nanoparticle film electrodes displayed redox behaviour by CV in acidic media but not in alkaline media, which suggests that protons take part in the electrochemical reaction. It was estimated that there were ~240 layers of nanoparticles deposited on the surface and that only ~1 % of these nanoparticles were electrochemically active. This was attributed to either the long chain surfactant (oleic acid) or the large number of layers of nanoparticles inhibiting the electron transfer process.

8. ELECTROCHEMICAL CHARACTERIZATION OF AN OLEYL - COATED MAGNETITE NANOPARTICLE-MODIFIED ELECTRODE 211

8.1 Introduction 213

8.2 Experimental 217

8.2.1 Chemical Reagents 217

8.2.2 Synthesis of Particles 217

8.2.3 SEM 218

8.2.4 Confocal Raman Spectroscopy/Microscopy 219

8.2.5 XPS 219

8.2.6 Electrochemical Experiments 219

8.3 Results and Discussion 220

8.3.1 Characterisation of Fe_3O_4 Nanoparticles 220

8.3.1.1 Physical Characterisation 220

8.3.1.2 Confocal Raman Spectroscopy 221

8.3.1.3 XPS 223

8.3.2 Electrochemical Characterisation 224

8.3.2.1 Electrochemical Behaviour in 0.1 M H_2SO_4 225

8.3.2.2 Electrochemical Characterisation in Varying Concentrations of H_2SO_4 231

8.4 Conclusions 233

8.5 References 234

Work presented in this section has been published in the journal, ChemElectroChem titled, “Electrochemical Characterization of an Oleyl - Coated Magnetite Nanoparticle-modified Electrode”.

8. Electrochemical Characterization of an Oleyl - Coated Magnetite Nanoparticle-modified Electrode

8.1 Introduction

Current interest in magnetic nanoparticles arises from their unique properties, including magnetic anisotropy and superparamagnetism. Magnetite (Fe_3O_4) nanoparticles have the strongest saturation magnetization compared to any other naturally occurring iron oxide.[1] Combined with properties such as low toxicity, good biocompatibility, high stability and low production costs, these particles have attracted a lot of interest in medical and biological applications.[2] There is also substantial interest in their use as magnetic fluids, in data storage, catalysis and as electrode materials.[3-5] Magnetite nanoparticles are also being investigated for their use in sensing[2,6-10] and supercapacitors.[11,12]

Various methods to prepare magnetic Fe_3O_4 nanoparticles are available, such as co-precipitation, hydrothermal and solvothermal synthesis, microemulsion, sonochemical hydrolysis, mechanical grinding and laser ablation.[13,14] One big advantage of using the chemical co-precipitation method, other than being convenient and cheap, is the ability to produce fine, high purity particles that can be easily stabilised with surfactants. The use of surfactants to stabilise these synthesised nanoparticles is crucial as Fe_3O_4 nanoparticles have high surface energies and tend to aggregate. They also have high chemical activity and are easily oxidised to Fe_2O_3, with concomitant loss in magnetism.[3] In this chapter, magnetic Fe_3O_4 nanoparticles

are synthesised via a chemical co-precipitation method in a continuously stirred tank reactor (CSTR), as used recently in the preparation of titanium oxide nanoparticles.[15] Oleic acid was chosen as the surfactant due to its ability to effectively stabilise the nanoparticle. The cis-double bond in the middle of the oleic acid allows the structure to kink which results in a very dense monolayer around the nanoparticles and highly uniform nanoparticles.

Electrochemical techniques such as cyclic voltammetry and differential pulse voltammetry have been used for the detection of metallic (nickel and copper oxide) nanoparticles within a mixture.[16-18] For these techniques to work the behaviour of the individual metallic oxide nanoparticles have to be first fully understood and an extensive literature has to be built with all the various metallic oxide nanoparticles. In this work the electrochemical behaviour of oleyl-coated Fe_3O_4 nanoparticles in an acidic medium is reported.

Electrochemical characterisation of solid-state nanomaterials is not as straightforward as that of liquid or gaseous substances. This complexity results from the way the nanoparticles interact with the electrode. For instance, solution phase voltammetry of nanoparticles dispersed in an aqueous medium is not as ideal as physically attaching the nanoparticle to the electrode surface because of the low rate of diffusion of nanoparticles in solution.[19] Four strategies for the electrochemical characterisation of solid-state materials have been reported: the use of (i) compact crystal electrodes, (ii) composite electrodes, (iii) film electrodes with embedded particles, and (iv) direct immobilisation of solid particles.[20] Each method has its advantages and disadvantages. There has been a significant amount of electrochemical characterisation of magnetite samples in powder form using the composite electrodes method, employing a carbon paste electrode (CPE).[21-24]

Rodriguez et al.[25] reported the electrochemical behaviour of magnetite nanoparticles embedded in a CPE immersed in an acidic medium. They observed cathodic and anodic currents, when scanning the potential from the open circuit potential and proposed the following reactions for the cathodic and anodic processes, respectively:

$$Fe_3O_4 + 8H^+ + 2e^- \rightleftharpoons 3Fe^{2+} + 4H_2O \quad (8.1)$$

$$2Fe_3O_4 + H_2O \rightleftharpoons 2Fe_2O_3 + 2H^+ + 2e^- \quad (8.2)$$

Magnetite, Fe_3O_4 is a mixture of iron (III) and iron (II), and these components undergo reactions depending on the applied potential. Fetisov et al.[24] studied the electrochemical reduction of magnetite microcrystals in an acidic medium on CPEs and they proposed that the cathodic reaction occurring follows equation 8.1.

Mckenzie and Marken[19] studied the behaviour of the oxidised form of Fe_3O_4, i.e. Fe_2O_3, on tin-doped indium oxide electrodes in a phosphate buffer of various pH values (pH 5 to pH 9). They found that the reduction peak was pH-dependent and that at a sufficiently high pH, the voltammetric signal broadened and eventually split into two. They attributed the reduction process to:

$$Fe_2O_3 + 6H^+ + 2e^- \rightleftharpoons 2Fe^{2+} + 3H_2O \quad (8.3)$$

which is similar to the reaction proposed for the reduction of Fe_3O_4 by Fetisov[24] and by Rodriguez.[25]

Santos et al.[26] studied the electrochemical behaviour of magnetite nanoparticles in DMSO-water (HCl) mixtures on a CPE and found that there were two cathodic current peaks present, attributed to the reduction of two Fe(III) species in different chemical environments. One peak was attributed to magnetite and the other to goethite, and the presence of goethite was attributed to a synthetic production route.

Encinas et al.[27] reported the electrochemical behaviour of magnetite powder in CPEs in an acidic medium and they found that repetitive potential cycling gave well-defined redox peaks due to the Fe(III)/Fe(II) redox couple. Additionally, White et al.[28] studied the electrochemistry of natural magnetite in NaCl electrolyte solution and concluded that a solid state Fe(III) reduction was followed by the formation of an oxidized layer, and subsequent release of Fe(II) into the solution.

A drawback to using CPEs is the difficulty in determining the amount of electroactive material located at the electrode surface due to the presence of the organic binder used to prepare the electrode. The voltammetric peak current is directly proportional to the amount of organic binder. In this article, a simpler approach to characterise solid-state nanoparticles is explored, which is analogous to employing film electrodes with embedded particles.[20] Cyclic voltammetry is used as the primary electrochemical technique to obtain information.

There has been significant research into the voltammetry of magnetite in the form of powder and microcystals, but there is only little information on the electrochemical characterisation of magnetite nanoparticles coated by a surfactant.[25] In this study, we report the electrochemical behaviour on a glassy carbon electrode of synthesised Fe_3O_4 nanoparticles coated with a layer of oleic acid. These nanomaterials were also characterised by scanning electron microscopy (SEM), confocal Raman spectroscopy, superconducting quantum interference device (SQUID) magnetometry, and X-ray photoelectron spectroscopy (XPS).

8.2 Experimental

8.2.1 Chemical Reagents

The following reagents were from Sigma-Aldrich and used as received without further purification. Nafion^{TM} 117 solution (5 % in a mixture of lower aliphatic alcohols and water), ethanol (99 %), sulphuric acid (98 %), potassium hydroxide (98 %), powder samples of magnetite (95 %) and hematite (99 %), iron(II) sulphate (97 %), iron(III) chloride (97 %), oleic acid (99 %) and sodium hydroxide (NaOH, 98 %). Ultra-pure water with a resistance of 18.2 MΩ cm was prepared by a Ultra-pure laboratory water purification system (Millipore Pty Ltd., North Ryde, NSW, Australia).

8.2.2 Synthesis of Particles

The synthesis of the particles was carried out by Dr. Deeptangshu Chaudhary from the department of Chemical Engineering in Curtin University.

The magnetic nanoparticles were prepared using a controlled volume-time reaction through a spinning disc with a continuously stirred tank reactor (CSTR).[15] This gave a tightly-controlled particle size distribution of the iron oxide nanoparticles, following a 5-stage process. Briefly, this involved controlling the stoichiometry of reaction, the volumetric flow-rate of reactants, residence time in a single pass reaction, temperature and product separation through agitation. Based on the design shown by Akindeju et al.[15] the two inlets, inclined at 60° to the horizontal, separately inject the reactants, namely, 0.2 M $FeCl_3$ and 0.2 M $FeSO_4$ in the ratio of 2:1, such that the reaction occurs just at the surface of the disc. The product was extracted out of the reaction chamber into a vessel where the temperature is maintained at 80 °C and then 1 M NaOH was added at 10 mL/min while the impellor speed was

controlled at 350 rpm (revolutions per minute); this batch volume is denoted as the aerosol reacting volume.[29] The tank reactor volume was controlled by additional deionized water and this effectively controls the particle aggregation and settling characteristics after the formation of the magnetite particles. The seeding particles were formed within the confined volume and the contact time for the reactants was controlled through the rotational speed of the disc. Overflow containing the seed particles from the ends of the disc was collected into the aqueous CSTR reacting volume to produce precipitates, and this can undergo further reactions and result in particle growth. The mixing rate (impeller rotation per second) and the degree of supersaturation are critical factors that limit the size and distribution of the nanoparticles formed. The nanoparticles continued to grow by layering until a critical particle size occurred and then the coating agent (0.1 % oleic acid) was stirred through the reactor tank at the rate 10 mL/min to allow uniform coating of the nanoparticle aggregates. This offers a relatively scalable, simple and continuous process for producing uniform and predictable particle size and size distribution and at a larger scale. The coated nanoparticle solution is diluted by 50% by adding methanol reagent and this solution is centrifuged at 1500 rpm for 3 minutes. The supernatant was then carefully decanted. A solvent exchange process consisting of repeated dilution of the concentrated nanoparticle solution with methanol followed by centrifugation was carried out 3-4 times.

8.2.3 SEM

Scanning electron microscopy (SEM) characterisation of the working electrode surface was performed using a Zeiss Neon 40 EsB model. A drop (1.5 μL) of Fe_3O_4 nanoparticles (in methanol) was drop-cast onto a 5 mm diameter glassy carbon disk (Pine Research Instrumentation, Durham, North Carolina, USA) and after solvent

evaporation the electrode was placed on the SEM sample stage without any additional sample preparation. The images were obtained using an accelerating voltage of 5 kV.

8.2.4 Confocal Raman Spectroscopy/Microscopy

Confocal Raman experiments were conducted using a WITec alpha300SAR (WITec, Ulm, Germany) equipped with a frequency doubled Nd:YAG laser (excitation wavelength: 531.87 nm). Experiments were performed using a 60× objective with cover glass correction (Nikon CFI, NA: 0.8), which focuses the laser to a spot of ~400 nm (lateral) and ~800 nm (vertical). The laser power at the sample position was kept below 0.5 mW. Spectra were obtained with 2 s integration time over five accumulations. Confocal Raman microscopy images spectra were recorded over an area of 30 μm × 30 μm with 100 × 100 pixels with an integration time of 100 ms. Images were constructed by applying a sum filter on the recorded spectra over a range from 655 cm^{-1} to 735 cm^{-1}.

8.2.5 XPS

XPS analysis was performed on a Quantum 2000 Scanning ESCA Microprobe (Physical Electronics Instruments, Chanhassen, MN, USA) having a Mg Kα radiation as the X-Ray source. Binding energies were calibrated using the C 1s peak referenced at 284.5 eV. Scans were conducted in the range of 0-1000 eV.

8.2.6 Electrochemical Experiments

Fe_3O_4 nanoparticles in methanol (1.5 μL, 0.13 M) were drop-cast onto a 3 mm diameter glassy carbon electrode (CH instruments, Austin, Texas, USA) surface and the solvent was allowed to evaporate for 10 minutes. Nafion™ 117 solution (6 μL) was drop cast onto the electrode surface to form a film. The Nafion™ film was

employed to stabilise the electrochemical response by holding the particles onto the surface. The prepared glassy carbon electrode was employed in a 3 electrode cell with a 0.5 mm diameter Pt coil counter electrode (BASi, West Lafayette, Indiana, USA, 25cm) and a Ag/AgCl/1 M KCl reference electrode (CH instruments, Austin, Texas, USA) inserted into a homemade glass cell containing 8 mL of aqueous sulfuric acid electrolyte solution. The electrolyte solution was purged with nitrogen gas for 15 minutes, to remove oxygen prior to the cyclic voltammetry experiments.

8.3 Results and Discussion

The synthesized Fe_3O_4 nanoparticles were first characterised by various techniques to determine their size, magnetic properties and homogeneity.

8.3.1 Characterisation of Fe_3O_4 Nanoparticles

8.3.1.1 Physical Characterisation

Figure 8.1 shows the topographic images of the glassy carbon electrode surface with drop-cast Fe_3O_4 nanoparticles taken using a scanning electron microscopy. SEM provides high resolution imaging of the topography of the electrode surface and also size and distribution of the particles on the surface. The average diameter of these particles was determined to be ca. 20 nm (using figure 8.1 d and the size analysis program on the SEM). In figure 8.1 a, cracking of the surface is obvious. This is often an issue with deposition of solution-based nanoparticles due to the way they dry, giving rise to cracks at the centre of the droplet and is well documented as the "coffee stain effect"[30] which leaves most of the particles concentrated on the outer side of the droplet. The increasing magnification of the images (figure 8.1, a to d) shows the distribution of the particles on the surface. The magnetic properties of the nanoparticles were determined using a superconducting quantum interference device

(SQUID) magnetometer by Dr. Deeptangshu Chaudhary from the department of chemical engineering in Curtin University (data not shown). Magnetic measurements made at zero-field-cooling (ZFC) and field-cooling (FC) revealed that the coated nanoparticles display superparamagnetic characteristics.

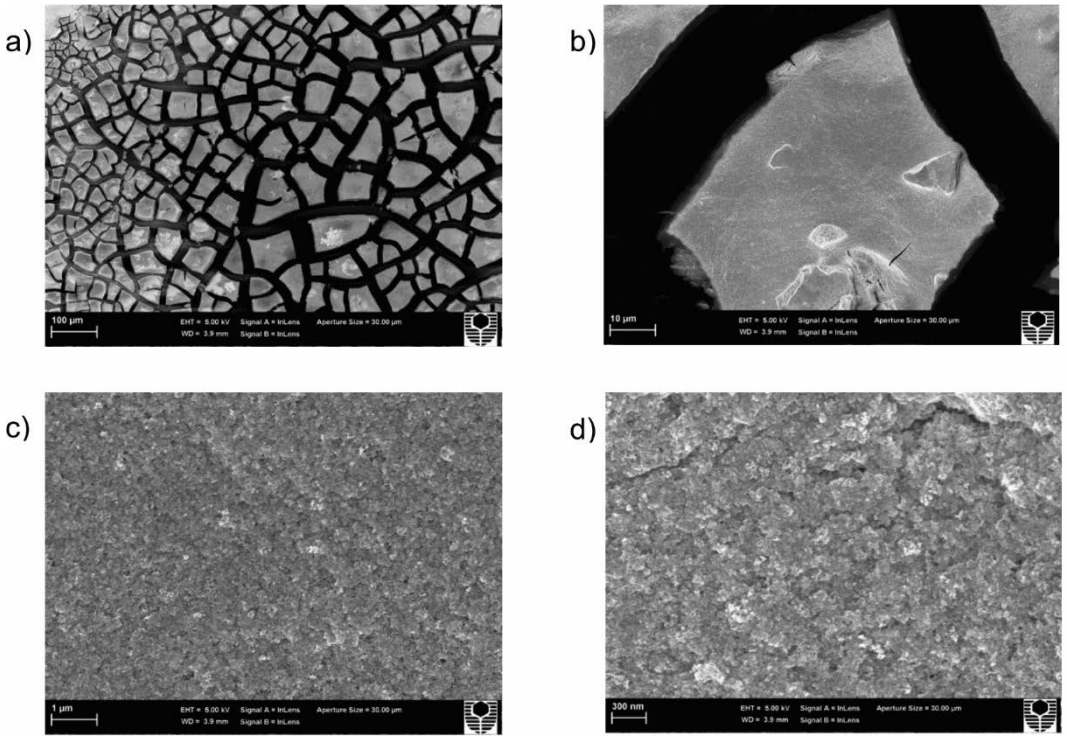

Figure 8.1: Scanning electron micrographs of Fe_3O_4 drop-cast on a glassy carbon electrode surface with varying magnifications. a) 100×, b) 1 000×, c) 10 000×, d) 25 000×.

8.3.1.2 Confocal Raman Spectroscopy

Raman spectroscopy was performed in order to 'fingerprint' the vibrational and rotational bands that are specific to Fe_3O_4. Several Raman spectroscopic studies[31-35] of Fe_3O_4 have been carried out and the characteristic bands for Fe_3O_4 are located at ca. 670, 538 and 306 cm^{-1}. Figure 8.2 shows the Raman spectrum obtained for the synthesized Fe_3O_4 nanoparticles, together with the spectra for pure magnetite and hematite. It can be seen that the spectrum of synthesized Fe_3O_4 nanoparticles closely resembles the pure magnetite sample. The absence of peaks at 205 cm^{-1} and 268 cm^{-1} further indicates that the synthesised material is indeed Fe_3O_4 and not

Fe_2O_3. As mentioned earlier, Fe_3O_4 nanoparticles are susceptible to oxidation, which would result in a loss of magnetisation. The spectrum suggested that the synthesised nanoparticles were not oxidised.

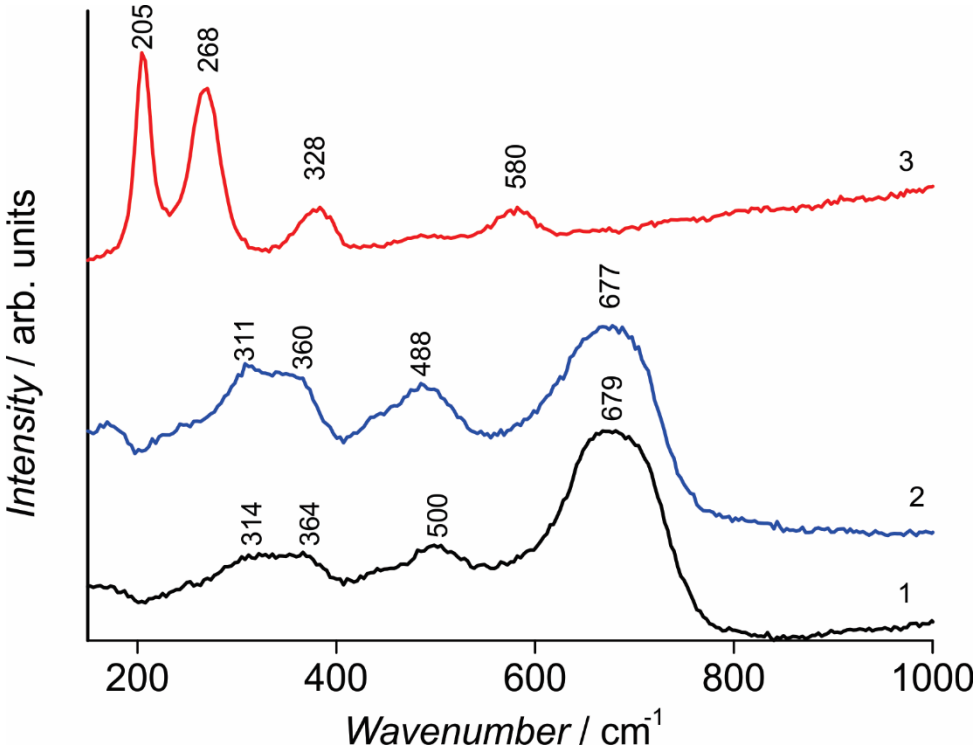

Figure 8.2: Raman spectra of synthesised Fe_3O_4 with oleic acid as the surfactant (black, 1), pure magnetite powder (blue, 2), pure hematite powder (red, 3)

The advantage of using confocal Raman spectroscopy is the ability to obtain an optical image and then scan a particular area within that image location which can give information on the homogeneity of the sample. Figure 8.3 shows an optical image of the Fe_3O_4 nanoparticles drop-cast and dried onto a glass slide. The colour profile that was generated by applying a sum filter on the recorded spectra over a range from 655 cm^{-1} to 735 cm^{-1} shows that the sample is very homogeneous.

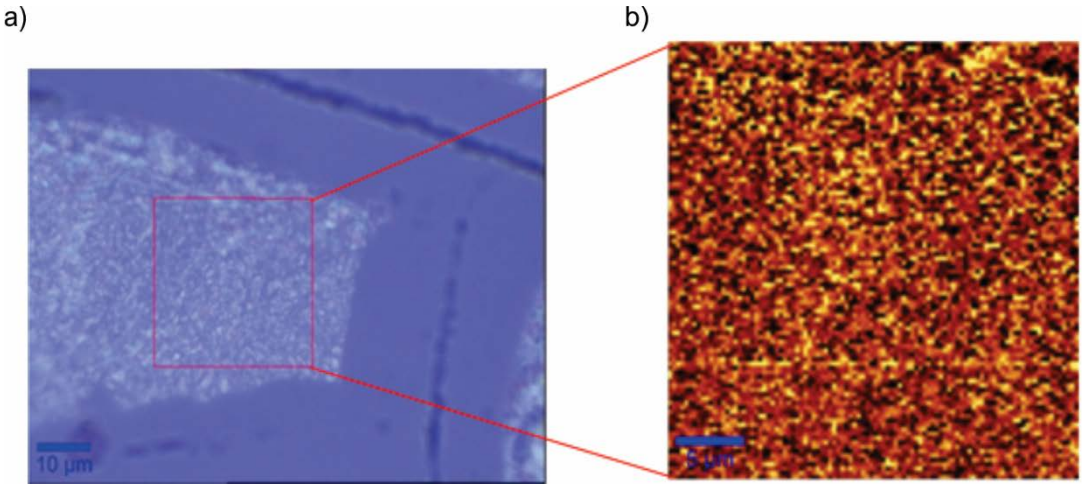

Figure 8.3: a) An optical image of Fe_3O_4 on a glass slide. b) Colour profile that was generated by applying a sum filter on the recorded spectra over a range from 655 cm^{-1} to 735 cm^{-1}

8.3.1.3 XPS

The XPS spectra of the magnetite nanoparticles in the C 1s, O 1s and Fe 2p region are shown in Figure 8.4. In Figure 8.4a it can be clearly seen that there are two C 1s peaks, positioned at 284.5 eV and 287.9 eV. The peak at 284.6 eV is due to carbon atoms in the aliphatic chain and the peak at 287.9 eV is believed to be due to the carboxylate component, which indicates that the oleic acid is absorbed to the surface of the nanoparticles.[36] The absence of a peak at 290 eV indicates that there is no free acid present on the oleic acid-coated nanoparticles.[36] Figure 8.4c shows the Fe 2p spectrum. The peaks at 711.2 eV and 724.9 eV are attributed to the Fe $2p_{3/2}$ and Fe $2p_{1/2}$ region, respectively. Magnetite powders without a surfactant have the characteristic peaks for the Fe $2p_{3/2}$ and Fe $2p_{1/2}$ region at ca. 710.6 eV and 724.1eV, respectively.[37,38] However, coated nanoparticles were shown to have a slightly higher binding energy[36,39] for the Fe $2p_{3/2}$ region at ca. 710.8 eV, 711.0 eV, and for the Fe $2p_{1/2}$ region at ca. 724.6 eV, 725.0 eV, which agrees well with our results. Together with the Raman spectroscopy results, the XPS results strongly indicate that oleic

acid-coated homogenous Fe_3O_4 nanoparticles were synthesized in solution with minimal free acid.

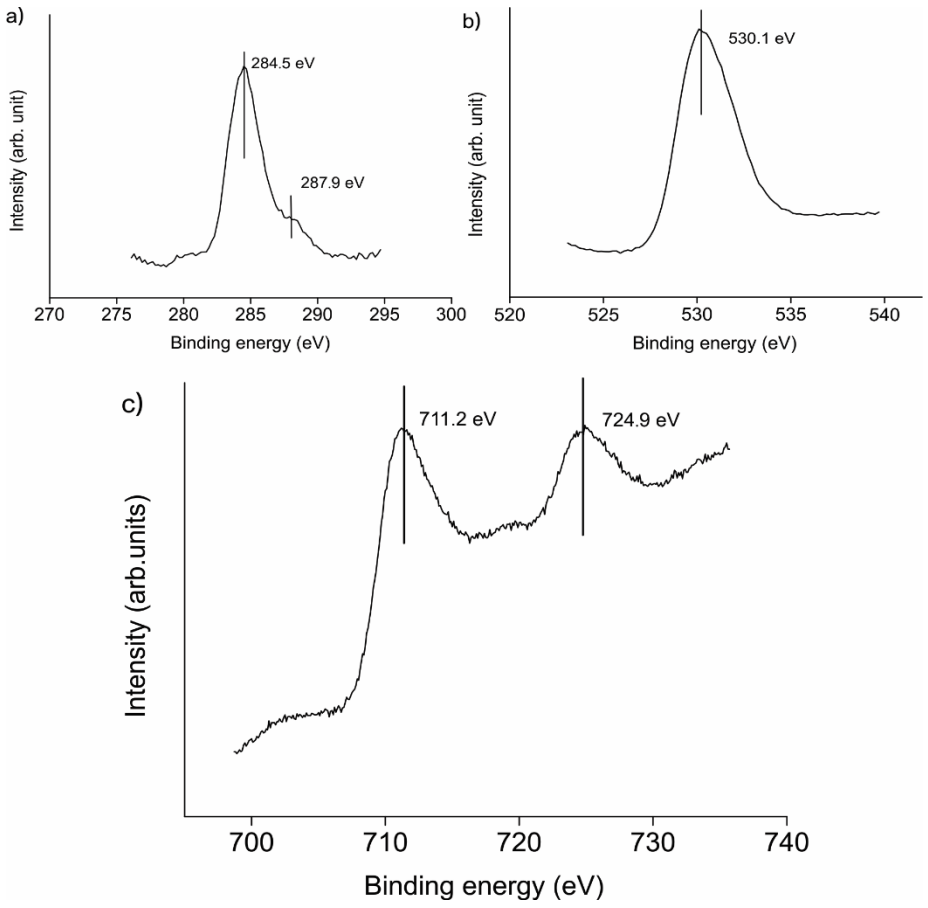

Figure 8.4: XPS Spectra obtained from Fe_3O_4 nanoparticles; a) C 1s region; b) O 1s region; c) Fe 2p region

8.3.2 Electrochemical Characterisation

A known amount of nanoparticles was drop-cast onto a clean glassy carbon electrode and covered with a film of the perfluorosulfonate ionomer, Nafion^{TM}. The purpose of Nafion^{TM} was to immobilise the particles onto the electrode surface and prevent dissolution into the solution. These electrodes are referred to here as Fe_3O_4/Nafion^{TM}/GC electrodes. Figure 8.5 shows the schematic of the nanoparticles on the electrode. Experiments were performed in KOH and H_2SO_4 aqueous electrolytes, but no electrochemical redox signal was apparent in the alkaline

medium. Hence, a thorough electrochemical study was performed in aqueous H_2SO_4 media. Additionally, electrodes coated with Fe_3O_4 nanoparticles without oleic acid coatings were studied and the measured currents were considerably higher compared the currents measured for the coated nanoparticles. However the electrochemical signal decreased rapidly over time. This might be due to the aggregation of the particles or the oxidative instability of the nanoparticles over time due to the absence of surfactants. Accordingly, only the coated nanoparticles were studied in detail. During the following voltammetric experiments, the open circuit potential was determined to be 0.4 V, corresponding to the mid-point potential obtained from cyclic voltammetry (CV) experiments.

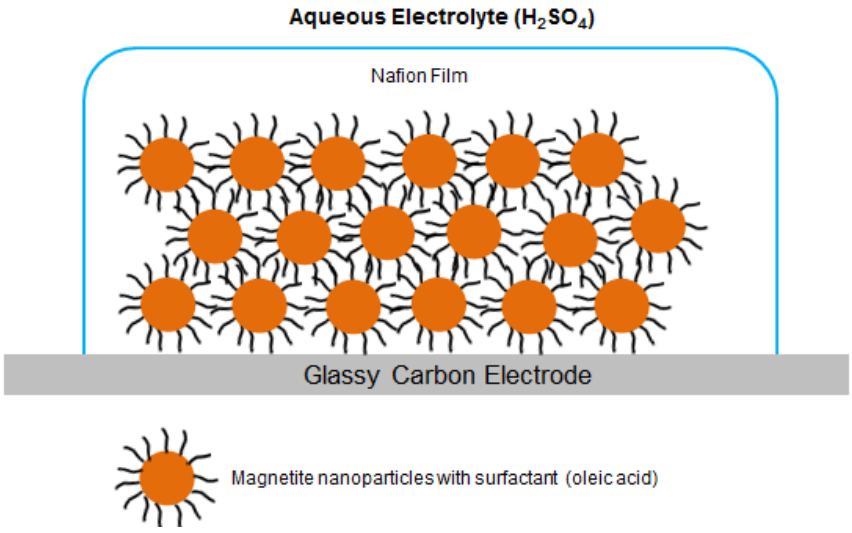

Figure 8.5: Cartoon showing the Fe_3O_4/Nafion^{TM}/GC electrode

8.3.2.1 Electrochemical Behaviour in 0.1 M H_2SO_4

Figure 8.6 shows a CV of a Fe_3O_4/Nafion^{TM}/GC electrode immersed in 0.1 M H_2SO_4, at a scan rate of 0.1 Vs^{-1}. The potential was scanned from -0.4 to 1.2 V and back to -0.4 V. An oxidative peak is observed at +0.69 V and a corresponding reductive peak at +0.23 V, with a peak-to-peak separation of ~470 mV. Several reduction reactions of magnetite have been proposed in the literature.[21-28] When the

initial potential of -0.4 V was applied, a significant cathodic current indicated that an electrochemical reaction occurred at this potential.

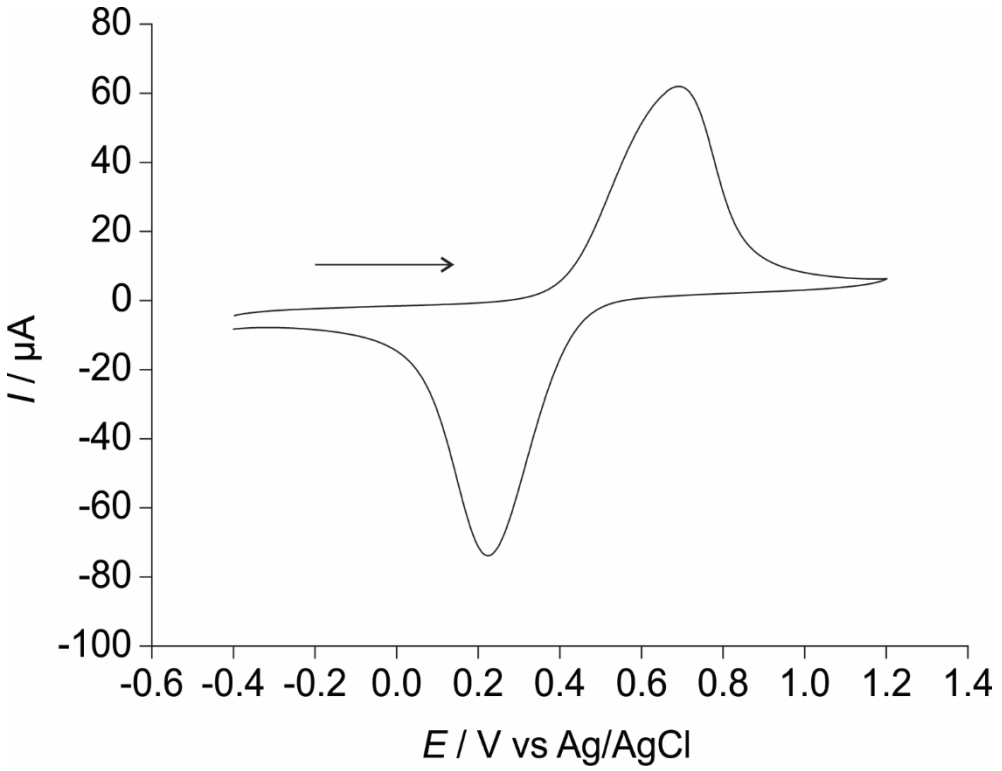

Figure 8.6: Cyclic voltammogram Fe_3O_4/Nafion™/GC electrodes in 0.1M H_2SO_4. Scan rate 0.1 V/s

Considering the literature and our experimental conditions, the reduction process occurring at this initial potential is:

$$Fe_3O_4 + 8H^+ + 2e^- \rightarrow 3Fe^{2+} + 4H_2O \qquad (8.4)$$

in which the iron(III) is reduced to iron(II), in agreement with the observations of Rodrigues et al.[25] and Fetisov et al.[24] Subsequent scanning from the initial potential (-0.4 V, figure 8.6) to +1.2 V and back yields a single oxidation peak and a single reduction peak on the forward and reverse scans, respectively. These are attributed to the one-electron oxidation and reduction processes:

$$Fe(II) \rightleftharpoons Fe(III) + e^- \qquad (8.5)$$

Similarly, when the initial potential is +1.2 V, an anodic current indicates that an oxidation process occurs at this potential. This is attributed to the immediate oxidation of the Fe_3O_4 on the electrode surface, according to the process:

$$2Fe_3O_4 + H_2O \rightarrow 2Fe_2O_3 + 2H^+ + 2e^- \qquad (8.6)$$

in which the iron (II) is oxidised to iron (III), in agreement with the work of Rodriguez et al.[25] The absence of redox peaks in alkaline electrolyte media further suggests that protons are required in the electrochemical reaction.

The bell-shaped peaks for the transitions between iron(III) and iron(II) (eq. 8.4, and figure 8.6) are reminiscent of thin-film voltammetric behaviour,[40] which is consistent with the manner in which the magnetite is drop-cast on the electrode surface and then covered with a Nafion^{TM} layer. The cation-exchange characteristics of Nafion^{TM} helps to keep any cationic products of the electrochemical reactions trapped at the surface. Additionally, this process also helps to prevent any physical loss of material from the surface. The large ΔE_p, ca. 470 mV at 0.1 Vs^{-1}, however, is not characteristic of a thin-film or surface-confined reaction with rapid kinetics. Figure 8.7 shows CVs of Fe_3O_4/Nafion^{TM}/GC electrode at different sweep rates. It can be seen that the ΔE_p increases with sweep rate, indicative of a quasi-reversible process. In solid-state voltammetry, the large ΔE_p has been attributed to large structural changes in the crystal lattice during the electrochemical conversion.[41,42]

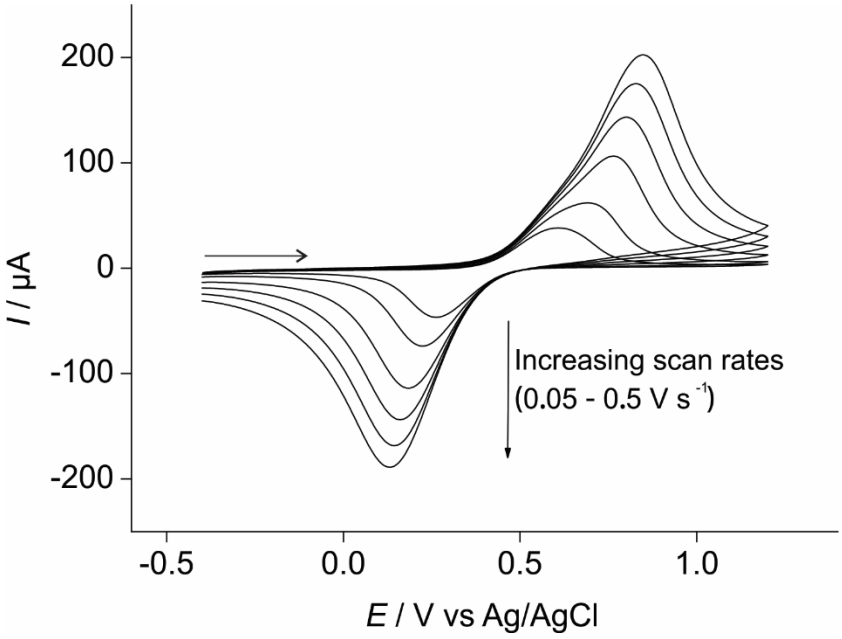

Figure 8.7: Cyclic voltammograms for Fe_3O_4/Nafion^{TM}/GC electrodes in 0.1M H_2SO_4 at increasing scan rates from 0.05 to 0.5V/s.

The current obtained for both the oxidative and reductive peak at various scan rates was plotted against the square root of scan rate (figure 8.8). A linear response was obtained, which suggests that the electrochemical process occurring is diffusion-controlled; however, the peak shape indicates otherwise and combined with the non-zero intercept suggests that complex kinetic processes are at play.

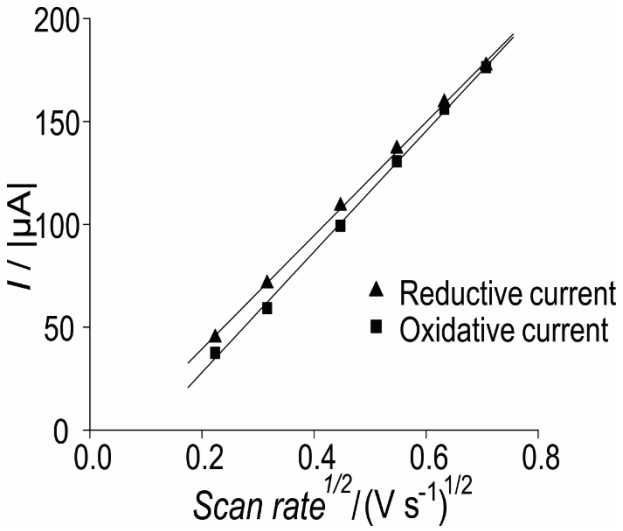

Figure 8.8: Plot of oxidative and reductive peak current vs square root of scan rate (obtained from CVs in figure 8.7)

Peak shapes in solid state voltammetry depend on several parameters, such as particle size distribution, surface reactivity relative to that of the bulk, changes in the kinetic regime, and electrode passivation[20] which may account for the shoulder before the oxidation peak in figure 8.7. Taking into account the proposed reaction mechanism and our experimental conditions, it is believed that the process is primarily a diffusion-controlled process, where the diffusion of protons from the electrolyte occurs through the Nafion™ film to reach the Fe_3O_4 nanoparticles.

The charge passed in the reaction was obtained by integrating the redox peaks in the CV. The moles of electrochemically-active material, *m*, were found using Faraday's law:

$$Q = mnF \tag{8.7}$$

where *Q* is the charge, *n* is the number of electrons taking part in the reaction and *F* is Faraday's constant. The charge *Q* was found to be 2.32 (± 0.13) $\times 10^{-4}$ C (oxidation peak), averaged over three different films. Since the peaks in the CVs are attributed to the one-electron transition between iron (II) and iron (III) oxidation states of the iron oxide material, *n* is equal to 1. Therefore the number of moles of iron that are electrochemically active was 2.40 x 10^{-9} moles. In comparison, the number of moles of iron drop-cast onto the electrode, determined via the volume and concentration of the nanoparticles deposited, was 1.95 x 10^{-7} moles. This suggests that only ca. 1 % of the material on the electrode surface is electroactive. This may be a consequence of the nanoparticles being coated with oleic acid, which insulates the surface, or due to the multilayer structure of the nanoparticles on the surface, such that only those close to the GC electrode surface are active.

Using the radius of the nanoparticles (10 nm) and the density of Fe_3O_4 (5.17 g cm^{-3})[43] it can be estimated that there are approximately 56,000 molecules of Fe_3O_4 in one nanoparticle. The amount of material placed onto the surface corresponds to ~2.08×10^{12} nanoparticles. The dried nanoparticle films were found to occupy a ca. 2 mm diameter disc in the centre of the 3 mm diameter GC electrode (a feature of the coffee stain effect mentioned previously, and confirmed via SEM) which gives 6.64×10^{17} nanoparticles per m^2 on the electrode. Assuming that the nanoparticles are arranged in a close-packed hexagonal array, for monolayer coverage we would expect there to be 2.76×10^{15} nanoparticles per m^2, giving approximately 240 layers of nanoparticles.

Experiments were performed on a series of Fe_3O_4/Nafion^{TM}/GC electrodes (Figure 8.9) to check the reproducibility of the films formed via solution casting and drying. The CVs show good reproducibility with a mean charge (Q) of 2.31(± 0.13) $\times 10^{-4}$ C for the oxidation and 2.33(± 0.2) $\times 10^{-4}$ C for the reduction.

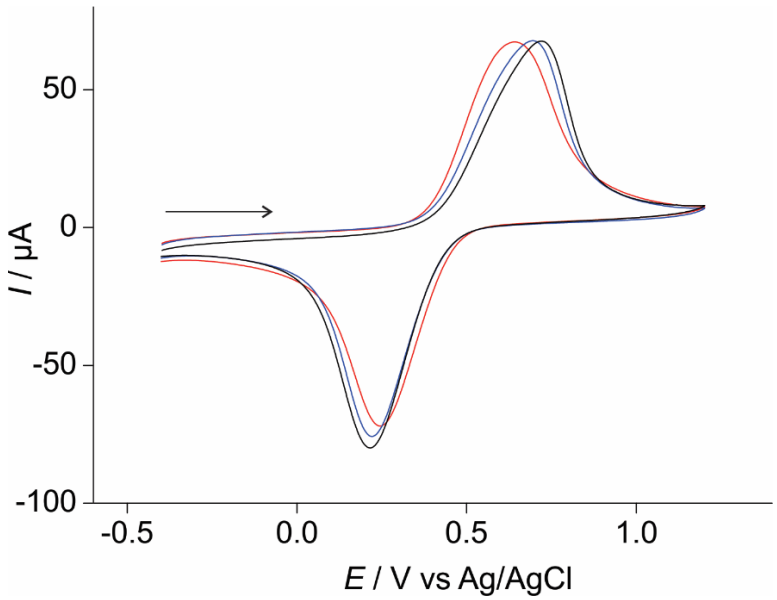

Figure 8.9: Cyclic voltammograms for Fe_3O_4 nanoparticles drop-cast on a GC electrode in 0.1 M of H_2SO_4 showing film reproducibility. Each colour represents a new film. Scan rate 0.1 V/s

To further examine the electrochemical behaviour, the initial potential was set at either extreme of the potential region (figure 8.10). The initial potentials serve to transform the Fe_3O_4 into either oxidised or reduced forms (according to equations 8.4 and 8.6) and the CV results in switching between these two forms. One scan (black) was from -0.4 V to 1.2 V and back to -0.4 V and the other CV (red) was in the opposite direction. It can be seen that there is minimal change in the currents and peak potentials, which shows excellent stability and reproducibility of the redox processes.

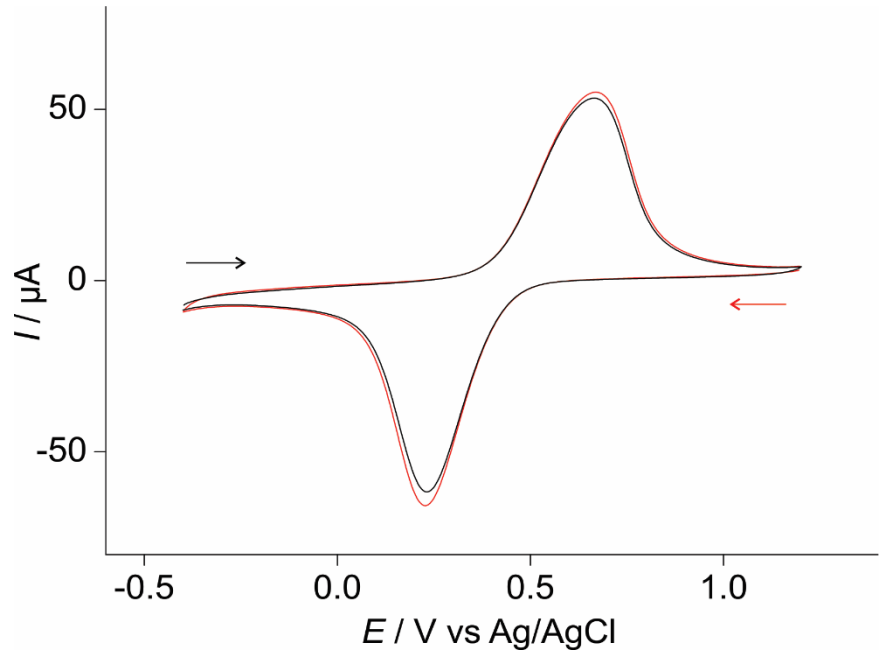

Figure 8.10: Cyclic voltammograms for Fe_3O_4 nanoparticles drop-cast on a GC electrode in 0.1 M of H_2SO_4. Red CV scanned from 1.2 V to -0.4 V. Black CV scanned from -0.4 V to 1.2 V. Scan rate 0.1 V/s.

8.3.2.2 Electrochemical Characterisation in Varying Concentrations of H_2SO_4

To further investigate the behaviour of the film in an acidic medium, the concentration of acid was varied. Figure 8.11 shows the CVs obtained with different concentrations of acid, ranging from 0.08 M to 0.4 M. According to the reaction mechanism proposed (equation 8.4) one would expect the currents to increase with

increased concentrations of protons, however this behaviour was not observed. The peak to peak separation for the different concentrations of acid was between 0.47 and 0.63 V without any systematic change. At higher concentrations of acid there was in fact a decrease in current (charge) which could be due to acid dissolution of magnetite. An extensive study of the dissolution of iron in iron oxides in nitric acid and sulphuric acid has been carried out by Salmimies et al.,[44] who found that at high enough concentrations of acid ranging between 0.1 to 0.4 M, the acidic dissolution of magnetite occurs. Other studies in various acidic media[45-47] have also shown the dissolution of iron oxides at high enough concentrations of acid.

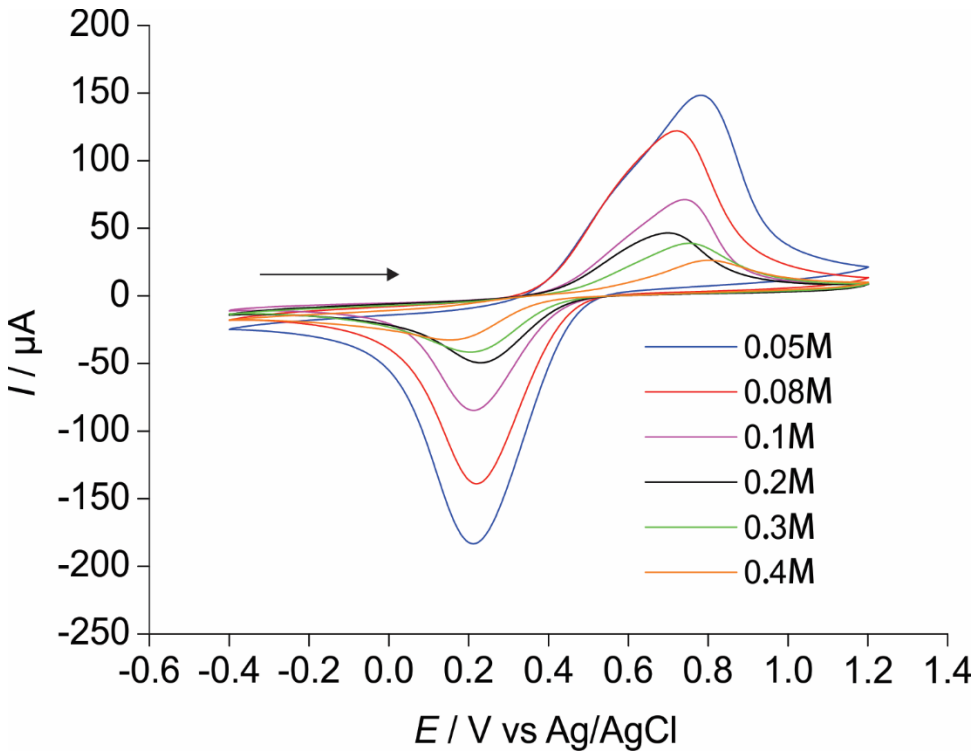

Figure 8.11: Cyclic voltammogram for Fe_3O_4/Nafion™/GC electrodes in varying concentrations of H_2SO_4 electrolyte from 0.08 to 0.4 M. Scan rate of 0.1V/s.

Figure 8.12 shows ten repetitive cyclic voltammograms for Fe_3O_4/Nafion™/GC electrodes in 0.1 M and 0.4 M H_2SO_4. It can be seen that stable voltammograms are only present in the 0.1 M electrolyte. There is a continuous decrease in both the

anodic and cathodic peak currents for experiments conducted in 0.4 M H_2SO_4, suggesting that there is a decreasing amount of material on the surface of the glassy carbon electrode, possibly dissolved by the higher concentration of acid.

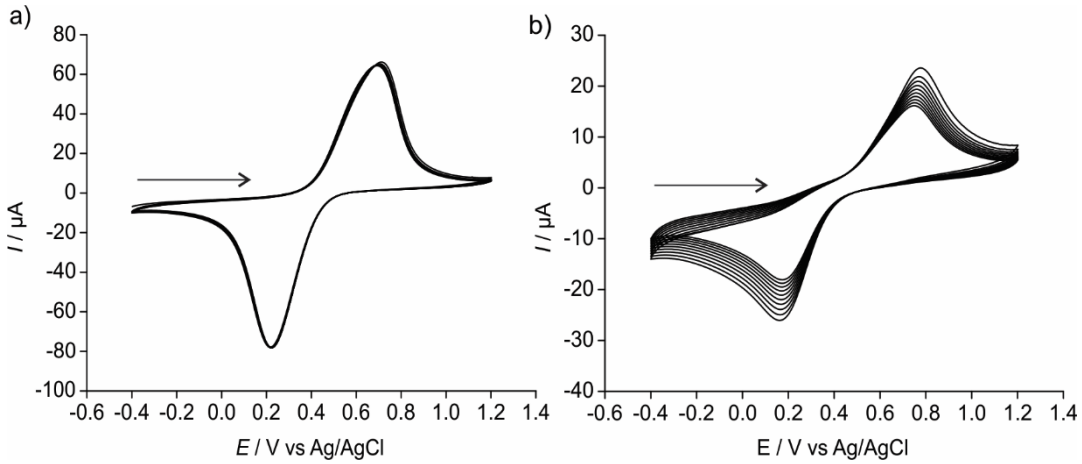

Figure 8.12: Ten repetitive cyclic voltammograms for Fe_3O_4/Nafion^{TM}/GC electrodes in a) 0.1M H_2SO_4 and b) 0.4M H_2SO_4. Scan rate 0.1V/s

8.4 Conclusions

The electrochemical behaviour of oleic acid-coated Fe_3O_4 nanoparticles in the form of a Fe_3O_4/Nafion^{TM}/GC electrode was examined. Additionally, a range of physical characterisation methods confirmed the properties of this material with a nanoparticle size of ~20 nm and having superparamagnetic behaviour.

The electrochemical study of the modified electrode performed in H_2SO_4 electrolyte solution showed that these nanoparticles were electrochemically active, producing anodic and cathodic peaks when cyclic voltammetry was performed. However, it was found that only ~1 % of the nanoparticle material was electrochemically active. This could be due either to the surfactant, oleic acid, inhibiting electron transfer, or the aggregation of a large amount of nanoparticles together during the droplet evaporation stage (“coffee stain” effect), or a combination of both. These results

open up new opportunities for mechanistic studies and analytical applications of magnetite nanoparticles.

8.5 References

(1) Cornell, R. M.; Schwertmann, U.: *The iron oxides: Structure, properties, reactions, occurrences and uses*; Wiley, 2003.
(2) Al-Ghamdi, A. A.; Al-Hazmi, F.; Al-Tuwirqi, R. M.; Alnowaiser, F.; Al-Hartomy, O. A.; El-Tantawy, F.; Yakuphanoglu, F. Synthesis, magnetic and ethanol gas sensing properties of semiconducting magnetite nanoparticles. *Solid State Sci.* **2013**, *19*, 111-116.
(3) Wu, W.; He, Q.; Jiang, C. Magnetic iron oxide nanoparticles: Synthesis and surface functionalization strategies. *Nanosc. Res. Lett.* **2008**, *3*, 397-415.
(4) Stanić, Z.; Stepanović, J.; Simić, Z. Voltammetric and potentiometric characterization of magnetite electrode for the assay of weak organic acids in non-aqueous media. *Polyhedron* **2012**, *45*, 43-47.
(5) Zhao, X.; Johnston, C.; Crossley, A.; Grant, P. S. Printable magnetite and pyrrole treated magnetite based electrodes for supercapacitors. *J. Mater. Chem.* **2010**, *20*, 7637-7644.
(6) Rossi, L.; Quach, A.; Rosenzweig, Z. Glucose oxidase–magnetite nanoparticle bioconjugate for glucose sensing. *Anal. Bioanal. Chem.* **2004**, *380*, 606-613.
(7) Bagherzadeh, M.; Ansari, S.; Riahi, F.; Farahbakhsh, A. A dopamine sensor based on pre-concentration by magnetic nanoparticles. *In. J. Electrochem.* **2013**, *2013*, 10.
(8) Cui, H.; Yang, W.; Li, X.; Zhao, H.; Yuan, Z. An electrochemical sensor based on a magnetic Fe3O4 nanoparticles and gold nanoparticles modified electrode for sensitive determination of trace amounts of arsenic(iii). *Anal. Meth.* **2012**, *4*, 4176-4181.
(9) Ai, Z.; Deng, K.; Wan, Q.; Zhang, L.; Lee, S. Facile microwave-assisted synthesis and magnetic and gas sensing properties of Fe_3O_4 nanoroses. *J. Phys. Chem. C* **2010**, *114*, 6237-6242.
(10) Fang, B.; Wang, G.; Zhang, W.; Li, M.; Kan, X. Fabrication of Fe_3O_4 nanoparticles modified electrode and its application for voltammetric sensing of dopamine. *Electroanal.* **2005**, *17*, 744-748.
(11) Qu, Q.; Yang, S.; Feng, X. 2D Sandwich-like heets of iron oxide grown on graphene as high energy anode material for supercapacitors. *Adv. Mater.* **2011**, *23*, 5574-5580.
(12) Mishra, A. K.; Ramaprabhu, S. Magnetite decorated multiwalled carbon nanotube based supercapacitor for arsenic removal and desalination of seawater. *J. Phys. Chem. C* **2010**, *114*, 2583-2590.
(13) Shen, Y. F.; Tang, J.; Nie, Z. H.; Wang, Y. D.; Ren, Y.; Zuo, L. Preparation and application of magnetic Fe_3O_4 nanoparticles for wastewater purification. *Sep. Purif. Technol.* **2009**, *68*, 312-319.
(14) Sun, J.; Zhou, S.; Hou, P.; Yang, Y.; Weng, J.; Li, X.; Li, M. Synthesis and characterization of biocompatible Fe_3O_4 nanoparticles. *J Biomed. Mater. Res. A* **2007**, *80A*, 333-341.

(15) Akindeju, M. K.; Pareek, V. K.; Tade, M. O.; Rohl, A. L. A novel spinning disc continuous stir tank and settler reactor (sdcstr) model for continuous synthesis of titania: a phenomenological model. *Chem. Eng. Commun.* **2011**, *198*, 73-84.
(16) Teo, W. Z.; Pumera, M. Simultaneous direct voltammetric determination of metal-oxide nanoparticles from their mixture (CuO/NiO). *ChemElectroChem* **2014**, *1*, 249-253.
(17) Teo, W. Z.; Ambrosi, A.; Pumera, M. Direct electrochemistry of copper oxide nanoparticles in alkaline media. *Electrochem. Commun.* **2013**, *28*, 51-53.
(18) Giovanni, M.; Ambrosi, A.; Pumera, M. The inherent electrochemistry of nickel/nickel-oxide nanoparticles. *Chem. Asian J.* **2012**, *7*, 702-706.
(19) McKenzie, K. J.; Marken, F. Direct electrochemistry of nanoparticulate Fe_2O_3 in aqueous solution and adsorbed onto tin-doped indium oxide. *Pure. Appl. Chem.* **2001**, *73*, 1885-1894.
(20) Grygar. T.; Marken, F.; Schröder, U.; Scholz, F. Electrochemical analysisis of solids. A review. Collection Czech. Chem. Commun. **2002**, 67, 163–208
(21) Allen, P. D.; Hampson, N. A.; Bignold, G. J. The electrodissolution of magnetite: Part I. The electrochemistry of Fe3O4/C discs-potentiodynamic experiments. *J. Electroanal. Chem. Interfacial Electrochem.* **1979**, *99*, 299-309.
(22) Allen, P. D.; Hampson, N. A.; Bignold, G. J. The electrodissolution of magnetite: Part II. The oxidation of bulk magnetite. *J. Electroanal. Chem. Interfacial Electrochem.* **1980**, *111*, 223-233.
(23) Das, C. M.; Sudersanan, M. Electrochemical studies of magnetite coating on carbon steel in ascorbic and picolinic acid. *J. Appl. Electrochem.* **2003**, *33*, 333-338.
(24) Fetisov, V.; Ermakov, A.; Belysheva, G.; Fetisov, A.; Kamyshov, V.; Brainina, K. Electrochemical dissolution of magnetite in acid solutions. *J. Solid State Electrochem.* **2004**, *8*, 565-571.
(25) Rodríguez-López, A.; Torres-Torres, D.; Mojica-Gomez, J.; Estrada-Arteaga, C.; Antaño-López, R. Characterization by electrochemical impedance spectroscopy of magnetite nanoparticles supported on carbon paste electrode. *Electrochim. Acta* **2011**, *56*, 8078-8084.
(26) Santos, F. J.; Varanda, L. C.; Ferracin, L. C.; Jafelicci, M. Synthesis and electrochemical behavior of single-crystal magnetite nanoparticles. *J. Phys. Chem. C* **2008**, *112*, 5301-5306.
(27) Encinas, P.; Lorenzo, L.; Tascón, M. L.; Vázquez, M. D.; Sánchez-Batanero, P. Electrochemical study of iron(II) and iron(III) compound mixtures in the solid state. Application to magnetite characterization. *J. Electroanal. Chem* **1994**, *371*, 161-166.
(28) White, A. F.; Peterson, M. L.; Hochella Jr, M. F. Electrochemistry and dissolution kinetics of magnetite and ilmenite. *Geochim. Cosmochim. Acta* **1994**, *58*, 1859-1875.
(29) Moody, E. G.; Collins, L. R. Effect of mixing on the nucleation and growth of titania particles. *Aerosol Sci. Technol.* **2003**, *37*, 403-424.
(30) Deegan, R. D.; Bakajin, O.; Dupont, T. F.; Huber, G.; Nagel, S. R.; Witten, T. A. Capillary flow as the cause of ring stains from dried liquid drops. *Nature* **1997**, *389*, 827-829.
(31) Shebanova, O. N.; Lazor, P. Raman spectroscopic study of magnetite ($FeFe_2O_4$): a new assignment for the vibrational spectrum. *J. Solid State Chem.* **2003**, *174*, 424-430.
(32) Verble, J. L. Temperature-dependent light-scattering studies of the Verwey transition and electronic disorder in magnetite. *Phys. Rev. B* **1974**, *9*, 5236-5248.

(33) De Faria, D. L. A.; Venâncio Silva, S.; De Oliveira, M. T. Raman microspectroscopy of some iron oxides and oxyhydroxides. *J. Raman Spectrosc.* **1997**, *28*, 873-878.
(34) Gasparov, L. V.; Tanner, D. B.; Romero, D. B.; Berger, H.; Margaritondo, G.; Forró, L. Infrared and Raman studies of the Verwey transition in magnetite. *Phys. Rev. B* **2000**, *62*, 7939-7944.
(35) Graves, P. R.; Johnston, C.; Campaniello, J. J. Raman scattering in spinel structure ferrites. *Mater. Res. Bull.* **1988**, *23*, 1651-1660.
(36) Zhang, L.; He, R.; Gu, H.-C. Oleic acid coating on the monodisperse magnetite nanoparticles. *Appl. Surf. Sci.* **2006**, *253*, 2611-2617.
(37) Yamashita, T.; Hayes, P. Analysis of XPS spectra of Fe^{2+} and Fe^{3+} ions in oxide materials. *Appl. Surf. Sci.* **2008**, *254*, 2441-2449.
(38) Kuznetsov, M. V.; Linnikov, O. D.; Rodina, I. V. X-ray photoelectron spectra of magnetite nanopowders after chromium(VI) sorption from aqueous solutions. *Inorg. Mater.* **2012**, *48*, 169-175.
(39) Yuan, Y.; Rende, D.; Altan, C. L.; Bucak, S.; Ozisik, R.; Borca-Tasciuc, D.-A. Effect of surface modification on magnetization of iron oxide nanoparticle colloids. *Langmuir* **2012**, *28*, 13051-13059.
(40) Bard, A. J.; Faulkner, L. R.: *Electrochemical methods: Fundamentals and applications*; Wiley, 2000.
(41) Bond, A. M.; Colton, R.; Daniels, F.; Fernando, D. R.; Marken, F.; Nagaosa, Y.; Van Steveninck, R. F. M.; Walter, J. N. Voltammetry, electron microscopy, and x-ray electron probe microanalysis at the electrode-aqueous electrolyte interface of solid microcrystalline cis- and trans-$Cr(CO)_2(dpe)_2$ and trans-$[Cr(CO)_2(dpe)_2]^+$ complexes (dpe = Ph2PCH2CH2PPh2) mechanically attached to carbon electrodes. *J. Am. Chem. Soc.* **1993**, *115*, 9556-9562.
(42) Shaw, S. J.; Marken, F.; Bond, A. M. Detection of new features associated with the oxidation of microcrystalline tetrathiafulvalene attached to gold electrodes by the simultaneous application of electrochemical and quartz crystal microbalance techniques. *Electroanal.* **1996**, *8*, 732-741.
(43) Yoon, T.; Kim, J.; Kim, J.; Lee, J. Electrostatic self-assembly of fe3o4 nanoparticles on graphene oxides for high capacity lithium-ion battery anodes. *Energies* **2013**, *6*, 4830-4840.
(44) Salmimies, R.; Mannila, M.; Kallas, J.; Häkkinen, A. Acidic dissolution of magnetite: experimental study on the effects of acid concentration and temperature. *Clays Clay Miner.* **2011**, *59*, 136-146.
(45) Bruyére, V. I. E.; Blesa, M. A. Acidic and reductive dissolution of magnetite in aqueous sulfuric acid: Site-binding model and experimental results. *J. Electroanal. Chem. Interfacial Electrochem.* **1985**, *182*, 141-156.
(46) Sidhu, P. S.; Gilkes, R. J.; Cornell, R. M.; Posner, A. M.; Quirk, J. P. Dissolution of iron oxides and oxyhydroxides in hydrochloric and perchloric acids. *Clays Clay Miner.* **1981**, *29*, 269-276.
(47) Chastukhin, A. E.; Izotov, A. D.; Gorichev, I. G.; Kutepov, A. M. Analysis of Fe_2O_3 and Fe_3O_4 dissolution kinetics in terms of the chain mechanism model. *Theor. Found. Chem. Eng.* **2003**, *37*, 398-406.

9. Synthesis and Characterisation of Platinum Macroporous Framework

Macroporous metallic materials have received a lot of attention recently for their use in electrochemical applications, due their properties such as large surface area, large pore volume and abundance of active sites for reactions. There are various ways to prepare macroporous structures but in this work the frameworks are electrochemically deposited. The main advantage of this is the ability to form the template in situ on the substrate electrode. In this work, macroporous platinum structures were synthesised using a 'bottom up' approach. First, polystyrene spheres (diameter 100 nm) suspended in water were dropcast onto a glassy carbon disk electrode. Platinum metal was then electrodeposited onto the electrode from a platinum salt solution (H_2PtCl_6 in 0.5 M H_2SO_4). The polystyrene spheres were then dissolved in THF, yielding a macroporous Pt framework with a much larger active surface area as compared to the bare disk electrode. The metal framework was then characterized using scanning electron microscopy to determine the distribution and the sizes of the pores. The electrochemical properties were assessed by cyclic voltammetry of two different redox couples, ferricyanide (inner sphere) and ferrocene (outer sphere), after activation in sulphuric acid.

9. SYNTHESIS AND CHARACTERIZATION OF PLATINUM MACROPOROUS FRAMEWORK **239**

9.1 Introduction **241**

9.2 Experimental **242**

9.2.1 Chemical Reagents 242

9.2.2 Electrochemical Experiments 243

9.2.3 SEM 243

9.3 Results and Discussion **243**

9.3.1 Synthesis of Metal Frameworks 243

9.3.2 SEM Characterisation 246

9.3.3 Electrochemical Characterisation 248

9.4 Conclusions **252**

9.5 References **253**

9. Synthesis and Characterization of Platinum Macroporous Framework

9.1 Introduction

Nanoporous materials are classified into three main categories by IUPAC.[1] Microporous refers to pore dimensions between 0.2-2 nm, mesoporous refers to materials with pore dimensions between 2-50 nm and macroporous is used for pore dimensions between 50-1000 nm. There has been a lot of work done on porous metal oxides as gas sensor materials,[2] however very little work on bare metal frameworks for amperometric gas sensing has been reported. Nanoporous metallic materials have received a lot of attention recently for their use in electrochemical applications[3-6] due their properties such as large surface area, large pore volume and abundance of active sites for reactions. There are various ways to prepare macroporous structures such as lithography, electroless deposition, hydrogen reduction of preformed macroporous oxides and electrochemical deposition.[3,7-9] Advantages of electrochemical deposition include the avoidance of contamination by residues from chemical syntheses and the ability to form the template in situ on the substrate electrode.

Most of the work in the area of gas sensing for these metal frameworks is modification of the working electrode surface for the oxygen electroreduction due to its importance in fuel cells. Kucernak et al.[10] reported the use of mesoporous platinum with pore dimensions of 3.4 nm for oxygen reduction and methanol oxidation and have found that about only one quarter of the pore surface area appears to be electrochemically active. Birkin et al.[11] reported the electrochemical reduction of oxygen on platinum microelectrodes after modification with mesoporous platinum and found that there was accelerated reduction kinetics together with efficient mass

transfer. Evans et al.[12] described the use of mesoporous platinum microelectrodes for the oxidation of hydrogen peroxide and found that there was a considerable increase in the surface area which produced higher currents and also enhanced the catalytic activity towards the oxidation. All these studies have been reported in an aqueous medium and to the best of my knowledge no work has been reported on the use of these metallic frameworks as electrode materials in an RTIL medium. In this work, macroporous platinum structures that were synthesised using a 'bottom up' approach using a polystyrene template will be characterised by scanning electron microscopy (SEM) and electrochemistry.

9.2 Experimental

9.2.1 Chemical Reagents

The following reagents were from Sigma-Aldrich and used as received without further purification: sulphuric acid (H_2SO_4, 98 %), ferrocene ($Fe(C_5H_5)_2$, 98 % purity), tetra-*N*-butylammonium perchlorate (TBAP, 98 % purity), potassium ferricyanide ($K_3[Fe(CN)_6]$), acetonitrile (MeCN, Sigma–Aldrich, 99.8 %), methanol (CH_3OH, 99.8 %), potassium chloride (KCl, 99 %) and chloroplatinic acid hexahydrate ($H_2PtCl_6 \cdot 6H_2O$). Ultra-pure water with a resistance of 18.2 MΩ cm prepared by an ultra-pure laboratory water purification system (Millipore Pty Ltd., North Ryde, NSW, Australia) and acetonitrile (MeCN, Sigma–Aldrich, 99.8 %) were used to make up the solutions and for washing the electrodes. An aqueous suspension of 100 nm polystyrene beads (polystyrene density of 1.06 g/cm^3) dissolved in deionized water containing a small amount of surfactant (not identified by distributer) and 2 mM of sodium azide (acts as an anti-microbial agent) from Phosphorex was used for the metal templating.

9.2.2 Electrochemical Experiments

The experiments were conducted in the modified T-cell (purchased from Pine Research Instruments) as explained in the general experimental section. A conventional three-electrode arrangement was employed, with a 5 mm diameter glassy carbon macro disk (purchased from Pine Research Instruments) as the working electrode, a 0.5 mm diameter silver wire (Sigma Aldrich) as the quasi-reference electrode and a 0.25 mm diameter Pt wire (Goodfellow) coil as the counter electrode. Due to the nature of the experimental setup (modified surfaces to be used for gas sensing) a Ag/AgCl reference electrode was not used therefore no comparison to peak potentials were made.

9.2.3 SEM

Scanning electron microscopy (SEM) characterisation of the working electrode surface was performed using a Zeiss Neon 40 EsB model and a Tescan Mira3 field emission scanning electron microscope. A thin layer of platinum coating was used for imaging the bare polystyrene beads on the glassy carbon surface. For all other samples the images were obtained without any additional sample preparation.

9.3 Results and Discussion

9.3.1 Synthesis of Metal Frameworks

Figure 9.1 shows a scheme for the expected Pt framework synthesis. First the 100 nm polystyrene beads were dispersed in methanol. Then the dispersed polystyrene beads (figure 9.2) were dropcasted using a syringe onto the macrodisk electrode. The macrodisk electrode was then left overnight in an oven with a constant temperature of 60°C to allow for solvent evaporation. The macrodisk electrode was then placed in

the custom made electrochemical cell (PINE setup). Then 500 µl of 5 mM H_2PtCl_6 in 0.5 M H_2SO_4 was placed in the "cup" on top of the electrode.

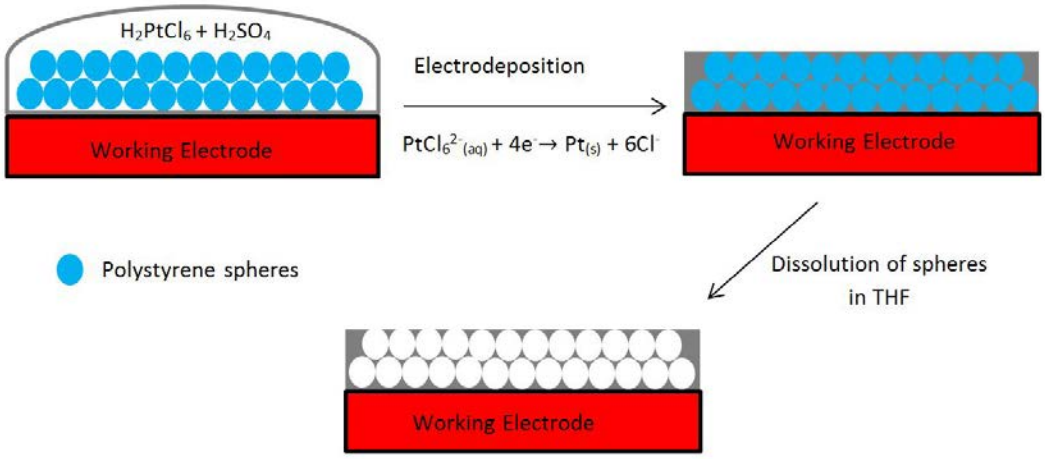

Figure 9.1: Scheme for Pt framework formation

Figure 9.2: Scanning electron micrograph of 100 nm polystyrene beads on a glassy carbon electrode surface.

Then platinum was electrodeposited using chronoamperometry. Chronoamperometric transients were achieved using a sample time of 1 s. The potential was stepped from a position of zero current (0.6 V) to a potential after the reduction peak of Pt ions to Pt metal ($PtCl_6^{2-}{}_{(aq)}+4e^- \rightarrow Pt_{(s)}+6Cl^-$) was observed (-

0.5 V) and the current was measured for 600 s. Figure 9.3 shows the chronoamperometric transients obtained for the deposition. The graph has both the chronoamperometric transients of the deposition of platinum on a glassy carbon surface in the presence and absence (control) of beads. Interesting behaviour was seen where there was fluctuations in the current with respect to the time. This could be due to the uneven surface on the electrode as a result of the beads that have been deposited or alternatively it could be due to the evolution of hydrogen due to the large negative potential used to deposit the platinum. It can be seen that the absolute current obtained in the presence of the beads are much higher as compared to the absence of beads which might be due to the platinum ions needing to travel much longer, through the beads to deposit, hence higher currents. After several deposition experiments, a time of 600 s was chosen as the ideal time for the deposition. If held for more than 600s platinum clusters are formed on the surface of the porous platinum structures thereby blocking the pores. After the deposition of platinum, the modified glassy carbon electrode was taken out and placed in a solution of tetrahydrofuran (THF) to dissolve the beads away and leave macroporous Pt structures. Then the electrodes were imaged under the SEM.

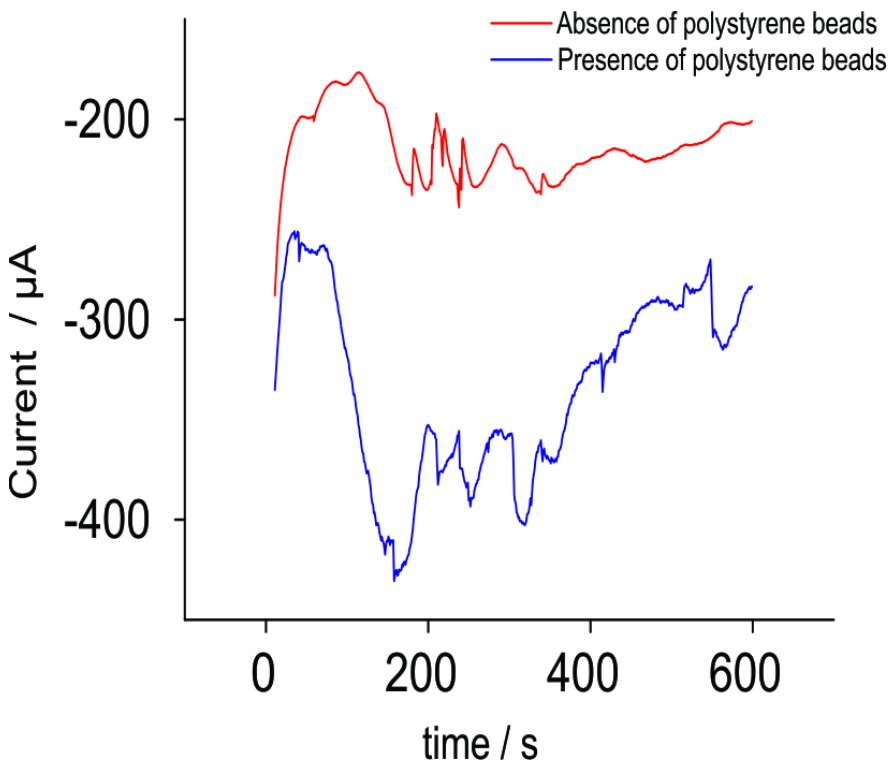

Figure 9.3: Chronoamperometric transient used to deposit platinum on glassy carbon surface modified with polystyrene beads (blue line). Red line = absence of polystyrene beads

9.3.2 SEM Characterisation

Figure 9.4 shows the SEM images of different areas on a glassy carbon electrode surface with the same magnification, showing distribution of the pores. Figure 9.4a and 9.4b shows the porous template that is formed on the surface and this reflects the majority of the glassy carbon surface. However there are also some sparse areas (figure 9.4c) and some areas where there are some platinum clusters/deposits (figure 9.4d) that are formed on top of the porous templates. Due to the way that the polystyrene beds are deposited on to the glassy carbon surface, controlling the homogeneity of the metal template is restricted.

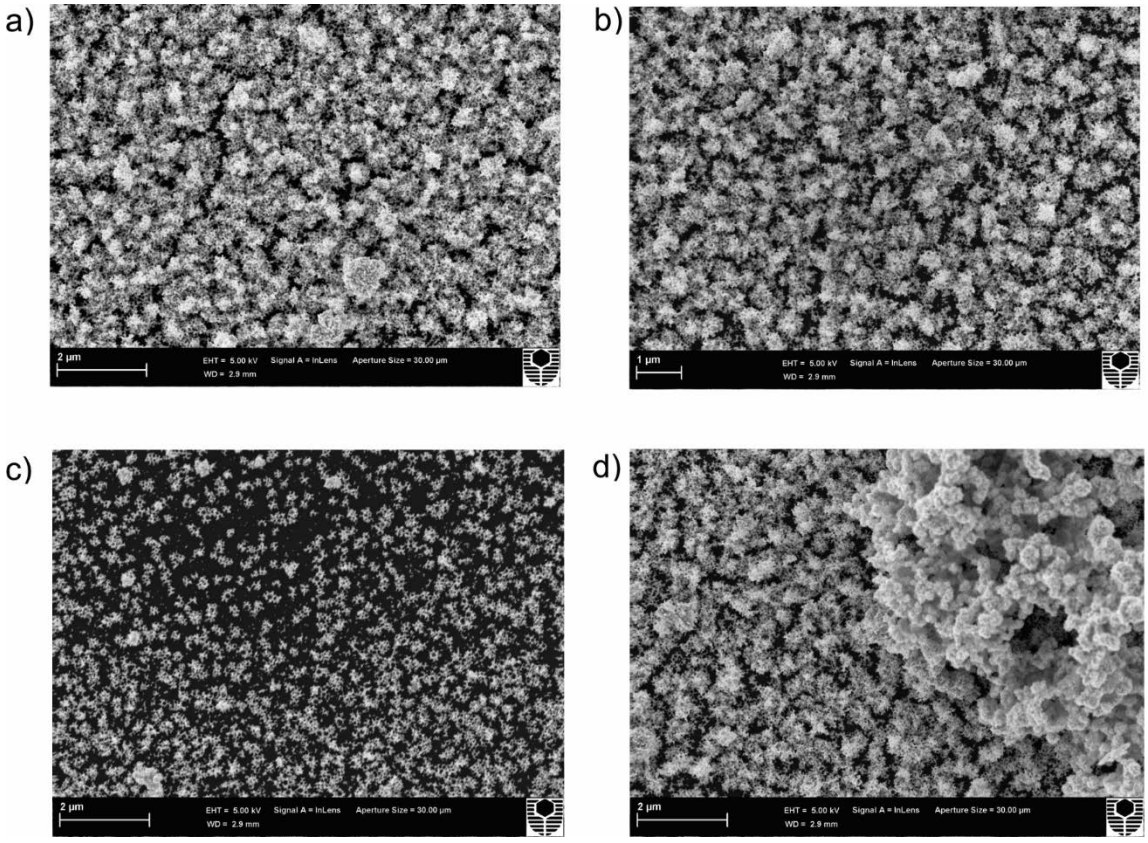

Figure 9.4: SEM images of different areas on a glassy carbon electrode surface at the same magnification showing the distribution of deposited Pt.

Figure 9.5 shows the magnification of figure 9.4b which gives us a more accurate value for the size of the pores. Pore sizes between 80 and 150 nm was observed. It is also visible from this image that the metal does not deposit evenly around the beads and this could be due to the way that the polystyrene beads have assembled on the electrode surface. Now that the metal templates have been physically characterised, the next step would be to characterise them electrochemically.

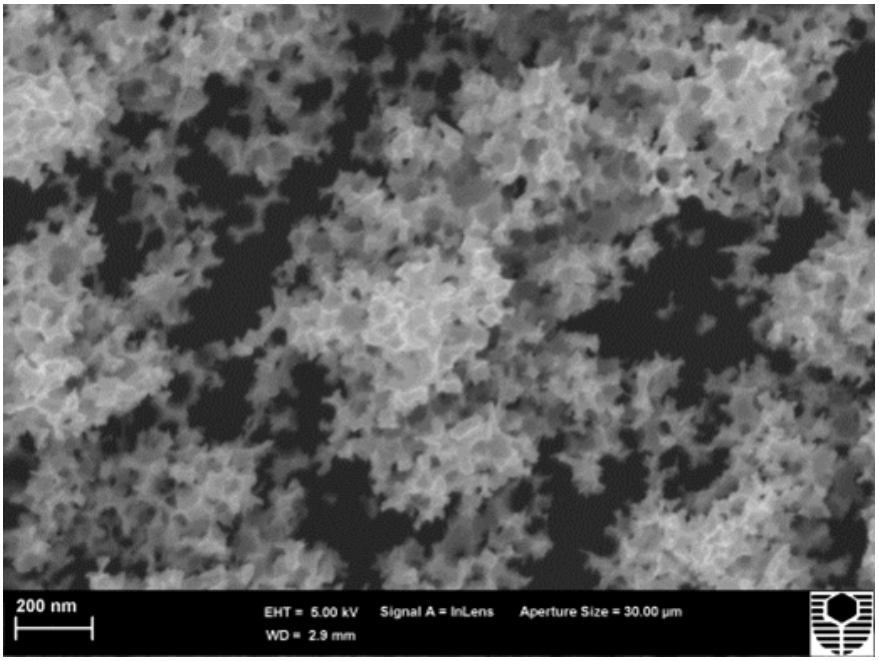

Figure 9.5: Increased magnification of the SEM image obtained in figure 9.4b to show the size of the pores.

9.3.3 Electrochemical Characterisation

The synthesised metal framework was characterised using two redox couples, an inner sphere redox species (Ferrocene) and an outer sphere redox species (Potassium Ferricyanide). The prepared Pt frameworks were also characterised in sulphuric acid. Cyclic voltammetry in an acidic medium is a well-known technique used to characterise platinum surfaces, due to the characteristic hydrogen adsorption/desorption and oxide formation/reduction peaks.[13]

Figure 9.6 shows the electrochemical behaviour of the Pt macroporous framework in 0.5 M H_2SO_4 (CV scan from 0 V to 1.2 V to -0.45 V and back to 0 V). The blue line is for the GC surface modified with the Pt macroporous framework and the red line is for the bare GC surface. As expected on the Pt macroporous framework modified GC electrodes there are four main regions that have been labelled. Region I is the oxidation of Pt and region II is the reduction of the formed Pt oxide. Peaks at III are the hydrogen adsorption region and peaks at IV are due to the hydrogen desorption.

All these regions are characteristic of platinum surfaces and, together with the images obtained from the SEM, it can be said that a macroporous platinum surface has been successfully synthesised. Furthermore there were no peaks present on the GC surface in sulphuric acid. It can be also seen that in region IV which is due to hydrogen desorption there is another peak in between the characteristic two peaks. The appearance of this peak is unusual and has been attributed to various factors such as distribution of various lattice planes, the potential dependent orientation of the Pt-H dipoles, absorption, oxidation of subsurface molecular hydrogen or subsurface/interstitial hydrogen adatoms[14-16] and a detailed study on this peak has been carried out by Inzelt et al.[14]

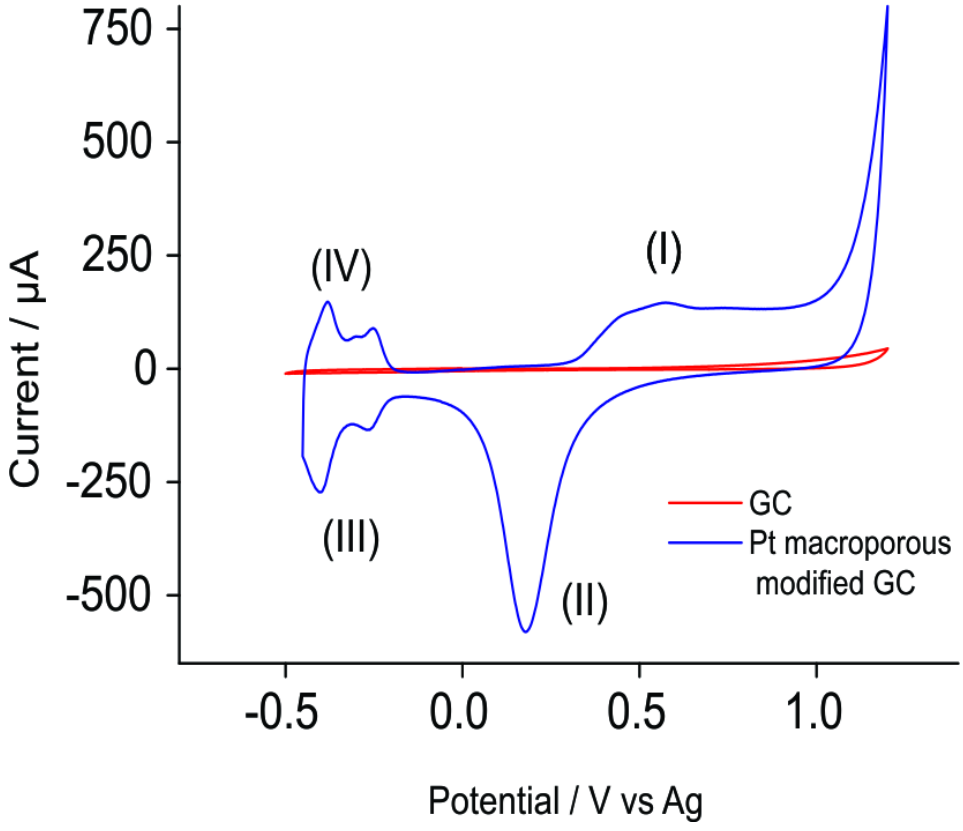

Figure 9.6: Electrochemical behaviour of Pt porous framework modified GC (blue) and bare GC (red) in 0.5 H_2SO_4.

The hydrogen adsorption/desorption peaks can be used to find the electrochemically active platinum surface area. This is performed by integrating the charge density associated with a monolayer adsorption of hydrogen of 210 μC cm^{-2} on a platinum surface.[17] The average charge obtained for the desorption and the adsorption (from figure 9.6) was 1.94×10^{-4} C which gives an area of 0.88 cm^2 for the platinum porous framework. The roughness factor of the electrode can be measured by dividing the area of the framework by the geometric area (0.196 cm^2) which gives a value of 4.5.

After characterising/activating in sulphuric acid the platinum framework was characterised using two different redox couples (Fc/Fc^+ and ferro/ferricyanide). In this work ferricyanide is used as the inner sphere probe and ferrocene is used as the outer sphere probe. An inner sphere electrode reaction is where the electroactive metal complex is bound to the electrode surface and electron transfer occurs through the ligand which is absorbed on the electrode through the inner Helmholtz plane.[18,19] Whereas, an outer sphere electrode reaction occurs at the outer Helmholtz plane which is separated by a solvent layer which makes the electrode-analyte interaction weak.[18,19] Therefore an inner sphere reaction is very surface sensitive as compared to an outer sphere reaction.

Figure 9.7 shows cyclic voltammetry scans of 2 mM ferrocene in 0.1 M TBAP/acetonitrile on both the Pt porous framework modified GC (blue, 0 V to 0.5 V and back to 0 V) and bare GC (red, 0.2 V to 0.7 V and back to -0.2 V). Peaks at 0.28 V and 0.51 V are due to the oxidation of Fe(II) to Fe(III) and peaks at 0.18 V and 0.41 V are due to the reverse process , reduction of Fe(III) to Fe(II). For both electrodes the peak currents were identical for both processes however there was a big shift in the peak potentials. This shift could be a combination of the unstable

reference electrode used which was Ag and also the different surface (Pt or GC) that the ferrocene is getting oxidised/reduced. The important point to note is that there is no increase in the current and the peak to peak separation is constant in both CVs.

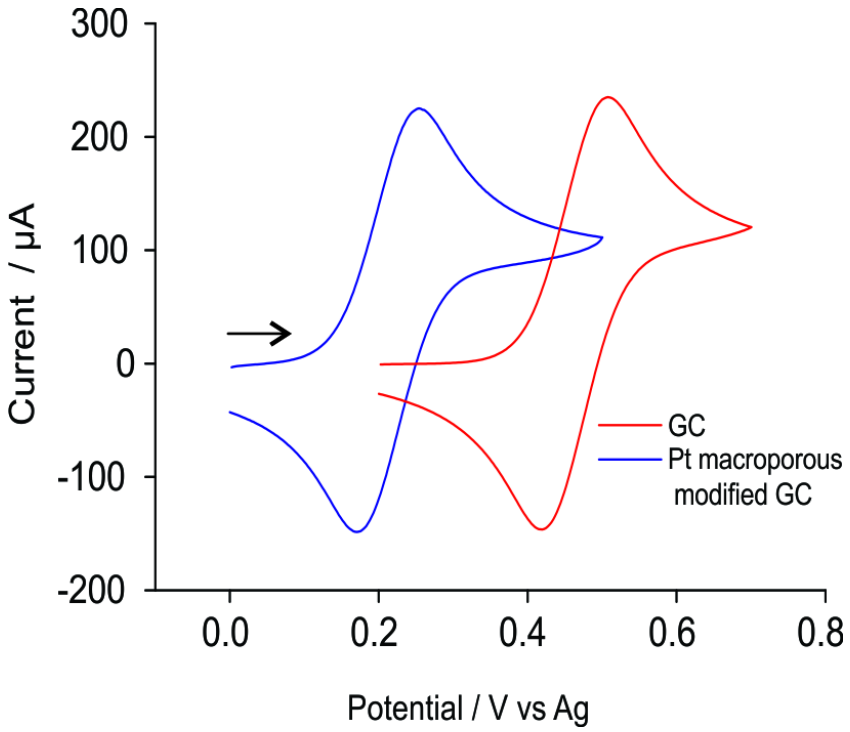

Figure 9.7: Cyclic voltammetry scans at a scan rate of 0.1 V/s of Pt porous framework modified GC (blue) and bare GC (red) in 2 mM ferrocene in 0.1 M TBAP/acetonitrile.

Figure 9.8 shows CV scans of 1 mM potassium ferricyanide in 0.1 M KCl on both Pt porous framework modified GC (blue, 0 .5 V to -0.2 V and back to 0.5 V) and bare GC (red, 0.5 V to -0.4 V and back to 0.5 V). Peaks at 0.14 V and 0 V are due to the reduction of Fe(III) to Fe(II) and peaks at 0.13 V and 0.21 V are due to the reverse process, oxidation of Fe(III) to Fe(II). The peak to peak separation for the Pt porous framework modified GC and the GC is 0.074 V and 0.126 V respectively. This big difference is due to the ferricyanide having faster kinetics on the Pt surface as compared to the GC surface. The currents on the Pt porous framework modified GC is higher than on the GC surface however this is accompanied by an increase in the capacitance. This can be explained by the increase in the surface area and also the

roughness of the electrode surface. Due to ferricyanide being an inner sphere redox couple which is surface sensitive, the changes in surfaces alters the behaviour of the analyte species.

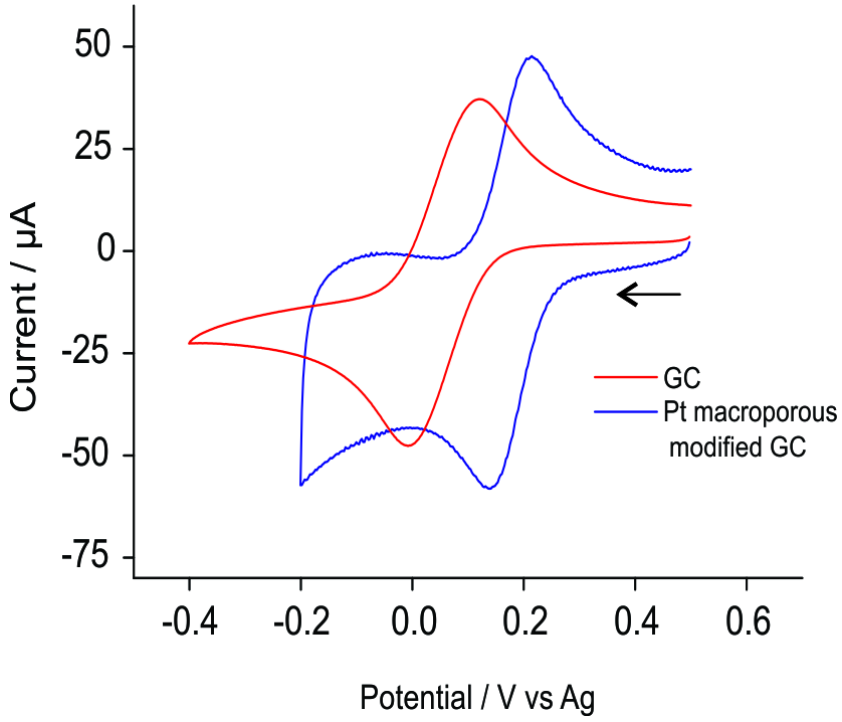

Figure 9.8: Cyclic voltammetry scans at a scan rate of 0.1 V/s of Pt porous framework modified GC (blue) and bare GC (red) in 1 mM potassium ferricyanide in 0.1 M KCl.

9.4 Conclusions

Platinum macroporous frameworks were synthesised successfully using a 'bottom up' approach where 100 nm polystyrene beads were used as the template. Scanning electron microscopy characterisation shows that a porous framework with pore dimensions between 80-150 nm was obtained, with concentration of metal framework differing in various areas on the electrode. Electrochemical characterisation using sulphuric acid showed that the active surface area of the pore structure was 0.88 cm^2 (via hydrogen desorption/adsorption peaks) improving the roughness of the electrode 4.5 times. Electrochemical studies using an outer sphere redox probe (ferrocene) showed no major changes in the CVs obtained other than a

shift in the peak potentials however experiments with an inner sphere probe (potassium ferricyanide) showed that the surface has indeed become much rougher as an increase in capacitance was observed. The next step would be to test the suitability of these nanomaterials for gas sensing (Chapter 10).

9.5 References

(1) IUPAC. Compendium of Chemical Terminology, 2nd ed. (the "Gold Book"). Compiled by McNaught, A.D.;Wilkinson,A. Blackwell Scientific Publications, Oxford, UK (1997). XML on-line corrected version: http://goldbook.iupac.org (2006-) created by Nic, M.; Jirat, J.; Kosata, B.
(2) Tiemann, M. Porous Metal oxides as gas sensors. *Chem. Europ J.* **2007**, *13*, 8376-8388.
(3) Bartlett, P. N.; Birkin, P. R.; Ghanem, M. A. Electrochemical deposition of macroporous platinum, palladium and cobalt films using polystyrene latex sphere templates. *Chem. Commun.* **2000**, 1671-1672.
(4) Gollas, B.; Elliott, J. M.; Bartlett, P. N. Electrodeposition and properties of nanostructured platinum films studied by quartz crystal impedance measurements at 10 MHz. *Electrochim. Acta* **2000**, *45*, 3711-3724.
(5) Chen, H.-Y.; Xu, Y.-F.; Kuang, D.-B.; Su, C.-Y. Recent advances in hierarchical macroporous composite structures for photoelectric conversion. *Energy Environm. Science* **2014**, *7*, 3887-3901.
(6) Attard, G. S.; Bartlett, P. N.; Coleman, N. R. B.; Elliott, J. M.; Owen, J. R.; Wang, J. H. Mesoporous platinum films from lyotropic liquid crystalline phases. *Science* **1997**, *278*, 838-840.
(7) Aal, A. A.; Al-Salman, R.; Al-Zoubi, M.; Borissenko, N.; Endres, F.; Höfft, O.; Prowald, A.; Zein El Abedin, S. Interfacial electrochemistry and electrodeposition from some ionic liquids:In situ scanning tunneling microscopy, plasma electrochemistry, selenium and macroporous materials. *Electrochim. Acta* **2011**, *56*, 10295-10305.
(8) Kim, O.-H.; Cho, Y.-H.; Kang, S. H.; Park, H.-Y.; Kim, M.; Lim, J. W.; Chung, D. Y.; Lee, M. J.; Choe, H.; Sung, Y.-E. Ordered macroporous platinum electrode and enhanced mass transfer in fuel cells using inverse opal structure. *Nat. Commun.* **2013**, *4*,2473
(9) Kuroda, Y.; Yamauchi, Y.; Kuroda, K. Integrated structural control of cage-type mesoporous platinum possessing both tunable large mesopores and variable surface structures by block copolymer-assisted Pt deposition in a hard-template. *Chem. Commun.* **2010**, *46*, 1827-1829.
(10) Kucernak, A.; Jiang, J. Mesoporous platinum as a catalyst for oxygen electroreduction and methanol electrooxidation. *Chem. Eng. J.* **2003**, *93*, 81-90.
(11) Birkin, P. R.; Elliott, J. M.; Watson, Y. E. Electrochemical reduction of oxygen on mesoporous platinum microelectrodes. *Chem. Commun.* **2000**, 1693-1694.
(12) Evans, S. A.; Elliott, J. M.; Andrews, L. M.; Bartlett, P. N.; Doyle, P. J.; Denuault, G. Detection of hydrogen peroxide at mesoporous platinum microelectrodes. *Anal. Chem.* **2002**, *74*, 1322-1326.

(13) Zhan, D.; Velmurugan, J.; Mirkin, M. V. Adsorption/desorption of hydrogen on Pt nanoelectrodes: Evidence of surface diffusion and spillover. *J. Am. Chem. Soc.* **2009**, *131*, 14756-14760.
(14) Berkes, B.; Inzelt, G. Generation and electrochemical nanogravimetric response of the third anodic hydrogen peak on a platinum electrode in sulfuric acid media. *J. Solid. State. Electrochem.* **2014**, *18*, 1239-1249.
(15) Frelink, T.; Visscher, W.; van Veen, J. A. R. The third anodic hydrogen peak on platinum; Subsurface H_2 adsorption. *Electrochim. Acta* **1995**, *40*, 545-549.
(16) Martins, M. E.; Zinola, C. F.; Arvia, A. J. Voltammetric response of hydrogen adsorbates on platinum in acid solutions: a possible H-adatom subsurface state. *J. Brazil. Chem. Soc.* **1997**, *8*, 363-370.
(17) Watt-Smith, M.; Friedrich, J.; Rigby, S.; Ralph, T.; Walsh, F. Determination of the electrochemically active surface area of Pt/C PEM fuel cell electrodes using different adsorbates. *J. Phys. D: Appl. Phys.* **2008**, *41*, 174004.
(18) Tanimoto, S.; Ichimura, A. Discrimination of inner-and outer-sphere electrode reactions by cyclic voltammetry experiments. *J. Chem. Educ.* **2013**, *90*, 778-781.
(19) Bard, A. J.; Faulkner, L. R.: *Electrochemical methods: fundamentals and applications*; Wiley, 2000.

10. Preliminary Studies of Nanomaterials for Methylamine Gas Sensing in a Room Temperature Ionic liquid

The electrochemical behaviour of methylamine gas in the room temperature ionic liquid [C_2mim][NTf_2] has been investigated on a bare glassy carbon electrode and glassy carbon electrode modified with either magnetite nanoparticles or platinum macroporous framework. While there was no change in the electrochemical behaviour of methylamine gas on the magnetite nanoparticles modified electrode, the platinum macroporous framework modified electrode displayed a few changes that warrant further investigation. These preliminary results open up opportunities for future research that uses nanomaterials as electrode surface modifiers for gas sensing research.

10. PRELIMINARY STUDIES OF NANOMATERIALS FOR METHYLAMINE GAS SENSING IN A ROOM TEMPERATURE IONIC LIQUID **255**

10.1 Introduction **257**

10.2 Experimental **257**

10.2.1 Chemicals and Reagents 257

10.2.2 Electrochemical Experiments 257

10.3 Results and Discussion **258**

10.3.1 Magnetite Nanoparticles 258

10.3.2 Platinum Macroporous Framework 260

10.4 Conclusions **262**

10.5 References **263**

10. Preliminary Studies of Nanomaterials for Methylamine Gas Sensing in a Room Temperature Ionic Liquid

10.1 Introduction

In this chapter some preliminary results will be shown for the detection of methylamine gas in the RTIL [C_2mim][NTf_2] using the nanomaterials that were characterised in chapters 8 and 9. The preliminary work shown here can pave the way for future studies, as discussed in the future work chapter (Chapter 11).

10.2 Experimental

10.2.1 Chemicals and Reagents

For reagents to synthesise oleyl coated magnetite nanoparticles and Pt macroporous framework please see chapter 8 and chapter 9 respectively. The RTIL 1-ethyl-3-methylimidazolium bis(trifluoromethylsulfonyl)imide ([C_2mim][NTf_2]) was synthesized according to standard literature procedures[1,2] and kindly donated by the group of Professor Christopher Hardacre at Queens University, Belfast. Ultra-pure water with a resistance of 18.2 MΩ cm prepared by an Ultra-pure laboratory water purification system (Millipore Pty Ltd., North Ryde, NSW, Australia) and acetonitrile (MeCN, Sigma–Aldrich, 99.8 %) were used for washing the electrodes before and after use with RTILs. Methylamine gas (0.2%, nitrogen fill) was purchased from CAC gases (Auburn, NSW, Australia). High purity nitrogen gas (99.9 %) was purchased from BOC gases (North Ryde, NSW, Australia) and used as a carrier gas.

10.2.2 Electrochemical Experiments

A conventional three-electrode arrangement was employed, utilizing the ‘PINE’ electrode t-cell setup (defined in experimental chapter 3) with glassy carbon macro

disk electrode (5 mm diameter) as the working electrode, a 0.25 mm diameter Pt wire (Goodfellow) coil as the counter electrode and a 0.5 mm diameter silver wire (Sigma Aldrich) as the quasi-reference electrode. For the magnetite experiments 2 × 1.5 µl of magnetite suspension was drop casted onto the electrode allowing the first drop to dry before the next drop was applied as explained in chapter 8. This was then used as the electrode for methylamine gas sensing. For the Pt macroporous framework, Pt was electrodeposited on a glassy carbon electrode in the same way as described in chapter 9 and then used for methylamine gas sensing.

10.3 Results and Discussion

10.3.1 Magnetite Nanoparticles

Figure 10.1 shows the cyclic voltammetric scans of methylamine gas on a magnetite nanoparticle modified GC electrode (red) and a bare GC electrode (blue) at a scan rate of 0.1 V/s when scanned from 0 to 2 V to -1.4 V and back to 0 V. It can be seen that there is a single oxidation peak, process I, at approximately 1.2 V followed by a small reduction feature at 0.1 V (peak III). The full mechanism for the electrochemical oxidation has been explained in chapter 4, where 4 peaks were present (I, II, III and IV). The absence of peaks II and IV is likely due to the nature of surface. Peaks at II and IV are due to the reduction of the solvated proton and the oxidation of protons. These two processes are only active on the Pt surface and not the GC surface.[3] However it can be seen for oxidation process I there is a double peak on both the GC and the GC modified with magnetite surface, possibly due to a slightly complicated reaction mechanism on the GC surface.

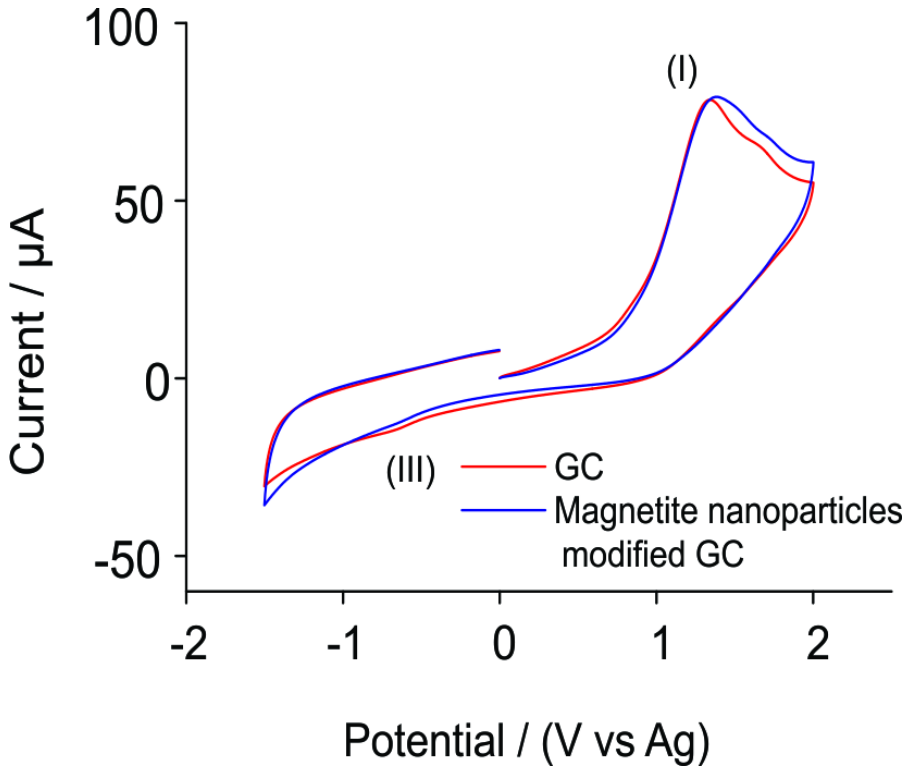

Figure 10.1: CV for the oxidation of 0.15 % Methylamine (nitrogen fill) on a 5 mm diameter GC electrode (red) and magnetite nanoparticle modified GC electrode (blue) in $[C_2mim][NTf_2]$ at a scan rate of 0.1 V/s.

It can be seen that both the CVs in figure 10.1 look very alike and the currents obtained for oxidation peak I is very similar which shows us that there is no increase in sensitivity as a result of using these nanoparticles. It could also indicate that the oxidation of methylamine gas is only occurring on the GC surface and not on the iron oxide nanoparticles that are on the GC surface. However an important point to note here is that there is no difference in the electrochemical behaviour of methylamine gas on both surfaces which might be advantageous for sensing purposes. This means that these nanoparticles could be investigated in a ferrofluidic form in an RTIL to create "membrane-less" and "spill-less" gas sensors as shown by Panchompoo et al.[4] who used a ferrofluid to demonstrate the electrochemical reduction of oxygen gas. They used an aqueous colloidal suspension of iron oxide nanoparticles, which were also prepared by a chemical co-precipitation technique, as the solvent on a Ni-O-

modified screen printed electrode for sensing oxygen gas while controlling the flow of the liquid using a magnet.

After the conclusion of the experiments the electrode was checked and the presence of the iron oxide nanoparticles on the electrode surface rules out the possibility that it has come out of the electrode and dissolved in the RTILs. If the magnetite nanoparticles were inactive, the GC surface would be partially blocked which would mean that the current response would have decreased, whereas if the magnetite particles were behaving like a regular conducting electrode, a response limited by the surface area of the top layer would be seen.

10.3.2 Platinum Macroporous Framework

Figure 10.2 shows the CV scans of methylamine gas on a Pt macroporous framework modified GC electrode (red) and a bare GC electrode (blue) at a scan rate of 0.1 V/s when scanned from 0 to 2 V to -1.4 V and back to 0 V. It can be seen that the behaviour of methylamine gas on both the electrodes is different. On the Pt macroporous framework modified GC electrode, it can be seen that there is a single broad oxidation wave, process I, at approximately 3 V followed by two reduction peaks at -0.2 V and -0.85 V (peaks II and III). It can also be seen that there is an oxidation feature (peak IV) at -0.5 V. This behaviour is similar to what was seen in chapter 4 on a Pt microelectrode where there were four peaks present. This signifies that the electrochemical oxidation of methylamine is probably occurring on the Pt macroporous framework. Whereas on the GC surface peaks II and peak IV are not visible due to the analyte species being not active on GC, as explained earlier.

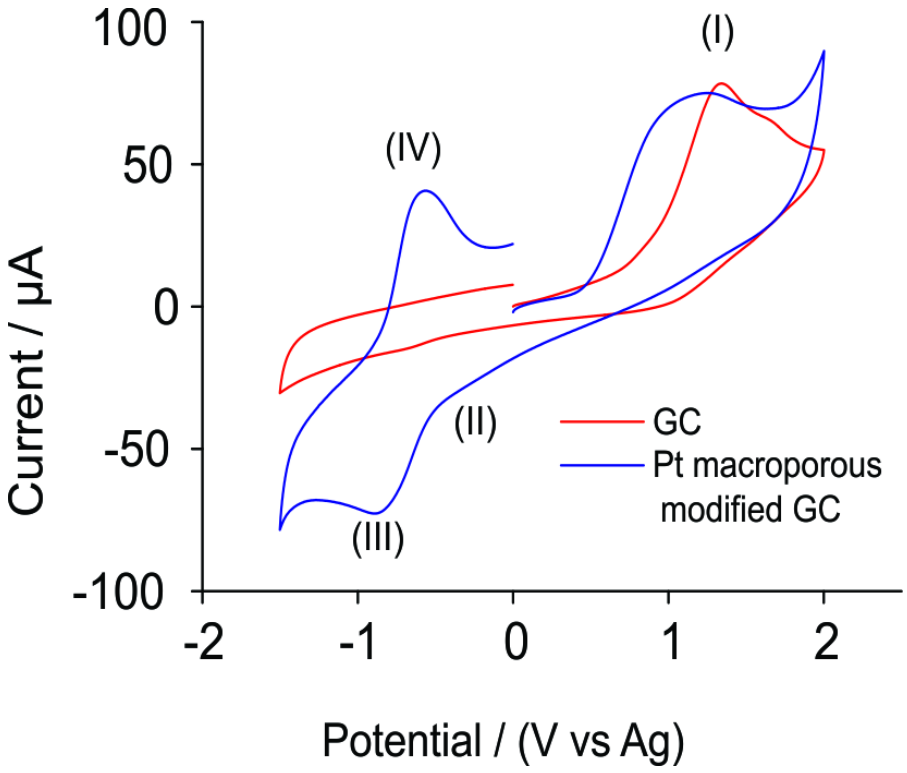

Figure 10.2: CV for the oxidation of 0.15 % Methylamine (nitrogen fill) on a 5 mm diameter GC electrode (red) and Pt macroporous framework modified GC electrode (blue) in $[C_2mim][NTf_2]$ at a scan rate of 0.1 V/s.

An interesting point to note is that the onset of the oxidation (process I) on the modified surface starts earlier which suggests that there is a possible catalytic activity due to the macroporous Pt structure. A noticeable difference between the two CVs is the charge produced for process I. The charge passed in a reaction follows the below equation (Faraday's law):[5]

$$Q = mnF \tag{10.1}$$

Where m is the moles of electrochemically-active material, Q is the charge, n is the number of electrons taking part in the reaction and F is Faraday's constant. Since both n and F is constant the difference in Q has to be accounted for by a change in the moles. It can be seen that for the modified GC surface the area under the CV graph is slightly larger than the unmodified GC surface which suggests that there is

more of the electroactive material that is being oxidised. The charge for the modified surface is 8.15×10^{-4} C and that for the bare GC surface is 7.16×10^{-4} C which is a slight increase (12 %) in the amount of electroactive material. However due to the roughness of the electrode surface it would be expected that a substantial increase is seen. Although a substantial increase in the current response is not seen, it is encouraging as these preliminary results show that the Pt frameworks are active for the electrochemical oxidation of methylamine gas and could be used as new electrode materials. Future studies are needed to fully understand the behaviour of these Pt frameworks.

10.4 Conclusions

Magnetite nanoparticles and platinum macroporous frameworks have been investigated for their suitability in methylamine gas sensing on a GC electrode in the RTIL, $[C_2mim][NTf_2]$. Similar behaviour was seen on a bare GC electrode and a magnetite modified GC electrode which suggests that the magnetite nanoparticles are not taking part in the reaction which opens up possibilities for using them as ferrofluidic electrochemical solvent without any interference. It was found that electrochemical oxidation of methylamine gas is possible on these Pt macroporous framework modified GC electrodes in the presence of RTILs which opens up possibilities of using them as new electrode materials. However no considerable increase in the currents was seen as a result of using these nanomaterials as might have been expected due to the increased surface area. These preliminary results are promising and paths the way for some future work which will be suggested in the next chapter.

10.5 References

(1) Bonhôte, P.; Dias, A.-P.; Papageorgiou, N.; Kalyanasundaram, K.; Grätzel, M. Hydrophobic, highly conductive ambient-temperature molten salts. *Inorg. Chem.* **1996**, *35*, 1168-1178.
(2) MacFarlane, D. R.; Meakin, P.; Sun, J.; Amini, N.; Forsyth, M. Pyrrolidinium imides: A new family of molten salts and conductive plastic crystal phases. *J. Phys. Chem. B* **1999**, *103*, 4164-4170.
(3) Ji, X.; Banks, C. E.; Silvester, D. S.; Aldous, L.; Hardacre, C.; Compton, R. G. Electrochemical ammonia gas sensing in nonaqueous systems: a comparison of propylene carbonate with room temperature ionic liquids. *Electroanal.* **2007**, *19*, 2194-2201.
(4) Panchompoo, J.; Ge, M.; Zhao, C.; Lim, M.; Aldous, L. The oxygen reduction reaction in ferrofluids: towards membrane-less and spill-less gas sensors. *ChemPlusChem* **2014**, *79*, 1498-1506.
(5) Bard, A. J.; Faulkner, L. R.: *Electrochemical methods: Fundamentals and applications*; Wiley, 2000.

11. Conclusions and Future Work

In this chapter, the general conclusions of the work performed throughout this thesis are summarised. Some future studies that could further improve the development of RTIL based gas sensors will also be suggested.

11. CONCLUSIONS AND FUTURE WORK **265**

11.1 Conclusions **267**

11.2 Future Work **269**

11.3 References **272**

11. Conclusions and Future Work

11.1 Conclusions

The work presented in this thesis provides information into the possibilities of using room temperature ionic liquids (RTILs) as solvents in amperometric gas sensors (AGSs) for the detection of highly toxic gases, namely methylamine, chlorine and hydrogen chloride. The electrochemical behaviour of these gases have been investigated in RTILs using electrochemical techniques such as cyclic voltammetry and chronoamperometry hoping to give a general understanding on the behaviour of these gases in RTILs.

The electrochemical behaviour of methylamine and hydrogen chloride gases were investigated in several RTILs and a highly complicated mechanism was observed for both gases. This highly complexed mechanism does not seem to affect the analytical utility as a linear calibration graph with reasonable limit of detections (LODs) was observed. The high currents observed for the analytical response suggests that both these gases have a high solubility which is a major advantage from a sensing perspective. It was also discovered that certain RTILs cannot be used to detect HCl gas as degradation of the ionic liquid occurred whereas similar behaviour was seen for the electrochemical behaviour of methylamine gas in the studied RTILs. For the detection of HCl gas an alternative indirect method of detecting has been proposed which involves the reduction of the protons. The electrochemical behaviour of chlorine gas has been investigated in $[C_2mim][NTf_2]$ and in contrast to a previous report the reduction of chlorine gas to chloride ions was found to be diffusion controlled instead of adsorption controlled which prompted the study of the analytical utility of chlorine gas in $[C_2mim][NTf_2]$ which was previously thought not possible. Highly linear calibration graphs were obtained with reasonable LODs. For

the first time a facile way of obtaining Henry's law constant of highly toxic gases in RTILs have also been proposed which opens up the possibilities for obtaining information of the relative solubility of highly toxic gases in two separate phases which would be very useful information for the development of AGSs.

The electrochemical behaviour of these three toxic gases was then investigated on screen printed electrodes (SPEs). Out of the various SPEs investigated, Pt SPEs proved to be the best SPE for the detection of these three gases, with comparable LODs to their microelectrode counterparts. The electrochemical mechanism of all these gases on these Pt SPEs were also the same as on Pt microelectrodes which is a good observation as it suggests that the paste/polymeric binder that is used to make these Pt SPEs do not react with the toxic gases in a detrimental way pathing the way for the development of cheap miniaturised portable AGSs based on SPE materials.

Nanomaterials such as magnetite nanoparticles and platinum macroporous frameworks were synthesised and characterised using various physical and electrochemical techniques. A range of characterisation methods confirmed that the particles were superparamagnetic and had a nanoparticle size of ~20 nm when synthesised via a chemical co-precipitation technique. Electrochemical characterisation using CV showed that the nanoparticles were electrochemically active in acidic media but not in alkaline media and an EC mechanism involving protons has been proposed. This electrochemical activity exhibited by these magnetic nanoparticles could be exploited by various electrochemical applications. Pt macroporous frameworks were also synthesised using a 'bottom up' approach via a polystyrene bead template and characterised by SEM. They were also electrochemically characterised using an inner sphere and an outer sphere redox

probe. Both these nanomaterials were then tested for their ability to improve the current response for methylamine gas sensing. Magnetite nanoparticles showed no significant change in the current response for methylamine oxidation suggesting that they do not take part in the reaction. It was encouraging that the Pt macroporous framework showed activity for the oxidation of methylamine gas which requires future work to fully understand this effect.

11.2 Future Work

This thesis has revealed some important information on the behaviour of these highly toxic gases in RTILs, but more work needs to be done before their application in commercial amperometric gas sensors.

Current technology to sense methylamine, chlorine and hydrogen chloride exist but is limited. There are currently no commercial AGSs available for methylamine, but there are other form of detections such as colorimetric (Sensidyne, 1-20 ppm, operating temperature up to 40°C) and photoionization detectors (Mil-Ram Technology, 0-200 ppm, operating temperature up to 55°C). Companies such as Membrapor and Alphasense manufacture AGSs for hydrogen chloride and chlorine in the range 0 to 20 ppm but the operating temperatures do not go above 50°C.

The LODs obtained for the gases in RTILs were good and it suggests that RTILS can be used as favourable solvents for the detection of these gases; however lower LODs is needed for real analytical applications (e.g. closer to exposure limit). The high viscosity of RTILs could prove to be a challenge in achieving lower LODs and this should be explored. One way to investigate this would be to perform the analytical utility studies using a lower concentration range. More sensitive electrochemical techniques such as differential pulse voltammetry (DPV) and square

wave voltammetry (SWV) could also be used to enhance the electrochemical signal. DPV and SWV are often employed as more sensitive techniques compared to cyclic voltammetry/linear sweep voltammetry due to the lower impact of the charging current. Some future work has been performed after the submission of this thesis where a much lower concentration range (0 to 80 ppm) was studied for the detection of both methylamine and hydrogen chloride gas on Pt SPEs in $[C_2mim][NTf_2]$ using linear sweep voltammetry, DPV and SWV.[1] Excellent linearity ($R^2 > 0.99$) was obtained for the concentration range studied with LODs between 1 to 4 ppm, which is less than the OSHA PEL limit for both methylamine (10 ppm) and hydrogen chloride (5 ppm) suggesting that RTIL/SPE based sensors have the potential to be used in commercial sensors. There has only been one report of LODs under 10 ppm for gases in RTILs, which was for ammonia gas on Pt printed electrodes,[2] but this is the first time such low LODs for methylamine and hydrogen chloride gas have been reported.

SPEs have been shown to be able to detect these highly toxic gases in RTILs. Response times of these gases on SPEs have already been improved as compared to microelectrodes due to thinner layers. However faster response times, which is vital for AGS, can be achieved by spin coating the RTIL/solvent on top of these SPEs thereby achieving an even thinner layer. This thinner layer would increase the rate of diffusion of the gas molecules to the electrode surface, giving faster response times of the analyte species which is important for real world applications.

To further develop the robustness of a RTIL/SPE based gas sensor gellified RTILs should be investigated on these SPEs for the detection of these toxic gases. RTILs can be mixed with polymers to create a gellified solvent[3] which would negate solvent

movement and would be very advantageous for field applications where portability is essential.

There are two main properties of RTILs that make them attractive for their application in an AGS. One is negligible vapour pressure and the other is high thermal stability. Since now the behaviour of these highly toxic gases has been understood in a range of RTILs at room temperature, the step forward would be to study the behaviour of these gases in RTILs in a range of temperatures preferably at high temperatures to check the viability of these RTILs. To understand the behaviour of these gases at high temperatures would allow the development of RTIL based gas sensors that withstand harsh conditions. Understanding the behaviour of these gases in RTILs in the presence of humidity, which represents more of a real world environment, is also needed before the development of RTIL based AGSs

Investigations in mixed gas environments that represent more real world situations (e.g. in air) will be needed in the future so the behaviour of these gases in the presence of gases such as oxygen and carbon dioxide, naturally present in the environment, is understood. This study is crucial before the commercialisation of RTIL based gas sensors for these toxic gases.

In this work two types of nanomaterials were investigated as possible surface modifiers to improve current response. Preliminary studies using the synthesised nanomaterials (magnetite nanoparticles and Pt macroporous framework) for gas sensing were presented. In the case of the magnetite nanoparticles (where no significant improvement current response was seen), future work should go into incorporating these magnetic magnetite nanoparticles into RTILs and studying the behaviour of the gases in this RTIL/magnetite mixture. This could open up the

possibility of controlling the solvent with the aid of a magnet[4] which could path the way for more robust spill-less sensors. In the case of the Pt macroporous framework experiments it was found that there was a slight increase in the active sites for the oxidation of methylamine gas and also a possible catalytic shift. The electrochemical behaviour of methylamine gas should be investigated on Pt macroporous frameworks with varying pore sizes and roughness. The pore sizes and roughness of each modified electrode should then be compared to the peak current, catalytic shift and charge under the CV curve for methylamine oxidation to further understand the behaviour of these Pt macroporous frameworks.

11.3 References

(1) Murugappan, K.; Silvester, D. Sensors for Highly Toxic Gases: Methylamine and Hydrogen Chloride Detection at Low Concentrations in an Ionic Liquid on Pt Screen Printed Electrodes. *Sensors* **2015**, *15*, 26866.
(2) Carter, M. T.; Stetter, J. R.; Findlay, M. W.; Patel, V. Rational design of amperometric gas sensors with ionic liquid electrolytes. *ECS Trans.* **2014**, *64*, 95-103.
(3) Lee, J.; Du Plessis, G.; Arrigan, D. W. M.; Silvester, D. S. Towards improving the robustness of electrochemical gas sensors: impact of PMMA addition on the sensing of oxygen in an ionic liquid. *Anal. Method.* **2015**.
(4) Panchompoo, J.; Ge, M.; Zhao, C.; Lim, M.; Aldous, L. The Oxygen Reduction Reaction in Ferrofluids: Towards Membrane-less and Spill-less Gas Sensors. *ChemPlusChem* **2014**, *79*, 1498-1506.

Appendix A

NMR spectrum for [C₄mim][PF₆]

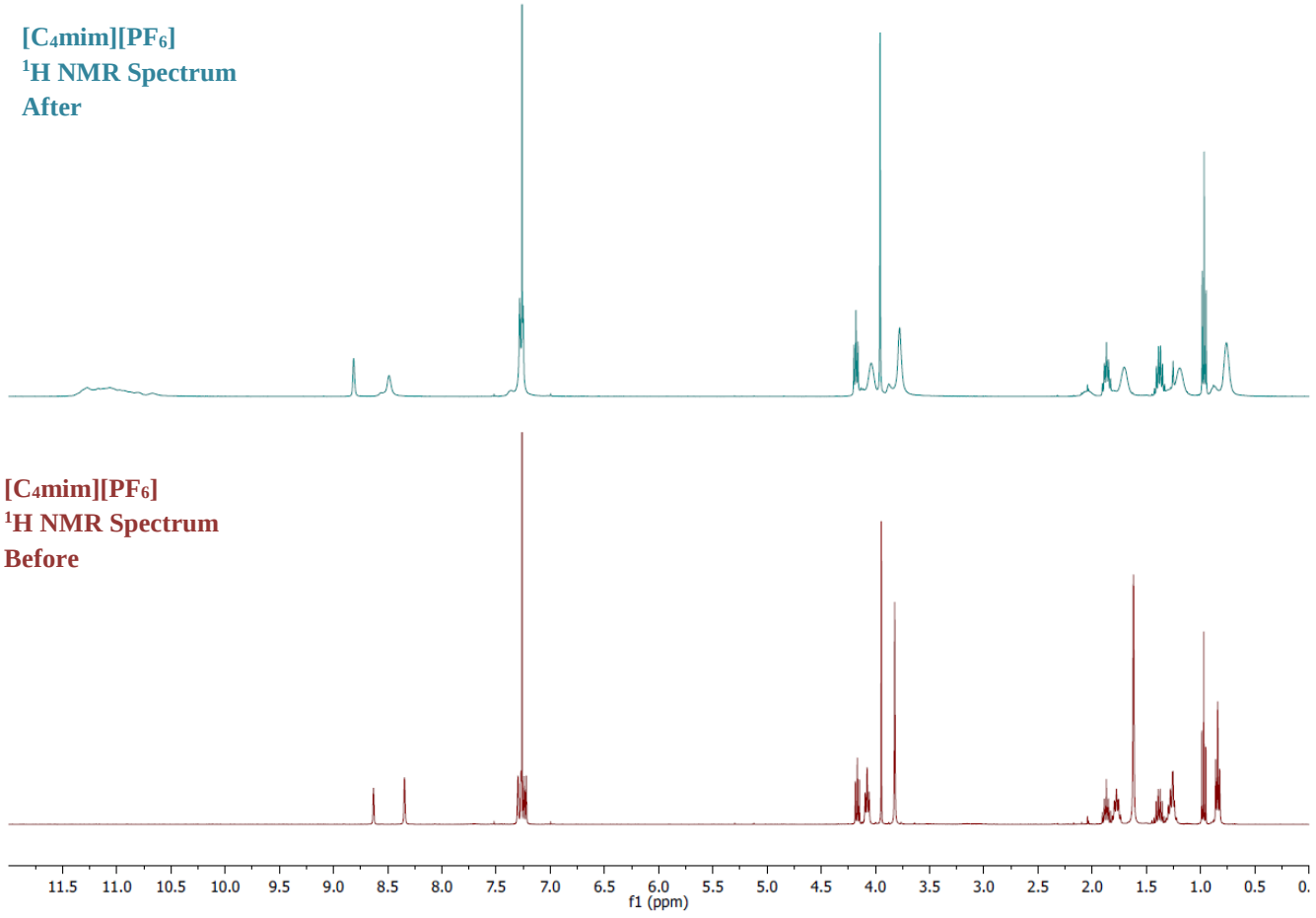

Figure A.1: NMR signals for ^{1}H in the RTIL, $[C_4mim][PF_6]$ before and after experiments with HCl

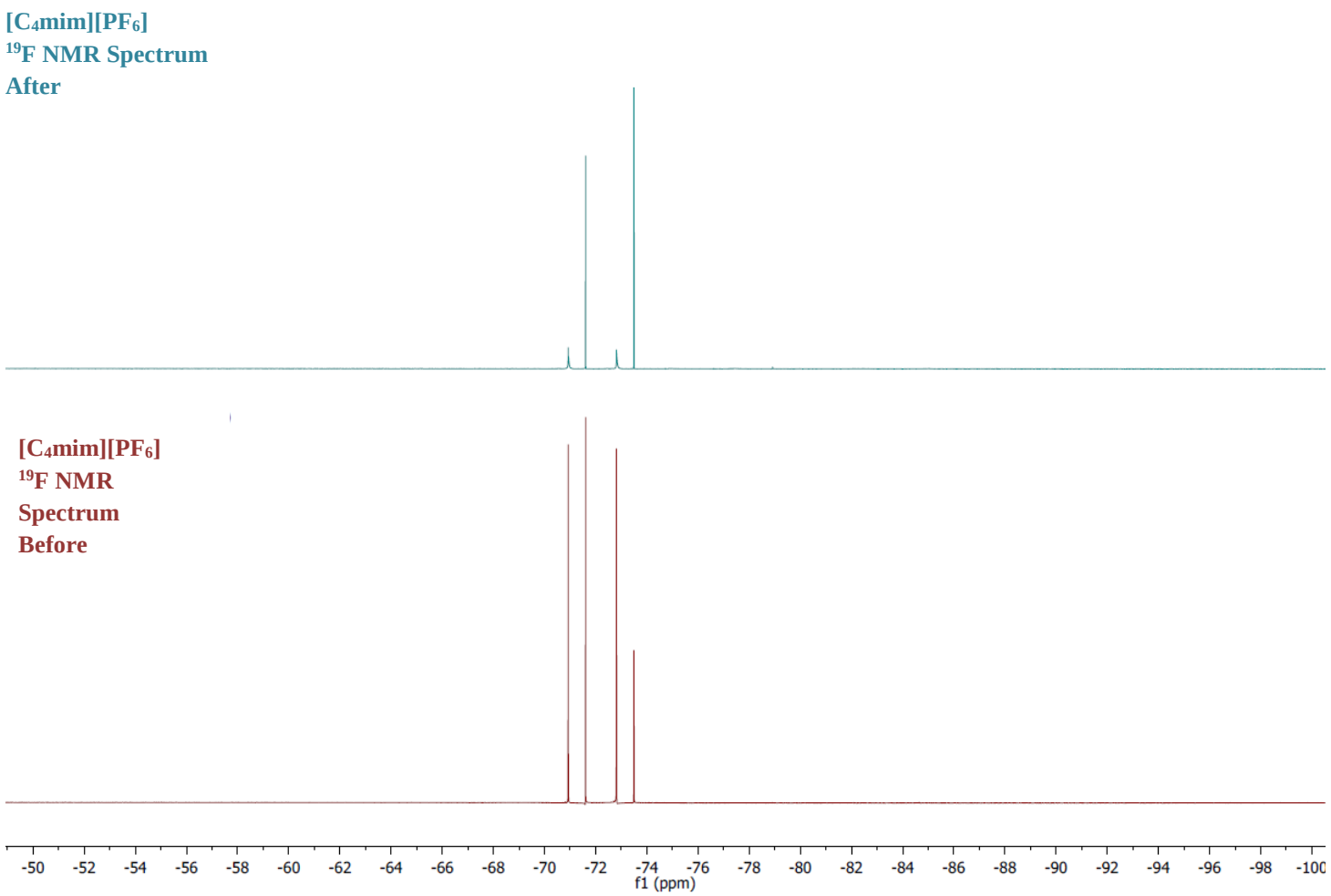

Figure A.2: NMR signals for ^{19}F in the RTIL, $[C_4mim][PF_6]$ before and after experiments with HCl

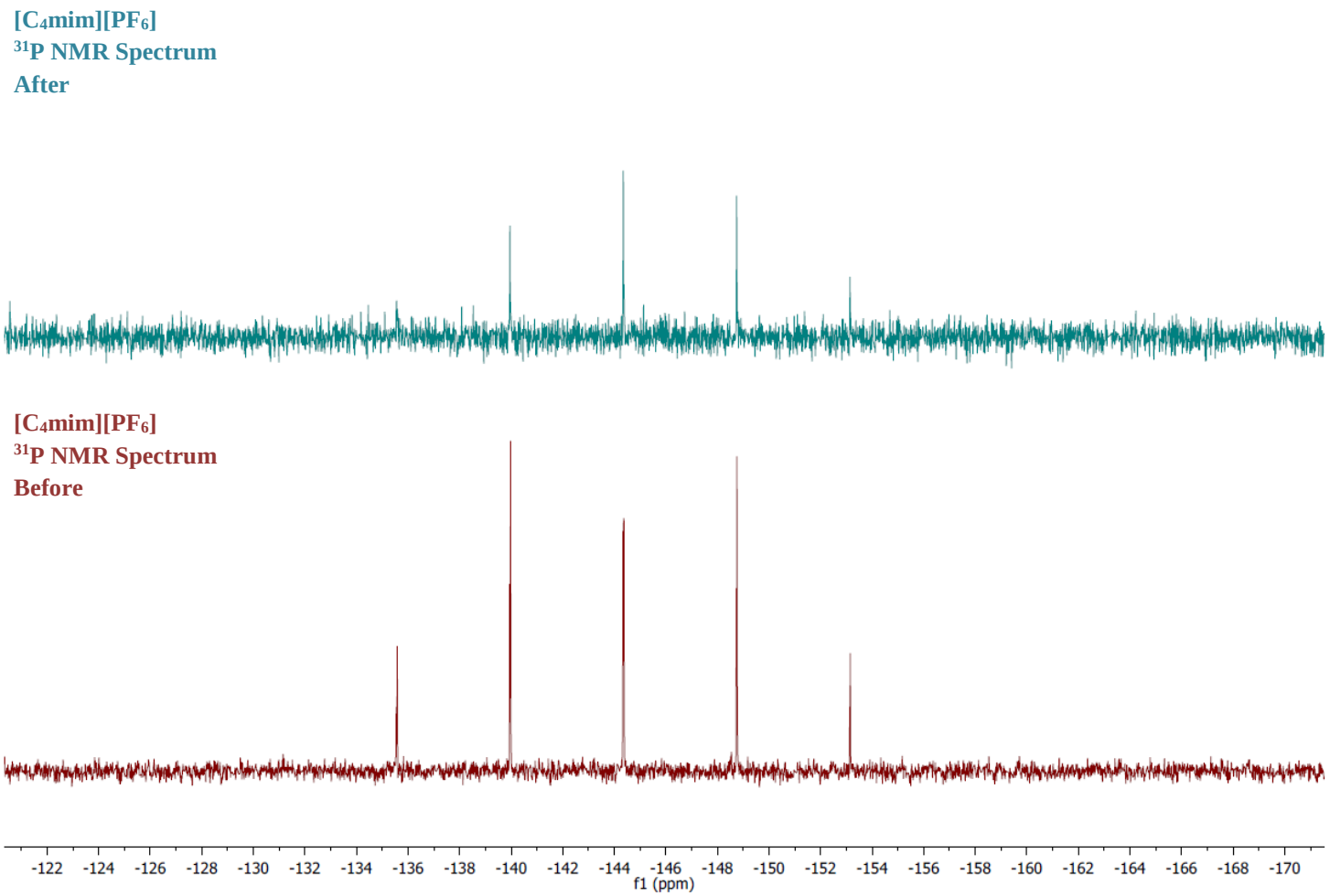

Figure A.3: NMR signals for ^{31}P in the RTIL, $[C_4mim][PF_6]$ before and after experiments with HCl

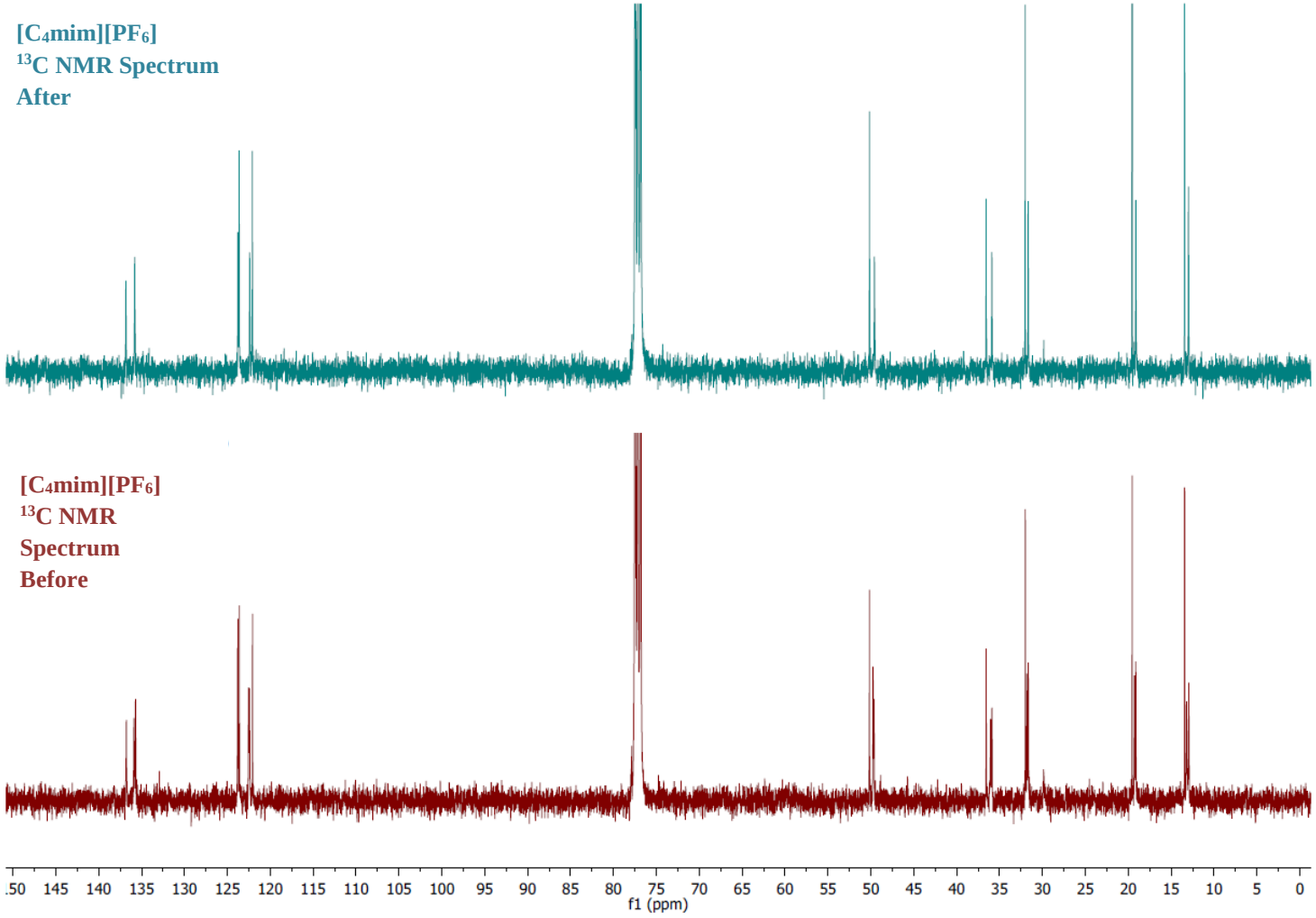

Figure A.4: NMR signals for ^{13}C in the RTIL, $[C_4mim][PF_6]$ before and after experiments with HCl

Appendix B

Journal Publications

1) Lee, J.; **Murugappan, K**.; Arrigan, D. M. W.; Silvester, D. S. "Oxygen Reduction Voltammetry on Platinum Macrodisk and Screen-Printed Electrodes: Reaction of the Electrogenerated Superoxide Species with Compounds Used in the Paste of Pt Screen-Printed Electrodes?" Electrochimica Acta. (2012) 101: 158-168. DOI: 10.1016/j.electacta.2012.09.104

2) **Murugappan, K**.; Silvester, D. S.; Chaudhary, D.; Arrigan, D. M. "Electrochemical Characterization of an Oleyl-coated Magnetite Nanoparticle-Modified Electrode" ChemElectroChem. (2014) 1: 1211-1218. DOI: 10.1002/celc.201402012
**Inside Cover (ChemElectroChem page, 1088)*

3) **Murugappan, K**.; Kang C.; Silvester, D. S. "Electrochemical Oxidation and Sensing of Methylamine Gas in Room Temperature Ionic Liquids" Journal of Physical Chemistry C. (2014) 118: 19232-19237. DOI: 10.1021/jp5061045

4) **Murugappan, K**.; Arrigan, D. M. W.; Silvester, D. S. "Electrochemical Behavior of Chlorine on Platinum MicroDisk and Screen Printed Electrodes in a Room Temperature Ionic Liquid:" Journal of Physical Chemistry C. (2015) 119: 23572-23579. DOI: 10.1021/acs.jpcc.5b07753

5) **Murugappan, K**.; Silvester, D. S. "Sensors for Highly Toxic Gases: Methylamine and Hydrogen Chloride Detection at Low Concentrations in an Ionic Liquid on Pt Screen Printed Electrodes." Sensors (2015) 15.10: 26866-26876. DOI: 10.3390/s151026866

6) **Murugappan, K**..; Silvester, D. S. "Electrochemical Studies of Hydrogen Chloride Gas in Several Room Temperature Ionic Liquids: Mechanism and Sensing:" Submitted to Physical Chemistry Chemical Physics. (2015)

Oral and Poster Presentations

1) 22nd Annual RACI Research and Development Topics Conference (Flinders University, Adelaide) December 2014
    - •Oral presentation entitled, **"The prospects of electrochemical sensing of Cl_2 gas in ionic liquids using screen printed electrodes"**
        - **Oral presentation award- 3rd best oral presentation*

2) 2014 RACI National Congress (Adelaide Convention Centre, Adelaide) December 2014
    - •Poster presentation entitled, **"The prospects of macroporous metallic frameworks for amperometric gas sensing"**

3) 65th Annual Meeting of the International Society of Electrochemistry (Lausanne Switzerland) August 2014
    - •Poster presentation entitled, **"Electrochemical behavior and analytical utility of toxic gases (chlorine and methylamine) in room temperature ionic liquids (RTILs): A comparison between microelectrodes and screen printed electrodes (SPEs)"**

4) 19th Australian/New Zealand Electrochemistry Symposium (CSIRO Clayton, Melbourne) December 2013
    - •Poster presentation entitled, **"Electrochemical toxic gas sensing of chlorine and methylamine in room temperature ionic liquids (RTILs): A comparison between microelectrodes and screen printed electrodes"**

5) 18th Australian Electrochemistry Symposium (Curtin University, Perth) April 2012
    - •Poster presentation entitled, **"Electrochemical sensing of ammonia gas in ionic liquids"**

6) 5th Australasian Symposium on Ionic Liquids (CSIRO Clayton, Melbourne) May 2012
    - •Poster presentation entitled, **"Ammonia gas sensing on screen-printed electrodes in ionic liquids"**

Appendix C

Inside Cover

Murugappan, K.; Silvester, D. S.; Chaudhary, D.; Arrigan, D. M. "Electrochemical Characterization of an Oleyl-coated Magnetite Nanoparticle-Modified Electrode" ChemElectroChem. (2014) 1: 1211-1218. DOI: 10.1002/celc.201402012

**Inside Cover (ChemElectroChem page, 1088)*